

# *International Advanced Researches and Engineering Journal*

e-ISSN  
**2618-575X**



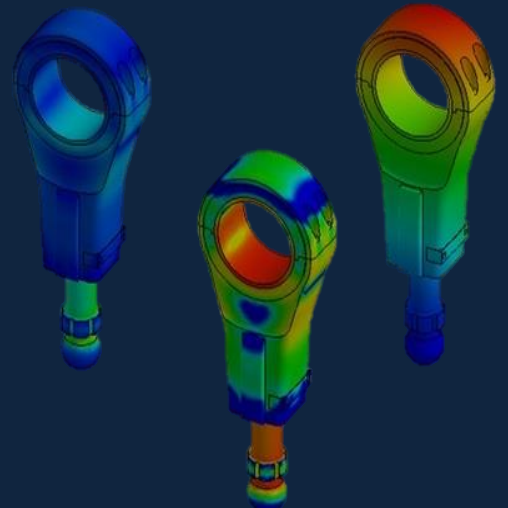
$$F=ma$$

$$E=mc^2$$

$$\int \frac{dy}{dx} dt$$

|               |              |
|---------------|--------------|
| <b>Volume</b> | <b>Issue</b> |
| <b>06</b>     | <b>02</b>    |

**August, 2022**





International Advanced Researches and Engineering Journal (IAREJ) is a double-blind peer-reviewed and publicly available online journal that has Editorial Board (<https://dergipark.org.tr/en/pub/iarej/board>). The editor in chief of IAREJ welcomes the submissions that cover theoretical and/or applied researches on **Engineering** and related science with Engineering. The publication language of the Journal is **English**. **Writing Rules** are given in Author Guidelines (<https://dergipark.org.tr/en/pub/iarej/writing-rules>). IAREJ publishes **original papers** that are research papers and technical review papers.

IAREJ publication, which is **open access**, is **free of charge**. There is no article submission and processing charges (APCs).

**IAREJ is indexed & abstracted in:**

Crossref (Doi prefix: 10.35860/iarej.)  
Directory of Open Access Scholarly Researches (ROAD)  
Directory of Research Journals Indexing (DRJI)  
EBSCO  
Google Scholar  
Index Copernicus (ICI Journal Master List)  
J-Gate  
TUBITAK ULAKBIM TR Dizin (TR index)  
WorldCAT

Authors are responsible from the copyrights of the figures and the contents of the manuscripts, accuracy of the references, quotations and proposed ideas and the Publication Ethics (<https://dergipark.org.tr/en/pub/iarej/page/4240>).

International Advanced Researches and Engineering Journal (IAREJ) allows the author(s) to hold the copyright of own articles.

©

IAREJ

15 August 2022



This is an open access issue under the CC BY-NC license (<http://creativecommons.org/licenses/by-nc/4.0/>).



e-ISSN: 2618-575X

Available online at [www.dergipark.org.tr/en](http://www.dergipark.org.tr/en)

INTERNATIONAL ADVANCED RESEARCHES  
and  
ENGINEERING JOURNAL

Journal homepage: [www.dergipark.org.tr/en/pub/iarej](http://www.dergipark.org.tr/en/pub/iarej)

International  
Open Access 

Volume 06  
Issue 02  
August, 2022

## Table of Contents

| Research Articles   | Pages   |
|---|---------|
| <a href="#">1. Non-linear displacement and deformation damage limits of reinforced concrete circular columns by analytical observations according to TBSC 2018</a><br><i>Saeid FOROUGHÍ and Bahadır YÜKSEL</i>  | 068-079 |
| <a href="#">2. Structural evolution of mechanically alloyed ODS steel powders during ball milling and subsequent annealing treatment</a><br><i>Emin SALUR</i>   | 080-089 |
| <a href="#">3. Post curing temperature effect on mechanical characterization of jute/basalt fiber reinforced hybrid composites</a><br><i>Berkay KARACOR and Mustafa ÖZCANLI</i>   | 090-099 |
| <a href="#">4. Examining the hydrophobic properties of electrospun oxide-induced polystyrene nanofibers for application in oil-water separation</a><br><i>Kemal DOĞAN, Ali Akbar HUSSAINI, Mehmet Okan ERDAL and Murat YILDIRIM</i>   | 100-105 |
| <a href="#">5. Hydroxyapatite coating processes with EPD method and investigation of mechanical properties of coatings</a><br><i>İbrahim AYDIN, Ali İhsan BAHÇEPINAR and Mehmet AYVAZ</i>   | 106-112 |
| <a href="#">6. Heat transfer system and feedback temperature controller design for safety process operation of phosphorous acid potassium salts production</a><br><i>Zeynep YILMAZER HİTİT, Pınar AYGENER, Efe YORGANCIOĞLU, Begum AKAGUN, Kemal KESENCİ, Suna ERTUNÇ and Bülent AKAY</i> | 113-122 |
| <a href="#">7. A study on the renewable energy potential of incineration of municipal solid wastes produced in Izmir province</a><br><i>Anıl BAŞARAN</i>  | 123-131 |
| <a href="#">8. A Mixed-Integer Linear Programming approach for university timetabling problem with the multi-section courses: an application for Hacettepe University Department of Business Administration</a><br><i>Akın ÖZKAN and Aydın ULUCAN</i>                                     | 132-141 |
| <a href="#">9. Predicting acceptance of the bank loan offers by using support vector machines</a><br><i>Mehmet Furkan AKÇA and Onur SEVLİ</i>   | 142-147 |
| <a href="#">10. Research on the success of unsupervised learning algorithms in indoor location prediction</a><br><i>Fatma Öney KOÇOĞLU</i>  | 148-153 |
| <a href="#">11. A real-time accurate positioning system using BLE and wireless mesh network in a shipyard environment</a><br><i>Nalan ÖZKURT, Hilal KILINÇ, Ekrem ÖZGÜRBÜZ and Hasan Hüseyin ERKAN</i>  | 154-160 |



### Research Article

## Non-linear displacement and deformation damage limits of reinforced concrete circular columns by analytical observations according to TBSC 2018

Saeid Foroughi <sup>a,\*</sup>  and S. Bahadır Yüksel <sup>a</sup> 

<sup>a</sup> Konya Technical University, Faculty of Engineering and Natural Sciences, Department of Civil Engineering, 42130, Konya / Turkey

| ARTICLE INFO   | ABSTRACT   |
|--|--|
| <p><i>Article history:</i><br/>Received 15 January 2022<br/>Accepted 08 June 2022<br/>Published 15 August 2022</p> <p><i>Keywords:</i><br/>Non-linear behavior<br/>Moment-curvature<br/>Performance level<br/>Deformation limit<br/>Plastic rotation</p> | <p>In the study, based on the non-linear calculation methods used to determine the seismic performance of structures in TBSC 2018, the stress-strain, moment-curvature, displacement capacity, plastic rotation limits, and deformation-based damage limit values of the reinforced concrete circular cross-section columns were calculated and compared according to different design parameters. The studied effects of the design parameters on the non-linear relation of reinforced concrete columns were also evaluated in terms of strength, curvature, and displacement ductility of the sections. All design parameters affecting the non-linear behavior and deformation limits of the reinforced concrete circular cross-section columns were taken into account. Deformation demands for reinforced concrete structural members are essential for detecting element damage. Based on TBSC (2018), non-linear relationships of reinforced concrete columns were obtained in order to calculate plastic hinge properties and deformation limits. For the Limited Damage, Controlled Damage, and Collapse Prevention performance levels defined for the structural elements in TBSC 2018, plastic rotation and deformation limit values were obtained according to the characteristic values calculated from the non-linear analyzes of reinforced concrete circular columns. For column models, damage limits and damage zones calculated based on TBSC 2018 were shown on the visually obtained moment-curvature relationships. Depending on the upper deformation limit values derived, cross-sectional deformation damage levels were determined and evaluated using the moment-curvature relationships. The variation of the non-linear behavior of column models by design parameters and deformation-based damage limits were examined both analytically and visually. The deformation limits remain in a safer direction as a result of increasing longitudinal and spiral reinforcement ratios for the reinforced concrete circular columns.</p> |

### 1. Introduction

In determining the earthquake safety of existing building systems, using methods that predict performance analysis is considered more appropriate. By using these methods based on the non-linear theory, the behavior of building systems under external loads and earthquake effects can be predicted, and earthquake performances due to displacements and deformations can be determined more realistically [1-2]. The performance-based design of reinforced concrete (RC) structures involves the designing of structures by calculating specific structural performance or damage limits using deformation-based methods under the influence of earthquakes. The deformation-based design method takes into account the non-linear behavior of the materials that make up the RC structural members [3]. This method is very important in terms of providing

the desired life safety performance target and criteria without a decrease in load carrying capacity under the effect of earthquake loads applied to RC structural elements [4]. Ductility of carrier elements is an important parameter in terms of structural safety. The ductility of the carrier elements that make up RC structures is the property that allows the structures to dissipate energy in the seismic region [5-6]. To be able to understand and realize the ductile seismic design of RC structures better, it is necessary to estimate the deformation capacity of structural bearing elements under effective earthquakes [7]. Many of the building collapses that have occurred in the past have been caused by insufficient column behavior. The main causes of column failures in buildings are shear failure and insufficient ductility capacity. In the performance assessment methods of existing structures, seismic codes generally determine the performance of

\* Corresponding author. Tel.: +90 332 205 17 71.

E-mail addresses: [saeid.foroughi@yahoo.com](mailto:saeid.foroughi@yahoo.com) (S. Foroughi), [sbyuksel@ktun.edu.tr](mailto:sbyuksel@ktun.edu.tr) (S.B. Yüksel)

ORCID: 0000-0002-7556-2118 (S. Foroughi), 0000-0002-4175-1156 (S.B. Yüksel)

DOI: [10.35860/iarej.1058369](https://doi.org/10.35860/iarej.1058369)

© 2022, The Author(s). This article is licensed under the CC BY-NC 4.0 International License (<https://creativecommons.org/licenses/by-nc/4.0/>).

structural elements on their plastic rotational capacities [8-10]. In the regulations, the damage limits that determine the performance are determined by taking into account the plastic rotations calculated by considering the material deformation limits [11].

Whereas strength-based seismic design focuses on the estimation of internal forces, performance-based design focuses on the estimation of deformations [12]. The deformation-based design and assessment method is more advantageous than the strength-based design method because it allows taking into account the non-linear behavior of the material. The purpose of the deformation-based design and assessment methods to be used to determine the structural performance of RC structures under earthquakes is to calculate the internal force demands for brittle behavior and the deformation demands for ductile behavior [1, 3, 13-14]. It is very important to know the behavior of RC columns under earthquake effects and to calculate the column damage limits for this behavior. The damage limits used in determining the performance can be calculated based on the amount of plastic rotation in the sections. Plastic rotation amounts are determined according to the deformation limits of the materials that make up the structure [15-21].

Guidelines and codes have been prepared recently to provide procedures and acceptance criteria for the seismic design and assessment of RC buildings. The Turkish Building Seismic Code (TBSC) [11] is among the most recent ones containing sections on the seismic assessment of existing and newly constructed RC buildings. In the TBSC code, assessment and acceptance criteria are given on the basis of the elements that make up the structural system. The performance level evaluations of load-bearing elements are generally made according to the performance-based displacement capacities determined for the members. These deformation limits depend on the dominant behavior mode of the members. In the existing codes issued for the seismic evaluation of RC buildings, plastic rotation is adopted as the amount of deformation, and chord rotation is adopted as the measure of deformation. Unlike others, TBSC gives deformation limits in terms of strains [22].

Accurate analysis of the non-linear behavior of RC structural members has always been an important subject of study because it provides a reliable estimate of the capacity and performance of buildings under seismic and vertical load effects. According to TBSC [11], non-linear behaviors such as material strengths, reinforcement configuration in the section, stress-strain, moment-curvature relations, and plastic hinge properties are taken into account in the calculation of the deformation-based damage limits for different performance levels in RC structural elements. In addition, in TBSC, deformation-based damage limits and damage zones are calculated

according to different performance levels for RC structural members [11].

In the study, non-linear inelastic calculation methods used to determine the earthquake performance of existing or newly built structures according to TBSC [11] were examined and stress-strain, moment-curvature, plastic rotation, and deformation-based damage limits of the designed RC circular column model were calculated. In order to obtain a more accurate simulation of the real structural behavior, non-linear moment-curvature relationships and stress-strain relationships of structural members should be investigated [23]. Based on TBSC [11], non-linear stress-strain, moment-curvature, and displacement relationships of the column sections to be considered in the analyses were first obtained in order to calculate the plastic rotation and deformation limit values. In previous studies, it has been observed that the moment-curvature, lateral force-peak displacement, curvature ductility, and displacement ductility behaviors of RC structural members are significantly affected by changes in the axial load, longitudinal and transverse reinforcement ratios [24-26]. It is known that the non-linear behavior of reinforced concrete structural members depends on many parameters such as axial load, concrete grade, displacement ductility, transverse and longitudinal reinforcement ratio, seismic performance level, and applied force-displacement history [27]. In the analyses, all the design parameters affecting the non-linear behavior such as axial load level, spiral reinforcement ratio, and concrete grade in RC circular columns were taken into account.

The basic philosophy in the design according to the deformation approach is based on the determination of the strength capacities of the elements that make up the structural system by non-linear analysis. The non-linear behavior of the designed RC column members was examined regarding the stress-strain obtained based on the real material behavior of concrete and reinforcing steel, and the moment-curvature relations according to different design parameters. Confined concrete strengths were calculated based on the Mander model [28] and the obtained stress-strain results were compared. Moment-curvature relations of RC columns were obtained with the SAP2000 [29] software by considering the non-linear behavior of concrete and reinforcing steel and presented graphically. Based on the characteristic values obtained from the non-linear analysis, damage limit values were calculated for the circular columns section. The plastic rotation and deformation limit values were calculated for the Limited Damage (SH), Controlled Damage (KH), and Collapse Prevention (GÖ) performance levels as defined in TBSC [11]. Based on the TBSC [11], deformation damage limits and damage regions were visually processed on the moment-curvature relations obtained for

RC columns. Thus, it was ensured that the deformation limits and regions to be monitored visually on the moment-curvature relations could be easily interpreted by the performance evaluation of the columns.

**2. Permitted Deformation Limits According to TBSC**

The damage limits calculated for different performance levels of RC structural members and the evaluation of damage status are very important in the performance-based seismic design of earthquake-resistant RC structures [30]. To be able to apply the life safety-oriented performance-based seismic design method of RC structures, it is necessary to quantify the seismic performance indexes for structural members [31]. In the performance assessment to be made in TBSC [11], SH, KH, and GÖ performance levels and damage limit values were defined for structural RC load-bearing elements. Regarding RC members, SH defines a limited amount of performance level, KH's strength can be achieved safely, and GÖ defines advanced non-linear behavior. For different performance levels, the limit values for reinforcing steel and concrete unit deformation according to the distributed plastic behavior model are given in Table 1. Plastic rotation limit values according to the lumped plastic behavior model for performance levels are given in Table 2. Plastic rotation values can be calculated based on the moment-curvature relations by taking into account the axial load level and material models in the load-bearing elements. The mechanical reinforcement ratio of the effective confining reinforcement ( $\omega_{we}$ ) is calculated as in Equation (1).

$$\omega_{we} = \alpha_{se} \rho_{sh,min} \frac{f_{ywe}}{f_{ce}}; f_{ywe}=1.2f_{yk}, f_{ce}=1.3f_{ck} \quad (1)$$

where  $\alpha_{se}$  is confinement effectiveness coefficient,  $\rho_{sh,min}$  is volumetric spiral reinforcement ratio,  $f_{ywe}$  and  $f_{ce}$  are expected yield strength of reinforcement and expected compressive strength of concrete,  $f_{ck}$  is the compressive strength of unconfined concrete, and ( $f_{ck}=30-50\text{MPa}$ ) and  $f_{yk}$  are yield strength of transverse reinforcement ( $f_{yk}=420\text{MPa}$ ).

The confinement effectiveness coefficient of the circular confining reinforcement in circular cross-section elements is given in Equation (2) and the volumetric ratio of the spiral confining reinforcement is given in Equation (3). In these equations,  $s$  and  $A_{os}$  are spacing and area of spiral reinforcement, and  $D$  is the concrete core dimension to center line of perimeter spiral reinforcement.  $n=1$  for spiral reinforcement.

$$\alpha_{se} = \left(1 - \frac{s}{2D}\right)^n \quad (2)$$

$$\rho_{sh} = \frac{2A_{os}}{Ds} \quad (3)$$

**3. Non-linear Behavior of Reinforced Concrete Columns**

According to TBSC [11], in the calculation of deformation and internal forces for different performance levels of RC structural elements, non-linear behavior such as material strengths, reinforcement configuration in cross-section, stress-strain, moment-curvature, displacement relationships, and plastic hinge properties are taken into account. Stress-strain relations proposed by Mander et al. [28] were used for unconfined and confined concrete models in the performance evaluation according to deformation with non-linear methods.

Table 1. Total unit deformations of concrete and reinforcing steel according to different performance levels [11]

| Deformation Limits | Concrete   | Reinforcement                               |
|--------------------|--|---|
| GÖ                 | a) $\epsilon_c^{(GÖ)} = 0.0035 + 0.04\sqrt{\omega_{we}} \leq 0.018$<br>b) $\epsilon_c^{(GÖ)} = 0.0035 + 0.07\sqrt{\omega_{we}} \leq 0.018$ | $\epsilon_s^{(GÖ)} = 0.40\epsilon_{su}$     |
| KH                 | $\epsilon_c^{(KH)} = 0.75\epsilon_c^{(GÖ)}$  | $\epsilon_s^{(KH)} = 0.75\epsilon_s^{(GÖ)}$ |
| SH                 | $\epsilon_c^{(SH)}=0.0025$   | $\epsilon_s^{(SH)}=0.0075$                  |

a) rectangular columns, beams, and shear walls, b) Columns with circular cross-sections

Table 2. Plastic rotations for different performance levels [11]

| Deformation Limits | Plastic Rotations  |
|--------------------|--|
| GÖ                 | $\theta_p^{(GÖ)} = \frac{2}{3} \left[ (\phi_u - \phi_y) L_p \left( 1 - 0.5 \frac{L_p}{L_s} \right) + 4.5 \phi_u d_b \right]$ |
| KH                 | $\theta_p^{(KH)} = 0.75\theta_p^{(GÖ)}$  |
| SH                 | $\theta_p^{(SH)} = 0$  |

$\phi_u$ ; Maximum curvature,  $\phi_y$ ; Yield curvature,  $L_p$ ; Plastic hinge length,  $L_s$ ; Shear span,  $d_b$ ; longitudinal reinforcement diameters.

The moment-curvature relations are required for the non-linear analysis of RC structures to predict section strength, stiffness, and ductility. For RC columns, the theoretical moment-curvature analysis can be done if the stress-strain relationships of both concrete and reinforcing steel are known. Accurate determination of the moment-curvature relationship of RC load-bearing elements is a reliable indicator of the load capacity of structures subjected to seismic loads [32].

In order to perform structural design under the influence of earthquakes and to examine the seismic behavior of the structure, first of all, the behavior of the materials and elements that make up the structure should be known. The behavior of the carrier element under the effect of simple flexural and normal force or only simple flexural can be examined by obtaining the moment-curvature relation, and the changes in ductility level and stiffness can be observed by looking at its behavior. The moment-curvature relations were calculated by considering the Mander unconfined and confined concrete model [28] and the material properties given for the reinforcing steel in Figure 2. The concrete model developed by Mander et al. [28] was used for unconfined and confined concrete models in the analysis of RC column models. According to the Mander model [28]; confinement effectiveness coefficient ( $k_e$ ), Effective lateral confining stresses applied to core concrete in x and y directions ( $f'_{lx}$  and  $f'_{ly}$ ), confined concrete compressive strength ( $f'_{cc}$ ), and the corresponding strain at maximum concrete stress ( $\epsilon_{cc}$ ) can be calculated by Equations (4-7), respectively. The maximum compressive strain in the confined concrete ( $\epsilon_{cu}$ ) can be found by Equation (8). In the equation,  $\rho_s$  is the volumetric ratio of the total transverse reinforcement [33].

$$k_e = \left(1 - \sum_i^n \frac{(w'_i)^2}{6}\right) \left(1 - \frac{S'}{2b_c}\right) \left(1 - \frac{S'}{2d_c}\right) / (1 - \rho_{cc}) \quad (4)$$

$$f'_{lx} = k_e \frac{A_{sx}}{s \cdot d_c} f_{yh} = k_e \cdot f_{lx} \quad (5)$$

$$f'_{ly} = k_e \frac{A_{sy}}{s \cdot b_c} f_{yh} = k_e \cdot f_{ly}$$

$$f'_{cc} = f'_{co} \left( -1.254 + 2.254 \sqrt{1 + \frac{7.94 f'_l}{f'_{co}}} - 2 \frac{f'_l}{f'_{co}} \right) \quad (6)$$

$$\epsilon_{cc} = \epsilon_{co} \left[ 1 + 5 \left( \frac{f'_{cc}}{f'_{co}} - 1 \right) \right] \quad (7)$$

$$\epsilon_{cu} = 0.004 + \frac{1.4 \rho_s f_{yw} \epsilon_{su}}{f'_{cc}} \quad (8)$$

For a comprehensive performance-based seismic assessment of existing or newly constructed RC framed structures, estimating the displacement capacity of the columns and their deformation relationships is crucial [34]. The displacement and deformation capacity of reinforced concrete columns are formed by sectional

damage under seismic loads [35]. The displacement ductility of RC load-bearing members is an important parameter characterizing the seismic response of RC structures. Additionally, displacement ductility can be used to determine whether a structural design based on earthquake codes will achieve the main goal of seismic design [36].

The ductile deformation capacity of RC columns as resistant to the effects of lateral loads is an important factor for achieving a better seismic performance in structures. Reinforced concrete columns designed with sufficient ductility typically prevent brittle fracture of structures. Ductility is an important property in terms of the determination of whether the seismic response of structures is suitable for the initial targets for which they were designed. The seismic design and evaluation of structural members should not only focus on strength but should also take into account the ductility of the members. In order to better understand and evaluate the ductile seismic design, the deformation capacity of the structural elements under the effect of severe seismic loads should be calculated [24]. The performance evaluation methods taken into account in obtaining the non-linear displacement capacity of the structural elements can be calculated by considering the plastic hinge and the displacement-controlled seismic design method [25]. The catastrophic deterioration of the mechanical strength of columns at final displacements is an important factor in terms of the seismic collapse of RC structures. Accurately calculating the deterioration of the mechanical strength is critical for evaluating the seismic collapse capacity of structures [37]. Reinforced concrete columns are exposed to lateral displacements under gravity loads and severe earthquake effects, and major damages occur in the plastic hinge regions where non-linear deformations occur. Deformations occur in the plastic hinge regions of the structural elements. To calculate large lateral displacement capacities, the structural members must have a large curvature capacity in the plastic hinge region.

The plastic hinge method is used in the seismic design and performance evaluation of RC columns according to displacement-based. In RC structural members, the lumped plastic rotation values ( $\theta_p$ ) along the length of the plastic hinge ( $L_p$ ) are calculated as shown in Equation (8). The bending displacement capacity ( $\Delta_u$ ) of RC columns is obtained as the sum of yield ( $\Delta_y$ ) and plastic displacements ( $\Delta_p$ ) (Equation 9). The term  $(\phi_u - \phi_y)L_p$  in the equation refers to the plastic rotation based on the assumption of plastic curvature, where the plastic hinge region is stacked at its center. In RC columns, the plastic hinge length ( $L_p$ ) shall be taken as half of the section height in the active direction ( $L_p = 0,50h$ ).  $\phi_y$  and  $\phi_u$  are yield and ultimate curvature values, respectively (Figure 1).

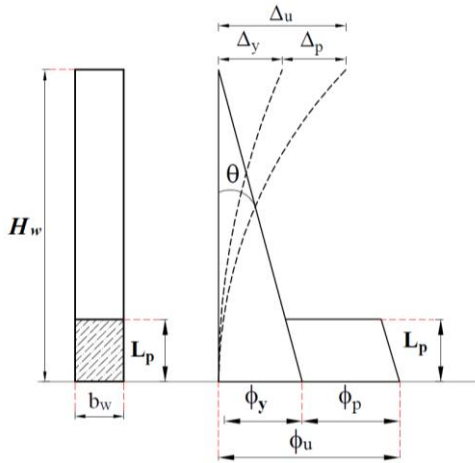


Figure 1. Theoretical model of elastic and plastic displacements in cantilever column

$$\theta_p = \varphi_p L_p = (\varphi_u - \varphi_y) L_p \tag{9}$$

$$\Delta_u = \frac{\varphi_y \times H_w^2}{3} + (\varphi_u - \varphi_y) L_p (H_w - 0.5 L_p) \tag{10}$$

**4. Materials and Method**

In this study, depending on the non-linear behavior and calculation methods, the seismic performance of RC column models was analytically investigated by considering the displacement capacity and the deformation-based damage limits. The displacement capacities are taken into account in the theoretical model of elastic and plastic displacements for the cantilever column. Deformation values for RC column models are calculated for SH, KH, and GÖ performance levels defined in TBSC [11]. Total unit deformation limits of concrete were calculated based on spiral ratios and plastic rotation limit values at axial loads, and they were examined for different performance levels. The unit deformations of reinforcing steel is calculated by multiplying the strain in reinforcement at ultimate strength with constant coefficients for different damage levels.

Circular cross-section columns are popular for column design of RC structures since their strength characteristics under seismic effects are similar in all directions. Therefore, circular column models with diameters of D=565mm and with the different concrete grades, spiral reinforcement diameters, spiral reinforcement spacing, and different axial loads were designed (Table 3 and Figure 2). How different design parameters such as material properties, axial load levels, rebar diameter, and spacing affected the non-linear behavior of the bearing elements and ductility criteria were calculated. Non-linear stress-strain, moment-curvature, and displacement capacity of RC columns were first obtained in order to calculate deformation limits and plastic hinge properties according to TBSC [11].

In RC column models, the total displacement values were obtained according to the yield, and plastic displacement values were calculated by taking into account the axial load levels acting on the section according to the plastic hinge length. For the calculation of the total peak displacement values of the RC columns, characteristic yield and ultimate curvature (pre-failure curvature) values were obtained from the section properties, plastic hinge length, and non-linear analysis. The results are presented and interpreted in tables and graphs. For RC circular cross-section columns, the deformation damage limits and damage regions obtained based on the TBSC [11] regulation are given visually on the moment-curvature relations. Thus, the deformation damage limits and regions to be monitored visually on the moment-curvature relations will be easily interpreted by the performance evaluation of the bearing elements. Elastic and plastic displacements of RC circular column models were analytically calculated based on the cantilever column model. Accordingly, deformation limits calculated according to TBSC [11] are valid for circular cantilever columns (column height, h=3500mm).

Table 3. Designed column section details

| Material (MPa) | Spiral Reinforcement |         | Axial Load (N/N <sub>max</sub> ) |
|----------------|----------------------|---------|----------------------------------|
|                | Diameters            | spacing |                                  |
| C30            |                      | 50mm    |                                  |
| C35            | Φ8mm                 | 55mm    | 0.10                             |
| C40            | Φ10mm                | 60mm    | 0.20                             |
| C45            | Φ12mm                | 65mm    | 0.30                             |
| C50            |                      | 70mm    | 0.40                             |
|                |                      | 75mm    |                                  |
|                |                      | 80mm    |                                  |

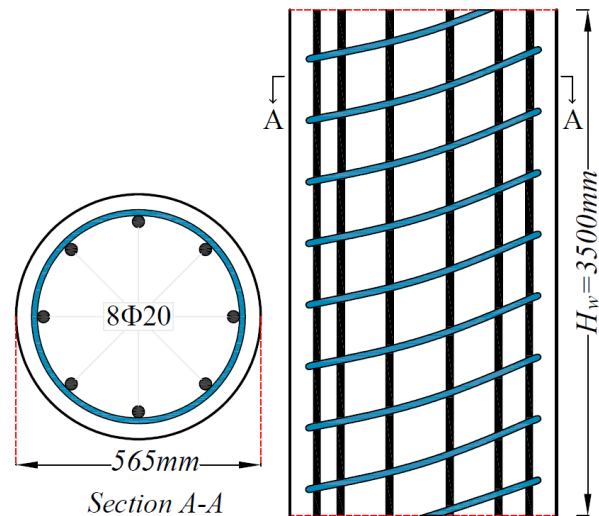


Figure 2. Sectional geometry and reinforcement layout view of the designed RC circular columns



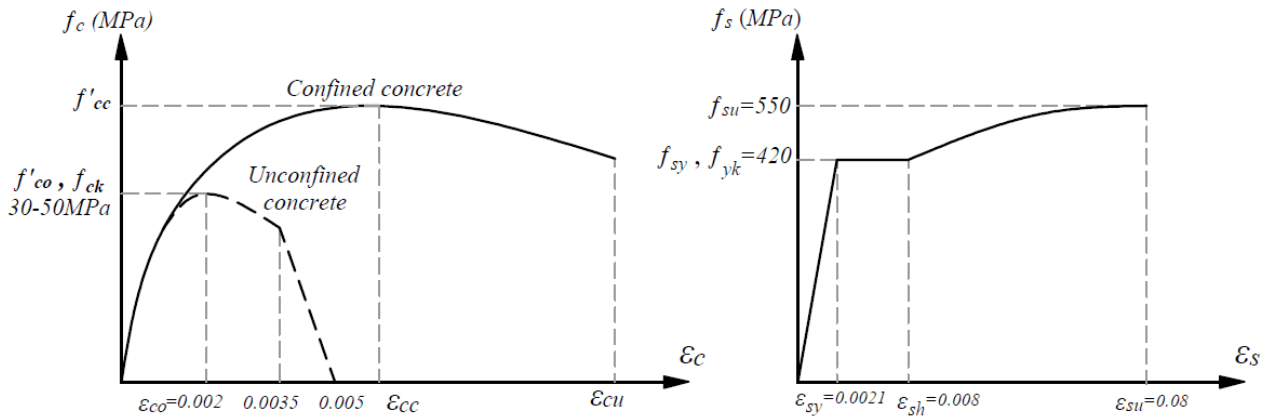


Figure 3 Stress-strain relationship for materials [11]

In the non-linear analysis of RC column models, the material models for concrete and reinforcing steel are given in Figure 3. The combined effect of seismic and vertical loads ( $N_{dm}$ ), cross-section area of RC column shall satisfy the condition  $A_c \geq N_{dm}/0.40f_{ck}$  [11]. In this study,  $N/N_{max}$  ratios of 0.10, 0.20, 0.30, and 0.40 were taken into account to investigate the effect of axial load levels on the non-linear analysis of RC circular columns.

In the designed circular column models, the minimum ratio of the spiral reinforcement and the volumetric ratio of the spiral reinforcement are taken into account based on the conditions given in TBSC [11] and ACI318 [39] regulations. TBSC [11] and ACI318 [39] state that the ratio of spiral reinforcement shall not be less than Equations (10) and (11).  $A_c$  and  $A_{ck}$  are gross section area and core concrete area of column, respectively.

## 5. Numerical Study

### 5.1 Stress-Strain Relation of Circular Columns

In the designed RC circular column models, the stress-strain relations for the confined concrete were obtained according to different spiral reinforcement ratios and concrete grade. The compressive stresses as a function of the compressive strain of the confined concrete were presented comparatively. The effect of the design parameters in the column sections on the stress-strain relationship of the confined concrete was calculated and compared (Figure 4). Although the yield strength of the spiral reinforcement used in the models was constant, it was concluded that the use of spiral reinforcement in different diameters and spacing values affects the lateral compressive strength of the designed reinforced concrete column sections. Increasing the spiral reinforcement ratio should be expected to have the same effect; therefore, it is normal for the section bearing capacity to increase when the spiral reinforcement is increased. As the spiral reinforcement spacing is reduced and the spiral reinforcement diameter increases, the ductility increases

due to the confining effect. For the constant spiral reinforcement spacing in circular cross-section column models, it was concluded that the compressive strength of the confined concrete, calculated with the increase of the spiral reinforcement diameter, increases. For constant concrete grade,  $\epsilon_{cc}$  and  $\epsilon_{cu}$  values increase as spiral reinforcement diameter increases (confined concrete has more ductile behavior). For the constant spiral reinforcement ratio, as the concrete grade increases, the  $f_{cc}$  also increases, but the confined concrete exhibits a brittle behavior ( $\epsilon_{cc}$  and  $\epsilon_{cu}$  values decrease). According to the constant spiral reinforcement diameter,  $\epsilon_{cc}$  and  $\epsilon_{cu}$  values decrease as spiral spacing and concrete grade increase. Since the longitudinal reinforcement ratio in the confined concrete models does not have a significant effect on the  $f_{cc}$ ,  $\epsilon_{cc}$ ,  $\epsilon_{cu}$  values and the ductility of the column sections, it was considered constant in this study.

$$\rho_s = 0.45 \left( \frac{A_c}{A_{ck}} - 1 \right) \frac{f_{ck}}{f_{yk}} \quad (11)$$

$$\rho_{sh} \geq 0.12 \left( \frac{f_{ck}}{f_{yk}} \right) \quad (12)$$

### 5.2 Moment-Curvature Relationships of Circular Columns

The moment-curvature analysis is required to calculate the non-linear behavior, strength, stiffness, and ductility of structural members. Moment-curvature relations are obtained according to different design parameters for circular column models. Moment-curvature relations of the designed RC circular section column models were obtained by making necessary analyses according to different design parameters, and investigations were made. The ductility of the RC column section can be expressed as the ratio of the maximum curvature to the yield curvature  $\mu_\phi = \phi_u/\phi_y$ . In the RC circular columns, the influence of different design parameters on the  $M-\phi$  and  $\mu_\phi$  are shown in Figures 5-6, respectively.

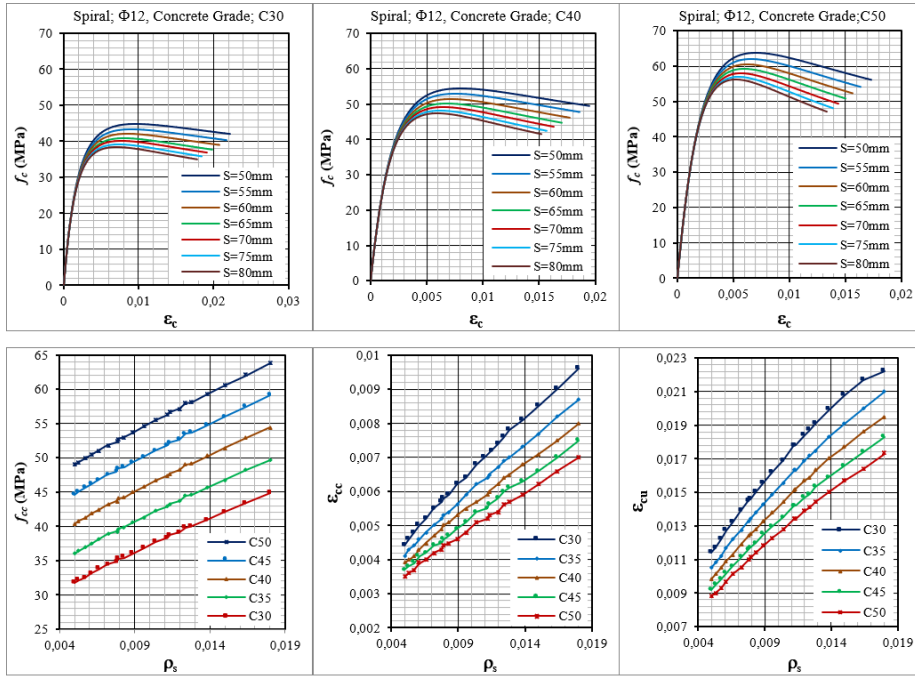


Figure 4. Stress-strain relationships of the RC circular columns according to Mander model

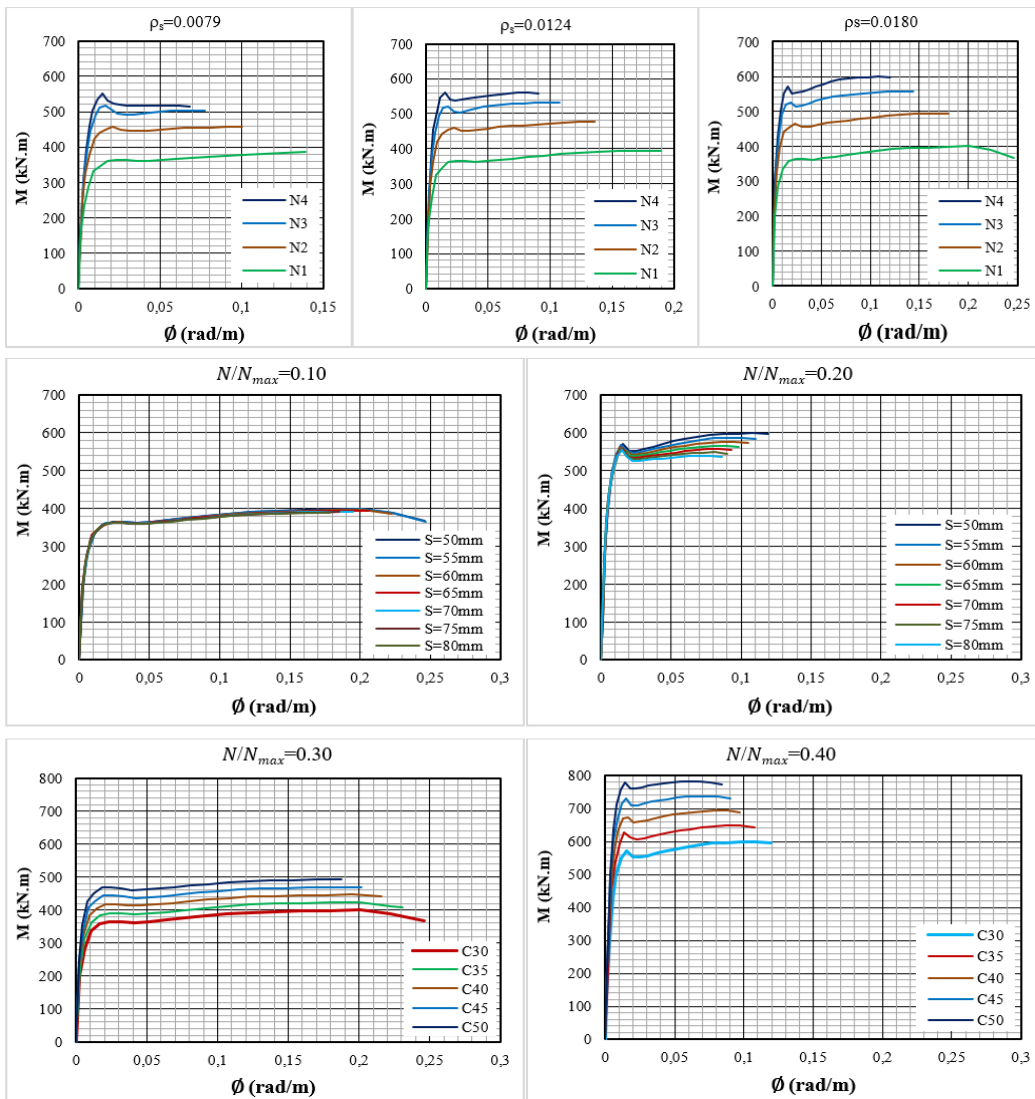


Figure 5. Moment-curvature relations for RC circular columns according to different design parameters

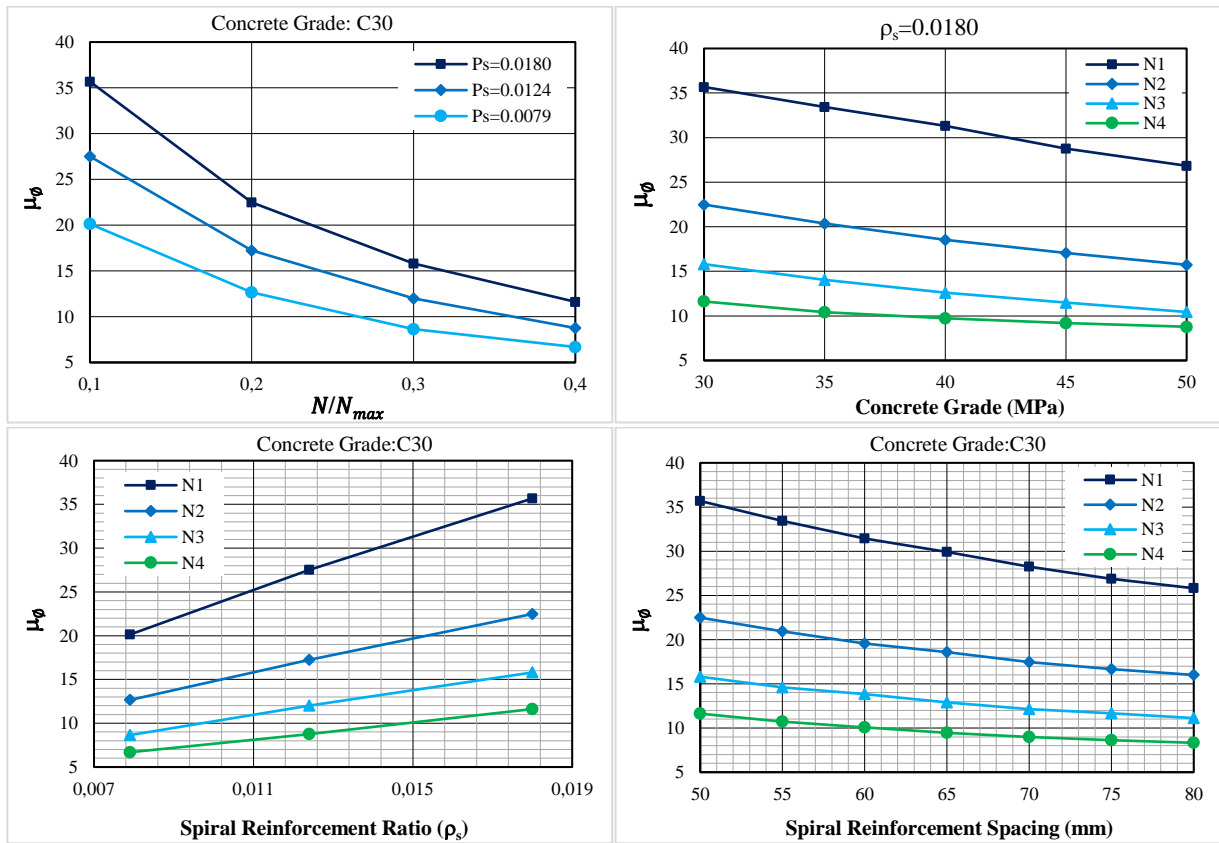


Figure 6. Influence of different parameters on the curvature ductility

When the moment-curvature analysis results of the RC circular column models are examined, it is seen that the variation of the axial load and spiral reinforcement has a significant effect on the non-linear behavior of the sections. For the constant spiral reinforcement and concrete grade, ductility values of column sections decrease as the axial load level increases. As a result of the increase in the spiral ratio, the moment capacity values of the column increase. As the moment bearing capacity increases with the increase in the spiral reinforcement ratio, the section ductility also increases. The spiral ratio is important for the ductility behavior of the columns and the curvature values increase significantly.

### 5.3 Non-linear Displacement of Circular Columns

In order to calculate the displacement capacity and ductility demands of RC circular cross-section columns, the  $\Delta_y$  and  $\Delta_p$  values according to the  $\phi_y$  and the length of the plastic hinge of the sections were calculated, and the  $\Delta_u$  value was obtained. The displacement ductility ( $\mu_\Delta$ ) values were calculated based on the calculated  $\Delta_y$  and  $\Delta_u$  values. The  $\Delta_u$  and  $\mu_\Delta$  values were calculated based on axial loads and plastic hinge analysis in circular columns.  $\Delta_y$  and  $\Delta_p$  were taken into account in the calculation of  $\Delta_u$  values of columns. In the RC circular columns, the influence of different design parameters on the  $\Delta_u$  and  $\mu_\Delta$  are shown in Figures 7 and 8 respectively.

There are differences in  $\phi_y$ ,  $\phi_u$ ,  $\Delta_y$ ,  $\Delta_p$ ,  $\Delta_u$  and  $\mu_\Delta$  values calculated for the axial load levels. As the axial load levels increase, the  $\Delta_p$ ,  $\Delta_u$  and  $\mu_\Delta$  values decrease. As the spiral reinforcement ratio increases, the  $\Delta_u$  and  $\mu_\Delta$  values increase. As the spiral spacing increases, the  $\Delta_u$  and  $\mu_\Delta$  values decrease. The  $\mu_\Delta$  value decreases with increasing  $\Delta_y$  values and decreasing  $\Delta_u$  values.

### 5.4 Deformation Limits for Different Performance Levels

According to the non-linear calculation method, one of the most important steps in performance evaluation is to determine the damage limits for different performance levels in the structural elements. Deformation demands, which are taken as a basis for the evaluation, are also of great importance in order to determine the damage that will occur to the structural elements. In the calculation of deformation limits and plastic hinge properties, three different deformation limits (GÖ, KH, and SH performance levels) defined in TBSC [11] were used. In TBSC [11], the deformation limits given for reinforcing steel at different performance levels are obtained by multiplying the unit deformation values corresponding to the tensile strength of reinforcing steel by constant coefficients. The deformation limits for the  $A_s$  constant values, GÖ, KH, and SH performance levels are given as  $\varepsilon_s^{(GÖ)} = 0.0320$ ,  $\varepsilon_s^{(SH)} = 0.0075$ , and  $\varepsilon_s^{(KH)} = 0.0240$ , respectively.  $\varepsilon_c$  limit values were calculated for different

spiral and longitudinal reinforcement ratios by taking into account the different performance levels. Plastic rotation limit values ( $\theta_p$ ) are functions of  $\phi_y$ ,  $\phi_u$ ,  $L_p$ ,  $L_s$ , and  $d_b$ . Therefore, parameters affecting  $\phi_y$  and  $\phi_u$  values, such as

concrete grade, axial load level, spiral ratio, and configuration of spiral reinforcement, also affect the  $\theta_p$  values. Deformation limits for different performance levels were calculated for the RC circular columns according to different parameters (Figure 9).

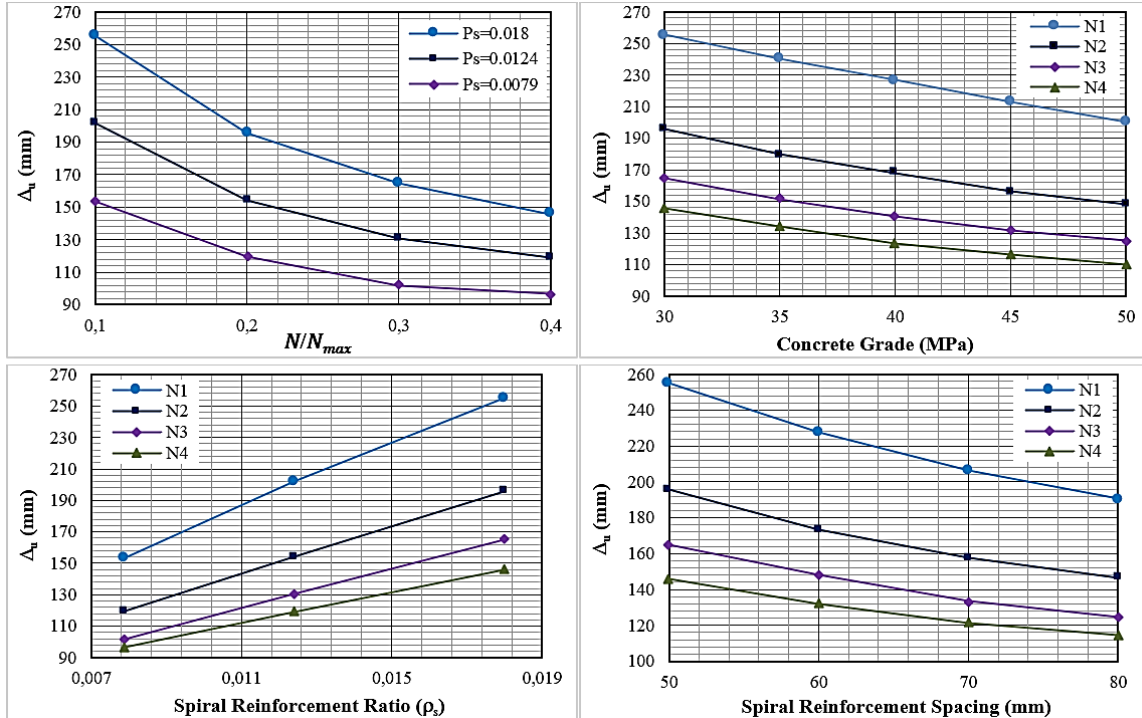


Figure 7. Influence of different design parameters on the ultimate displacement

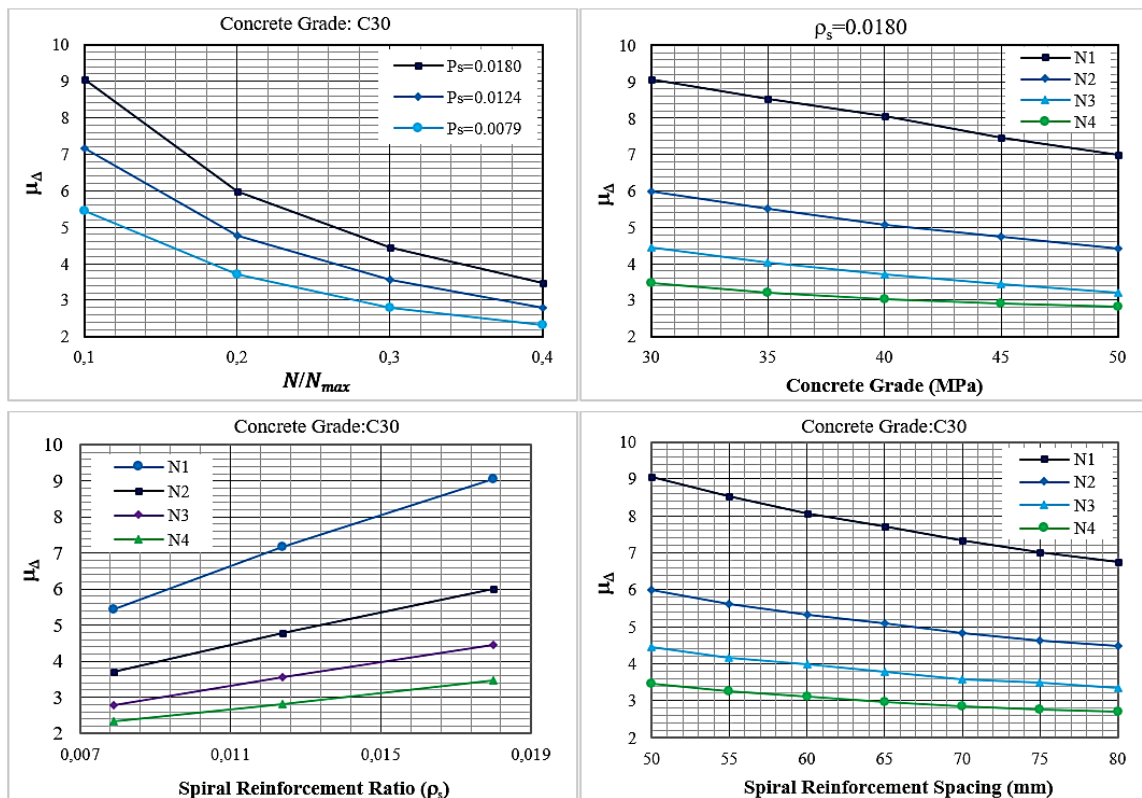


Figure 8. Influence of different design parameters on the displacement ductility

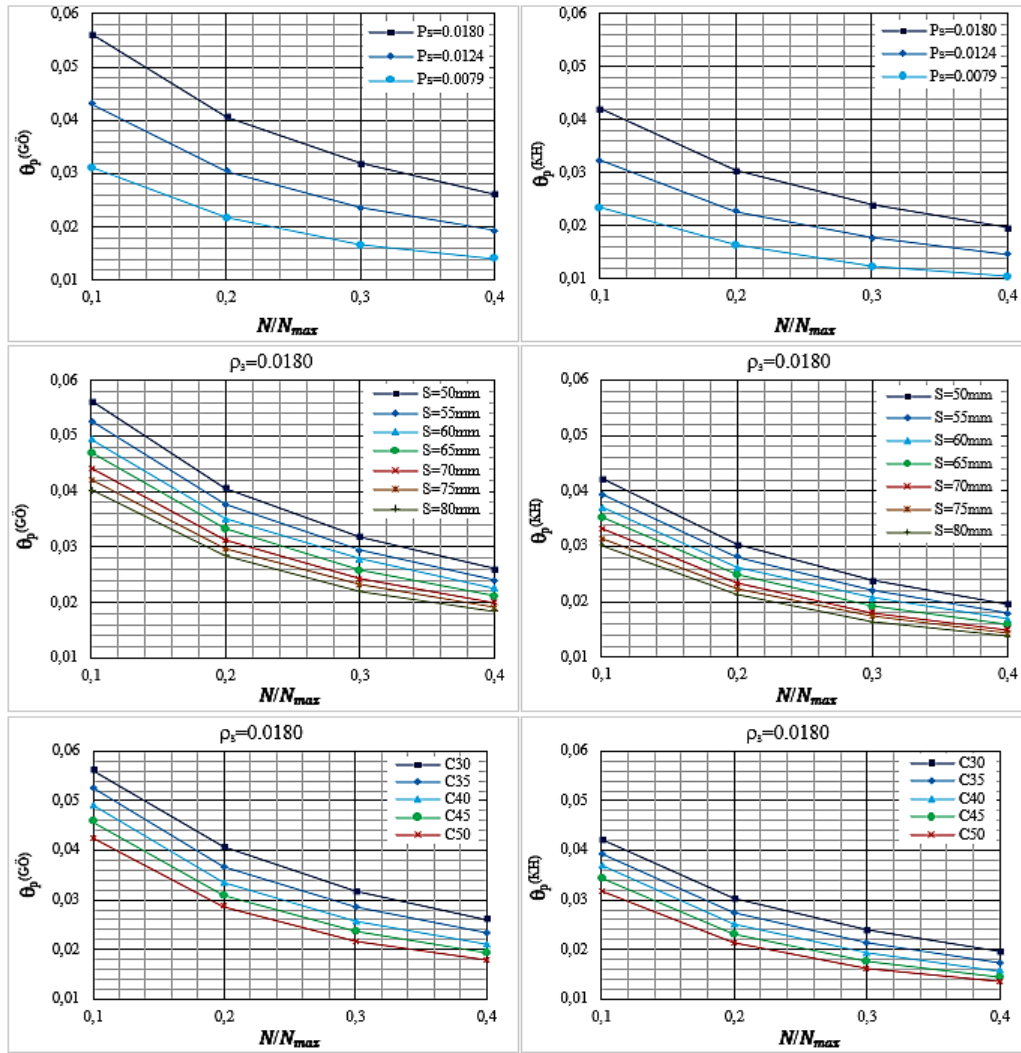


Figure 9. Deformation limits according to different parameters

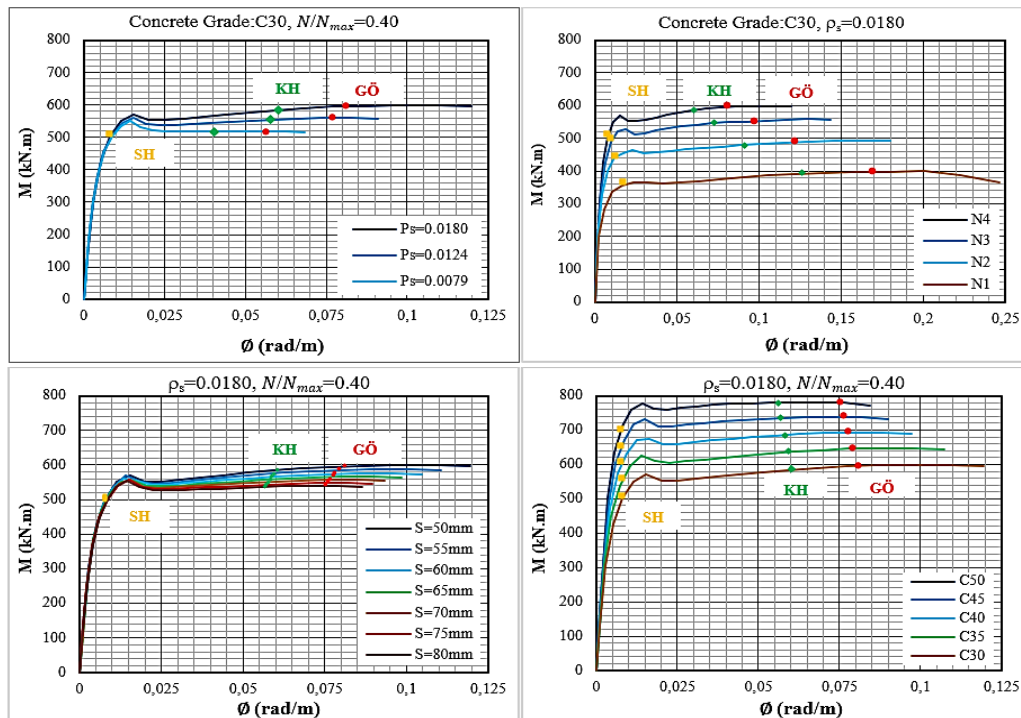


Figure 10. Moment-curvature relationship deformation limits distribution

The deformation limits for the concrete ( $\varepsilon_c^{(G\ddot{O})}$ ,  $\varepsilon_c^{(KH)}$ ) are calculated based on the expected strength of reinforcement steel and concrete ( $f_{ye}$ ,  $f_{ce}$ ), reinforcement ratio of the confined reinforcement ( $\rho_{sh}$ ), and the configuration of the spiral reinforcement. Deformation limit for the SH performance level of the confined concrete is given as constant value ( $\varepsilon_c^{(SH)} = 0.0025$ ). The  $\varepsilon_c^{(G\ddot{O})}$  and  $\varepsilon_c^{(KH)}$  damage limits vary based on different spiral reinforcement diameters and spiral reinforcement spacing. Total unit deformation limit values corresponding to different performance levels of RC column models were obtained based on TBSC [11]. Depending on the deformation upper limit values obtained, cross-sectional deformation damage levels were determined by the excel software, and they are shown on the moment-curvature graphs (Figure 10).

## 6. Conclusions

The ratio of spiral reinforcement affects the non-linear behavior of RC columns and their deformation limits and plastic hinge properties. In this study, definitions of structural performance levels were presented, and for members, performance indicator limits, which are mainly based on definitions of material deformation limits for each structural performance level, were achieved. It was determined that  $\varepsilon_c^{(G\ddot{O})}$  ve  $\varepsilon_c^{(KH)}$  values decrease as spiral reinforcement spacing increases for the constant concrete grade and longitudinal and spiral reinforcement diameter.  $\varepsilon_c^{(G\ddot{O})}$ ,  $\varepsilon_c^{(KH)}$  values increase with the increase of the spiral reinforcement diameter for the constant concrete grade, longitudinal reinforcement diameter, and spiral reinforcement spacing. In addition, for the designed column sections,  $\varepsilon_c^{(G\ddot{O})}$  and  $\varepsilon_c^{(KH)}$  values increase with increasing concrete grade for constant longitudinal and spiral reinforcement ratio.

$\theta_p^{(G\ddot{O})}$  and  $\theta_p^{(KH)}$  deformation damage limits vary based on the moment-curvature relationship and axial load levels. The values of  $\theta_p^{(G\ddot{O})}$  and  $\theta_p^{(KH)}$  decrease with the increase of spiral reinforcement ratio for constant concrete grade and axial load levels. The values of  $\theta_p^{(G\ddot{O})}$  ve  $\theta_p^{(KH)}$  increase with the increase of spiral reinforcement diameter for the constant concrete grade, axial load level, and spiral reinforcement spacing. As the concrete grade increases for the constant axial load level, spiral reinforcement diameter, and spacing,  $\theta_p^{(G\ddot{O})}$  and  $\theta_p^{(KH)}$  values decrease by a little difference.  $\theta_p^{(G\ddot{O})}$  and  $\theta_p^{(KH)}$  values decrease with increasing axial load level for constant concrete grade and spiral reinforcement ratio. One of the most important steps in the performance evaluation according to the non-linear

calculation method is to determine the deformation damage limits and plastic rotation limits of G $\ddot{O}$ , KH, and SH in the structural members. Because of increasing spiral reinforcement ratios, deformation damage limits of the RC columns remain in the safer direction.

## Declaration

The authors declared no potential conflicts of interest with respect to the research, authorship, and/or publication of this article. The authors also declared that this article is original, was prepared in accordance with international publication and research ethics, and ethical committee permission or any special permission is not required.

## Author Contributions

The design of RC column models, analysis plan, statistical analysis, data collection, writing article, and evaluation of the results was shared by S. Foroughi and S.B. Yüksel.

## Acknowledgment

The authors thank the Scientific Research Projects Coordination Office of Konya Technical University for supporting this study with project number 211104011.

## References

1. Elci, H., and Goker, K. A., *Comparison of Earthquake Codes (TEC 2007 and TBEC 2018) In Terms of Seismic Performance of RC Columns*, international Journal of Scientific and Technological Research, 2018. **4** (6): p. 9-21.
2. Kaya, M. P., *Mevcut Betonarme Binaların Deprem Performanslarının Belirlenmesinde Doğrusal ve Doğrusal Olmayan Yöntemlerin Karşılaştırılması Üzerine Sayısal Bir İnceleme*, Yüksek Lisans Tezi, İstanbul Teknik Üniversitesi Fen Bilimleri Enstitüsü, İstanbul, 2006.
3. Aydemir, C., Kırçıl, M. S., Hancıoğlu, B., and Zorbozan, M., *Betonarme Kolonların Hasar Sınır Eğriliklerinin Belirlenmesi*, İMO Teknik Dergi, 2011. **22** (109): p. 5613-5642.
4. Aldemir, M. A., Kazaz, İ., *Evaluation Of Deformation Limits in Codes for Reinforced Concrete Columns*, Eskişehir Technical University Journal of Science and Technology B- Theoretical Sciences, 2018. **6**: p. 225 - 233.
5. Bouzid, H., and Kassoul, A., *Curvature Ductility of High Strength Concrete Beams According to Eurocode 2*, Structural Engineering and Mechanics, 2016. **58**(1): p. 1–19.
6. Bouzid, H., and Kassoul, A., *Curvature Ductility Prediction of High Strength Concrete Beams*, Structural Engineering and Mechanics, 2018. **66**(2): p. 195–201.
7. Chen, X.C., Bai, Z.Z., and Au, F.T.K., *Effect of Confinement on Flexural Ductility Design of Concrete Beams*, Computers and Concrete, 2017. **20**(2): p. 129–143.
8. Elçi, H., *Experimental Investigation of Section Damage Limits for Reinforced Columns with Low Strength Concrete According to TBSC 2018*, Bitlis Eren University Journal of Science and Technology, 2021, **10** (4): p. 1373-1385.
9. ASCE Standard, 41, Seismic Evaluation and Retrofit of

- Existing Buildings, (ASCE/SEI 41-17), Published by the American Society of Civil Engineers, Reston, Virginia, pp. 20191-4382, USA, 2017.
10. Eurocode 8. Design of structures for earthquake resistance: Part 1: General rules, seismic actions and rules for buildings, BS EN 1998-1:2004.
  11. TBSC, Specification for Buildings to be Built in Seismic Zones, 2018, Ministry of Public Works and Settlement Government of the Republic of Turkey.
  12. Sucuoğlu, H., *Performans Esaslı Deprem Mühendisliği*, 3. Türkiye Deprem Mühendisliği ve Sismoloji Konferansı, 14–16 Ekim, 2015. İzmir.
  13. Aydemir, C., Aydemir, M. E., *Betonarme Kirişlerin Hasar Sınırlarının Deneysel Gözlemlerle İrdelenmesi*. İMO Teknik Dergi, 2017. **28** (4): p. 8023-8049.
  14. Foroughi, S., Jamal, R., and Yüksel, S. B., *Effect of Confining Reinforcement and Axial Load In Determining Deformation Based Damage Limits*, Journal of Engineering Sciences and Design, 2020. **8** (4): p. 1042-1052.
  15. Işıltan, Ö., *Betonarme Kolonlar için TDY 2007, EUROCODE 8 ve FEMA 356 ile Yapılan Performans Değerlendirmelerinin Deney Sonuçlarıyla Karşılaştırılması*, Yüksek Lisans Tezi, İstanbul Teknik Üniversitesi, Fen Bilimleri Enstitüsü, İstanbul, 1-159, 2010.
  16. Acun, B., Sucuoğlu, H., *Betonarme Kolonların Şekildeğiştirme Performans Sınırlarının Deneysel Gözlemlerle Değerlendirilmesi*, İMO Teknik Dergi, 2011. **22** (108): p. 5523-5541.
  17. Yavaş, A., Türker, K., *Experimental Investigation of Strain Based Damage Limits in Turkish Earthquake Code for RC Columns*. SDU International Technological Sciences, 2012. **4** (2): p.102-114.
  18. Hasgöl, U., Yavaş, A., Türker, K., Terzi, M., Birol, T., *DBYBHY-2007’de Tanımlanan Hasar Kriterlerinin Betonarme Kolon Elemanlar için İncelenmesi*, Uludağ Üniversitesi Mühendislik Fakültesi Dergisi, 2016. **21** (2): p. 499-514.
  19. Ulutaş, H., *DBYBHY (2007) ve TBDY (2018) Deprem Yönetmeliklerinin Kesit Hasar Sınırları Açısından Kıyaslanması*, Avrupa Bilim ve Teknoloji Dergisi, 2019. **17**: p.351-359.
  20. Türker, K., *Türkiye Deprem Yönetmeliğindeki Performans Esaslı Statik Yöntemlerin Düşey Rijitlik Düzensizliği Bulunan Çerçeveler Üzerinde Karşılaştırılması*, Pamukkale Üniversitesi Mühendislik Bilimleri Dergisi, 2014. **20** (3): p. 70-77.
  21. Kazaz, İ., and Gülkan P., *Süneklik Düzeyi Yüksek Betonarme Perdelerdeki Hasar Sınırları*, İMO Teknik Dergi, 2012. **23** (114): p. 6113-6140.
  22. Yakut, A., and Solmaz, T., *Performance Based Displacement Limits for Reinforced Concrete Columns Under Flexure*, 15 WCEE, 2012. LISBOA.
  23. Foroughi, S., Yüksel, S. B., *Investigation of Deformation-Based Damage Limits of RC Columns for Different Seismic Codes*, Journal of Engineering Research (JER), 2021. Online First Articles.
  24. Foroughi, S., and Yüksel, S.B., *Investigation of Non-linear Behavior of High Ductility Reinforced Concrete Shear Walls*, International Advanced Researches and Engineering Journal, 2020. **4**(2): p. 116–128.
  25. Foroughi, S., and Yüksel, S. B., *Deformation Based Damage Limits of the Ductile Reinforced Concrete Shear Walls*, Journal of Advanced Research in Natural and Applied Sciences, 2021. **7** (2): p. 244–255.
  26. Foroughi, S., and Yüksel S. B., *Investigation of Deformation Based Damage Limits of Reinforced Concrete Column*, International Journal of Engineering Research and Development, 2019. **11**(2): p. 584-601.
  27. Sasani, M., *Life-Safety And Near-Collapse Capacity Models For Seismic Shear Behavior of Reinforced Concrete Columns*, ACI Structural Journal, 2007. **104** (1): p. 30-38.
  28. Mander, J.B., Priestley, M.J.N., and Park, R., *Theoretical Stress–Strain Model for Confined Concrete*, Journal of Structural Engineering (ASCE), 1988. **114**(8): p.1804–1826.
  29. SAP 2000, Structural Software for Analysis and Design, Computers and Structures, Inc, USA.
  30. Zhong, J., Ni, M., Hu, H., Yuan, W., Yuan, H. and Pang, Y., *Uncoupled Multivariate Power Models for Estimating Performance-Based Seismic Damage States of Column Curvature Ductility*, Structures, 2022. **36**: p. 752-764.
  31. Liu, X., Jiang, H., Ye, Y. and Guo, Z., *Deformation-Based Performance Index of Corroded Reinforced Concrete Beams*, Journal of Building Engineering, 2021. **34** (2): 101940.
  32. Foroughi, S., Jamal, R., and Yüksel, S. B., *Effect of Confining Reinforcement and Axial Load Level on Curvature Ductility and Effective Stiffness of Reinforced Concrete Columns*, El-Cezeri Journal of Science and Engineering (ECJSE), 2020. **7** (3): p. 1309 – 1319.
  33. Paulay, T., and Priestley, M.J.N., *Seismic Design of Reinforced Concrete and Masonry Buildings*, John Wiley and Sons, Inc, 1992. New York, USA.
  34. Özdemir, M. A., Kazaz, İ., and Özkaya, S. G., *Evaluation and Comparison of Ultimate Deformation Limits for Reinforced Concrete Columns*, Engineering Structures, 2017. **153**:p. 569-581.
  35. Cansız, S., Aydemir, C. and Arslan, G., *Comparison of Displacement Capacity of Reinforced Concrete Columns With Seismic Codes*, Advances in Concrete Construction, 2019. **8** (4): p. 295–304.
  36. Perez, J.C.V., and Mulder, M.M, *Improved Procedure for Determining the Ductility of Buildings under Seismic Loads*, Revista Internacional de Metodos Numericos para Calculo y Diseno en Ingenieria, 2018. **34**(1): Article number 27.
  37. Li, L., Wang, W. and Shi, P., *Modelling Catastrophic Degradation of Flexural-Dominated RC Columns at Ultimate Displacements Based on Fibre Beam-Column Model*. Journal of Building Engineering, 2022. **45**: 103476.
  38. ACI318, Building code requirements for reinforced concrete and commentary, American Concrete Institute Committee, 2014. ISBN: 978-0-87031-930-3.



## Research Article

## Structural evolution of mechanically alloyed ODS steel powders during ball milling and subsequent annealing treatment

Emin Salur <sup>a,\*</sup> <sup>a</sup>Selcuk University, Faculty of Technology, Department of Metallurgical and Materials Engineering, Konya 42075, Turkey

## ARTICLE INFO

## Article history:

Received 18 February 2022

Accepted 29 May 2022

Published 15 August 2022

## Keywords:

Annealing  
Ball milling  
Hardness  
9Cr-ODS

## ABSTRACT

In the present work, a novel 9Cr oxide-dispersion strengthened (ODS) steel powders with  $Y_2O_3$  (0.5 wt%) dispersoids were synthesized by high planetary ball milling at different time intervals (2, 8, and 16 hours). The structural and crystallographical evolution of the produced powders during the ball milling and post-annealing treatment were evaluated by SEM, XRD, and micro-Vickers hardness analyses. The SEM results showed that the fine dispersions of powders were achieved with the extending milling time. When milling time was 8h, it was observed that the mean size of powders increased maximum level of 101  $\mu m$  and then dramatically reduced to 5  $\mu m$  at latest milling time (16h). The XRD data revealed that the crystallite size of ODS powders diminished gradually with increasing milling time. Plus, all reflection peaks of the Fe, Cr, W, Mo expanded and the diffraction peaks of the  $Y_2O_3$ , W progressively disappeared with the increasing milling time. The hardness results revealed that the increasing milling time was beneficial for hardness improvement, due to dominant strain hardening mechanism and it developed from 160 to 334 Hv after 16h of milling protocol. To understand high temperatures characteristics such as grain growth, phase transformation, and hardness of produced powders, 16h milled powders subjected to post-annealing treatments at 700 °C and 900 °C for 1 h. When pure Fe and Cr peaks were observed in the non-annealed powders, no evident reflection peak of  $Y_2O_3$  was observed. However, all pure Fe and Cr reflection peaks became narrower and  $Y_2O_3$  reflection exhibited more sharper tendency with increased annealing temperatures, which resulted in increased grain growth and formation of Fe-based oxide structures.

### 1. Introduction

Oxide-dispersion strengthened (ODS) alloys contain very fine oxide particles and they are mainly used for structural applications for nuclear power plant constructions as piping and cladding tubes [1]. They are most important candidates for the fuel cladding materials owing to their extreme temperature strength, as well as their thermal stability at elevated temperatures and excellent resistance to corrosion [2-6]. The most diverse feature that differentiate ODS steels from other structural systems is that they have fine dispersoids comprising of several oxide based structures such as  $Al_2O_3$ ,  $Y_2O_3$ ,  $Ce_2O_3$  or uniformly dispersed Y-Al-O, Y-Ti-O constituents at a high number density in the matrix [7, 8]. These nanoscale particles throughout the matrix, cause the secondary phase particles to prevent the movement of dislocations during deformation and resultant an increment of the density of dislocations in the material [9, 10].

ODS alloys are chiefly produced by the powder metallurgical ways, including ball milling/mechanical alloying of mixed powders with well dispersed oxide structures and followed consolidation and heating treatments [11]. The microstructural evolution and mechanical performance of ODS alloys greatly depends on process variables and chemical compositions. Generally,  $Y_2O_3$ ,  $Ce_2O_3$ ,  $La_2O_3$ , MgO,  $ZrO_2$  [12, 13] are added into ODS alloys as dispersed particles. Regarding the introduction of these dispersoids to the material system, which can generally harden the material, Y-based oxide structures are the foremost preferred ones due to its low solution ability in the base matrix, thermodynamically stable characteristics, and lattice divergence that favors their influence as dislocation propagation inhibiting dispersoids and their excellent irradiation stability performance [14].

Li et al. [7] examined that the influence of different types of nanoscales oxides ( $Y_2O_3$ ,  $Ce_2O_3$ ,  $La_2O_3$ ) on the

\* Corresponding author. Tel.: +90 332 223 3392.

E-mail addresses: [esalur@selcuk.edu.tr](mailto:esalur@selcuk.edu.tr) (E. Salur)

ORCID: 0000-0003-0984-3496 (E. Salur)

DOI: [10.35860/iarej.1075508](https://doi.org/10.35860/iarej.1075508)© 2022, The Author(s). This article is licensed under the CC BY-NC 4.0 International License (<https://creativecommons.org/licenses/by-nc/4.0/>).



microstructure changes and mechanical properties of produced 14Cr-ODS steels. As well as superb thermal stability of  $Y_2O_3$ , they found that the  $Y_2O_3$  added ODS alloys exhibit higher yield strength, have a lower particle size distribution and thus have a higher number density.

In the past, several studies regarding the effect of small quantity addition of rare elements (RE) on the structural and mechanical characteristics of ODS alloys have been published [2, 3, 15-17]. The outcomes of these studies reveal that alloys composing of these elements exhibit higher mechanical performance and well-balanced uniform oxide particles compared with other traditional ODS alloys without containing these elements. Hoelzer et al. [18] were prepared 4 different samples comprising of 0, 0.25, and 0.3  $Y_2O_3$  wt% added 14Cr-ODS employing two diverse methods. They reported that the nanoparticles added alloys showed remarkably higher strength than oxide strengthened alloys for elevating temperatures. Meanwhile, the ductility performance of the oxide strengthened alloys was superior to that of the nanoparticles strengthened alloys. Xu et al. [19] found that the diverse annealing treatments was a crucial effect on the compositional fluctuations and design of nanoscale oxide dispersion performance. They reported that when annealing temperature reached to 1100 °C or above, the Ti enrich shell gradually vanished, and only Y-Zr rich oxide structures were stayed in structure. Various elements such as Hf, Ni, Ti and Zr added ODS steels have superior creep rupture strength than other ODS steels which does not include such elements [16, 20]. So, it is very important to clearly describe the microstructural and morphological changes of such minor elements during the mechanical alloying process, followed by the annealing or sintering parameters to be performed [3].

9Cr-ODS steel is an encouraging candidate material for nuclear energy powerhouses, a system that requires superior mechanic attitude at increased temperatures [21]. In particular powder metallurgy, the fabrication process has come across some challenges in obtaining precise composition control [22]. Some of the diffusing atoms, such as Cr, V, Nb, W, and Mo significantly influence mechanical properties. This is thought to happen by microstructural evolutions. Besides, the main contribution to the advanced mechanical and creep performance in comparison with other martensitic-based steels is assigned to the presence of the nanoscopic oxide precipitations in the matrix, which hinder the mobility of dislocations called as Orowan looping mechanism [23]. Hence, the mean interparticle distance between oxides in the matrix is one of the manipulating parameters that regulate the material system's microstructural changes and resultant mechanical properties. The solution limit of Y in Fe is also very poor at room temperature [24]. Thus, it is hard to solve Y into Fe matrix by conventional metallurgy process. Hence, ball

milling method is frequently chosen by various researchers to fabricate new Fe-based ODS steels [25, 26].

In this work, 9Cr prealloyed powders was selected matrix material and it was reinforced with  $Y_2O_3$  0.5 wt% to produced ODS nanocomposite powders. The main purpose of this study was to examine size and structural changes of reinforcement phase ( $Y_2O_3$ ) and the difference in the morphological structure and hardness properties of the mixed particles during ball milling and post-annealing treatment. This study exhibits recent improvements in the procedure of scrutinization of new generation 9Cr-ODS nanocomposite powders, to supply significant knowledge for microstructure control and hardness aspect in the context of structure-performance framework. In this regard, the combined influence of ball milling duration and annealing temperature on the microstructural evolution, particle size, crystal structures, and hardness properties of milled powders was assessed by using scanning electron microscopy (SEM), particle size analyzer and X-ray powder diffraction (XRD) analyses, energy-dispersive X-ray spectroscopy (EDX), and consequently hardness measurements.

## 2. Experimental Method

The prealloyed 9Cr ferritic powders consisting of Fe–9Cr–1Mo–1W–0.2V (wt%) composition plus nanosized ceramic powders of  $Y_2O_3$  (0.5 wt%) (Nanografi, Turkey) was milled in a Retsch PM 200 high planetary ball milling device, utilizing 125 ml tungsten carbide (WC) jar and 7.5 mm WC balls maintaining a 15:1 ball to powder (BPR) weight ratio. The ball milling operation was performed under air atmosphere for 2, 8, and 16 hours employing rotation speed of 350 rpm with time interval i.e., milling operation was conducted 30 min and then rested 15 min till planned milling duration. The goal of such a milling procedure was to prevent increase high-temperature causing recrystallization in the plastically deformed powders. To eliminate severe cold welding and agglomeration, total amount of 2 wt% stearic acid was gradually added in milling system during each milling time was finished. Subsequently, 16 h milled powders were annealed at 700 °C, and 900 °C for 1 h in Protherm brand furnace. The particle size values and their distribution behavior after the milling was analyzed by particle size analyzer (Malvern Mastersizer 2000) using laser diffraction in wet distribution. The morphological alterations of the produced powders were monitored by scanning electron microscope (SEM, Zeiss Evo-LS10). Besides, an energy dispersive X-ray spectroscopy (EDX) module in the same SEM instrument was utilized to assess the chemical differences and dispersion behavior of the synthesized powders. A high-resolution X-ray powder diffractometer curves were collected by (Malvern Xpert<sup>3</sup>) XRD instrument to evaluate the differences in the phase composition and to identify phase formation for different

milling times.

According to available knowledge in the literature review [27, 28], the micro-Vickers hardness test was selected since it is suitable for multiphase structures due to its remarkably harder and smaller diamond indenter which minimize potential damage to the material during testing. The hardness test was performed with respect to different milling times in an ex-situ model. From each set powder group, a little amount of milled powders mounted in a 15 mm diameter bakelite and it left till fully cured. To calculate the hardness precisely, a smooth and homogenous sample surface is required. Thus, the bakelite molds were gently ground up to 2000 mesh fine SiC abrasive papers and ultimately, they polished to a reproduce finishing surface employing ultra-fine alumina paste (Ra: 0.25  $\mu\text{m}$ ). The micro-Vickers hardness measurement of each group was done utilizing a digital Innovatest W-HV400 Vickers-hardness tester under a constant load of 25 g and dwelling time of 15 s. To supply exactness and repeatability in the measurements, three identical samples were evaluated from each powder group. From each batch set, at least five different measurements were performed to insure accurate statistical sample and they were presented along with standard deviations and exemplary indentation figures. A schematic representation of the milling method and powder characterizations are illustrated in Figure 1.

### 3. Results and Discussions

#### 3.1 Variation of Particle Shape and Size

Figure 2 exhibits the SEM images of initial 9Cr powders and 9Cr-ODS ferritic powders with respect to different milling times. Figure 3 shows the minimum ( $d_{0.1}$ ), average

( $d_{0.5}$ ), maximum ( $d_{0.9}$ ) particle size of the milled powders. Considering both Figure 2 and 3, it was observed that the as-received (unmilled) powders showed irregular shape with an average particle size of 92  $\mu\text{m}$ . It was seen that the 2h milled powders were slightly flattened, and the mean size of the particles was about 89  $\mu\text{m}$ . The main reasons for such a little reduction were both the applied low milling time (2h) and the high effectiveness of the initial process control agent (stearic acid) on the milling systematics. After milling of 8h, the average size of the powders reached to maximum levels (100  $\mu\text{m}$ ) because the powders subjected to cold-welding and repetitive flattened mechanism and like as ‘corn-flakes structure’ was observed in the microstructure as shown in Figure 2. One reason for the observed particle shapes can be originated from shearing effect of hard WC milling balls on the 9Cr-ODS ferritic matrix powders. Such an inspections were commonly monitored by several researchers conducting a study on the mechanical alloying of similar systems [29, 30]. Further deformation up to 16h, the particle shape totally transformed into randomly fractured irregular shaped smaller pieces as shown in Figure 2. The average size of this powder system dramatically decreased to minimum level of 5  $\mu\text{m}$  (See Figure 3) because of excessive work hardening and dominant fracture mechanism during the milling duration between 8h and 16h.

The monitored drastic reduction in powder size could also be assigned to the step by step fragmentation of thinned flakes (as indicated in Figure 4) into randomly fractured minor particles along with priorly existence of smaller irregular shaped powders. On the other hand, various researchers announced that the reduction in particle size was proof that fragmentation of flakes, creating new powder surface area [31].

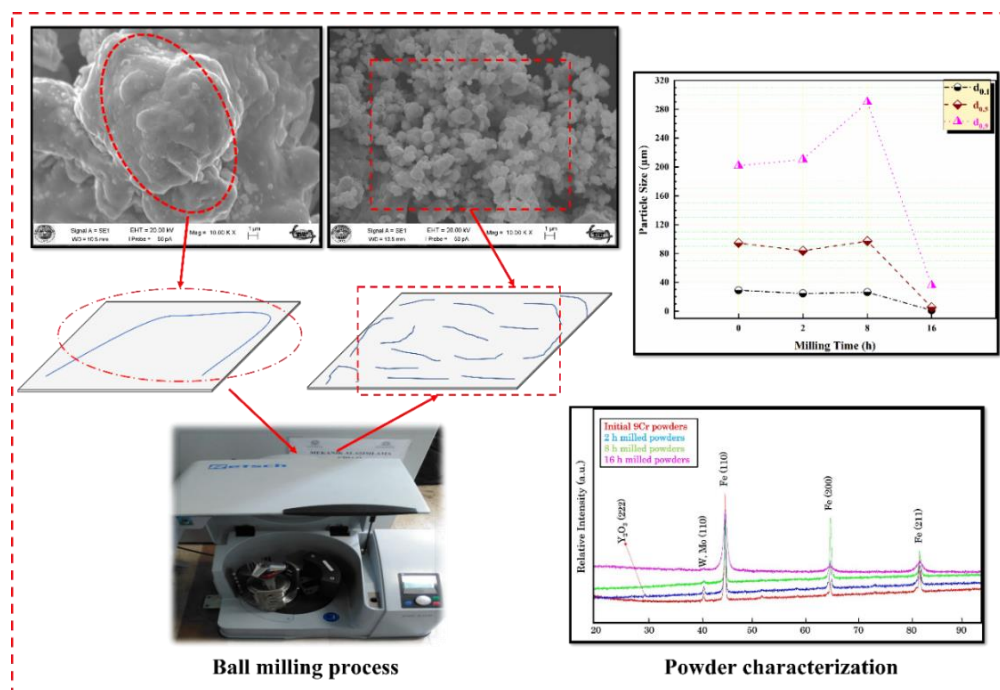


Figure 1. Schematic representation of ODS principle and milling operation, experimental setup and measurements

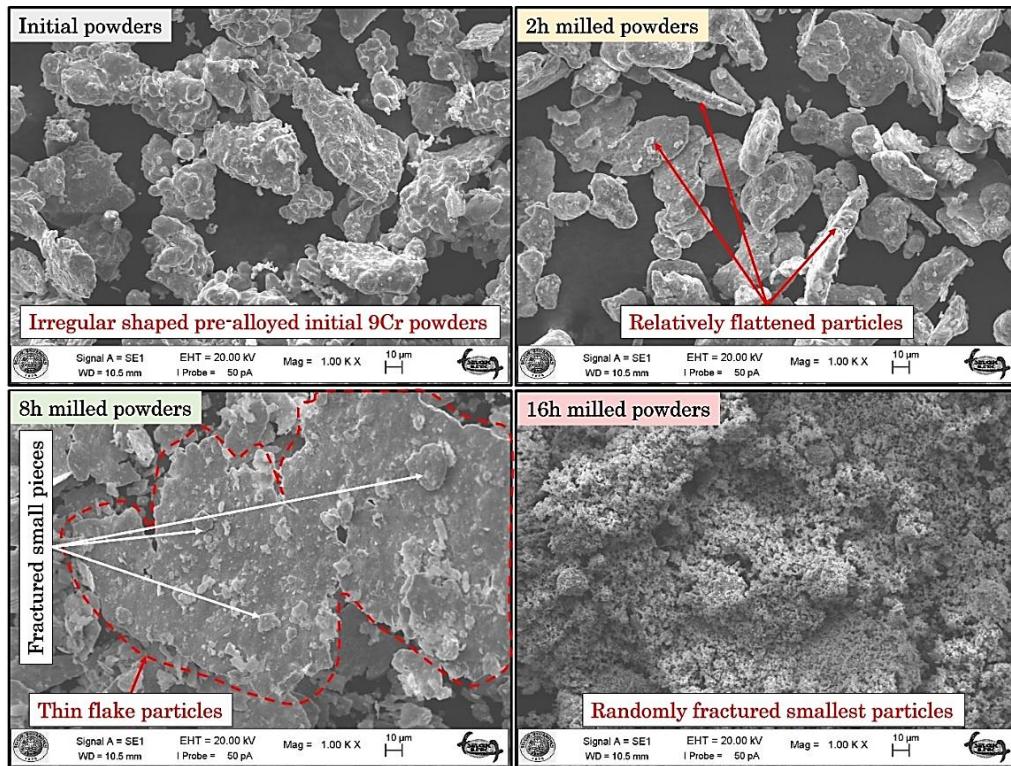


Figure 2. Particle shape changes of 9Cr unmilled powders and milled 9Cr-ODS powders at different milling times

The kind and quantity of process control agent (PCA) is one of the most important parameters affecting kinetics of mechanical alloying. Employing insufficient amount of PCA, the surface area of the powders covered by the PCA is restricted. In this case, overdone-cold welding is still going on and alloying is not given a chance. Nevertheless, if the sufficient amount of PCA can completely cover the surface area of the powders, the excess cold welding mechanism does not occur [32]. An equilibrium is fulfilled between cold welding and fracture mechanism, and alloying takes place instantly. As the increasing specific surface area, the effect of PCA has reached the desired level and alloying has occurred.

As shown in Figure 5, particle size distribution behavior of the initial powders displayed a homogeneous tendency. Since the low milling duration (2h) and effective PCA in the milling operation, a wide range of initial powders protected their initial shape and thus no discernible size distribution behavior was observed except for shifting towards lower angle due to reduced particle size. Plus, the particle morphology of the unmilled and 2h milled powders was nearly equiaxial as compared to further milling systems, as can be confirmed by examining Figure 2 and 5. However, this tendency gradually altered up to 16h milling duration. A broadened peak distribution towards to high particle size was achieved after 8h milled powders owing to numerous flake pieces resulted from rolling effect of milling medium. When

16h milled powders were examined, particle size distribution varied within a narrow range with bimodal distribution meaning it has two different peaks. Nevertheless, these peaks were monitored in the quietly low side of particle size. The reason for this is that the flake-structure powders were fractured with prolonged milling time and as a result of these fractures, the smallest particles were formed in all milling operation. This is a significant indication that the particle size powders are nonuniformly dispersed. In addition, as shown in the Figure 4, the cross sections of the powders reached about 800 nm due to the ball-wall, ball-ball and powder-powder collisions and this leads to easier breakage of the powders with random fragmentation resulting two diverse peaks in distribution behavior. After milling 16h, the mean particle size dramatically decreases from 101  $\mu\text{m}$  to 5  $\mu\text{m}$ , as shown in Figure 3. Considering particle size and morphology analyses, it can be assumed that the ball milling operation consist of two stages: cold-welding and fracture mechanism [33]. Firstly, initial powders experienced severe plastic deformation under the rolling effect of WC balls, and it led to flakes with very thin cross section, as depicted earlier in Figure 4. Secondly, such a thinned powders were effortlessly fragmented into minor sizes due to high impact of powder-powder, powder-jar, powder-ball crashes. As can be obviously experienced, ball milling process not only resulted in the shift of average size to lower values but also benefited the distribution tendency to narrow zone.

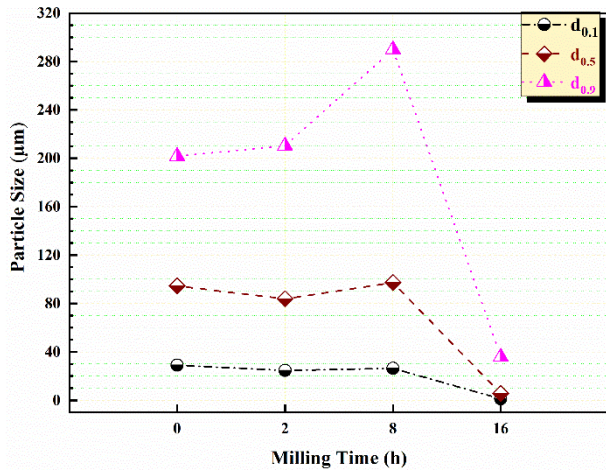


Figure 3. The differences in minimum, average, and maximum particle size for unmilled and milled powders with regard to increasing milling time

3.2 XRD and Crystal Structure Analyses

Figure 6 illustrates the XRD patterns of unmilled and milled powders. The monitored diffraction peaks belong to the Fe, Cr, W, Mo, and Y<sub>2</sub>O<sub>3</sub> materials. However, no detectable diffraction peak was observed for V due to its quite low concentration (0.2 wt%) below the resolution limit of XRD instrument. As the increasing ball milling time, it was appeared that the peak intensity of Y<sub>2</sub>O<sub>3</sub> vanished, which was assigned to its well distribution in the Fe matrix and accompanying reduction in particle size due to brittle solid behavior of hard ceramic Y<sub>2</sub>O<sub>3</sub> phase. On the other hand, the diffraction intensities of Fe base metal and alloying elements decreased along with increased peak wideness except for 8h milled systems (to be explained in detail further). Considering available information in the classical theory of XRD, the widening reflection peak implies that the

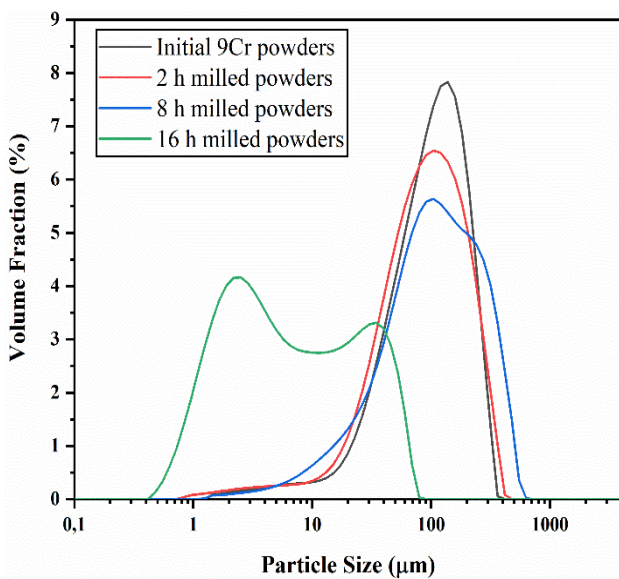


Figure 5. The variation on the particle size distribution behavior of powders in regard to milling duration

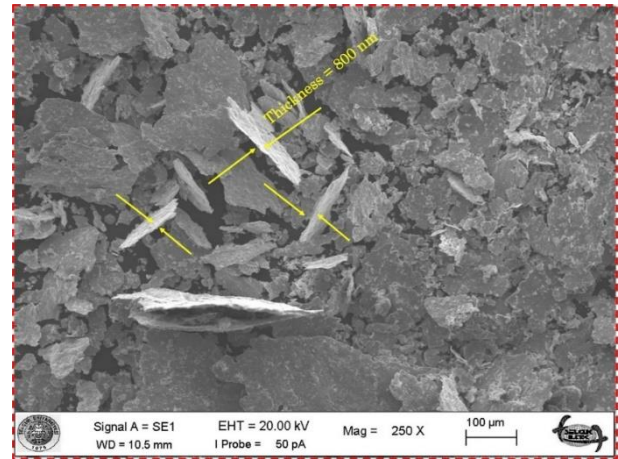


Figure 4. SEM image, indicating cross-section view of thinned flake 9Cr-ODS particles after 8h of milling

crystallite size or domain size reduces accompanying increasing lattice strain dependence on milling time [34]. At first glance, it was glittered that the (200) diffraction peak intensity of 8h milled powders (as described in green color) remarkably increased, and it also showed approximately same intensity in the main reflection of (110) direction. This observation perfected the particle shape image of illustrated in Figure 4, where flakes of 800 nm thickness were detected in 8h milled 9Cr-ODS powders. The detected texture formation was ascribed to the plastic deformation provoked by the thinned flake particles from the rolling effect of rigid milling medium [35]. Increasing milling time up to 16h resulted in vanishing of texture formation on the particles. The disappeared texture was related to the development of smaller particles because of the fragmentation of platelets or flakes after 16h of milling, as depicted prior in Figure 2.

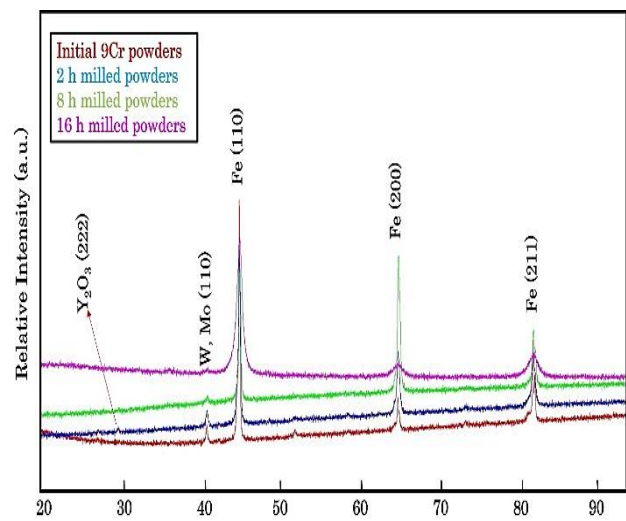


Figure 6. XRD diffraction patterns showing planes and phases of initial and milled powders at different milling duration

The crystallite (domain) size of the (110) and (200) diffraction curves of the produced powders evaluated by XRD data utilizing Scherrer equation [36] with respect to ball milling time is illustrated in Figure 7. As shown in Figure 7, increasing milling time resulted in reduction in crystallite size and concomitant widening of full width at half-maximum (FWHM) in the (110) reflection of Fe which is expected by virtue of ball milling and solid solution mechanism resulted by decreased crystallite size (D) with extended milling time. Severe and repeated collision of powders-ball-jar changed the crystallite size of main reflection (110) from 132.19 nm to 14.12 nm. Also, it could be inferred that prolonging milling time resulted in increment in both lattice distortion and dislocation numbers because dislocations, voids, interstitials, and other metallurgical defects led to intense plastic deformation during mechanical milling operation [37]. Hence, one observes that the mechanical alloying process not only improve the grain refinement of the powders but also augments both strain storage on the lattice and dislocation density. However, crystallite size increased up to 85 nm on (200) reflection which was attributed texture formation on this crystallographic direction, as described earlier in Figure 4 and 6. However, farther milling process created strict plastic deformation as a consequence high energy milling which was led to randomly arranged grain boundaries as barriers to dislocation movement and initiated solid-solution mechanism so, the domain size went down to 11.25 nm on (200) direction plane.

The micro-Vickers hardness of the 9Cr-ODS steel powders against different milling times is presented in Figure 8. The hardness of the powders improved from 160.74 Hv to 334.63 Hv with increasing milling time because of excessive plastic deformation of the powder particles. The synthesized powders exhibit excellent hardness properties than that of the traditional plastic deformation routes [38].

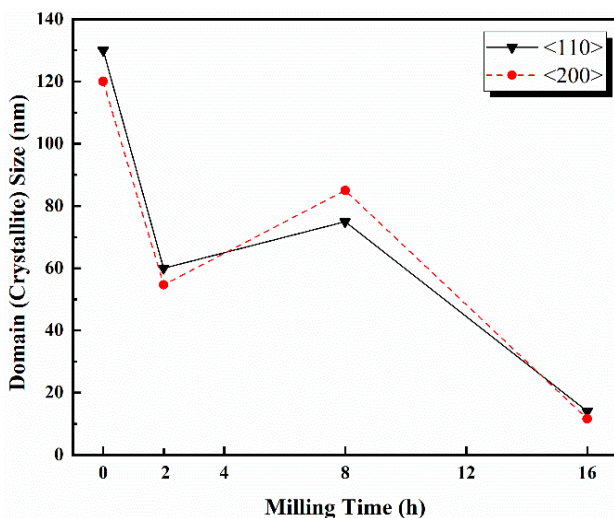


Figure 7. The alterations on the crystallite size of (110) and (200) plane direction of powders for different milling times

### 3.3 Hardness Properties of Milled Powders

These milled powders subjected to strain hardening owing to prolonged milling duration which results in an enhancement in hardness of the particles. Such an improvement on hardness of produced powders can be defined by several cooccurring factors. The grain refinement mechanism is the prominent one among them. Following Hall-Patch principle, which defines the correlation between hardness/strength of polycrystalline samples and the grain size, as the grain size decreases the hardness increases. This equation can be also utilized by different modified constants for nano-crystalline materials [39]. Another crucial factor is the increased stored energy on the lattice originating from the high dislocation density triggered by improving milling time. Moreover, different mechanisms such as dispersion, precipitation, and solid solution hardening/strengthening are also effective in increasing the hardness/strength of the powders [40].

### 3.4 Effect of Annealing Treatment on The Produced Powders

The high temperature development of the 16h milled powders can lead to precipitates, different phase transformations and grain growth mechanisms. To comprehend such an effect, XRD analysis was done on the annealed 16h milled powders. Figure 9 illustrates the XRD curves of as-milled (16h) and annealed powders at temperatures 700 °C and 900 °C. It was observed that all reflections exhibited a gradual decrement in FWHM meaning increment in crystallite size as a function of temperatures. The any intermetallic phases were not encountered in as-milled powders due to small amount of  $Y_2O_3$  and strain triggered peak widening influence. The 700 °C annealed powders showed a  $Fe_3O_4$  peaks. As for 900 °C, it was detected that  $Fe_2O_3$  peaks in addition to  $Fe_3O_4$ . These peaks were monitored earlier for different 9Cr-ODS powders, that increased milling time resulted in the aggregation of extra O in the material system and later these O react with the base Fe matrix to develop different Fe-O forms, which finally led to the development of  $Fe_2O_3$  and  $Fe_3O_4$  phases during elevating annealing temperature [41]. The present observations also showed good agreement with these studies. Moreover, the crystallite size of the main reflection of Fe was assessed utilizing Scherrer method, and chart describing the differences of crystallite size with respect to annealing temperature was illustrated in Figure 10. As the annealing temperature elevated, the crystallite increased to 67.25 nm and 160.53 nm for 700 and 900 °C, respectively. Figure 11 shows the hardness results with exemplary indentation of the annealed powders. The micro-Vickers hardness of the 16h milled powders slightly increased from 324.71 Hv to 325.35 Hv for 700 and 900 °C, respectively. It was observed that there were no clear changes among diverse annealing temperatures.

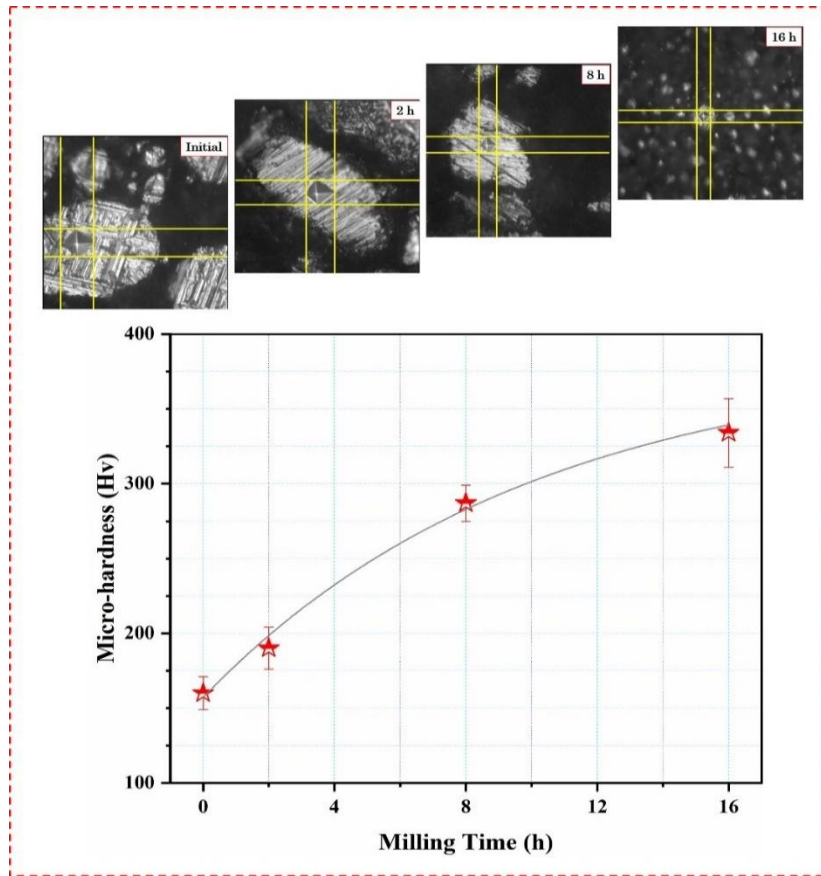


Figure 8. The micro-Vickers hardness changes of the milled powders with exemplary indentation images for different milling times

However, the annealed powders exhibited lower hardness as compared to as-milled powders, which was correlated with grain growth during elevating temperature, and it resulted in deteriorated hardness. On the other hand, oxide based intermetallic formation such  $Fe_2O_3$  and  $Fe_3O_4$  was beneficial for hardness due to their hard ceramic phases.

Concomitant influence of grain growth and formation of intermetallic, which were unfavorable and favorable impact on hardness resulted in such an indiscernible difference on hardness performance. One reason for this case could be originated from combined influences grain coarsening and

disappearing of structural defects inside of the powders due to thermal softening triggered by elevating annealing temperatures as reported by Nowik and Oksiuta [42].

To evaluate the aforementioned beneficial parameters on the hardness, SEM-EDS analysis was performed for 16h milled powders. The composition in the spectrum of 16h milled 9Cr-ODS powders employing EDX analysis showed in Figure 12. Figure represented atomic and weight percentage of content of distributed elements and their keV values.

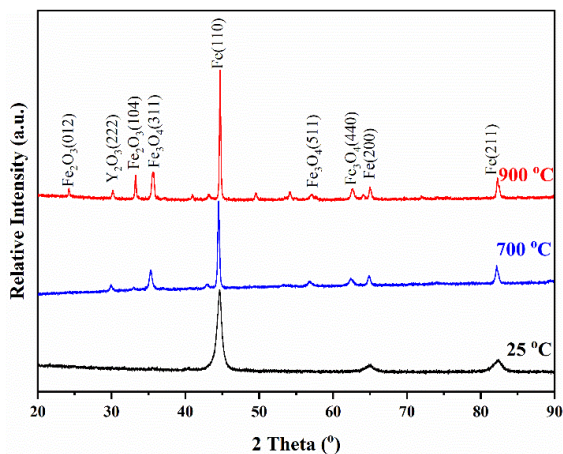


Figure 9. Crystallographical evolution of 16h milled 9Cr-ODS powders after annealing in ambient temperature, 700, and 900 °C

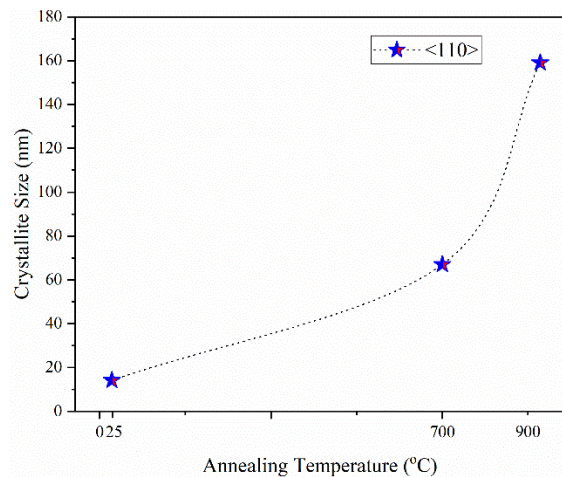


Figure 10. Dependence of crystallite size of 16h milled 9Cr-ODS powders for different annealing temperatures

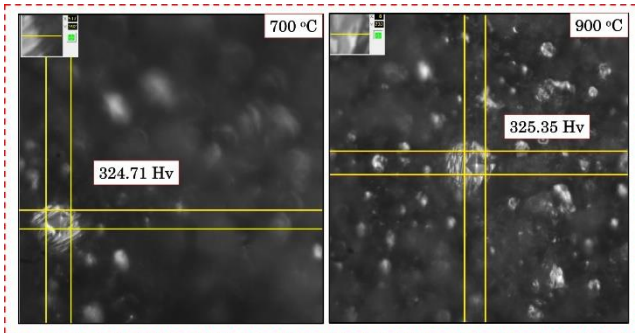


Figure 11. The micro-Vickers hardness and exemplary indentation images of annealed 16h milled nanocomposites powders

The constituent of dispersed elements was comprised of Fe, Cr, W, Mo, Y, O, and C, which were existent in the pre-alloyed and milled 9Cr-ODS powders. Even at small region, after 16h of milling protocol a well-balanced mixture of alloying elements was observed. As observed EDS analysis, alloying and reinforcement elements exhibiting uniform dispersion behavior throughout the matrix, may also lead to dispersion hardening mechanism.

To supply hypothesis about the uniform dispersion of hard ceramic  $Y_2O_3$  phases and alloying elements EDX line analysis was also performed. As shown in Figure 13, the spectra of constituent elements of 16h milled 9Cr-ODS powders were detected with nearly same distribution behavior. Such an observations were proofed that followed milling protocol i.e., 16h of milling time was sufficient for uniform dispersion of alloying and reinforcement elements. These observations agreed with great extend to XRD and hardness results.

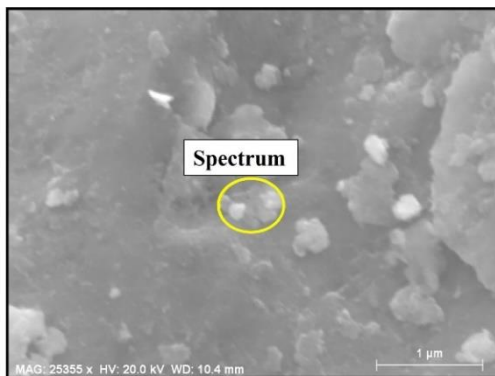


Figure 12. Results of the EDS analysis taken from indicated spectrum of 16h milled powders

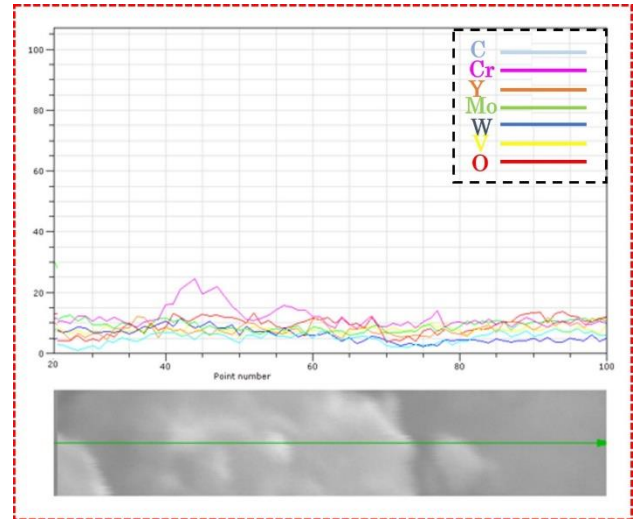


Figure 13. EDS line analysis of 9Cr-ODS powders milled for 16 h

#### 4. Conclusions

In this paper, the 9Cr-ODS powders were synthesized by high planetary ball milling with different milling times (2, 8, and 16 h). The influences of milling duration on the microstructure, crystal structure and hardness properties of the produced powders were analyzed within the scope of structure-performance relationships. It was observed that the 16h milling protocol developed the minimum particle size (5  $\mu\text{m}$ ) as compared to initial form (92  $\mu\text{m}$ ) and these powders exhibited almost single phase (Fe) with solutioned alloying elements. Besides, it was observed that the strain hardening, Orowan precipitation and solid solution hardening mechanisms triggered by collisions of milling systematic constituents (powder, ball, and jar) were presumed to most dominant factors on the hardening properties. Such an effects led to an increment on the powder hardness 160 to 334 Hv for initial prealloyed 9Cr powders and 16h milled 9Cr-ODS powders, respectively. However, no discernible difference was observed as a result of the formation of beneficial intermetallic on the increase in hardness and the simultaneous occurrence of the harmful grain growth mechanism after annealing treatment of 16h milled powders. Based on observed outcomes, it could be concluded that despite increasing temperatures, the produced 9Cr-ODS nanocomposite powders did not compromised of its hardness and that the materials produced by the applied methods in here are a new alternative for high temperature applications.

#### Declaration

The author(s) declared no potential conflicts of interest with respect to the research, authorship, and/or publication of this article. The author(s) also declared that this article is original, was prepared in accordance with international publication and research ethics, and ethical committee permission or any special permission is not required.

## Author Contributions

E. Salur is responsible for all sections of the paper

## References

- McClintock, D.A., M.A. Sokolov, D.T. Hoelzer, and R.K. Nanstad, *Mechanical properties of irradiated ODS-EUROFER and nanocluster strengthened 14YWT*. Journal of Nuclear Materials, 2009. **392**(2): p. 353-359.
- Li, S., Z. Zhou, J. Jang, M. Wang, H. Hu, H. Sun, and L. Zhang, *The influence of Cr content on the mechanical properties of ODS ferritic steels*. Journal of Nuclear Materials, 2014. **455**(1-3): p. 194-200.
- Li, W., T. Hao, R. Gao, X. Wang, T. Zhang, Q. Fang, and C. Liu, *The effect of Zr, Ti addition on the particle size and microstructure evolution of yttria nanoparticle in ODS steel*. Powder Technology, 2017. **319**: p. 172-182.
- Chen, C.L. and Y.M. Dong, *Effect of mechanical alloying and consolidation process on microstructure and hardness of nanostructured Fe-Cr-Al ODS alloys*. Materials Science and Engineering: A, 2011. **528**(29-30): p. 8374-8380.
- Zinkle, S. and N. Ghoniem, *Operating temperature windows for fusion reactor structural materials*. Fusion Engineering and Design, 2000. **51**: p. 55-71.
- Klueh, R.L., J.P. Shingledecker, R.W. Swindeman, and D.T. Hoelzer, *Oxide dispersion-strengthened steels: A comparison of some commercial and experimental alloys*. Journal of Nuclear Materials, 2005. **341**(2-3): p. 103-114.
- Li, Z., Z. Lu, R. Xie, C. Lu, Y. Shi, and C. Liu, *Effects of Y<sub>2</sub>O<sub>3</sub>, La<sub>2</sub>O<sub>3</sub> and CeO<sub>2</sub> additions on microstructure and mechanical properties of 14Cr-ODS ferrite alloys produced by spark plasma sintering*. Fusion Engineering and Design, 2017. **121**: p. 159-166.
- Chen, C., P. Wang, and G. Tatlock, *Phase transformations in yttrium-aluminium oxides in friction stir welded and recrystallised PM2000 alloys*. Materials at High Temperatures, 2009. **26**(3): p. 299-303.
- He, P., J. Hoffmann, and A. Möslang, *Effect of milling time and annealing temperature on nanoparticles evolution for 13.5% Cr ODS ferritic steel powders by joint application of XAFS and TEM*. Journal of Nuclear Materials, 2018. **501**: p. 381-387.
- Gökmese, H., B. Bostan, T.A. Yilmaz, and U. Tasci, *TEM characterization and synthesis of nanoparticle B<sub>4</sub>C by high-energy milling*. International Advanced Researches and Engineering Journal, 2019. **3**(3): p. 195-201.
- Aktas, S. and E.A. Diler, *A review on the effects of micro-nano particle size and volume fraction on microstructure and mechanical properties of metal matrix composites manufactured via mechanical alloying*. International Advanced Researches and Engineering Journal, 2018. **2**(1): p. 68-74.
- Raghavendra, K.G., A. Dasgupta, P. Bhaskar, K. Jayasankar, C.N. Athreya, P. Panda, S. Saroja, V.S. Sarma, and R. Ramaseshan, *Synthesis and characterization of Fe-15 wt.% ZrO<sub>2</sub> nanocomposite powders by mechanical milling*. Powder Technology, 2016. **287**: p. 190-200.
- Hoffmann, J., M. Rieth, R. Lindau, M. Klimenkov, A. Möslang, and H.R.Z Sandim, *Investigation on different oxides as candidates for nano-sized ODS particles in reduced-activation ferritic (RAF) steels*. Journal of Nuclear Materials, 2013. **442**(1-3): p. 444-448.
- Kotan, H., K.A. Darling, R.O. Scattergood, and C.C Koch, *Influence of Zr and nano-Y<sub>2</sub>O<sub>3</sub> additions on thermal stability and improved hardness in mechanically alloyed Fe base ferritic alloys*. Journal of alloys and compounds, 2014. **615**: p. 1013-1018.
- Ukai, S., M. Harada, H. Okada, S. Nomura, S. Shikakura, K. Asabe, T. Nishida, and M. Fujiwara, *Alloying design of oxide dispersion strengthened ferritic steel for long life FBRs core materials*. Journal of Nuclear Materials, 1993. **204**: p. 65-73.
- Kimura, A., R. Kasada, N. Iwata, H. Kishimoto, C.H. Zhang, J. Isselin, P. Dou, J.H. Lee, N. Muthukumar, T. Okuda, M. Inoue, S. Ukai, S. Ohnuki, T. Fujisawa, and F. Abe, *Development of Al added high-Cr ODS steels for fuel cladding of next generation nuclear systems*. Journal of Nuclear Materials, 2011. **417**(1-3): p. 176-179.
- Isselin, J., R. Kasada, A. Kimura, T. Okuda, M. Inoue, S. Ukai, S. Ohnuki, T. Fujisawa, and F. Abe, *Effects of Zr addition on the microstructure of 14% Cr4% Al ODS ferritic steels*. Materials transactions, 2010. **51**(5): p. 1011-1015.
- Hoelzer, D. T., J. Bentley, M.A. Sokolov, M.K. Miller, G.R. Odette, and M.J. Alinger, *Influence of particle dispersions on the high-temperature strength of ferritic alloys*. Journal of Nuclear Materials, 2007. **367**: p. 166-172.
- Xu, H., Z. Lu, S. Ukai, N. Oono, and C. Liu, *Effects of annealing temperature on nanoscale particles in oxide dispersion strengthened Fe-15Cr alloy powders with Ti and Zr additions*. Journal of Alloys and Compounds, 2017. **693**: p. 177-187.
- Toloczko, M.B., D.S. Gelles, F.A. Garner, R.J. Kurtz, and K. Abe, *Irradiation creep and swelling from 400 to 600 C of the oxide dispersion strengthened ferritic alloy MA957*. Journal of nuclear materials, 2004. **329**: p. 352-355.
- Xu, Z., S. Liu, L. Song, X. Yang, Y. Zhao, and X. Mao, *Effect of silicon on oxidation behavior of 9Cr-ODS steel at 650° C*. Fusion Engineering and Design, 2021. **167**: p. 112384.
- Polat, G., A.B. Batibay, and H. Kotan, *Understanding microstructural evolution and hardness of nanostructured Fe89.5Ni8Zr2.5 alloy produced by mechanical alloying and pressureless sintering*. Engineering Science and Technology, an International Journal, 2020. **23**(5): p. 1279-1284.
- Xu, S., Z. Zhou, F. Long, H. Jia, N. Guo, Z. Yao, and M.R. Daymond, *Combination of back stress strengthening and Orowan strengthening in bimodal structured Fe-9Cr-Al ODS steel with high Al addition*. Materials Science and Engineering: A, 2019. **739**: p. 45-52.
- Kotan, H., *Effect of Y and nano Y<sub>2</sub>O<sub>3</sub> additions on grain growth and hardness of nanocrystalline austenitic stainless steels produced by mechanical alloying*. Journal of the Faculty of Engineering and Architecture of Gazi University, 2019. **34**(3): p. 1266-1272.
- Kotan, H., *Thermal stability, phase transformation and hardness of mechanically alloyed nanocrystalline Fe-18Cr-8Ni stainless steel with Zr and Y<sub>2</sub>O<sub>3</sub> additions*. Journal of Alloys and Compounds, 2018. **749**: p. 948-954.
- Darling, K.A., M. Kapoor, H. Kotan, B.C. Hornbuckle, S.D. Walck, G.B. Thompson, M.A. Tschopp, L.J. Kecskes, *Structure and mechanical properties of Fe-Ni-Zr oxide-dispersion-strengthened (ODS) alloys*. Journal of Nuclear Materials, 2015. **467**: p. 205-213.
- Mihalache, V. I. Mercioniu, A. Velea, P. Palade, *Effect of the process control agent in the ball-milled powders and SPS-consolidation temperature on the grain refinement, density and Vickers hardness of Fe14Cr ODS ferritic alloys*. Powder Technology, 2019. **347**: p. 103-113.



28. Sandim, H.R.Z., R.A. Renzetti, A.F. Padilha, D. Raabe, M. Klimenkov, R. Lindau, and A. Möslang, *Annealing behavior of ferritic–martensitic 9% Cr–ODS–Eurofer steel*. *Materials Science and Engineering: A*, 2010. **527**(15): p. 3602-3608.
29. Shi, W., L. Yu, C. Liu, Z. Ma, H. Li, Z. Wang, Y. Liu, Q. Gao, and H. Wang, *Evolution of  $Y_2O_3$  precipitates in ODS-316 L steel during reactive-inspired ball-milling and spark plasma sintering processes*. *Powder Technology*, 2022. **398**: p. 117072.
30. Song, Q.S., Y. Zhang, Y.F. Wei, X.Y. Zhou, Y.F. Shen, Y.M. Zhou, and X.M. Feng, *Microstructure and mechanical performance of ODS superalloys manufactured by selective laser melting*. *Optics & Laser Technology*, 2021. **144**: p. 107423.
31. Salur, E., C. Nazik, M. Acarer, I. Savkliyildiz, and E.K. Akdogan, *Ultrahigh hardness in  $Y_2O_3$  dispersed ferrous multicomponent nanocomposites*. *Materials Today Communications*, 2021. **28**: p. 102637.
32. Salur, E., M. Acarer, and İ. Şavkliyildiz, *Improving mechanical properties of nano-sized TiC particle reinforced AA7075 Al alloy composites produced by ball milling and hot pressing*. *Materials Today Communications*, 2021. **27**: p. 102202.
33. Salur, E., A. Aslan, M. Kuntoglu, and M. Acarer, *Effect of ball milling time on the structural characteristics and mechanical properties of nano-sized  $Y_2O_3$  particle reinforced aluminum matrix composites produced by powder metallurgy route*. *Advanced Powder Technology*, 2021. **32**(10): p. 3826-3844.
34. Salur, E., *Synergistic effect of ball milling time and nano-sized  $Y_2O_3$  addition on hardening of Cu-based nanocomposites*. *Archives of Civil and Mechanical Engineering*, 2022. **22**(2): p. 1-18.
35. Doğan, K., M.I. Ozgun, H. Subutay, E. Salur, Y.R. Eker, M. Kuntoglu, A. Aslan, M.K. Gupta, M. Acarer, *Dispersion mechanism-induced variations in microstructural and mechanical behavior of CNT-reinforced aluminum nanocomposites*. *Archives of Civil and Mechanical Engineering*, 2022. **22**(1): p. 1-17.
36. Patterson, A., *The Scherrer formula for X-ray particle size determination*. *Physical review*, 1939. **56**(10): p. 978.
37. Bicer, H., E.K. Akdogan, I. Savkliyildiz, C. Haines, Z. Zhong, and T. Tsakalakos, *Thermal expansion of nano-boron carbide under constant DC electric field: An in situ energy dispersive X-ray diffraction study using a synchrotron probe*. *Journal of Materials Research*, 2020. **35**(1): p. 90-97.
38. Albaaji, A.J., E.G. Castle, M.J. Reece, J.P. Hall, and S.L. Evans, *Effect of ball-milling time on mechanical and magnetic properties of carbon nanotube reinforced FeCo alloy composites*. *Materials & Design*, 2017. **122**: p. 296-306.
39. Xiong, H., Z. Li, X. Gan, L. Chai, and K. Zhou, *High-energy ball-milling combined with annealing of TiC powders and its influence on the microstructure and mechanical properties of the TiC-based cermets*. *Materials Science and Engineering: A*, 2017. **694**: p. 33-40.
40. Tekin, M., G. Polat, Y.E. Kalay, and H. Kotan, *Grain size stabilization of oxide dispersion strengthened CoCrFeNi- $Y_2O_3$  high entropy alloys synthesized by mechanical alloying*. *Journal of Alloys and Compounds*, 2021. **887**: p. 161363.
41. Ohtsuka, S., S. Ukai, M. Fujiwara, T. Kaito, and T. Narita, *Improvement of 9Cr-ODS martensitic steel properties by controlling excess oxygen and titanium contents*. *Journal of Nuclear Materials*, 2004. **329**: p. 372-376.
42. Nowik, K. and Z. Oksiuta, *Microstructure, Grain Growth and Hardness of Nanostructured Ferritic ODS Steel Powder during Annealing*. *Metallography, Microstructure, and Analysis*, 2021. **10**(3): p. 355-366.



## Research Article

# Post curing temperature effect on mechanical characterization of jute/basalt fiber reinforced hybrid composites

Berkay KARAÇOR <sup>a,\*</sup>  and Mustafa ÖZCANLI <sup>a</sup> 

<sup>a</sup>Cukurova University, Faculty of Engineering, Dept. of Automotive Engineering, Adana, 01330, Turkey

### ARTICLE INFO

#### Article history:

Received 18 March 2022

Accepted 21 June 2022

Published 15 August 2022

#### Keywords:

Basalt fiber

Hybrid composites

Jute fiber

Mechanical properties

Post-curing temperature

### ABSTRACT

Fiber-reinforced polymer composites have a fast-growing performance in many areas of engineering as a replacement for metallic materials due to their low density, low cost, specific mechanical characteristics, and lower energy consumption. The efficiency of fiber-reinforced polymer composites at high temperatures is an issue that requires to be well investigated before this type of composite can be used in important engineering fields. The aim of this study is to examine the change in mechanical properties of homogeneous and hybrid composites prepared from epoxy resin reinforced with jute fabric and basalt fabric at three diverse post-curing temperatures (50°C, 70°C, and 90°C). The vacuum-assisted resin transfer molding process was used to fabricate the laminated composites. The tensile strength and microhardness values of post-cured homogeneous and hybrid composite samples were determined by tensile tests and Vickers hardness measurements. A water absorption test was also performed to determine the water absorption capacity of the fabricated composites. After tensile testing of the fabricated structures, the effect of post-curing temperatures on the interaction of the fiber-matrix interface was investigated by scanning electron microscopy analysis. The results indicate that with increasing the post-curing temperature from 50 °C to 90 °C, an improvement of 45.48% in tensile strength and 34.65% in hardness is achieved for the hybrid composites. Moreover, the results of the water absorption test show that the increased post-curing temperature reduces the water absorption capacity of the hybrid composites by 3.53 times.

## 1. Introduction

In the automotive field, worldwide competition is a leading force in the emergence of improved and new materials, in order to reduce costs, maintain the ecological balance, and also maintain the share of commercial sales. In this competition, light mass designs are revealed and the desired requirements are met by the sector stakeholders' orientation to innovative materials [1]. During recent years, the usage of fiber-reinforced composite materials has been increasing for these innovative materials. Especially natural fiber reinforcements have created a remarkable recognition among researchers due to factors such as having low density compared to synthetic fibers, being cost-effective, being produced from natural sources, and being environmentally friendly [2]. Compared to synthetic fibers, the biodegradability of natural fibers, less damage to processing equipment and greater flexibility, improved composite surface quality in molded parts, and minimal health hazards are among the important

advantages. For this reason, low-cost, light natural fibers such as abaca, sisal, hemp, flax, coconut, jute fiber can narrow the use of synthetic fibers in many areas [3], [4]. Moreover, natural fibers also have some critical disadvantages. The hydrophilic nature of natural fibers creates an issue in these cellulose-containing fibers that will significantly affect their mechanical features as well as their physical properties. Since the chemical nature of both the fibers and the matrix are diverse, it can lead to inoperative stress transmission during the formation of an interface of the produced composites [5], [6]. For this, the hybridization process of natural and synthetic fiber reinforcements contributes to the usage of natural fibers in structural applications. While the low mechanical characteristics of natural fibers are improved by the hybridization process, the cost of the other reinforcing element used, the damage to the environment, etc. factors are minimized [7]. Jute fibers are one of the most cost-effective natural fibers cultivated in countries such as

\* Corresponding author. Tel.: +90-322-338-6600; Fax: +90-322-338-6945

E-mail addresses: [bkarakor@cu.edu.tr](mailto:bkarakor@cu.edu.tr) (B. Karacor), [ozcanli@cu.edu.tr](mailto:ozcanli@cu.edu.tr) (M. Ozcanli)

ORCID: 0000-0001-5208-366X (B. Karacor), 0000-0001-6088-2912 (M. Ozcanli)

DOI: [10.35860/iarej.1089568](https://doi.org/10.35860/iarej.1089568)

© 2022, The Author(s). This article is licensed under the CC BY-NC 4.0 International License (<https://creativecommons.org/licenses/by-nc/4.0/>).

India, China, Nepal, Bangladesh, and Thailand. In addition, it has many application areas such as aircraft, furniture sector, including the automotive sector. The high strength/weight ratio, good insulation features, mechanical features, and thermal features of jute fibers are effective in the preference of jute fibers in these areas. Whereas the lower density, specific strength per unit cost, specific stiffness, and strength in jute fibers are comparable to glass fibers, it is better than glass fibers in terms of specific modulus, besides jute is superior in terms of cost per module [8]–[10]. The use of light, low-cost natural fibers in many industries, including the automotive industry, is replacing a large part of the traditional materials used. Especially in automotive, the reinforcement of natural fibers to interior and exterior parts not only gives ecological sensitivity and recyclability without sacrificing safety but also affects fuel economy by reducing vehicle weight. Thus, the global CO<sub>2</sub> balance will not only be kept at a stable level even so will contribute to global sustainability by reducing dependency on petroleum-based products [11]–[13]. One of the fibers that have the potential to be used in the automotive sector is basalt fibers from the mineral fiber class. When basalt fibers are compared with vegetable natural fibers, it is seen that they have a higher modulus of elasticity and tensile strength. It is a green material that does not harm the ecological environment, has a cost of less than one-tenth of carbon fiber, and exhibits notably diverse characteristics from other fibers. Basalt rock fibers are nonflammable and explosion-proof, as well as atoxic reaction with water or air. It is stated that basalt-based composites can be used instead of steels and known reinforced plastics. Basalt fibers have good moisture, fatigue, and vibration resistance and exhibit superior characteristics in terms of acoustic insulation compared to other fibers [14]–[17]. However, many determinants like the type of matrix used in the production of composites, the filling material, the orientation of the fabric, and the production methods affect the mechanical characteristics of the hybrid composite. Researchers use various techniques to enhance mechanical characteristics in hybrid composites. They discovered that with this applied modification and chemical treatment, the fibers improved in mechanical characteristics, water resistance, and fire resistance compared to untreated composites [18]. Cangül et al. [19] conducted an experimental study to crosscheck the water solubility capacity and water absorption characteristics of the resins using four distinct resins. They commented that water solubility and water absorption in composite resin matrices are seen as one of the critical issues that change the chemical, physical, and mechanical structures of resins, the matrix and filler structure of the resin should be carefully examined to eliminate this effect. An accelerated aging effect has been created on composite laminates, and

the mechanical responses that occur in laminates over time have been investigated. In the research, in which jute and basalt fibers were used as reinforcement elements with two different sequencing orders, it was observed that the hybridize operation of basalt fibers to jute fibers significantly increased the resistance to environmental aging [20]. Surana et al. [21] examined the mechanical and vibration characteristics of the samples they prepared using basalt fiber and epoxy. Whereas it was observed that 2% filling material gave the best results in the tensile test, it was understood that 4% filling material was the critical value in the vibration test. Kumar and Singh [22] examined the impact of fiber orientation on impact strength, flexural strength, tensile strength, and hardness in basalt fiber reinforced epoxy hybrid composites. In the mechanical test outcomes, the best values were obtained for the composite specimens with a fiber orientation angle of 90°, as the composite specimens with a fiber orientation of 45° showed the lowest values. In an investigation of Darshan and Suresha [23], in which basalt fiber was hybridized with silk fiber, it was aimed to produce new composite material by incorporating basalt fiber in different weight ratios into silk fiber composites. It has been found that the composites composed of 25% by weight silk fiber and 25% by weight basalt fiber give the most optimum mechanical properties for use in structural engineering applications. In another search in which basalt and jute fiber were used, the walnut shell was mixed with epoxy resin in weight ratios between 0% and 15% (0%, 5%, 10%, 15%) to form composite material. It was found that the mechanical features were improved in the composites with higher walnut shell ratios by weight [24]. In an investigation in which nano graphene was used as filling material, the friction coefficients and specific wear rates of the products produced by producing homogeneous jute fabric composite, homogeneous basalt fabric composite, and hybrid basalt/jute fiber composite were investigated. In the results, the hybrid composites with the lowest specific wear rate and coefficient of friction are those containing 0.4% by weight graphene [25]. The mechanical characteristics of composite laminates in which jute fiber is combined in different ratios (20%, 30%, and 50%) were analyzed both experimentally and numerically. It was expressed in the results that the mechanical properties improved as the Jute fiber ratio increased in the combination [26]. In the microscopic and macroscopic examination of fiber metal layer composites in four different arrays consisting of basalt, jute, and aluminum, it was found that weak adhesion occurred between jute fibers and aluminum in the interfacial connections. It was stated that the poor adhesion of jute fibers with epoxy was the basis of the loss in mechanical features [27]. By the time these studies in the literature are examined, it has been observed that there is not enough research to investigate

the effect of temperature on composite materials. It is known that temperature is a very important parameter in composites both during production and during operation. Almeida-Chetti et al. [28] investigated how curing temperatures on four different composite resins influence the modulus of elasticity and flexural strength of the resins. It was determined that there was an augment in both the modulus of elasticity and the flexural strength of the post-cured composites. In the search made by Singh et al. [29], it was investigated how the post cure temperature varying between 80°C and 130°C would affect the mechanical characteristics of composites produced with jute fiber and epoxy resin. Whilst there was an increment in elastic modulus, flexural strength, and tensile strength up to 100°C, temperatures after 100°C had a negative impact on mechanical properties. The impact strength, on the other hand, had the highest value when the post curing temperature was at 80°C, while its increase from this temperature negatively affected the impact strength. It has also been found that the post-curing process improves the ratio of the material's loss modulus to the storage modulus, resulting in the development of the fiber matrix interface [30]. The effects of various operating temperatures during production were investigated, although the effects of different curing temperatures have been discussed in previous studies, it was found that the study on the effects of post-curing on tensile strength, hardness, and water absorption values of Jute and Basalt fibers and their hybrid composites is lacking in the literature. In this work, pure jute composites, pure basalt composites, and hybrid jute/basalt composites were fabricated using Jute and Basalt fabrics and epoxy resin. The fabricated composites were exposed to post-curing at 50°C, 70°C, and 90°C for 1 hour. It was investigated how these three different post-curing temperatures on the fabricated products in tests of tensile strength, hardness, and water absorption were scrutinized. The microscopic effects of the three different post-cure temperatures on the manufactured composites were also analyzed using scanning electron microscopy.

## 2. Material and Methods

### 2.1 Material

Jute plain woven texture and Basalt plain woven texture were supplied by companies in Istanbul. These textures were utilized as reinforcement materials. These texture characteristics used in this research are listed in Table 1. The fabric specimens are indicated in Figure 1. Also, the fabric stacking sequences are indicated in Figure 2.

In this work, the related hardener LH160 and the epoxy resin L160 were utilized as matrix material. The hardener and epoxy resin were procured by Kompozitshop. The specific characteristics of the matrix assembly are listed in Table 2. A weight ratio of 100:25±2 was chosen for the mixture of epoxy resin and hardener, taking into account the

values given by the manufacturer and data from previous studies.

In this research, twenty-seven composite samples were prepared for homogeneous and hybrid composite structures with two different fabrics and three different post-curing temperatures. The fabrics were placed with unidirectional and inter-ply structure. The pattern names given to the samples for the composite laminates fabricated are listed in Table 3.

After the samples were cured in a furnace at 50°C, 70°C, and 90°C for 1 hour, the cutting process was carried out with a waterjet device in the test sizes defined in the norms.

Table 1. Fabric characteristics [31], [32]

| Fabric        | Weight (g/m <sup>2</sup> ) | Thickness of fabric (mm) | Warp (tex) | Weft (tex) |
|---------------|----------------------------|--------------------------|------------|------------|
| Jute fabric   | 250                        | 0.4                      | -          | -          |
| Basalt fabric | 200                        | 0.2                      | 200        | 200        |



Figure 1. Fabric specimens: a) Jute fabric b) Basalt fabric

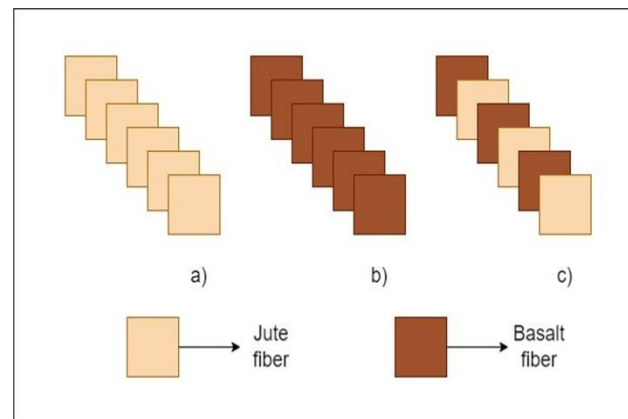


Figure 2. Fabric stacking sequences of: a) Jute fabric b) Basalt fabric c) Jute/Basalt fabric hybrid structure

Table 2. Hardener and epoxy characteristics [33]

|                                | LH160 Hardener | L160 Epoxy   |
|--------------------------------|----------------|--|
| Density (g / cm <sup>3</sup> ) | 0.96-1.0       | 1.13-1.17  |
| Viscosity (mPas)               | 10-50          | 700-900  |
| Actuation temperature (°C)     | -              | 60 / +50 except heat treatment<br>-60 / +80 by performing heat treatment |
| Refractor index                | 1.520-1.521    | 1.548-1.553  |
| Mensuration circumstances      | 25°C           | 25°C   |

Table 3. Naming of prepared specimens

| Pattern name | Textile versions                               |
|--------------|--|
| J            | Jute fabric                                    |
| B            | Basalt fabric                                  |
| JE           | Jute fiber reinforced homogeneous composite    |
| BE           | Basalt fiber reinforced homogeneous composite  |
| JBE          | Jute/ Basalt fiber reinforced hybrid composite |

## 2.2 Method

The VARTM technique has been utilized in the manufacturing of hybrid composites comprise of epoxy resin reinforced with jute and basalt fabric. In this technique, a vacuum force is the main factor to remove the air that may be in the reinforcement material and to ensure that the resin enters the mold. Ensuring tightness is the most critical step in the fabrication process. All samples were produced at 20°C ± 2°C and a pressure of 1 bar. First, the production area was surrounded with vacuum sealing tape, according to the dimensions of the fabrics, which were cut according to the standard dimensions. After the fabrics are lined up on the area in a predetermined order, peel fabric, infusion mesh, and vacuum foil are laid on top in order. Hose connections for resin inlet and outlet were then connected to the system, and the resin prepared in the determined mixing ratios was infused into the system. The vacuum pump was operated at a pressure of one bar for approximately two hours until excess resin movement ceased. The samples were cured within 24 hours after the pump was turned off. The samples taken after 24 hours were cured in a furnace at 50°C, 70°C, and 90°C for 1 hour and then prepared for waterjet cutting.

## 2.3 Tensile Testing

The tensile test was carried out to specify the mechanical features of the composite products produced in the scope of the study. Specimens with 250 mm length, 25 mm width and 2.5 mm thickness were prepared for the

tensile test according to the ASTM D3039 standards. The tests were performed using the ALSA Hydraulic test device in KOLUMAN Automotive Industry Laboratory. ASTM D 3039 rule was taken into account when tensile testing the materials, and the test was carried out by adjusting the cross-head speed to 2 mm/min [34]. The apparatus with a capacity of 98000 kN load cell was utilized to construct tensile tests as is indicated in Figure 3. The experiments were performed at 20°C ± 2°C temperature and the sample sizes were entered into the computer program before starting the test. After the test, the values of tensile strength, modulus of elasticity, and strain rate values of the manufactured products were reached. From the average of the results of the 5 samples tested for homogeneous and hybrid composite structures, the values related to the tensile strength of the manufactured specimens were obtained.

## 2.4 Hardness Testing

The hardness value of the composite products manufactured in the study was assigned by the Vickers hardness method. The measured Vickers hardness values are directly related to the applied load and the area created by the impression on the test surface of the material. The ASTM E92-17 standard was taken as a reference when measuring the hardness of the samples, and the measurement was made by selecting the force value of 0.2 kgf using an AOB Lab product machine. Specimens with 70 mm length, 70 mm width and 1.5 mm thickness were prepared for hardness test. [35]. Fifteen hardness measurements were performed on the prepared sample surfaces and the average of the 15 values was recorded as the Vickers hardness value of the composite product.



Figure 3. Tensile testing machine

## 2.5 Water Absorption Analysis

The objective of this analysis is to specify the water absorption capacity of the samples produced in normal water, taking into account ASTM D-5229 standards [36]. For the water absorption test, the samples were produced in the dimensions of 100 mm length, 100 mm width and 2 mm thickness and prepared for the test. The three composite samples were tested with water during their stay in the container. First, the dry weights of the produced products were measured on a digital balance, then the samples were immersed in water for 120 h and the samples were weighed at regular intervals and the amount of water absorbed was noted periodically. The test was implemented at room temperature. Tap water was used in the containers in which the samples were placed. The preference for tap water is because there are also studies using tap water, and these studies also yield close results to real results.

## 2.6 Morphological Analysis

The SEM FEI Quanta 650 Field Emission device was used to examine and analyze the surface morphology of the produced composite samples. The surface conductivity of the samples was increased by gold spraying and the surface coating was performed. The aggrandizement capacity of the instrument is in the range of 6-1,000,000 x times and can be operated at 30 kV. With this analysis, it will be possible to observe the fracture surface of the composite samples and explore the interfacial properties such as fiber-matrix interactions, matrix cracks in the material, fiber shrinkage, fiber breakage, and fiber-matrix bond separation.

## 3. Result and Discussions

### 3.1 Tensile Test Results

In the scope of this research, tensile test outcomes are given in Figure 4. The standard deviations in the test results were  $\pm 3.94$ ,  $\pm 19.92$ , and  $\pm 7.82$  for the J, B and JB samples at 50°C,  $\pm 7.87$ ,  $\pm 22.96$ , and  $\pm 5.08$  for the J, B and JB samples at 70°C, respectively. These deviation values for 90°C are  $\pm 1.06$ ,  $\pm 17.91$ , and  $\pm 4.78$  for J, B and JB samples, respectively. According to the results obtained, the post-curing temperature being 90°C instead of 50°C caused an increase in the tensile strength value of hybrid jute/basalt composites and homogeneous jute composites, while a decline in tensile strength value was observed in homogeneous basalt composites. Increasing the post curing temperature above 70°C in homogeneous jute and basalt composites had a negative impact on the tensile strength. It has been stated in the studies that this situation is associated with the glass transition temperature of polymers. The outcomes of the study displayed that the tensile strength value of the samples produced did not change when the glass transition temperature was exceeded in the material.

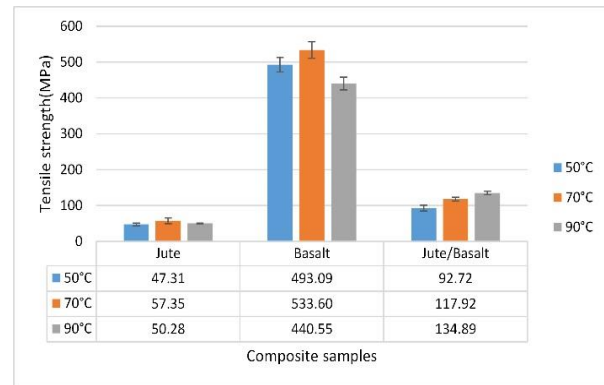


Figure 4. Tensile test results

In a study in which the hybridization process of jute fiber was performed, it was expressed that the tensile strength and flexural strength values declined by rising the post cure temperature from 60 °C to 90 °C [37], [38]. In this study, a tensile strength increment of 21.22% in homogeneous jute composites and 8.21% in homogeneous basalt composites was observed at post-curing temperature increasing from 50 °C to 70 °C. In hybrid jute/basalt composites, on the other hand, increasing post-cure temperature from through 50 °C to 70 °C provided a tensile strength increase of 27.18%, as increasing post-cure temperature from 70 °C to 90 °C provided a 14.39% increase in tensile strength. Besides, compared to homogeneous jute composites, the tensile strength of hybrid jute/basalt composites increased by 1.96, 2.06, and 2.68 times at 50 °C, 70 °C, and 90 °C post curing temperatures, respectively, with hybridization process. This reflects the positive impact of increasing the post-cure temperature on the tensile strength values of the hybridization process.

Table 4 displays the elastic modulus and elongation rate results of produced composites. As the elastic modulus results are evaluated, the rise in post-cure temperature from 50°C to 90°C in parallel with the tensile strength value results had a positive effect on homogeneous jute composites and hybrid jute/basalt composites, while it had a negative effect on homogeneous basalt composites. In the results of the elongation rates, the impact of post-cure temperature increase was similar to the tensile strength and elastic modulus results. In the study where the post curing temperatures at 60 °C, 80 °C, and 100 °C were analyzed using jute fabric, it was found that the elastic modulus value increased with increasing post curing temperature [39]. Raising the post-cure temperature from 50 °C to 90 °C led to an elastic modulus increase of 1.58 times in homogeneous jute composites and 1.44 times in hybrid jute/basalt composites. Whilst these rates tend to increase by 1.02 times at post-curing temperatures rising from 50°C to 70°C in homogeneous basalt composites, post curing temperature increasing from 70°C to 90°C caused a 1.14 times decline in elastic modulus value.

Table 4. Elastic modulus and elongation rate results

| Post-cure temperature | Elastic modulus (MPa) |              |              | Post-cure temperature | Elongation rate (%) |           |             |
|-----------------------|-----------------------|--------------|--------------|-----------------------|---------------------|-----------|-------------|
|                       | Jute                  | Basalt       | Jute/Basalt  |                       | Jute                | Basalt    | Jute/Basalt |
| 50°C                  | 993.2±21.52           | 5749.2±24.78 | 1227±49.13   | 50°C                  | 4.22±0.22           | 9.76±0.27 | 6.26±0.39   |
| 70°C                  | 1139.4±31.76          | 5892.8±21.48 | 1464.4±65.8  | 70°C                  | 4.24±0.23           | 9.94±0.27 | 6.52±0.18   |
| 90°C                  | 1567.4±18.9           | 5148.8±20.04 | 1768.2±62.57 | 90°C                  | 4.56±0.13           | 9.3±0.27  | 6.34±0.17   |

In the previous studies, it has been found that the features of tensile strength at different temperatures applied to hybrid composites using basalt fibers vary depending on the temperatures [38]. Elevated the post-cure temperature from 50°C to 90°C in percent elongation rates resulted in an increase of 1.01 times in hybrid jute/basalt composites and 1.08 times in homogeneous jute composites.

### 3.2 Hardness Test Results

Figure 5 gives the microhardness results of prepared composites in this research. It indicates that Vickers hardness value increases with increasing post curing temperatures both in homogeneous composites and hybrid composites. It can be shown that the enhanced cross-links formed by the post-curing process in the polymer matrix resin make the composite structure more robust, causing an increase in the hardness value due to the increased post-curing temperature. In a study in which the hardness test was performed by rising the post-cure temperature from 40°C to 80°C, it was determined that the hardness value enhanced with the post-cure temperature [40]. Increasing the post curing temperature from 50°C to 90°C resulted in an increase of 36.15%, 19.53%, and 34.65% in Vickers hardness values for JE, BE, and JBE, respectively. As the post-cure temperature is increased from 50°C to 70°C, these rates are 28.86%, 12.6%, and 7.97% for JE, BE, and JBE, respectively, in Vickers hardness values. Increasing the post-cure temperatures from 70°C to 90°C increases the Vickers hardness values by 5.66%, 6.16%, and 24.71% for JE, BE, and JBE, respectively. While the standard deviation values were ±23.67, ±20.07, and ±25.05 in J, B and JB samples, respectively, at 50°C, they were ±10.32, ±22.3, and ±27.53 in J, B and JB samples at 70°C. These values are ±12.64, ±14.24, and ±20.55 for J, B and JB samples at 90°C, respectively.

### 3.3 Water Absorption Analysis Results

Figure 6, 7 and 8 gives the water absorption analysis outcomes of produced samples. Because of the hydrophilic nature of jute fibers, the highest water absorption was observed in homogeneous jute fiber composites. Basalt fibers from mineral fibers did not absorb as much water as jute fibers. In previous studies, basalt fiber was successful in preventing water penetration into the fiber-matrix interface

by showing better water-repellent behavior in basalt hybridization application in composites [41]. In JE composite structures, the water absorption rates of 7.31%, 6.14%, and 8.94% were observed in the samples applied post-cure temperatures of 50°C, 70°C, and 90°C, respectively. These increase rates were found as 0.42%, 0.25%, and 0.24% in BE structures at post-cure temperatures of 50°C, 70°C, and 90°C, respectively. In JBE structures, water absorption was 1.66% at 50 °C, 0.74% at 70 °C, and 0.47% at 90 °C. From this, it is observed that the water absorption of the hybrid composites made with basalt fiber and jute fiber is significantly less, and the water absorption of the jute fibers is significantly inhibited by the basalt fibers. Water absorption is also affected by the cell wall, the lumen, the gap between fiber and resin, and poor interfacial bonding [42]. It is obtained from the results in the graph that the water absorption decreases with the increase of post-curing temperatures. This is an indication that the polymer epoxy matrix forms stronger bonds as the post-cure temperature rises, reducing the water absorption capacity of the fibers.

### 3.4 SEM Analysis Results

The images from Figure 9 to Figure 17 show the SEM analysis images of the structures after the tensile test performed after the post-cure temperatures of 50°C, 70°C, and 90°C were applied. SEM analysis image of homogeneous jute fiber composites applied at 50°C post curing temperature is given in Figure 9.

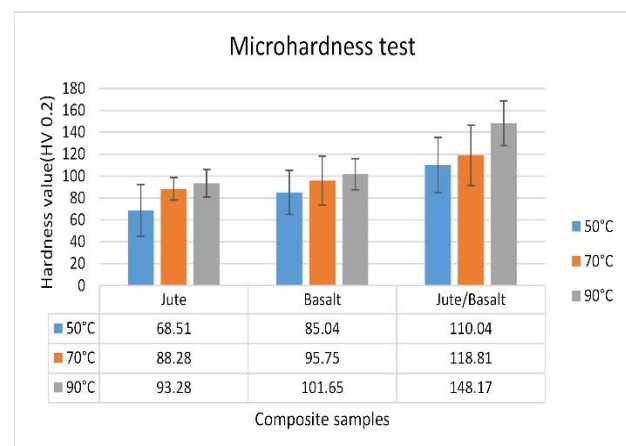


Figure 5. Hardness test results

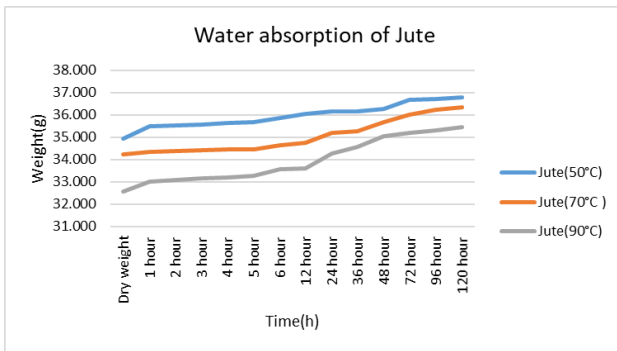


Figure 6. Water absorption analysis results of Jute composite

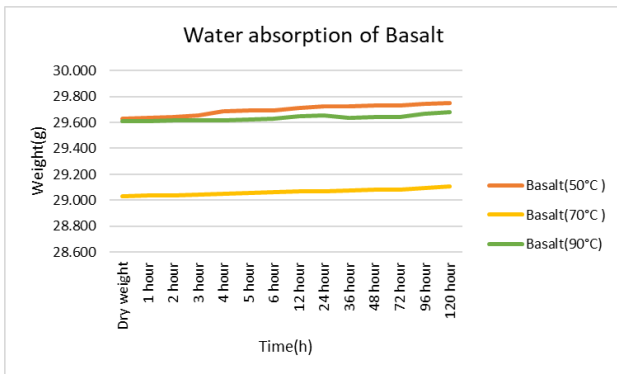


Figure 7. Water absorption analysis results of Basalt composite

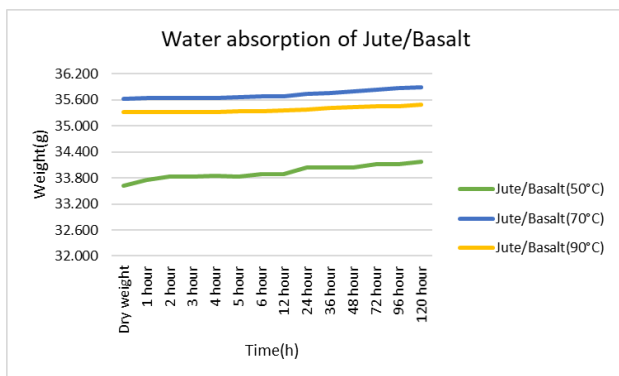


Figure 8. Water absorption analysis results of Jute/Basalt hybrid composites

Whilst voids are seen in the JE structure, there are almost no void structures in the BE structures in Figure 10. Fiber shrinkage and fiber elongation were detected in JE structures, and homogeneous fiber breaks were detected in BE structures. In the JBE structures in Figure 11, it was understood that due to the strong bonding of the matrix resin and the fibers, no voids were observed, fiber shrinkage and elongation of the jute fibers were observed, while basalt fibers broke into fiber bundles. In the samples after the tensile test, fiber breaks and fiber shrinkage due to mechanical load are also observed at different post-curing temperatures in the hybridization of jute fiber with different fabrics [43]. It is seen that the jute fiber structures in Figure 12 show fiber shrinkage. In the comparison of BE structures in Figure 13 and Figure 11, it was determined that basalt fibers were broken in bundles and homogeneously and did

not show fiber shrinkage or elongation.

By the time the JE structures in Figure 15 are checked against the JE structures in Figure 9 and Figure 12, it was found that the gaps between the matrix resin and the fibers increased. This can be expressed by the fact that natural fibers and matrix structures have different chemical structures and do not form a good bond between them [30]. In the comparison of BE structures in Figure 13 and Figure 16, it was seen that the resin did not completely cover the matrix in BE structures that were post-cured at 90 °C, indicating that there was not as much bonding between the matrix and the resin as in BE structures that were post-cured at 70 °C. This explains why the tensile strength value of Basalt fiber samples when 90°C post curing temperature is applied is less than the tensile strength value of the samples for which 70°C post curing temperature is applied. As the JBE structures in Figure 17 and Figure 14 are checked against the structures in Figure 11, it was observed that resin and fibers showed good adhesion. Moreover, less fiber breakage and shrinkage were observed in Figures 14 and 17 compared to the JBE structures in Figure 11.

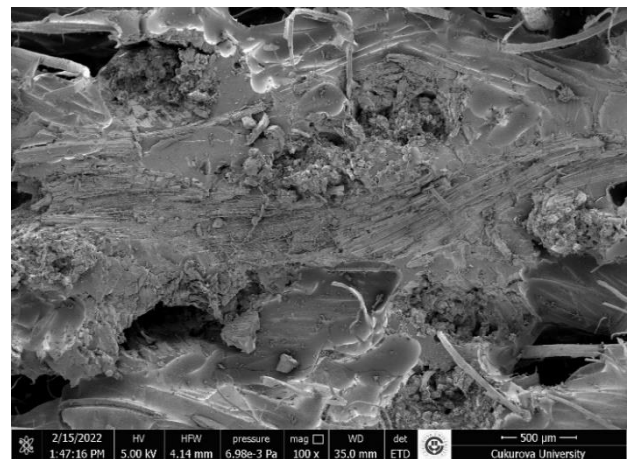


Figure 9. JE composites at 50°C post cure temperature SEM micrograph

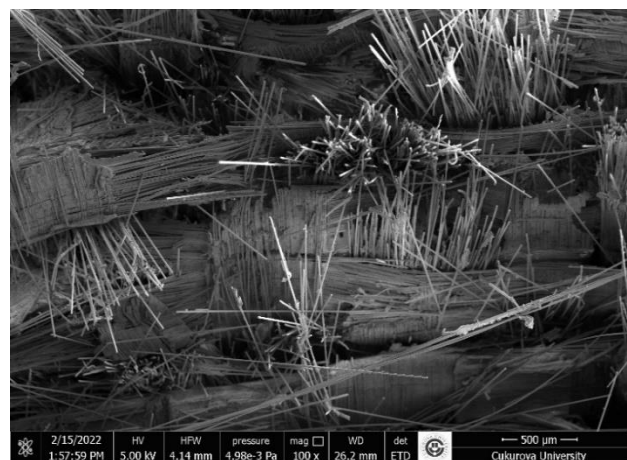


Figure 10. BE composites at 50°C post cure temperature SEM micrograph



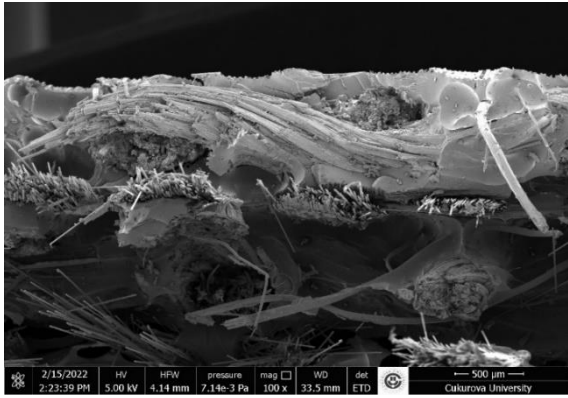


Figure 11. JBE composites at 50°C post cure temperature SEM micrograph

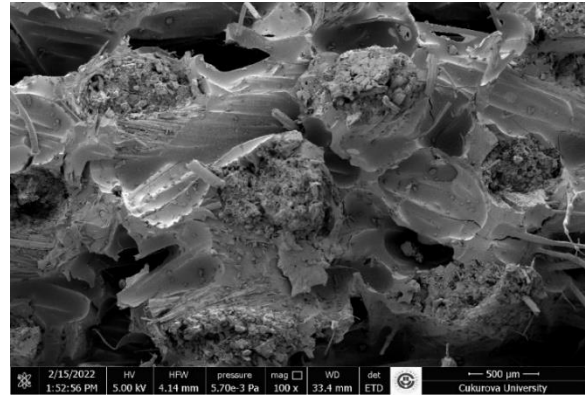


Figure 15. JE composites at 90°C post cure temperature SEM micrograph

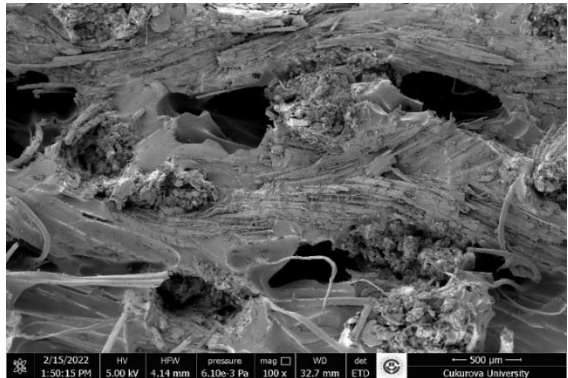


Figure 12. JE composites at 70°C post cure temperature SEM micrograph

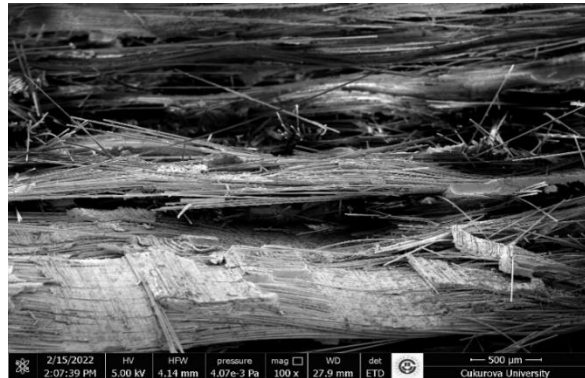


Figure 16. BE composites at 90°C post cure temperature SEM micrograph

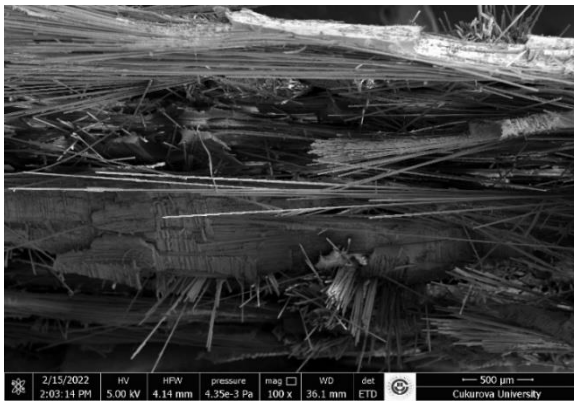


Figure 13. BE composites at 70°C post cure temperature SEM micrograph



Figure 17. JBE composites at 90°C post cure temperature SEM micrograph

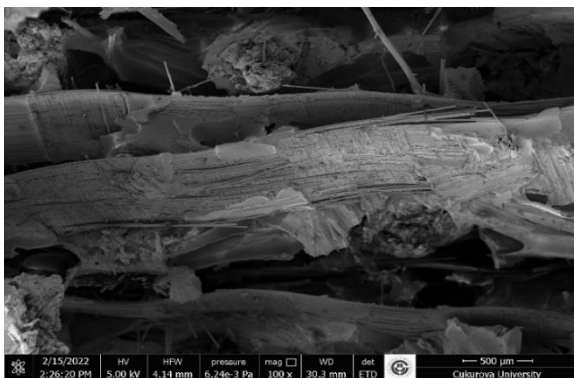


Figure 14. JBE composites at 70°C post cure temperature SEM micrograph

#### 4. Conclusions

In the present study, the effect of three different post-curing temperatures on the mechanical characteristics and water absorption rate of homogeneous and hybrid woven composites reinforced with jute and basalt fibers was investigated. The outcomes of the tensile tests demonstrated that increasing the post-cure temperatures from 50 °C to 90 °C resulted in an increase in tensile strength of 1.06 times for homogeneous jute fiber composites and 1.45 times for hybrid jute/basalt composites. For homogeneous basalt fibers, increasing the post-cure temperature from 50 °C to 70 °C brought about 1.08 times increment in tensile strength,

while rising the post-cure temperature from 70 °C to 90 °C decreased the tensile strength value. Whereas increasing the post-cure temperature for hybrid composite samples improves the mechanical properties, increasing the post-cure temperature above 70 °C for homogeneous jute and basalt fibers commonly do not result in a positive increase in the mechanical features of the material. According to the results of the Vickers hardness test, both the homogeneous jute and basalt composites and the hybrid jute/basalt composites exhibited higher hardness values with increasing post-cure temperature. Elevated the post-cure temperature from 50 °C to 90 °C led to an increase of 1.36 times for homogeneous jute fiber composites, 1.19 times for homogeneous basalt fibers, and 1.35 times for hybrid jute/basalt fibers. The water absorption results show that the water absorption rate generally decreases with elevated post-cure temperature. This can be ascribed to the fact that the resin forms a stronger bond with the fibers and prevents it from interfering with the fiber-matrix interaction. The results of the SEM analysis also indicate that the data obtained from the physical examination of the homogeneous and hybrid composite structures confirm the results of the tensile tests. Although increasing post-cure temperatures have shown different effects on hybrid and homogeneous composite structures, increasing the post-cure temperature usually has a favorable impact on the mechanical features. In terms of both environmental impact and cost, the use of natural and mineral fiber reinforced composites by hybridization and application of high post-curing temperatures will exhibit superior characteristics for interior and exterior trim parts in the automotive industry compared to other hybrid structures.

### Declaration

The authors declared no potential conflicts of interest with respect to the research, authorship, and/or publication of this article. The authors also declared that this article is original, was prepared in accordance with international publication and research ethics, and ethical committee permission or any special permission is not required.

### Author Contributions

B. Karacor developed the methodology and experimental study. M. Ozcanli supervised and prepared the manuscript.

### Nomenclature

*J* : Jute fabric  
*B* : Basalt fabric  
*JE* : Jute fiber reinforced homogeneous composite  
*BE* : Basalt fiber reinforced homogeneous composite  
*JBE* : Jute/ Basalt fiber reinforced hybrid composite  
*VARTM* : Vacuum Assisted Resin Transfer Molding  
*ASTM* : American Society of Testing Materials

*HV* : Hardness Value

*SEM* : Scanning Electron Microscope

### References

- Adam H., *Carbon fibre in automotive applications*. Materials and Design, 1997. **18**(4–6): p. 349–355.
- Rajak D. K., D. D. Pagar, R. Kumar, and C. I. Pruncu, *Recent progress of reinforcement materials: A comprehensive overview of composite materials*. Journal of Materials Research and Technology, 2019. **8**(6): p. 6354–6374.
- Ramli N., N. Mazlan, Y. Ando, Z. Leman, K. Abdan, A. A. Aziz, and N. A. Sairy, *Natural fiber for green technology in automotive industry: A brief review*. IOP Conference Series: Materials Science and Engineering, 2018. **368**(1): p. 012012.
- Begum K. and M.A. Islam, *Natural Fiber as a substitute to Synthetic Fiber in Polymer Composites: A Review*. Research Journal of Engineering Sciences, 2013. **2**(3): p. 46–53.
- Mohammed L., M. N. M. Ansari, G. Pua, M. Jawaid, and M. S. Islam, *A Review on Natural Fiber Reinforced Polymer Composite and Its Applications*. International Journal of Polymer Science, 2015. **2015**: p. 1–15.
- Bledzki A. K. and J. Gassan, *Composites reinforced with cellulose*. Progress in Polymer Science, 1999. **24**: p. 221–274.
- Ali A., M. A. Nasir, M. Y. Khalid, S. Nauman, K. Shaker, S. Khushnood, K. Altaf, M. Zeeshan and A. Hussain, *Experimental and numerical characterization of mechanical properties of carbon/jute fabric reinforced epoxy hybrid composites*. Journal of Mechanical Science and Technology, 2019. **33**(9): p.4217–4226.
- Alves C., P. M. C. Ferrao, A. J. Silva, L. G. Reis, M. Freitas, L. B. Rodrigues, D. E. Alves, *Ecodesign of automotive components making use of natural jute fiber composites*. Journal of Cleaner Production, 2010. **18**(4): p. 313–327.
- Keya K. N. , N. A. Kona, F. A. Koly, K. M. Maraz, M. N. Islam, and R. A. Khan, *Natural fiber reinforced polymer composites: history, types, advantages, and applications*. Materials Engineering Research, 2019. **1**(2): p. 69–87.
- Mohanty A. K., M. Misra, and G. Hinrichsen, *Biofibres, biodegradable polymers and biocomposites: An overview*. Macromolecular Materials and Engineering, 2000. **276–277**(1): p. 1–24.
- Drzal L. T., A. K. Mohanty, and M. Misra, *Bio-composite materials as alternatives to glass fibre reinforced composites for automotive applications*. Magnesium, 2001. **40**: p. 386–390.
- Jeyanthi S. and J. J. Rani, *Influence of natural long fiber in mechanical, thermal and recycling properties of thermoplastic composites in automotive components*. International Journal of Physical Sciences, 2012. **7**(43): p. 5765–5771.
- Holbery J. and D. Houston, *Natural-fiber-reinforced polymer composites in automotive applications*. JOM, 2006. **58**(11): p. 80–86.
- Chimeremeze C. P. and O. D. Anayo, *Economic Advantages and Sustainability of Basalt Civil / Structural Materials for Nigerian Modern Engineering Structures ; Positive Impact on Landfilling Construction*. International Journal of Advances in Mechanical and Civil Engineering, 2019. **6**(2): p. 45–51.
- Zhou H., B. Jia, H. Huang, and Y. Mou, *Experimental Study on Basic Mechanical Properties of Basalt Fiber Reinforced*

- Concrete*. Materials, 2020. **13**(6): p. 1362.
16. Tóth L. F., J. Sukumaran, G. Szebenyi, A. Kalacska, D. Fauconnier, R. Nagarajan and P. De Baets, *Large-scale tribological characterisation of eco-friendly basalt and jute fibre reinforced thermoset composites*. Wear, 2020. **450–451**(March): p. 203274.
  17. Yuvaraj M., M. Rajmohan, G. Naveen, and S. Mohanraj, *Mechanical Characterisation of Basalt Based Composite Materials*. Proceedings of the IOSR Journal of Mechanical and Civil Engineering (IOSR-JMCE), 2014. (November): p. 70–76.
  18. Bahrami M., J. Abenojar, and M. Á. Martínez, *Recent Progress in Hybrid Biocomposites: Mechanical Properties, Water Absorption, and Flame Retardancy*. Materials, 2020. **13**(22): p. 5145.
  19. Cangül S., Ö. Adıgüzel, S. Tekin, F. Öztekin, and Ö. Satıcı, *A Comparison of the Water Absorption and Water Solubility Values of Four Different Composite Resin Materials*. Cumhuriyet Dental Journal, 2018. **21**(4): p. 335–342.
  20. Fiore V., T. Scalici, F. Sarasini, J. Tirilló, and L. Calabrese, *Salt-fog spray aging of jute-basalt reinforced hybrid structures: Flexural and low velocity impact response*. Composites Part B: Engineering, 2017. **116**: p. 99–112.
  21. Surana I., D. J. Pandya, N. H. Padmaraj, S. Hegde, and K. N. Chethan, *Influence of filler material on mechanical and vibration properties of basalt/epoxy composites*. Materials Research Express, 2019. **6**(8): p. 085342.
  22. Kumar N. and A. Singh, *Study the effect of fiber orientation on mechanical properties of bidirectional basalt fiber reinforced epoxy composites*. Materials Today: Proceedings, 2021. **39**: p. 1581–1587.
  23. Darshan S. M. and B. Suresha, *Effect of basalt fiber hybridization on mechanical properties of silk fiber reinforced epoxy composites*. Materials Today: Proceedings, 2021. **43**: p. 986–994.
  24. Dhiman P. and H. Sharma, *Effect of walnut shell filler on mechanical properties of jute-basalt hybrid epoxy composites*. Materials Today: Proceedings, 2021. **44**: p. 4537–4541.
  25. Kishore M., M. Amrita, and B. Kamesh, *Tribological properties of basalt-jute hybrid composite with graphene as nanofiller*. Materials Today: Proceedings, 2021. **43**: p. 244–249.
  26. Alagarasan K., R. Ramkumar, and K. Dhanesh Prabu, *Fabrication and Mechanical Testing of Natural ( Jute ) Fibre Composite Material*. International Journal for Innovative Research in Science & Technology, 2016. **3**(06): p. 78–83.
  27. Zareei N., A. Geranmayeh, and R. Eslami-Farsani, *Interlaminar shear strength and tensile properties of environmentally-friendly fiber metal laminates reinforced by hybrid basalt and jute fibers*. Polymer Testing, 2019. **75**(February): p. 205–212.
  28. Almeida-Chetti V. A., R. L. Macchi, and M. E. Iglesias, *Effect of post-curing treatment on mechanical properties of composite resins*. Acta odontologica latinoamericana : AOL, 2014. **27**(2): p. 72–76.
  29. Singh J. I. P., S. Singh, and V. Dhawan, *Effect of Curing Temperature on Mechanical Properties of Natural Fiber Reinforced Polymer Composites*. Journal of Natural Fibers, 2018. **15**(5): p. 687–696.
  30. Ozkur S., M. Leskovšek, B. Golja, A. Demsar, H. Sezgin, and I. Yalcin-Enis, *Characterization of Thermo-mechanical and Morphological Properties of Jute Fabric Reinforced Epoxy/AESO Bio-composites*. Fibers and Polymers, 2021. **22**(12): p. 3414–3424.
  31. Kumascı, *Technical Properties of Jute(250 gr per metresquare)*. [cited 2021 28 Dec]; Available from <https://www.kumasci.com/urun/kanavice-jut-telis-cuval-kumasi-ham-en-sik-jut-10-onz/1316>.
  32. Kompozitshop, *Technical properties of basalt fiber*. [cited 2021 28 Dec]; Available from: <https://www.kompozitshop.com/bazalt-fiber-kumas-200grm2-plain>.
  33. Kompozitshop, *Epoxy and hardener*. [cited 2021 28 Dec]; Available from: <https://www.kompozitshop.com/epoksi-recine-ve-sertlestirici>.
  34. ASTM D3039/D3039-M *Standard Test Method for Tensile Properties of Polymer Matrix Composite Material*.
  35. ASTM E92-17 *Standard Test Methods for Vickers Hardness and Knoop Hardness of Metallic Materials*.
  36. ASTM D 5229/D 5229M – 92, *Standard test method for moisture absorption properties and equilibrium conditioning of polymer matrix composite materials*.
  37. Mann G. S., L. P. Singh, and P. Kumar, *Experimental Investigation of Effect of Curing Temperature on Mechanical Properties of Hybrid Composites*. International Journal of Technical Research & Science, 2020. **05**(03): p. 10–15.
  38. Cao S., Z. Wu, and X. Wang, *Tensile properties of CFRP and hybrid FRP composites at elevated temperatures*. Journal of Composite Materials, 2009. **43**(4): p. 315–330.
  39. Karacor B. and M. Özcanlı, *Different Curing Temperature Effects on Mechanical Properties of Jute/Glass Fiber Reinforced Hybrid Composites*. International Journal of Automotive Science and Technology, 2021. **5**(4): p. 358–371.
  40. Aruniit A. , J. Kers, A. Krumme, T. Poltimäe, and K. Tall, *Preliminary Study of the Influence of Post Curing Parameters to the Particle Reinforced Composite's Mechanical and Physical Properties*. Material Science(Medziagotyra), 2012. **18** (3): p. 256–261.
  41. Almansour F. A., H. N. Dhakal, and Z. Y. Zhang, *Effect of water absorption on Mode I interlaminar fracture toughness of flax/basalt reinforced vinyl ester hybrid composites*. Composite Structures, 2017. **168**: p. 813–825.
  42. Ramesh Kumar S. C. , R. V. P. Kaviti, L. Mahesh, and B. M. Mohan Babu, *Water absorption behavior of hybrid natural fiber reinforced composites*. Materials Today: Proceedings, 2022. **54**: p. 187-190.
  43. Ramesh M., R. Vimal, K. H. Hara Subramaniyan, C. Aswin, B. Ganesh, and C. Deepa, *Study of Mechanical Properties of Jute-Banana-Glass Fiber Reinforced Epoxy Composites under Various Post Curing Temperature*. Applied Mechanics and Materials, 2015. **766–767**: p. 211–215.



## Research Article

## Examining the hydrophobic properties of electrospun oxide-induced polystyrene nanofibers for application in oil-water separation

Kemal Doğan<sup>a,\*</sup> , Ali Akbar Hussaini<sup>b</sup> , Mehmet Okan Erdal<sup>c,\*</sup>  and Murat Yildirim<sup>b</sup> 

<sup>a</sup>Selçuk University, Institute of Science, Department of Nanotechnology and Advanced Materials, Konya, 42130, Turkey

<sup>b</sup>Selçuk University, Faculty of Science, Department of Biotechnology, Konya, 42130, Turkey

<sup>c</sup>Necmettin Erbakan University, Meram Vocational School, Konya, 42090, Turkey

## ARTICLE INFO

## ABSTRACT

## Article history:

Received 17 February 2022

Accepted 21 June 2022

Published 15 August 2022

## Keywords:

Nanofiber

Polystyrene

Water-oil separation

Nanofibers have great importance in the membrane technology used in hydrophobic surface filtration studies applied to water-oil separation products. This study improves upon the hydrophobic properties of electrospun polystyrene-based nanofibers by increasing surface contact angles. As a result, nanofibers have been produced by adding ZnO, MoO<sub>3</sub>, NiO, SiO<sub>2</sub>, and TiO<sub>2</sub> additives to the polystyrene (PS)/dimethylformamide (DMF) polymer solution at 5% of the mass. Surface contact angle (CA), fourier-transform infrared spectroscopy (FTIR), and scanning electron microscope (SEM) images of the nanofibers were taken. The obtained results were evaluated and show the fiber diameter to range from 555 to 1553 nm. The addition process was observed to be able to affect the polystyrene fiber's ability to retain water. Moreover, surface contact angle of polystyrene increased to 143° by TiO<sub>2</sub> addition. Furthermore, the highest oil-carrying capacity is concluded to have been observed on the SiO<sub>2</sub> and MoO<sub>3</sub> doped fibers.

### 1. Introduction

Oil plays a vital role in the modern industrial world. Despite being a necessary raw material for a variety of chemical and synthetic polymer fabrications, it is not found in all regions of the world. Moreover, undesirable accidents occur while processing it, such as in its transportation, usage, and storage. This causes not only a loss of energy but also threatens the environment [1]. Accidents in crude oil transportation have created undeniable catastrophes requiring clean-up operations, with 5,000 tons of oil spilled annually between 2010–2014 [2]. The most noteworthy examples of major accidents have been the Torrey Canyon (1967), Amoco Cadiz (1978), Atlantic Empress (1979), Exxon Valdez (1990), and ABT Summer (1991) spills that resulted in major environmental impacts [3]. Furthermore, oil spills could have critically negative effects on marine life, endangering the lives of seaweed (*Codium tomentosum*, *Codium barbata*), algae (*Ulva lactuca*), mollusks, (*Mytilus galloprovincialis*, *Ostrea edulis*, *Patella vulgata*), crustaceans (*Crangon crangon*) and fish (*Gobius niger*, *Solea*, *Trigla lucerna*) species [4].

A vast amount of research is found on the parameters of oil/water separation applications. Surface porosity and breakthrough pressure are considered the main parameters affecting the efficiency of membrane filters for oil/water separation applications [5]. Another study from Hazlett investigated and highlighted other main parameters such as surfactant concentration, fiber size and material, bed depth, packing density, water content, and continuous phase flow field velocity [6]. Bansal et al. [7] also investigated parameters such as droplet size, interfacial tension, inflow velocity, pressure drop, emulsion concentration, pore size, fiber fineness, permeability, and thickness.

Several technologies have been developed recently, including the air flotation, selective adsorptions, and filters (membranes) effective at oil/water separation and wastewater treatments [8]. Conventional methods also have been used worldwide for water/oil separation, such as burning, biodegradation via microorganisms, reduction of oil and water density differences, and evaporation of volatile components [9]. Rohrbach et al. [10] synthesized a hydrophilic and oleophobic cellulose-based filter with

\* Corresponding author. Tel.: +90 332 205 10 00.

E-mail addresses: [kdogan@harran.edu.tr](mailto:kdogan@harran.edu.tr) (K. Doğan), [aliakbar.hussaini.1994@gmail.com](mailto:aliakbar.hussaini.1994@gmail.com) (A.A. Hussaini), [moerdal@erbakan.edu.tr](mailto:moerdal@erbakan.edu.tr) (M.O. Erdal), [muratyildirim@selcuk.edu.tr](mailto:muratyildirim@selcuk.edu.tr) (M. Yildirim)

ORCID: 0000-0002-9770-8069 (K. Doğan), 0000-0002-7128-9994 (A.A. Hussaini), 0000-0003-4469-3438 (M.O. Erdal),

0000-0002-4541-3752 (M. Yildirim)

DOI: [10.35860/iarej.1075031](https://doi.org/10.35860/iarej.1075031)

© 2022, The Author(s). This article is licensed under the CC BY-NC 4.0 International License (<https://creativecommons.org/licenses/by-nc/4.0/>).

over 99% efficiency at 89.6 L/m<sup>2</sup>h water flux. Wei et al. [11] have fabricated oxidized poly (arylene sulfide sulfone) (O-PASS) nanofibers via electrospinning. The obtained nanofiber exhibited significant hydrophobicity and 99% efficiency at high water flux 623.1 L/m<sup>2</sup>h. In another study, Cheng et al. [12] have fabricated superhydrophobic nanofibers with separation efficiency of about 99.6% via coaxial electrospinning, containing polydimethylsiloxane (PDMS)/polyvinylidene fluoride (PVDF). Liu et al. [13] fabricated a water-repellent SiO<sub>2</sub> cotton fiber with a high oil-absorption capacity and adequate buoyancy. Shin & Chase [14] added a 1% mix of polyamide nanofibers to glass-fiber filter media, improving the separation efficiency to 84% from 71%. In addition, Secerov Sokolovic & Sokolović [15] investigated the effects of polyethylene, polyester, and polyurethane polymeric fibers on non-Brownian oil. Speth et al. [16] developed a new and scientifically based design method for fiber-bed coalescers. In another study, Shin & Chase [17] determined the effect of wettability on the coalescence mechanism.

Electrospinning is a simple, convenient and cost-effective technique for preparing separation membranes. Nanofibers are advantageous due to their large surface area, low energy consumption, and nanoscale-sized pores that are useful for achieving high separation efficiency [18]. A membrane with a large surface area can contact, adsorb, and coalesce a dispersed liquid [19]. Qiao et al. [20] produced polystyrene (PS)/polyacrylonitrile (PAN) sorbents with a high oil-absorption capacity using the electrospinning method. The oil absorption capacities (OAC) of PS/PAN sorbent in pump oil, peanut oil, diesel, and gasoline have been measured as 194.85, 131.7, 66.75 and 43.38 grams of oil per gram of absorbent (g/g), respectively. Zhu et al. [21] examined the oil/water selectivity and adsorption mechanism of polyvinyl chloride (PVC)/polystyrene (PS) electrospun fibers as sorbent materials. The PVC/PS nanofibers showed significant oil absorption capacities of 146, 119, 38 and 81 g/g for engine oil, peanut oil, diesel, and ethylene glycol, respectively.

This study produces nanofiber materials by adding ZnO, MoO<sub>3</sub>, NiO, SiO<sub>2</sub>, and TiO<sub>2</sub> to the PS/DMF solution. The morphological properties of the obtained nanofibers are characterized by scanning electron microscope (SEM), surface contact angle (CA) measurements, and fourier-transform infrared spectroscopy (FTIR) graphs. The resulting fiber surfaces were immersed in an oil/water emulsion to determine their oil absorption capacities.

## 2. Materials and Method

All chemicals (PS, ZnO, MoO<sub>3</sub>, NiO, SiO<sub>2</sub> and TiO<sub>2</sub>) were purchased from Sigma Aldrich. PS is added to the

*N,N*-dimethyl formamide (DMF) solvent at a mass of 17% and mixed using a magnetic stirrer. After mixing for 30 minutes, a homogeneous 17% PS solution was obtained, after which the solution was loaded into a stainless-steel needle syringe with a diameter of 1.2 mm. With the unadulterated sample, nanoparticles were added at a weight-to-volume (w/v) ratio of 5% to the 17% polymer solution, and then the electrospinning process was performed. The electrospinning was carried out in a laboratory environment at room temperature. The voltage of 12-18 kV was applied, and the distance between the needle tip and the collector was 13-17 cm. In order to determine the oil absorption capacities (OAC) of the produced fibers, sunflower frying oil that was used repeatedly and supplied by a local cafeteria was added to the pure water at a ratio of 5 g/L and mixed.

By measuring the dry masses of fibers and their mass after absorbing oil, the oil absorption rates can be determined in two different ways. Firstly, it can be calculated by measuring the weights of the sorbents and oil using the following formula capacity (Equation 1) called as The gravimetric sorption capacity [22]:

$$\text{Absorbance capacity (\%)} = \frac{(m_{s,o} - m_s)}{m_s} \quad (1)$$

where  $m_s$  and  $m_{s,o}$  are the sponge's masses before and after sorption. It can also be gained using the Equation (2):

$$\text{OAC} = \left[ \frac{(W_3 - W_2 - W_4)}{\left(1 - \frac{m_c}{100}\right) W_1} \right] \quad (2)$$

where  $W_1$  is the weight of the sample before the addition of oil in grams (g),  $W_2$  is the weight of the syringe assembly (syringe chamber, filter paper, test tube, and sample in grams),  $W_3$  is the weight of the syringe assembly after the centrifuge (syringe chamber, filter paper, test tube, sample, and absorbed oil in grams),  $W_4$  is the weight of oil absorbed by the empty filter paper after the centrifuge in grams, and  $m_c$  is the initial moisture content of the sample [23].

## 3. Results

### 3.1. SEM Analysis

Electron microscope photos were taken under 15kV at a magnification of 5000X for all samples. Average fiber diameters were calculated from the SEM images. Average fiber diameters were calculated as 767 nm for the undoped sample and 760 nm, 1553 nm, 680 nm, 555nm, and 822 nm for samples doped respectively with ZnO, MoO<sub>3</sub>, NiO, SiO<sub>2</sub>, and TiO<sub>2</sub>. A homogeneous distribution without the formation of a beaded structure in the fibers can be seen in Figure 1. These surface formations are thought to reduce the angle of contact.

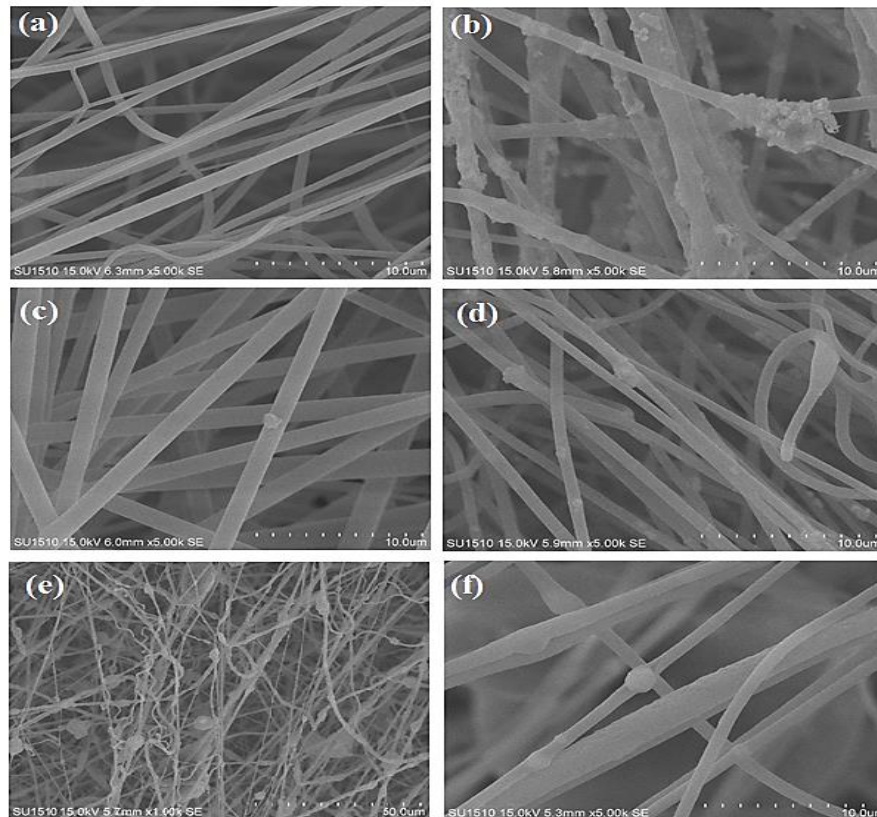


Figure 1. SEM images of a) Undoped PS, b) PS/ZnO, c) PS/MoO<sub>3</sub>, d) PS/NiO, e) PS/SiO<sub>2</sub>, and f) PS/TiO<sub>2</sub> nanofibers

In Figure 1e, the silicon dioxide particles significantly affected the fiber structure compared to the other doped samples. Although no beaded structures occurred, small lumps can be seen on all samples. In Figures 1c, 1d, and 1f, smooth surfaces were obtained as a result of the more homogeneous distribution of the additive in the solution, with lumps rarely being seen on the surface of the added fibers.

### 3.2. Fourier-Transform Infrared Spectroscopy (FTIR) Analysis

The chemical structure of the material is identified using FTIR. Figure 2 provides the FTIR diagrams obtained for the nanofibers containing 17% PS and 5% ZnO, MoO<sub>3</sub>, NiO, SiO<sub>2</sub>, or TiO<sub>2</sub> as an additive. Generally, CH<sub>2</sub>, OH, and C=O bonds are typically observed above 1,500 cm<sup>-1</sup>. Aromatic C-H bond vibrations were observed between 3050-3000 cm<sup>-1</sup>. Moreover, aliphatic C-H absorptions were observed at 3000-2850 cm<sup>-1</sup>. Meanwhile, peaks in the range of 1440-1610 cm<sup>-1</sup> belong to the double bond voltage C=C in the aromatic ring. Peaks from the Si-O-Si bonds were seen at 1040-1060 cm<sup>-1</sup>, and peaks evaluable as belonging to the O-Si-O bond were seen at 746-766 cm<sup>-1</sup>. The peaks at 1450 cm<sup>-1</sup> correspond to stretching in styrene ring [24]. The numerous peaks between 1030 and 548 cm<sup>-1</sup> are due to CH deformation. The reference bands

used are and the symmetric CH<sub>2</sub> stretching band at 2851 cm<sup>-1</sup> for PS [25].

### 3.3. Contact Angle (CA) Analysis

Materials with a surface water contact angle greater than 90° are considered to be hydrophobic. A hydrophobic surface can easily be developed using building blocks with low surface energy or through surface modification [26]. Wettability is considered to be a true solid surface feature that defines the contact between a liquid and a solid surface and is often characterized using a liquid droplet contact angle (CA).

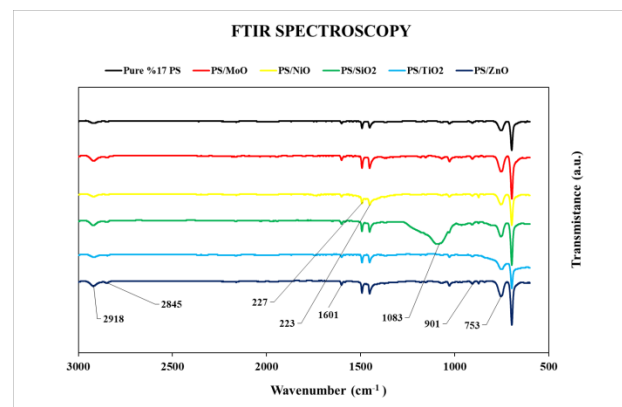


Figure 2. FTIR spectrums of the PS, PS/ZnO, PS/MoO<sub>3</sub>, PS/NiO, PS/SiO<sub>2</sub> and PS/TiO<sub>2</sub> nanofibers

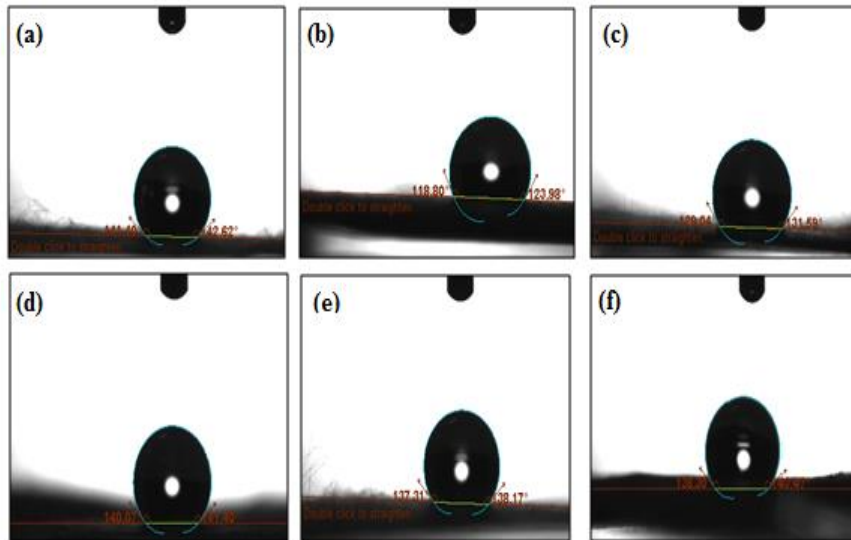


Figure 3. Contact angle measurements of a) undoped PS, b) PS/ZnO, c) PS/MoO<sub>3</sub>, d) PS/NiO, e) PS/SiO<sub>2</sub>, and f) PS/TiO<sub>2</sub>

The wetness of the obtained nanofibers was determined via static water contact angle measurements. In order to measure the static water contact angle of deionized water (DI) on the obtained nanofibers, a goniometer was used. Deionized water was provided using a syringe pump (KDS Legato 100) and a stainless-steel needle (EFD, internal and external diameters of 250 and 520  $\mu\text{m}$  respectively) at a flow rate of 180  $\mu\text{L}/\text{hour}$ . The contact angle was measured after resting the drop of deionized water on the PS nanofiber membrane for 5 seconds. All measurements and experiments were carried out in laboratory ambient conditions at room temperature. Contact angle measurements of the fibers are shown in Figure 3. The average static water contact angle was obtained from measurements taken in five different positions on the same sample. The contact angle graphs of the samples are shown Figure 4.

### 3.4. Oil Absorption Capacity Analysis

The obtained nanofibers were added to the ionized water as shown in Figure 4b. Samples were prepared by cutting 20×20 mm squares from the fabricated fibers and immersing them in the oil/water solution. It was carried out at room temperature. It was stirred in magnetic stirrer for 30 minutes at 500 rpm. The masses of the oil fibers were measured as shown in Figure 4c. The Oil carrying capacity (%) is calculated by the equation 1 and listed in Table 1. According to Table 1, the oil absorption capacity of unadulterated PS and the ZnO, MoO<sub>3</sub>, NiO, SiO<sub>2</sub> and TiO<sub>2</sub>-doped PS nanofibers were respectively measured as 68%, 24%, 103%, 70%, 114%, and 95% g/g. All the fabricated samples can be seen to have exhibited the potential to absorb oil and separate oil from water. The highest oil-carrying capacity is concluded to have been observed on the SiO<sub>2</sub> and MoO<sub>3</sub> doped fibers.

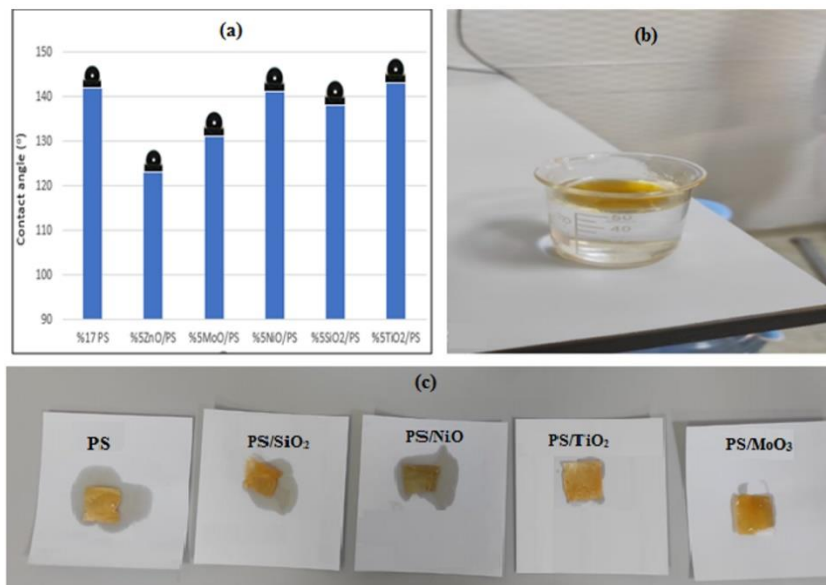


Figure 4. (a) Contact angle graphs of undoped PS, PS/ZnO, PS/MoO<sub>3</sub>, PS/NiO, PS/SiO<sub>2</sub>, and PS/TiO<sub>2</sub> nanofibers, (b) Oil absorption capacity measurement solution of fibers and (c) Oil absorption capacity of fibers after measurement

Table 1. Mass Measurements of the Waste Oil and Fiber Sample

| Materials  | Oil carrying capacity (%) | Water Contact Angle | References |
|--|---------------------------|---------------------|------------|
| PS/carbon nanotubes foam                             | 98.4                      | 161.2°              | [27]       |
| PS-SO <sub>3</sub> H/nylon                           | ~100                      | 158.0°              | [28]       |
| NTs/PS@AuNPs   | 99.4                      | 145.0°              | [29]       |
| PMHS-TEOS-derived xerogel and PS                     | 20.9                      | 154.0°              | [30]       |
| polystyrene@Fe <sub>3</sub> O <sub>4</sub> nanofiber | 92-95                     | 162.0°              | [31]       |
| PS-g-CNT   | >99.94                    | 152.0°              | [32]       |
| PS nanofiber   | 68                        | 142.6°              | This study |
| PS/ZnO nanofiber                                     | 24                        | 123.9°              | This study |
| PS/SiO <sub>2</sub> nanofiber                        | 114                       | 138.1°              | This study |
| PS/NiO nanofiber                                     | 70                        | 141.4°              | This study |
| PS/MoO <sub>3</sub> nanofiber                        | 103                       | 131.5°              | This study |
| PS/TiO <sub>2</sub> nanofiber                        | 95                        | 143.4°              | This study |

#### 4. Conclusions

This study successfully fabricated PS/DMF nanofibers using the electrospinning method. ZnO, MoO<sub>3</sub>, NiO, SiO<sub>2</sub>, and TiO<sub>2</sub> nanoparticle additives were added to the nanofibers, and the resulting SEM, FTIR, and surface contact angle measurements of the produced nanofibers were examined in detail. According to the analysis results, the need for more studies can be concluded in order to optimize the contribution ratio to nanofibers. Regarding to SEM images, nanofibers have been distributed homogeneously without any beaded structure formation. Moreover, average fiber diameters are calculated as 767 nm for undoped sample and 760 nm, 1553 nm, 680 nm, 555 nm and 822 nm for ZnO, MoO<sub>3</sub>, NiO, SiO<sub>2</sub> and TiO<sub>2</sub> doped samples, respectively.

In order to separate water using these nano-porous materials, nanofibers must have at least a 145° surface contact angles with the water. However, the obtained results were found to be less than this value. Apart from the production method being the right choice, the PS/DMF ratio was also expected to have an effect on the desired contact angle values. In addition, although the added oxides were thought to have a hydrophobic effect, they did not exhibit the expected effect. The added particles were assumed would increase the expected effect of clinging to the outer surfaces of the nanofibers. However, the highest oil-carrying capacity is concluded to have been observed on the SiO<sub>2</sub> and MoO<sub>3</sub> doped fibers. In addition, no correlation was detected between the average fiber diameters and surface contact angle.

#### Declaration

The authors declared no potential conflicts of interest with respect to the research, authorship, and/or publication of this article. The authors also declared that this article is original, was prepared in accordance with

international publication and research ethics, and ethical committee permission or any special permission is not required.

#### Author Contributions

K. Dogan and M.O. Erdal developed the methodology. K. Dogan performed the analysis. A.A. Hussaini and M. Yildirim wrote the manuscript. M. Yildirim and M.O. Erdal supervised and improved the study. All authors proofread the manuscript.

#### References

- Galieriková, A., and M. Materna., *World Seaborne Trade One of Main Cause for Oil Spills?*. Transportation Research Procedia, 2020. **44**: p. 297–304.
- Brussaard, C. P. D., Peperzak, L., Beggah, S., Wick, L. Y., Wuerz, B., Weber, J., Arey, J. S., Burg, B. Van Der, Jonas, A., Huisman, J., & Meer, J. R. Van Der., *Immediate ecotoxicological effects of short-lived oil spills on marine biota*. Nature Communications, 2016. **7**: p. 11206.
- Cakir, E., Sevgili, C., and Fiskin, R., *Modelling of possible tanker accident oil spills in the Istanbul Strait in order to demonstrate the dispersion and toxic effects of oil pollution*. Transportation Research Part D: Transport and Environment, 2021. **90**: 102662.
- Yildiz, S., Sönmez, V. Z., Sivri, N., Loughney, S., and Wang, J., *Modelling of possible tanker accident oil spills in the Istanbul Strait in order to demonstrate the dispersion and toxic effects of oil pollution*. Environ Monit Assess, 2021. **193**: 538.
- Yue, X., Li, Z., Zhang, T., Yang, D., and Qiu, F., *Design and fabrication of superwetting fiber-based membranes for oil/water separation applications*. Chemical Engineering Journal, 2019. **364**: p. 292–309.
- Hazlett, R.N., *Fibrous Bed Coalescence of Water Steps in the Coalescence Process*. Industrial & engineering chemistry fundamentals, 1969. **8**(4): p. 625–632.
- Bansal, S., Arim, V.V., Stegmaier, T., and Planck, H., *Effect of fibrous filter properties on the oil-in-water-emulsion separation and filtration performance*. Journal of



- Hazardous Materials, 2011. **190**(1–3): p. 45–50.
8. Deng, D., Prendergast, D.P., MacFarlane, J., Bagatin, R., Stellacci, F., and Gschwend, P.M., *Hydrophobic Meshes for Oil Spill Recovery Devices*. ACS Applied Material Interfaces, 2013. **5**(3): p. 774–781.
  9. Kordjazi, S., Kamyab, K., and Hemmatinejad, N., *Superhydrophilic/oleophobic chitosan/acrylamide hydrogel: an efficient water/oil separation filter*. Advanced Composites Hybrid Materials, 2020. **3**(2): p. 167–176.
  10. Rohrbach, K., Li, Y., Zhu, H., Liu, Z., Dai, J., Andreasen, J., and Hu, L., *A cellulose based hydrophilic, oleophobic hydrated filter for water/oil separation*. Chemical Communication, 2014. **50**: p. 13296-13299.
  11. Wei, Z., Lian, Y., Wang, X., Long, S., and Yang, J., *A novel high-durability oxidized poly (arylene sulfide sulfone) electrospun nanofibrous membrane for direct water-oil separation*. Separation and Purification Technology, 2020. **234**: 116012.
  12. Cheng, XQ., Jiao, Y., Sun, Z., Yang, X., Cheng, Z., Bai, Q., Zhang, Y., Wang, k., and Shao, L., *Constructing Scalable Superhydrophobic Membranes for Ultrafast Water–Oil Separation*. ACS Nano, 2021. **15**(2): p. 3500–3508.
  13. Liu, F., Ma, M., Zang, D., Gao, Z., and Wang, C., *Fabrication of superhydrophobic/superoleophilic cotton for application in the field of water/oil separation*. Carbohydrate Polymers, 2014. **103**: p. 480–487.
  14. Shin, C., and Chase, G.G., *Separation of Water-in-Oil Emulsions Using Glass Fiber Media Augmented with Polymer Nanofibers*. Journal of Dispersion Science and Technology, 2006. **27**(4): p. 517-522.
  15. Sokolović, R.M., and Sokolović, S.M., *Effect of the Nature of Different Polymeric Fibers on Steady-State Bed Coalescence of an Oil-in-Water Emulsion*. Industrial & engineering chemistry research, 2004. **43**(20): p. 6490–6495.
  16. Speth, H., Pfenning, A., Chatterjee, M., and Franken, H., *Coalescence of secondary dispersions in fiber beds*. Separation and purification technology, 2002. **29**(2): p. 113-119.
  17. Shin, C., and Chase, G., *The effect of wettability on drop attachment to glass rods*. Journal of colloid and interface science, 2004. **272**(1): p. 186–190.
  18. Fan, L., Yan, J., He, H., Deng, N., Zhao, Y., Kang, W., and Cheng, B., *Electro-blown spun PS/PAN fibrous membrane for highly efficient oil/water separation*. Fibers and Polymers, 2017. **18**(10): 1988-1994.
  19. Shin, C., and Chase, G.G., *Water-in-Oil Coalescence in Micro-Nanofiber Composite Filters*. AIChE journal, 2004. **50**(2): p. 343-350.
  20. Qiao, Y., Zhao, L., Li, P., Sun, H., and Li, S., *Electrospun polystyrene/polyacrylonitrile fiber with high oil sorption capacity*. Journal of Reinforced Plastics and Composites, 2014. **33**(20): p. 1849-1858.
  21. Zhu, H., Qiu, S., Jiang, W., Wu, D., and Zhang, C., *Evaluation of Electrospun Polyvinyl Chloride/Polystyrene Fibers As Sorbent Materials for Oil Spill Cleanup*. Environmental science & technology, 2011. **45**(10): p. 4527-4531.
  22. Pham, V.H., and Dickerson, J.H., *Superhydrophobic Silanized Melamine Sponges as High Efficiency Oil Absorbent Materials*. ACS applied materials & interfaces, 2014. **6**(16): p. 14181-14188.
  23. Wang, N., Maximiuk, L., Fenn, D., Nickerson, M.T., Hou, A., *Development of a method for determining oil absorption capacity in pulse flours and protein materials*. Cereal Chemistry, 2020. **97**(6): p. 1111-1117.
  24. George, G., and Anandhan, S., *Glass fiber-supported NiO nanofiber webs for reduction of CO and hydrocarbon emissions from diesel engine exhaust*. Journal of Materials Research, 2014. **29**(20): p. 2451-2465.
  25. Mylläri, V., Ruoko, T-P., Syrjälä, S., *A comparison of rheology and FTIR in the study of polypropylene and polystyrene photodegradation*. Journal of Applied Polymer Science, 2015. **132**(28): 42246.
  26. Ma, W., Zhang, Q., Hua, D., Xiong, R., Zhao, J., Rao, W., Huang, S., Zhan, X., Chen, F. and Huang, C., *Electrospun fibers for oil-water separation*. Rsc Advances, 2016. **6**(16): p. 12868-12884.
  27. Shan, W., Du, J., Yang, K., Ren, T., Wan, D., and Pu, H., *Superhydrophobic and superoleophilic polystyrene/carbon nanotubes foam for oil/water separation*. Journal of Environmental Chemical Engineering, 2021. **9**(5): p. 106038.
  28. Wang, L., Zhang, J., Wang, S., Yu, J., Hu, W., and Jiao, F., *Preparation of a polystyrene-based super-hydrophilic mesh and evaluation of its oil/water separation performance*. Journal of Membrane Science, 2020. **597**: p. 117747.
  29. Zhang, L., Gu, J., Song, L., Chen, L., Huang, Y., Zhang, J., and Chen, T., *Underwater superoleophobic carbon nanotubes/core-shell polystyrene@Au nanoparticles composite membrane for flow-through catalytic decomposition and oil/water separation*. Journal of Materials Chemistry A, 2016. **4**(28): 10810-10815.
  30. Guo, P., Zhai, S-R., Xiao, Z-Y., Zhang, F., An, Q-D., Song, X-W., *Preparation of superhydrophobic materials for oil/water separation and oil absorption using PMHS-TEOS-derived xerogel and polystyrene*. Journal of sol-gel science and technology, 2014. **72**(2): p. 385-393.
  31. Moatmed, S.M., Khedr, M.H., El-dek, S.I., Kim, H-Y., and El-Deen, A.G., *Highly efficient and reusable superhydrophobic/superoleophilic polystyrene@ Fe3O4 nanofiber membrane for high-performance oil/water separation*. Journal of Environmental Chemical Engineering, 2019. **7**(6): p. 103508.
  32. Gu, J., Xiao, P., Chen, J., Liu, F., Huang, Y., Li, G., ... & Chen, T. *Robust preparation of superhydrophobic polymer/carbon nanotube hybrid membranes for highly effective removal of oils and separation of water-in-oil emulsions*. Journal of Materials Chemistry A, 2014. **2**(37): p. 15268-15272.

**Research Article**

## Hydroxyapatite coating processes with EPD method and investigation of mechanical properties of coatings

**Ibrahim Aydin<sup>a</sup>** , **Ali İhsan Bahçepinar<sup>a,\*</sup>**  and **Mehmet Ayvaz<sup>b</sup>** 

<sup>a</sup>Celal Bayar University, Vocational School of Manisa Technical Sciences Department of Machinery and Metal Technologies, Manisa, 45140, Turkey

<sup>b</sup>Celal Bayar University, Vocational School of Manisa Technical Sciences, Electronics And Automation Department, Manisa, 45140, Turkey

**ARTICLE INFO***Article history:*

Received 12 April 2022

Accepted 10 August 2022

Published 15 August 2022

*Keywords:*

Electrophoretic deposition

Hydroxyapatite

Ti6Al4V

SS 316L

**ABSTRACT**

This paper reports on electrophoretic deposition of hydroxyapatite coatings on 316L stainless steel and Ti6Al4V alloy. Coatings were carried out at 60 sec. deposition time and voltage values of 40, 80, 120, 160 Voltage. Suspension: It was prepared by using Ethanol, Hydroxyapatite, Polyvinyl Alcohol, Sodium dodecyl sulfate, N-N-Dimethylformamide chemicals. The findings and results acquired at the end of the study have been presented and discussed. When the Ca/P values calculated in the study are examined, it was seen that there are values close to the ideal Ca/P ratio (1.67) in all parameters. When the roughness values are examined, it was seen that coatings close to the ideal surface roughness value (1-1.5  $\mu\text{m}$ ) are obtained. When the nano indentation test results were evaluated, it was observed that coatings suitable for shell bone implants were obtained.

**1. Introduction**

Ti and its alloys and 316 L stainless steels (SS) have been used in orthopedic and dental applications because of their biocompatibility and high mechanical properties [1].

The human body has a corrosive environment because of the natural ions in its structure [2]. SS 316L and Ti6Al4V alloy are implant materials with high corrosion resistance [3]. Although their corrosion resistance is high, it is normal for implant materials to be affected by this environment. Because they will be exposed to this corrosive environment for a long time. The use of metal implants in this corrosive environment can causes of the harmful ions in their structure to in the body. Some ions in metal implants have carcinogenic and allergenic effects [4,5]. Therefore, direct use of these implants is not preferred.

HA has high biocompatibility and bioactivity. It is also a calcium phosphate-based bio ceramic material that forms the main inorganic compound of human bones and teeth [4-8]. The reason why HA is preferred in biomedical applications is its osteoconductive and biocompatibility properties [7-10]. The biggest disadvantage of HA is low mechanical properties. This prevents its application as a direct implant [11-14]

Since direct application of metallic biomaterials in implantation processes is not supported, it is a preferred application to be coated with HA, which has high biocompatibility and bioactivity [15-16].

With this application, the high bioactivity and biocompatibility of HA is combined with the high mechanical properties of the metal implant, resulting in a superior biomaterial. In addition, HA acts as a barrier between the implant and the body, cutting off the contact of metal ions with the body and preventing the release of ions into the body [4,17].

Different methods are used for HA coating processes on metal implants. These; electrophoretic deposition (EPD), electrochemical deposition, thermal spray coating, Biomimetics, sol-gel, spray coating and plasma spray coating [18-25]. The EPD method has attracted attention in recent years [25-26]. EPD starts with the movement of charged particles in a stable suspension with the effect of an applied electric field and is completed by the accumulation of moving particles on the implant material surface [25-28].

The reasons why EPD is preferred that the coatings are obtained in a short time, the coatings are homogeneous, the cost is low, and the possibility of coating complex

\* Corresponding author. Tel.: +90 236 234 4461; Fax: +90 232 260 1004.

E-mail addresses: [ibrahim.aydin@cbu.edu.tr](mailto:ibrahim.aydin@cbu.edu.tr) (I. Aydin), [ali.bahcepinar@cbu.edu.tr](mailto:ali.bahcepinar@cbu.edu.tr) (A.İ. Bahçepinar), [m.ayvaz@cbu.edu.tr](mailto:m.ayvaz@cbu.edu.tr) (M. Ayvaz)

ORCID: 0000-0002-1006-2067 (I. Aydin), 0000-0002-9744-0146 (A.İ. Bahçepinar), 0000-0002-9671-8679 (M. Ayvaz)

DOI:10.35860/iaiej.1102381

© 2022, The Author(s). This article is licensed under the CC BY-NC 4.0 International License (<https://creativecommons.org/licenses/by-nc/4.0/>).

materials [20-30].

In this study, coating surfaces were performed by SEM, EDS and XRD analysis. In addition, microhardness, Modulus of Elasticity (E), surface roughness and thickness were determined. All the results were discussed and contrasted with the studies in the literature. Thus, a contribution to the literature has been made.

## 2. Materials and Methods

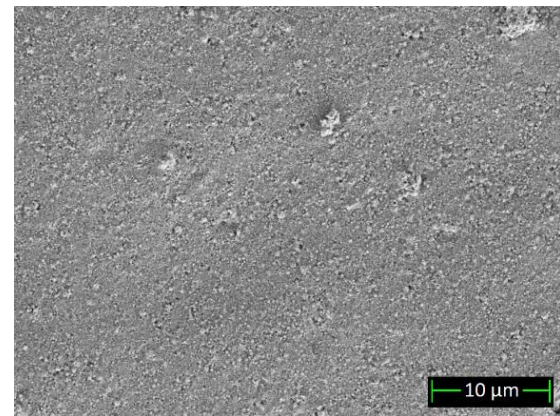
In this study, Ti6Al4V alloy and SS 316L were preferred to be used as substrate. The substrate materials to be used in the coating process was cut as  $D=20\text{mm}$ ,  $h=10\text{mm}$ . In order for the substrates to be clean, they were cleaned in an ultrasonic bath in 70% ethyl alcohol solution for 30 minutes, washed with distilled water and dried again. In order to clean the oxide layers formed on the substrates, the surfaces were wearied with acid solution. This wearing was carried out in 95% distilled water, 2% HF, 3%  $\text{HNO}_3$  solution. The substrates were kept in this solution and then washed with distilled water in an ultrasonic bath. 320x sanding process was applied to the substrate material surfaces. After the sanding process, it was washed with distilled water and ethyl alcohol. Then was made ready for the coating process.

Ethanol of 99.8 percent purity was used as solvent to prepare the coating suspension in the EPD process. 1 g HA and 0.001 g SDS were added to 100 mL of ethanol. Then were mixed in a magnetic stirrer to disperse the HA particles homogeneous. To increase the adhesion strength of HA particles, 1 g PVA and 10 ml N, N-Dimethylformamide chemicals were added to the suspension [31]. In order to ensure the stability of the prepared suspension, the suspension pH was adjusted to 4. The substrates to be used in the coating process were arranged as cathode and anode. The distance between the substrate were fixed to 10 mm. Prepared substrate were immersed in a stable suspension and connected to the DC power source. The coating process was carried out in 60 seconds of deposition time and 40, 80, 120, 160 V values.

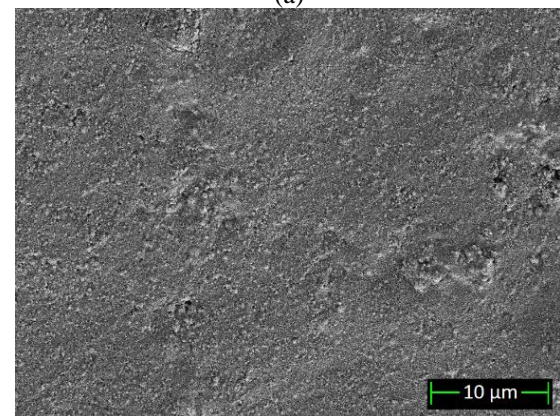
## 3. Results and Discussion

The microstructure analysis of the coated substrate was performed by using a ZEISS Gemini 500 model scanning electron microscope (SEM). 2500X images of the results in the SEM are given in Figure 1 and 2. When Figure 1 and 2 were examined, it was clear that HA coating the surface of the substrate in a homogeneous and intense manner.

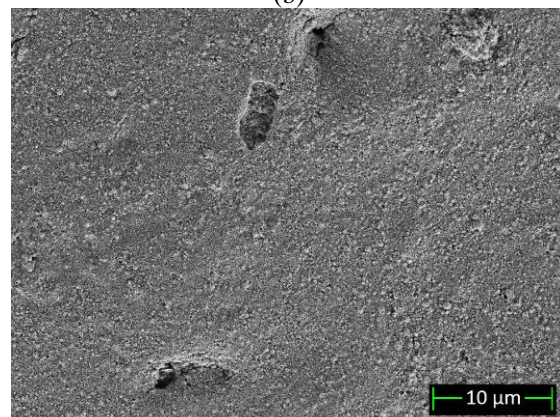
The elemental components of the coated substrate were determined by using an EDX detector on SEM. One example of EDS analysis result is given in Figure 3. When Figure 3 was examined, it was seen that calcium phosphate structure was formed in the coating.



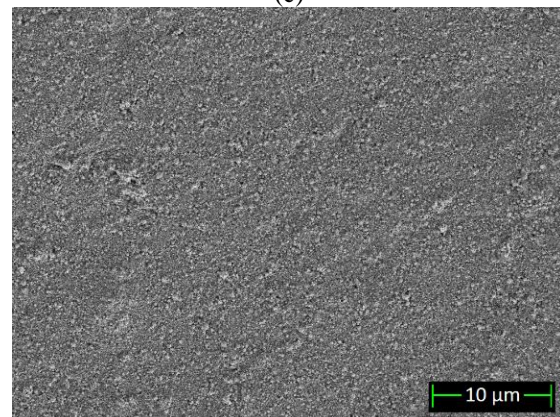
(a)



(b)



(c)



(d)

Figure 1. SEM images of HA-coated Ti6Al4V alloys a) 40V /60s, b) 80V/60s, c) 120V/60s, d) 160V/60s

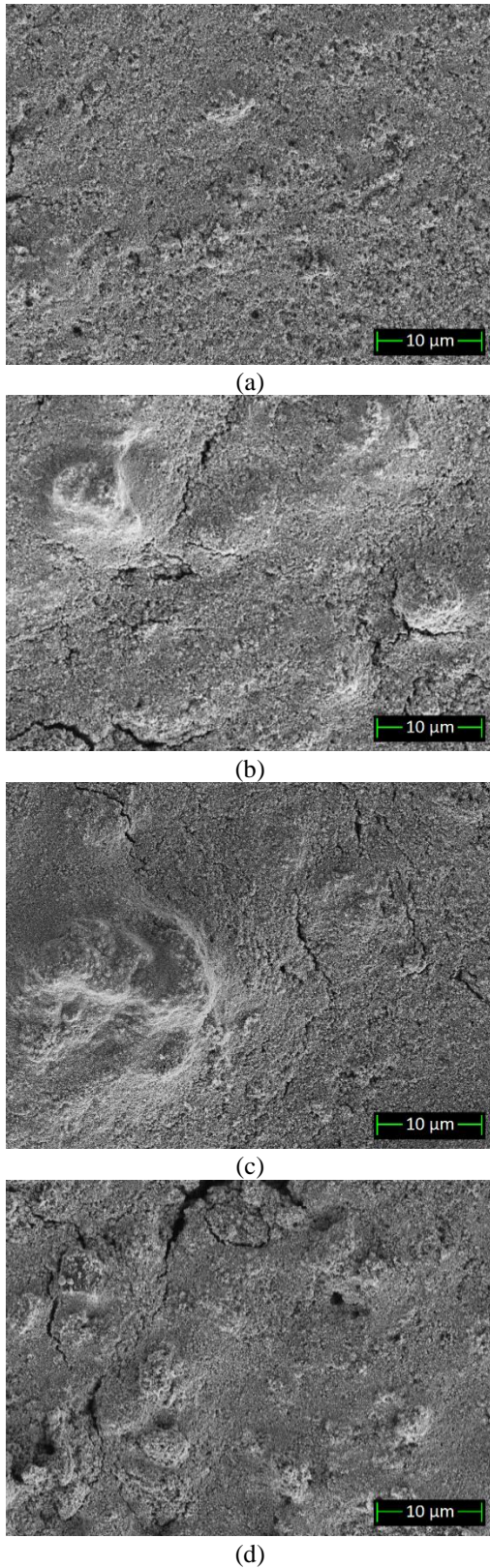


Figure 2. SEM images of HA-coated SS 316L a) 40V/60s, b) 80V/60s, c) 120V/60s, d) 160V/60s

For each parameter, the Ca/P ratio is given in Figure 4. In the literature, some of the Ca/P ratios obtained are as follows: 1.66 [27], 1.61, 1.65, 1.72, 1.73 [32], 1.59, 1.63, 1.66, 1.72 [33]. Ideal Ca/P proportion was determined in the literature for HA covers at 1.67 [34]. There are values in all parameters close to the ideal Ca/P ratio.

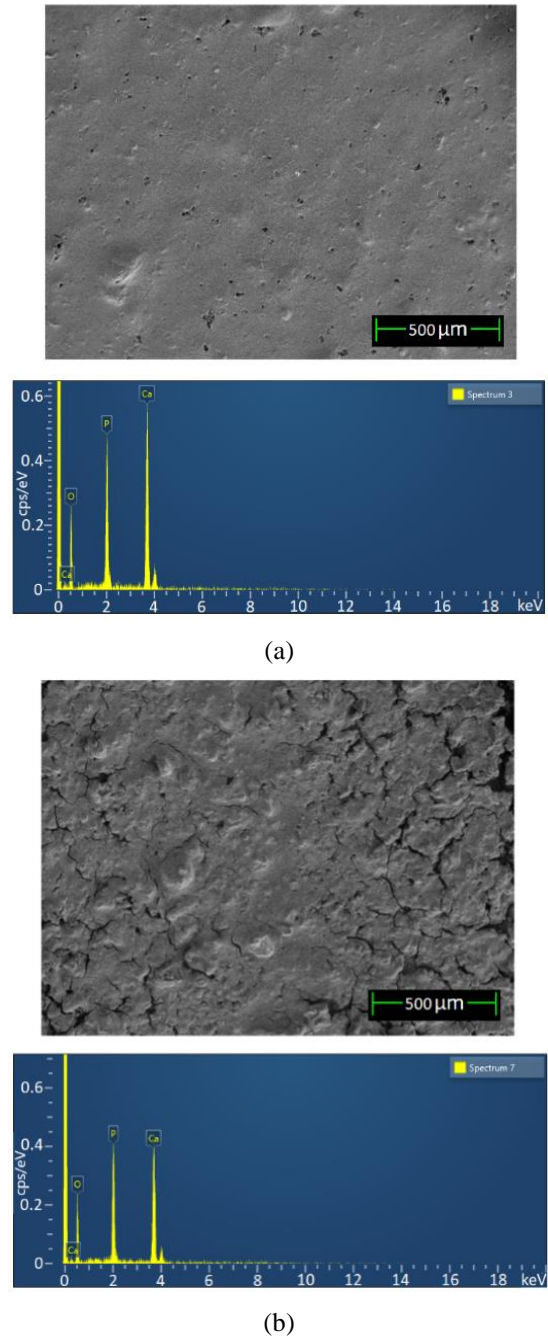


Figure 3. EDS analysis result of HA-coating (120V/60s) a) Ti6Al4V alloys, b) SS 316L

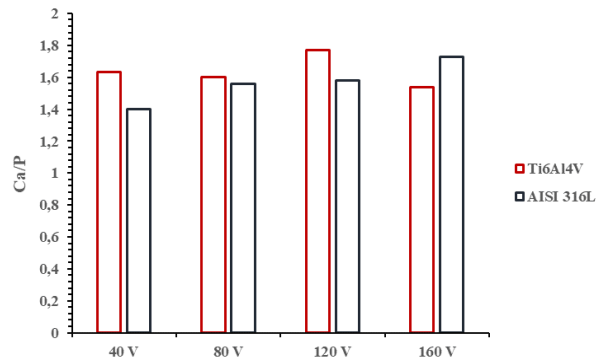


Figure 4. Ca/P ratios for different voltage values

Phase analysis of coated substrate was carried out XRD device at the Manisa Celal Bayar University-Applied Science Research Centre was used. The XRD analysis result of HA coatings applied to Ti6Al4V and SS 316L substrates was shown in Figure 5 and 6. When Figure 5 and 6 were examined, it was showed that HA powders preserved their structure during electrophoretic deposition, as in the literature [6, 35].

In the literature, some peak points of HA crystals obtained are as follows: 2 Theta= 26.0078°, 28.1945°, 32.2494°, 34.1778°, 39.9130°, 48.1571° and 50.5511° [32]. 2 Theta= 26.06°, 31.62° [35]. 2 Theta= 25.91°, 28.94°, 31.78°, 32.19°, 32.93°, 34.10°, 39.80°, 46.71° and 49.49° [7]. 2 Theta= 25.7182°, 28.7945°, 31.6402°, 32.0520°, 32.6648°, 32.7802°, 33.8369°, 33.926°, 39.6934°, 46.2985°, 49.3822°, and 70.7743° [33].

The thickness of the HA coatings was measured with a ElektroPhysik MiniTest 730/Sensor FN 1.5 HD trademark device. Measurements were made 5 times for each coating parameter and the averages were taken. The values of the coating thicknesses were given in Figure 7. When Figure 7 were examined, it was observed that the coating thicknesses increase as the voltage value increases.

The thicknesses of HA coatings obtained by EPD method in the literature were follows: 4.38, 5.43, 7.60, 9.42  $\mu\text{m}$  [32]. 5.86, 7.73, 9.72 and 12.11  $\mu\text{m}$  [33]. 10  $\mu\text{m}$  [35]. 29.35  $\mu\text{m}$  [36]. 2.6, 2.8, 4.2  $\mu\text{m}$  [21].

The measurement of surface roughness (Ra) values was carried out with the Roughness Tester PCE-RT 1200 model device. Results were obtained in micrometres. Five measurements were made on each coating surface and the results were averaged. Evaluation results were given in Figure 8.

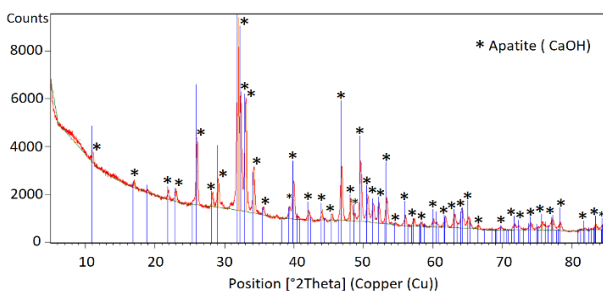


Figure 5. XRD Analysis Results of HA-Coated Ti6Al4V Alloys

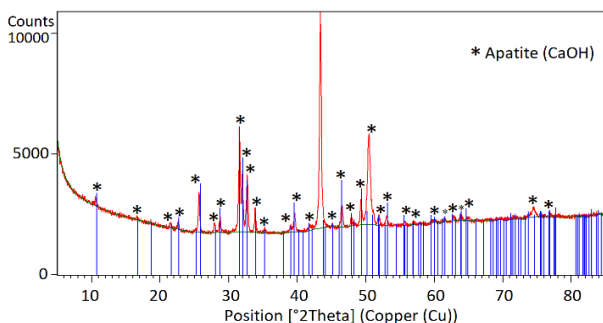


Figure 6. XRD Analysis Results of HA-Coated SS 316L

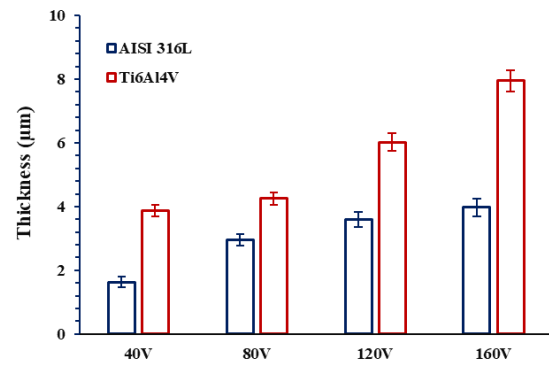


Figure 7. The Average Thicknesses of HA Coatings

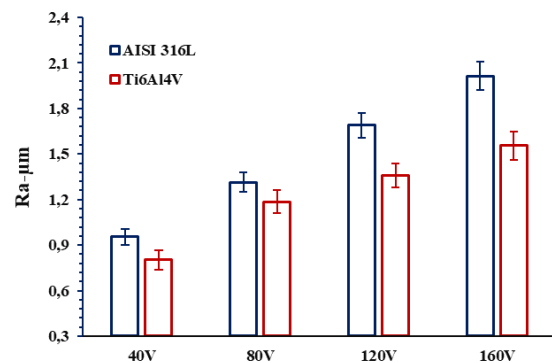


Figure 8. The Average Roughnesses of HA Coatings

When Figure 8. were examined, it was seen that successful results have been obtained. In addition, It was observed that the surface roughness of the coatings increases as the voltage value increases. The ideal surface roughness was measured of between 1-1,5  $\mu\text{m}$  in the literature [4]. Surface roughness of HA coatings obtained by EPD method in the literature were as follows: 0.818, 1.055, 1.552 and 1.673  $\mu\text{m}$  [32]. 1.18, 1.95, 2.26 and 2.83  $\mu\text{m}$  [33]. 1.26  $\mu\text{m}$  [36]. 1.8  $\mu\text{m}$  [4].

Hardness and elastic modulus (E) of the coatings were investigated by using the indentation test device in the Middle East Technical University Central Laboratory. Tests conducted by this tester were performed under the load-unload test mode by applying a test force of 5 mN. Berkovich tip was used in the indentation process. At least 3 measurements were made for each substrate and Microhardness and E values were calculated by taking the average of these measurement results. The test results were showed Figure 9 and 10.

There are differences in the mechanical properties of the bones in different parts of the human body. For example, the E values is 0.001-0.01 GPa in joint cartilage, 0.05-0.5 GPa in cancellous bone, 1 GPa in tendon-bone, and 7-30 GPa in shell bone [2]. When Figure 9 and 10 were examined, it was seen that the HA coatings obtained in some parameters were applicable for shell bone implants.

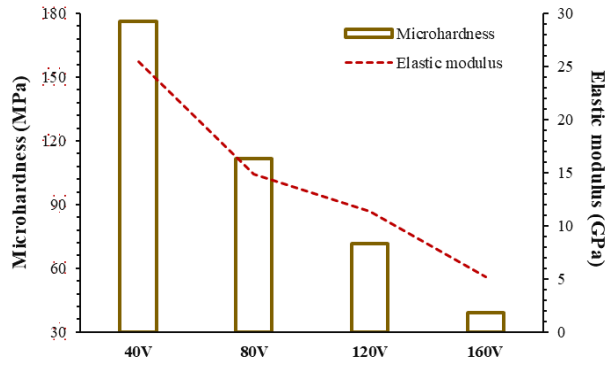


Figure 9. Vickers Hardness and Elasticity Modulus Values of HA-Coated SS 316L

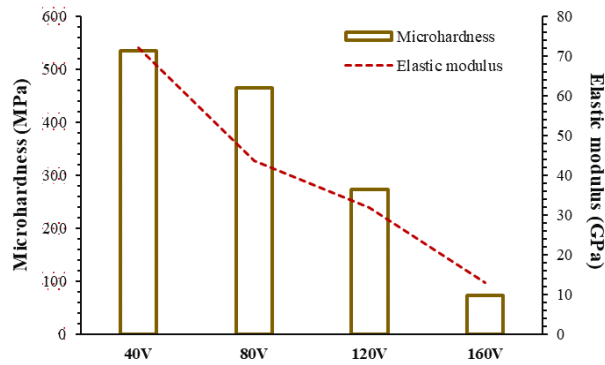


Figure 10. Vickers Hardness and Elasticity Modulus Values of HA-coated Ti6Al4V Alloys

Drevet et al. observed that the hardness value was 5.4-153.5 MPa and the E value was between 5.2-19 GPa in HA coatings which they applied to Ti6Al4V implants with EPD method with different parameters [27]. Bartmanski et al. observed that the hardness value was 0.0112-0.1349 GPa and the E value was between 1.25-30.31 GPa in HA coatings which they applied to Ti13Zr13Nb implants with EPD method with different parameters [36].

#### 4. Conclusions

In this study, HA coating processes were performed on Ti6Al4V alloy and SS 316L implants using the EPD method. Obtained results are given below.

- When the SEM images of the HA coatings created as a result of the study, it was seen that there are homogeneous coatings on the substrate material surfaces in all parameters.
- When the EDS analysis results were examined, it was observed that calcium phosphate structure was formed in all parameters. In the literature, the ideal Ca/P ratio of HA coatings has been determined as 1.67 [34]. When the Ca/P values calculated in the study, it is seen that there are values close to the ideal Ca/P ratio in all parameters.
- When the surface roughness results were examined,

it was observed that the surface roughness of the coatings increases as the voltage value increases. Surface roughness values of HA coatings applied to Ti6Al4V alloy implants were 0.803-1.554  $\mu\text{m}$ , Surface roughness values of HA coatings applied to SS 316L implants were obtained between 0.955 and 2.013  $\mu\text{m}$ . In the literature, the ideal surface roughness value was determined between 1-1.5  $\mu\text{m}$  [37]. When the roughness values were examined, it was observed that coatings close to the ideal surface roughness value was obtained.

- When the coating thickness results were examined, it was observed that the coating thicknesses increase as the voltage value increases. The thickness values of HA coatings applied to Ti6Al4V alloy implants were 3.87-7.95  $\mu\text{m}$ , and the thickness values of HA coatings applied to SS 316L implants were between 1.63-3.97  $\mu\text{m}$ .
- When the indentation test results were examined, it was observed that the hardness and E values of the coatings decrease as the voltage value increases. The hardness values of the HA coatings applied to the Ti6Al4V alloy implants were 72.432-534.74 MPa, E values were between 13.035-72.074 GPa, the hardness values of the HA coatings applied to the SS 316L implants were 39.038-176.067 MPa, and the E values were between 5.185-25.469 GPa. The E values is 0.001-0.01 GPa in joint cartilage, 0.05-0.5 GPa in cancellous bone, 1 GPa in tendon-bone, and 7-30 GPa in shell bone [2]. When the results were evaluated, it was observed that coatings applicable to shell bone implants were obtained.

#### Declaration

The author(s) declared no potential conflicts of interest with respect to the research, authorship, and/or publication of this article. The author(s) also declared that this article is original, was prepared in accordance with international publication and research ethics, and ethical committee permission or any special permission is not required.

#### Author Contributions

İ. Aydın developed the methodology. A.İ. Bahçepinar performed the analysis. M. Ayvaz supervised and improved the study. İ. Aydın and A.İ. Bahçepinar wrote the manuscript together. M. Ayvaz proofread the manuscript.

#### Acknowledgment

This work supported by the Manisa Celal Bayar University Scientific Research Projects Coordination Unit (project no: 2018-224), Turkey

## References

- Prabakaran, K., Thamaraiselvi, T. V. and Rajeswari, S., *Electrochemical evaluation of hydroxyapatite reinforced phosphoric acid treated 316L stainless steel*. Trends Biomaterials, 2006. **19**: p. 84-87.
- Aydin, I., Cetinel, H., Pasinli, A. and Yuksel, M., *Preparation of hydroxyapatite coating by using citric acid sodium citrate buffer system in the biomimetic procedure*. Materials Testing, 2013. **55**(10): p. 782-788.
- He, G., and Hagiwara, M., *Ti alloy design strategy for biomedical applications*. Materials Science and Engineering: C, 2006. **26**(1): p. 14-19.
- Javidi, M., Javadpour, S., Bahrololoom, M. E. and Ma, J. J. M. S., *Electrophoretic deposition of natural hydroxyapatite on medical grade 316L stainless steel*. Materials Science and Engineering: C, 2008. **28**(8): p. 1509-1515.
- Bogdanoviciene, I., Beganskiene, A., Tonsuaadu, K., Glaser, J., Meyer, H. J. and Kareiva, A., *Calcium hydroxyapatite, Ca<sub>10</sub>(PO<sub>4</sub>)<sub>6</sub>(OH)<sub>2</sub> ceramics prepared by aqueous sol-gel processing*. Materials Research Bulletin, 2006. **41**(9): p. 1754-1762.
- Farrokhi-Rad, M., *Electrophoretic deposition of hydroxyapatite nanoparticles: effect of suspension composition on the electrochemical potential difference at deposit/suspensions interface*. Materials Research Express, 2018. **5**(8): 085005.
- Iqbal, N., Nazir, R., Asif, A., Chaudhry, A. A., Akram, M., Fan, G. Y. and Hussain, R., *Electrophoretic deposition of PVA coated hydroxyapatite on 316L stainless steel*. Current Applied Physics, 2012. **12**(3): p. 755-759.
- Tian, Q., Lin, J., Rivera-Castaneda, L., Tسانhani, A., Dunn, Z. S., Rodriguez, A. and Liu, H., *Nano-to-submicron hydroxyapatite coatings for magnesium-based bioresorbable implants—deposition, characterization, degradation, mechanical properties, and cytocompatibility*. Scientific reports, 2019. **9**(1): p. 1-27.
- Surmenev, R. A., *A review of plasma-assisted methods for calcium phosphate-based coatings fabrication*. Surface and Coatings Technology, 2012. **206**(8-9): p. 2035-2056.
- Suchanek, K., Bartkowiak, A., Perzanowski, M., Marszałek, M., Sowa, M. and Simka, W., *Electrochemical properties and bioactivity of hydroxyapatite coatings prepared by MEA/EDTA double-regulated hydrothermal synthesis*. Electrochimica Acta, 2019. **298**: p. 685-693.
- Miranda, G., Sousa, F., Costa, M. M., Bartolomeu, F., Silva, F. S., and Carvalho, O., *Surface design using laser technology for Ti6Al4V-hydroxyapatite implants*. Optics & Laser Technology, 2019. **109**: p. 488-495.
- Luo, J., Jia, X., Gu, R., Zhou, P., Huang, Y., Sun, J. and Yan, M., *316 L stainless steel manufactured by selective laser melting and its biocompatibility with or without hydroxyapatite coating*. Metals, 2018. **8**(7): 548.
- Marques, A., Miranda, G., Silva, F., Pinto, P., and Carvalho, Ó., *Review on current limits and potentialities of technologies for biomedical ceramic scaffolds production*. Journal of Biomedical Materials Research Part B: Applied Biomaterials, 2021. **109**(3): p. 377-393.
- Zhou, H. and Lee, J., *Nanoscale hydroxyapatite particles for bone tissue engineering*. Acta biomaterialia, 2011. **7**(7): p. 2769-2781.
- Curcio, M., Rau, J. V., Santagata, A., Teghil, R., Laureti, S. and De Bonis, A., *Laser synthesis of iron nanoparticle for Fe doped hydroxyapatite coatings*. Materials Chemistry and Physics, 2019. **225**: p. 365-370.
- Zhou, W., Hu, Z., Wang, T., Yang, G., Xi, W., Gan, Y. and Hu, J., *Enhanced corrosion resistance and bioactivity of Mg alloy modified by Zn-doped nanowisker hydroxyapatite coatings*. Colloids and Surfaces B: Biointerfaces, 2020. **186**: 110710.
- Kwok, C. T., Wong, P. K., Cheng, F. T. and Man, H. C., *Characterization and corrosion behavior of hydroxyapatite coatings on Ti6Al4V fabricated by electrophoretic deposition*. Applied surface science, 2009. **255**(13-14): p. 6736-6744.
- Rodrigues Jr, L. F., Tronco, M. C., Escobar, C. F., Rocha, A. S. and Santos, L. A. L., *Painting method for hydroxyapatite coating on titanium substrate*. Ceramics International, 2019. **45**(12): 14806-14815.
- Asri, R. I. M., Harun, W. S. W., Hassan, M. A., Ghani, S. A. C. and Buyong, Z., *A review of hydroxyapatite-based coating techniques: Sol-gel and electrochemical depositions on biocompatible metals*. Journal of the mechanical behavior of biomedical materials, 2016. **57**: p. 95-108.
- 20-Qi, J., Chen, Z., Han, W., He, D., Yang, Y. and Wang, Q., *Effect of deposition parameters and heat-treatment on the microstructure, mechanical and electrochemical properties of hydroxyapatite/titanium coating deposited on Ti6Al4V by RF-magnetron sputtering*. Materials Research Express, 2017. **4**(9): 096409.
- Dudek, K. and Goryczka, T., *Electrophoretic deposition and characterization of thin hydroxyapatite coatings formed on the surface of NiTi shape memory alloy*. Ceramics International, 2016. **42**(16): p. 19124-19132.
- Yu, H. N., Hsu, H. C., Wu, S. C., Hsu, C. W., Hsu, S. K. and Ho, W. F., *Characterization of nano-scale hydroxyapatite coating synthesized from eggshells through hydrothermal reaction on commercially pure titanium*. Coatings, 2020. **10**(2): 112.
- Villardell, A. M., Cinca, N., Garcia-Giralt, N., Dosta, S., Cano, I. G., Nogués, X. and Guilemany, J. M., *In-vitro comparison of hydroxyapatite coatings obtained by cold spray and conventional thermal spray Technologies*. Materials Science and Engineering: C, 2020. **107**: 110306.
- Ngo, T. T., Hiromoto, S., Pham, S. T. and Cao, N. Q., *Adhesion properties of hydroxyapatite and octacalcium phosphate coating layers to AZ31 alloy formed at various pH values*. Surface and Coatings Technology, 2020. **381**: 125187.
- Pawlik, A., Rehman, M. A. U., Nawaz, Q., Bastan, F. E., Sulka, G. D. and Boccaccini, A. R., *Fabrication and characterization of electrophoretically deposited chitosan-hydroxyapatite composite coatings on anodic titanium dioxide layers*. Electrochimica Acta, 2019. **307**: p. 465-473.
- Avcu, E., Baştan, F. E., Abdullah, H. Z., Rehman, M. A. U., Avcu, Y. Y. and Boccaccini, A. R., *Electrophoretic deposition of chitosan-based composite coatings for biomedical applications: A review*. Progress in Materials Science, 2019, **103**: p. 69-108.
- Drevet, R., Jaber, N. B., Fauré, J., Tara, A., Larbi, A. B. C. and Benhayoune, H., *Electrophoretic deposition (EPD) of nano-hydroxyapatite coatings with improved mechanical properties on prosthetic Ti6Al4V substrates*. Surface and Coatings Technology, 2016. **301**: p. 94-99.
- Molaei, A., Lashgaroo, M., and Yousefpour, M., *Effects of electrophoretic parameters on chitosan-based nanocomposite coatings*. Journal of the Australian Ceramic Society, 2020. **56**(1): p. 1-10.

29. Singh, S., Singh, G. and Bala, N., *Corrosion behavior and characterization of HA/Fe<sub>3</sub>O<sub>4</sub>/CS composite coatings on AZ91 Mg alloy by electrophoretic deposition*. Materials Chemistry and Physics, 2019. **237**: 121884.
30. Horandghadim, N., Khalil-Allafi, J. and Urgen, M., *Influence of tantalum pentoxide secondary phase on surface features and mechanical properties of hydroxyapatite coating on NiTi alloy produced by electrophoretic deposition*. Surface and Coatings Technology, 2020. **386**: 125458.
31. Boccaccini, A. R., Keim, S., Ma, R., Li, Y. and Zhitomirsky, I., *Electrophoretic deposition of biomaterials*. Journal of the Royal Society Interface, 2010. **7**(5): p. 581-613.
32. Aydın, İ., Bahçepinar, A. İ., Kırman, M., & Çipiloğlu, M. A., *HA coating on Ti6Al7Nb alloy using an electrophoretic deposition method and surface properties examination of the resulting coatings*. Coatings, 2019. **9**(6): 402.
33. Aydın, İ., Bahçepinar, A. İ. and Gül, C., *Surface characterization of EPD coating on AZ91 Mg alloy produced by powder metallurgy*. Revista de Metalurgia, 2020. **56**(3): e176.
34. Urist, M. R., Lietze, A. and Dawson, E., *Beta-tricalcium phosphate delivery system for bone morphogenetic protein*. Clinical orthopaedics and related research, 1984. **187**: p. 277-280.
35. Kumar, R. M., Kuntal, K. K., Singh, S., Gupta, P., Bhushan, B., Gopinath, P. and Lahiri, D., *Electrophoretic deposition of hydroxyapatite coating on Mg-3Zn alloy for orthopaedic application*. Surface and Coatings Technology, 2016. **287**: p. 82-92.
36. Bartmanski, M., Zielinski, A., Majkowska-Marzec, B. and Strugala, G., *Effects of solution composition and electrophoretic deposition voltage on various properties of nanohydroxyapatite coatings on the Ti13Zr13Nb alloy*. Ceramics International, 2018. **44**(16): p. 19236-19246.
37. Wennerberg, A., *The importance of surface roughness for implant incorporation*. International Journal of Machine Tools and Manufacture, 1998. **38** (5-6): p. 657-662.





## Research Article

**Heat transfer system and feedback temperature controller design for safety process operation of phosphorous acid potassium salts production****Zeynep Yilmazer Hitit<sup>a,\*</sup> , Pinar Aygener<sup>a</sup> , Efe Yorgancioglu<sup>b</sup> , Begum Akagun<sup>b</sup> , Kemal Kesenci<sup>b</sup> , Suna Ertunç<sup>a</sup> and Bülent Akay<sup>a</sup>** <sup>a</sup>Ankara University, Faculty of Engineering, Department of Chemical Engineering; 06100 Tandogan, Ankara, Turkey<sup>b</sup>Safa Tarim A.S.; 42030 Karatay, Konya; Turkey

## ARTICLE INFO

## Article history:

Received 04 February 2022

Accepted 08 June 2022

Published 15 August 2022

## Keywords:

Feedback temperature control

Model parameters

Neutralization

Phosphorous acid

Potassium salts

## ABSTRACT

The phosphorous acid salts are widely used in the industry because of the effective treatment against various fungal diseases encountered in plants. The production process is exothermic and, with high temperatures around 94°C achieved, significant risks were observed in terms of occupational health and safety. Therefore, the aim is to design a control system that will make this production process reliable for human health, economic and ecological damage. For this purpose, studies were carried out to determine the optimum operating mode, heat transfer system, and temperature controller design to prevent a sudden temperature rise. First, the overall heat transfer coefficient between the reactor and the jacket was determined as 51.0930 W/m<sup>2</sup>°C and, the refrigerant was chosen as cooling water with 1.271 g/s flow rate which is relatively more economical and accessible. The model parameters of the system were determined with a detailed dynamic analysis by giving positive and negative step inputs to the cooling water flow rate and then obtaining model parameters through reaction curve and linear regression methods. By using the obtained model parameters theoretical P, PI and PID parameters were calculated by Cohen Coon and, Ziegler-Nichols approaches, and the success of controller parameters was tested, simulated with the MATLAB Simulink program and lastly, successful temperature control was achieved in the experimental system.

**1. Introduction**

Ensuring the nourishment of humanity is an issue that has been studied for centuries. Pesticides are being developed as an alternative solution for this situation. Today, about 80% of pesticides used in agriculture are applied in developed countries [1]. Pesticides having an important role in food production are in use to keep crops healthy against insects, fungi, weeds, and other pests. They are not only known to maintain and/or increase crop yields, but they also indicate how many time crops can be grown on the same field per year. This is particularly important in countries experiencing food shortages [2]. However, there are dangers in the use of pesticides. Pesticides affect the health of thousands of people worldwide each year [3, 4]. This toxic effect of pesticides to humans can cause both acute and chronic health problems, depending on the exposure time and type [2, 5, 6].

Compounds whose active ingredient is phosphorous acid (H<sub>3</sub>PO<sub>3</sub>) show pesticidal properties in many plants. However, for phosphorous acid products to provide a nourishing effect to the plant, must be produced under suitable conditions, continuously and sustainably. Since the pH value of the phosphoric acid, which is an aqueous solution of phosphorous acid, is approximately 1.5, it should not be directly contacted with the plant, as it can cause permanent damage to the plant [7]. Therefore, for efficient and effective product formation, the active ingredient and weak acid, phosphorous acid (H<sub>3</sub>PO<sub>3</sub>), need a neutralization reaction with a strong base. Mono and dipotassium phosphide (KH<sub>2</sub>PO<sub>3</sub> and K<sub>2</sub>HPO<sub>3</sub>) are formed because of the exothermic reaction of phosphonic acid, which is an aqueous solution of phosphorous acid, and potassium hydroxide. These products, which have a liquid soluble (SL) form, are expected to be pH-neutral solutions

\* Corresponding author. Tel.: +90 312 203 3433; Fax: +90 312 212 7464.

E-mail addresses: [zyilmazer@ankara.edu.tr](mailto:zyilmazer@ankara.edu.tr) (Z.Y. Hitit), [paygener@gmail.com](mailto:paygener@gmail.com) (P. Aygener), [efeyorgancioglu@outlook.com](mailto:efeyorgancioglu@outlook.com) (E. Yorgancioglu), [begumakagun@icloud.com](mailto:begumakagun@icloud.com) (B. Akagun), [kemal.kesenci@safatarim.com](mailto:kemal.kesenci@safatarim.com) (K. Kesenci), [ertunc@eng.ankara.edu.tr](mailto:ertunc@eng.ankara.edu.tr) (S. Ertunç), [bakay@ankara.edu.tr](mailto:bakay@ankara.edu.tr) (B. Akay)

ORCID: 0000-0001-9078-191X (Z.Y. Hitit), 0000-0002-8767-5654 (P. Aygener), 0000-0001-9303-7299 (E. Yorgancioglu),

0000-0002-8021-1582 (B. Akagun), 0000-0003-0767-1029 (K. Kesenci), 0000-0002-0139-7463 (S. Ertunç), 0000-0002-2541-490X (B. Akay)

DOI: [10.35860/iaorej.1067660](https://doi.org/10.35860/iaorej.1067660)© 2022, The Author(s). This article is licensed under the CC BY-NC 4.0 International License (<https://creativecommons.org/licenses/by-nc/4.0/>).

(preferably between 6.2-6.7) to provide nutritional benefit while not harming the plant to which they are applied [8]. Potassium phosphide salts both have a direct toxic effect against plant pathogens and activate the natural defense mechanisms of plants by reducing the effects of diseases and/or eliminating diseases. Thus, they make a double effect. Systemically up and down movements of the plants in the vascular system of the plants, including the root system, which is quickly absorbed by the plant and roots to ensure maximum and yielding usage [9]. In addition to acting by walling up the pathogen inside the fungus, killing the surrounding cells in disease formation or insect invasion, and preventing further fungal growth, the plant also activates its immune defense system. During this, other fungitoxic compounds accumulations and metabolic changes, resistance inducers are set off to response more. The remaining part of the plant starts to produce other compounds to increase its resistance against possible infection(s) or attack in other parts of the plant [10]. Induced resistance (IR) and systemic acquired resistance (SAR) and are known two responses. To survive against any negative influence from the outside, plants have the ability to prepare their immune systems against microbial pathogens. This results in robust and rapid stimulation of defense mechanisms after a possible pathogen bombard [11–13]. An example of this stimulation is SAR, which is defined as the immune response of plants to pathogen attacks [13]. Activation of SAR causes broad-spectrum systemic resistance evolution [14–17]. Determining the biochemical changes that cause the resistance state is important for the development of plant protection chemicals, SAR, which is a new model of genetically developed disease resistance [16]. Induced or induced resistance (IR) is the mechanism by which plants deliberately meet specific microbes. This system aims to provide resistance against infection by pathogens in treated plants. Stimulated plant defenses are expected to involve the lignification of cell walls. This is achieved by the addition of chemical cross-links to cell wall peptides. Thus, infection in the plant becomes hard [18]. During the production of potassium salts of phosphorous acid, which is an efficient and effective pesticide, heat release occurs. In other words, the potassium phosphide production reaction is exothermic. When this situation is not taken under control, it contains risks such as reactor explosion, formation of toxic by-product(s), decrease in product yield, and significant ecological and economic damage [19–22]. The rapid depletion of the input concentrations and thus the rapid change in the transformation not only increases the reaction temperature but also prevents the formation of the chemical kinetic model of the reaction. It is essential to design a system that will control the temperature to eliminate possible hazards and to develop an efficient production process. Due to this

need, the type and optimum flow rate of the cooling fluid that can absorb the heat released in the reactor during the production of mono and dipotassium phosphide salts were determined and a PID (Proportional Integral Derivative) controller was designed to provide temperature control with the selected refrigerant. In industrial applications, PI and PID controllers are favorably and broadly employed [23]. While most of the PID controllers were used as analog in the past, controllers used with digital signals and computers are frequently encountered today [24]. In recent years; system identification and adaptation schemes are being developed to create PI and PID controllers that are optimal for the design objectives studied [23, 25–27]. The design of PI and PID controllers for linear systems and different design techniques for nonlinear systems are mysteries [23, 28–30]. Due to the non-linear parameter variations and disturbances, PI or PID controllers design procedures have problems in closed loop system [23, 31]. The lack of clarity regarding the selection of parameters of the sampling period and discrete-time responses for PI or PID control systems is another disadvantage of the current state of the problem [23, 32]. Where a mathematical model of a system is available, it is possible to specify the parameters of the controller. However, if a mathematical model is not created, an experimental method is needed to determine the parameters. In-process control systems, controller setting can be defined as of obtaining controller parameters for reaching the desired output. This operation is an important term for control systems as it allows optimization of another operation and minimizes the error of measured output and the setpoint [25, 33, 34].

This paper, it is aimed to design the optimum process control system in order to the heat released during the reaction. For this purpose, optimum operating mode and reactant (input), heat transfer coefficient between reactor and jacket, optimum refrigerant type, and flow rate were determined. By using Cohen-Coon and Ziegler-Nichols adjustment methods; P, PI and PID parameters were calculated and their performance and applicability were examined using MATLAB Simulink, MATLAB Simulink Tuning, and VISIDAQ programs and plugins.

## 2. Materials and Methods

The main purpose of process control is to ensure quality production under safe and efficient operational conditions. Process control is concerned with how to achieve and maintain these goals. Values such as product concentration, temperature and pressure must be controlled for product quality and continuity in large-scale, integrated processing plants such as refineries. Numerous transaction variables can be manipulated for these purposes. Feedback control systems keep controlled variable at the desired value by the adjustment of manipulated variable [35]. Process control can be defined as sequential control, which is a

state-based process that follows each other until a process is completed, or continuous control, which includes the observation and adjustment of fixed process parameters. [36]. In this study, it is aimed to determine the model parameters and to create a process control system in the exothermic production process at high temperatures. For this purpose, after determining the overall heat transfer coefficient (U) of the reaction, the system was simulated, and the refrigerant type and flow rate were decided. Since the thermodynamic properties of the production reaction of potassium phosphite salts, which is a neutralization reaction with significant risks, are not encountered in the literature, to determine the heat generated as a result of the reaction, insulation was made around the reactor to be used with 1 cm and 2 cm thick air and elastomeric rubber foam, respectively, and the heat transfer of the reactor with the external environment was minimized. The properties of the insulation material are given in Table 1. After the reactor was insulated, the reaction environment was simulated by sending 39 W of heat to the system for 4000 s with a submersible heater. Thus, 156000 J of heat was given to the system with the help of a submersible heater. The heat generated in the reactor was calculated using Equation (1).

A jacketed and stirred glass reactor with a diameter of 10 cm and a height of 20 cm was used to determine the overall heat transfer coefficient. Experiments were carried out repetitively with two different fluid types, water, and ethylene glycol, at different flow rates. Equation (2) was used for the calculation of the entire heat transfer coefficient (U). Here Q; the amount of heat received by the cooling water (W), U; total heat transfer coefficient ( $\text{W/m}^2\text{°C}$ ), A; heat transfer area ( $\text{m}^2$ ),  $\Delta T_{ln}$  ( $\text{°C}$ ); is the logarithmic mean of the temperature difference between the reactor and the jacket cooling water. The heat transfer area is calculated as  $0.063 \text{ m}^2$  by Equation (3).

### 2.1 Determination of Model and Control Parameters

In a system where the reactor temperature is controlled, the feedback control loop operates to adjust the flow rate of the coolant supplied to the jacket to bring the reactor temperature in the system to the set point. In the feedback control system, the reactor internal temperature ( $T_R$ ) is measured as electrical signals using a thermocouple, and the temperature value with a transducer creates digital signals that the computer can understand. The value of the measured electrical signals is compared with the determined temperature value (reference value) and the error value is calculated. The controller calculates the flow rate of the cooling water ( $F_{cw}$ , mL/min) using the calculated error value and sends it to the peristaltic pump, which is the last control element, to transmit to the process. Thus, the cooling water flow rate is adjusted. Depending on the flow rate, the amount of heat transferred from the

reactor to the jacket, and therefore the temperature inside the reactor changes. This cycle repeats over and over like this. When the temperature in the reactor ( $T_R$ ) reaches the set point, the cooling water flow rate and the temperature inside the reactor remain at a constant value unless an external effect is given. In case the system deviates from the setpoint due to any possible factor, the cooling water flow rate is adjusted again to reach the desired set point.

$$Q = m \times C_p \times \Delta T \quad (1)$$

$$Q = U \times A \times \Delta T_{ln} \quad (2)$$

$$A = \pi \times D \times L \quad (3)$$

In this paper, in which the PID controller was selected, firstly the dynamics of the system under the step input was examined and the success of the controller was examined by calculating the controller parameters with the help of the model parameters. It is expected that the system will become stable at a constant temperature value given by the help of a submersible heater at a constant cooling water flow rate. In order to examine the dynamic behavior of the system, positive and negative effects are given to the system that has become stable.

The transfer function of the system which was given depending on the Equation (4) for first order system with time delay was obtained by using the reaction curve and linear regression methods with the help of the recorded in-reactor temperature data. In Equation [4]  $K_p$  is the gain of the process,  $\theta$  is the dead time of process, and  $\tau$  is the process time constant. P, PI, PID parameters were calculated with Ziegler Nichols and Cohen Coon control parameter calculation methods.

$$G_{(s)} = \frac{K_p(e^{-\theta s})}{\tau s + 1} \quad (4)$$

Table 1. Properties of insulation material

| Technical Properties                     | Standard      | Unit | Coolflex Plate   |
|--|---------------|------|------------------|
| Thermal conductivity                     | EN<br>12667   | W/mK | 0.032 (-20°C)    |
|  |               |      | 0.034 (0°C)      |
|  |               |      | 0.036 (40°C)     |
|  |               |      | 0.040 (+60°C)    |
| Water vapor diffusion                    | EN<br>12086   | -    | $\mu \geq 10000$ |
| Fire unit                                | EN<br>13501-1 | -    | B-s3-d0          |
| Temperature strength                     | EN<br>14706   | °C   | Max +110         |
| Soluble chlorine ion level               | EN<br>13468   | -    | 500              |
| pH                                       | EN<br>13468   | -    | 6-8              |
| Flexibility                              |               | -    | Perfect          |
| Ozone                                    |               | -    | Good             |
| Strength to chemicals (oil, mineral oil) |               | -    | Good             |
| Mold formation and scent                 |               | -    | No               |

The calculated control parameters were tested theoretically in the system simulated with the MATLAB/Simulink program, the results were compared, and their performances were examined. As a result, the model parameters of a batch exothermic neutralization reactor with cooling jacket were found and the controller was designed with the help of the mathematical model.

## 2.2 Dynamic Behavior of the System

To obtain the model parameters to be used in the design of the process control system, the glass reactor with a reaction volume of 2 L and a jacket volume of 1.5 L is insulated to minimize heat loss. Thermocouples were connected to the inside of the reactor, the cooling water inlet, and the cooling water outlet, and the temperature data were recorded throughout the reaction, the mixer was placed in the reactor to ensure full mixing, the cooling water flow rate was adjusted with the help of a peristaltic pump, and a submersible heater connected to the variac system was placed. All data obtained during the experiment were recorded to the computer with the help of a transmitter and I/O card. To examine the system dynamics, positive and negative load effects are given to the cooling water flow rate of the system. The dynamic regions ( $S_1$ - $S_3$ ) created by the time variation of the temperature inside the reactor under the positive and negative effects given to the cooling water flow rate are given in Figure 1.  $S_1$  of these dynamic regions; the region where the first steady condition is met for constant cooling water inlet-outlet temperatures and velocities,  $S_2$ ; the region formed by giving a positive step effect to the cooling water flow rate and  $S_3$  is; represents the region formed by giving a negative step effect to the cooling water flow rate. The step effects on the flow rate, the response of the process, and the variation of the heat supplied to the system with the help of variac over time are given in Figures 2-3, respectively.

## 3. Results and Discussion

The temperature difference ( $\Delta T_R$ ) inside the reactor was measured and since it was known that there was 1500 mL of water in the reactor, the heat released in the reactor was calculated. Accordingly, since the sum of the heat taken by the water in the reactor and the cooling water in the jacket will be equal to the heat given to the reactor, the heat taken by the cooling water in the jacket should be 92704 J. The mass flow rate ( $\dot{m}_{cw}$ ) of the cooling water was determined with the help of the temperature difference ( $\Delta T$ ) measured in the jacket and the heat values received by the coolant in the jacket.

In jacket-cooled exothermic reactors where water is used as the refrigerant, the heat transfer coefficient of the wall between the outer jacket and the inner tank was calculated with the help of Equation (2). The values used for all calculations and the calculation results are given in Table 2.

To determine the most appropriate refrigerant flow rate most accurately, theoretical calculations were made to observe the outlet temperatures of the coolant to be obtained with different flow rates, and the changes in the cooling water outlet temperature ( $T_{cwo}$ ) at different cooling water flow rates ( $\dot{m}_{cw}$ ) are given in Table 3. For the cooling water in the jacket to take the determined temperature, the liquid should be sent to the jacket at a high flow rate. However, when Table 3 is examined, it is seen that increasing the cooling water flow rate to be sent to the jacket reduces the temperature difference. When working at low flow rates, the cooling water outlet temperature will be high as the water will stay in the system for a longer time, which is a situation that should be avoided as it contains risks.

## 3.1 Determination of Optimum Cooling Fluid

With the test results given in Table 2 and Table 3, optimum working conditions were determined in cases where the refrigerant is water. However, to examine the use of one or several different refrigerants that can be used as an alternative to water, detailed literature research has been carried out. As a result of the research, ethylene glycol ( $(\text{CH}_2\text{OH})_2$ ) is known to be widely used especially in the production of polyester fiber; alternative refrigerant was deemed appropriate. To determine the flow rate of this determined refrigerant, just like for water, repeated experiments were carried out. For safe production, the mass flow rate of the fluid to cool the heat released ( $\dot{m}_{ceg}$ ) was determined as 0.95 g/s using the temperature difference ( $\Delta T_R$ ) given in Table 2 and Equation (1).

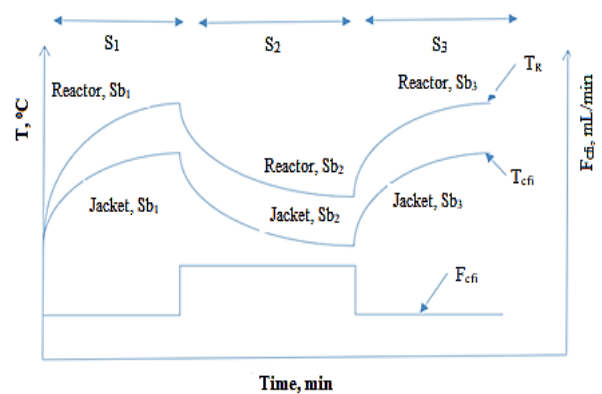


Figure 1. Dynamic zones due to the change in the cooling water flow rate at the reactor temperature; t: time (minute); T: Temperature ( $^{\circ}\text{C}$ );  $S_1$ : the region where the first steady condition is met for constant cooling water inlet-outlet temperatures and velocities;  $S_2$ : the region formed by giving a positive step effect to the cooling water flow rate;  $S_3$ : represents the region formed by giving a negative step effect to the cooling water flow rate;  $S_{b1}$ : jacket outlet of cooling water temperature in zone 1;  $S_{b2}$ : jacket outlet of cooling water temperature in zone 2;  $S_{b3}$ : jacket outlet of cooling water temperature in zone 3;  $F_{cfi}$ : cooling fluid flow rate at the inlet (mL/min);  $T_{cwo}$ : cooling water outlet temperature ( $^{\circ}\text{C}$ );  $T_R$ : the reactor inside temperature ( $^{\circ}\text{C}$ )

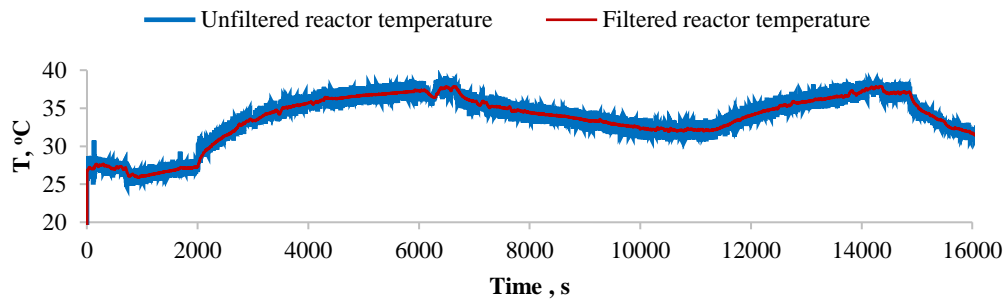


Figure 2. Reactor temperature change over time

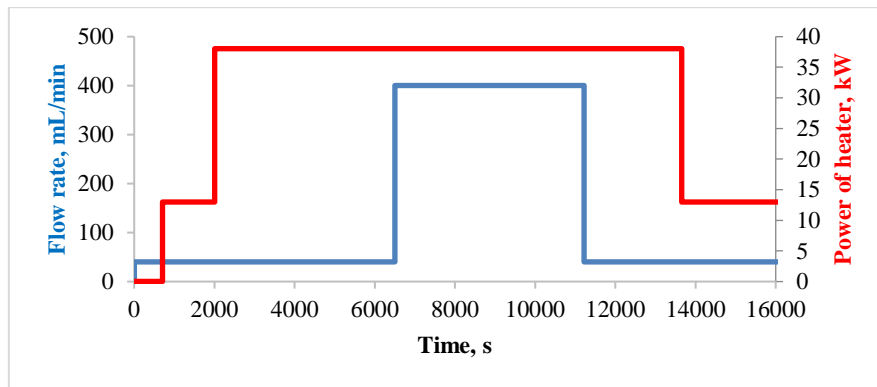


Figure 3. Cooling water flow rate and power of heater over time

Table 2. Results of data used in the wall heat transfer coefficient

| $T_R$   |       | $T_{cwi}$ |       | $\Delta T_R$ | $\Delta T_{cwo}$ | $\Delta T_L$ | Flow rate | Power | The heat taken by water in the reactor | Heat taken by jacket cooling water | A              | U                   |
|---------|-------|-----------|-------|--------------|------------------|--------------|-----------|-------|--|------------------------------------|----------------|---------------------|
| Initial | Final | Initial   | Final | °C           | °C               | °C           | g/s       | W     | kJ                                     | kJ                                 | m <sup>2</sup> | W/m <sup>2</sup> °C |
| 27.3    | 37.4  | 20        | 30    | 10.1         | 13.3             | 7.2          | 0.42      | 39    | 63.3                                   | 92.7                               | 0.06           | 51.09               |

Table 3. Investigation of changes in cooling water outlet temperature  $T_{cwo}$  at different cooling water flow rates ( $\dot{m}_{cw}$ )

| $\dot{m}_{cw}$ , g/s | 0.20  | 0.30  | 0.40  | 0.50  | 0.54  | 0.60  | 0.70  | 0.80  | 0.90  | 1.00  | 1.10  |
|----------------------|-------|-------|-------|-------|-------|-------|-------|-------|-------|-------|-------|
| $\Delta T$ , °C      | 27.74 | 18.49 | 13.87 | 11.09 | 10.30 | 9.25  | 7.93  | 6.94  | 6.16  | 5.55  | 5.04  |
| $T_{cwo}$ , °C       | 47.74 | 38.49 | 33.87 | 31.09 | 30.30 | 29.25 | 27.93 | 26.94 | 26.16 | 25.55 | 25.04 |

Table 4. Investigation of outlet temperatures ( $T_{cego}$ ) at different cooling ethylene glycol flow rates ( $\dot{m}_{ceg}$ )

| $\dot{m}_{ceg}$ , g/s | 0.2   | 0.30  | 0.40  | 0.50  | 0.60  | 0.70  | 0.80  | 0.90  | 0.95  | 1.00  | 1.10  |
|-----------------------|-------|-------|-------|-------|-------|-------|-------|-------|-------|-------|-------|
| $\Delta T$ , °C       | 49.11 | 32.74 | 24.55 | 19.64 | 16.37 | 14.03 | 12.27 | 10.91 | 10.33 | 9.82  | 8.93  |
| $T_{cego}$ , °C       | 69.11 | 52.74 | 44.55 | 39.64 | 36.37 | 34.03 | 32.27 | 30.91 | 30.33 | 29.82 | 28.93 |

To determine the most suitable refrigerant flow rate, theoretical calculations were made to observe the outlet temperatures of the coolant to be obtained with different flow rates, and the results are given in Table 4.

Since the total heat that the refrigerant in the jacket will take for 4000 seconds is 92704 J, it is seen in Table 4 that the temperature difference decreases with the increase in the flow rate of the ethylene glycol to be sent to the jacket to take

this heat. When operating at low flow rates, ethylene glycol will stay in the system longer, just like when water is used as the fluid, so the outlet temperature of the coolant will be high. This should be avoided as it involves risk.

Figure 4, created with the data shown in Table 3 and Table 4, gives an idea about the range of flow rates according to the outlet temperatures of different fluids sent to the jacket. According to this, it is seen that they have approximate exit temperatures because of sending water to the jacket at a flow rate of 0.5-1.1 g/s and ethylene glycol at a flow rate of 0.9-1.1 g/s. At the same time, it is seen in Figure 4 that the water flow rate sent to the jacket is less than the ethylene glycol flow rate to obtain the same outlet temperature in the coolant. For this reason, when water is used to cool this system, it has been seen that approximately  $\frac{1}{2}$  less substance can be used than ethylene glycol and considering that it is relatively more economical and not a toxic chemical, it has been decided that the use of water as a refrigerant will be more appropriate. After determining that water is relatively more suitable among the two different refrigerants compared, the optimum flow rate for water should be determined by considering the cost calculation. As a result of the assumption that all 39 W of heat sent to the reactor is taken by the jacket, the exact flow rate of the cooling water was determined as 0.906 g/s. Since the change of the flow rate changes the heat transfer area and thus the overall heat transfer coefficient, the new heat transfer area is calculated as 0.066 m<sup>2</sup>. While the height of the jacket to receive this heat was determined as the same as the reactor height, the diameter of the jacket was calculated as 0.1050 cm and the jacket capacity in this direction was calculated as 1.7 L. As a result of all these studies, considering the cost and environmental impact as a refrigerant, using water at an optimum flow rate of 1.271 g/s was determined as the optimum value.

### 3.2 Dynamic Behavior of The System

**Determination of steady state parameters of the system-S1 zone:** The reactor heat transfer system design parameters were investigated by repeated experiments under different conditions. First, it is necessary to determine the steady-state parameters of the process. During the experiment, which was started by keeping the cooling water flow rate and heater power constant, the inlet-outlet temperatures of the reactor and the cooling water were measured, and the results were recorded. This process was continued until the second steady state was observed. With the results obtained, the changes in the temperature in the reactor and the cooling water temperature passed through the jacket over time were graphically created. Thus, the steady-state operating parameters of the reactor were determined. To obtain the response of the reactor, the step input was given to the system at a specified time after the reactor was operated in a steady state for a while. The variation of the temperature inside the reactor with time is shown in Figure 1.

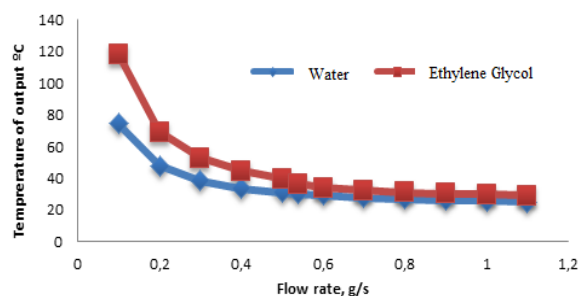


Figure 4. Output temperatures of water and ethylene glycol used as refrigerants at different flow rates

**Determination of the variation of reactor temperature with negative/positive step inputs given to the cooling water flow rate ( $S_2$  and  $S_3$  zones):** After reaching a steady-state, positive and negative step effects were given to the cooling water flow rate to examine the control efficiency of the reactor. It is necessary to examine the effect of these step effects on the output variable for the open-loop system. In the experiments carried out for this purpose, the temperature of the environment where the reaction conditions were not met was stabilized with the help of variac and positive and negative step inputs were given to the cooling water flow rate while the inlet temperature was constant at room temperature (20 °C). Firstly, the coolant flow rate was 40 mL/min. A positive step input was given to the system when the temperature was steady, and the reactor temperature was approximately 38°C.

As a result of the positive step input, the cooling water flow rate increased approximately 10 times and reached 400 mL/min.

The reactor temperature decreased and reached a steady state again at a temperature of about 33 °C. Similarly, changes in the system were observed by giving a negative step input to the system. Initially, the reactor temperature was steady at 32°C and the cooling water flow rate was 400 mL/min. The cooling water flow rate declined to 40 mL/min after the given negative step input, the temperature inside the reactor dropped to 36 °C.

**Determination of process model and control parameters:** In this paper, to examine the dynamic behavior of the system, the control parameters were calculated with the help of model parameters by giving positive and negative step effects, and thus the success of the controller was examined. The model parameters formed by the positive and negative effects given to the system by two different methods, namely "Linear Regression Method" and "Reaction Curve Method", were examined.

**Determination of Process Model Parameters by Linear Regression Method:** The result of the positive step effect given to the cooling water flow rate ( $S_2$  region); the flow rate was increased from 40 mL/min to 400 mL/min. The positive step effect and reaction curve given is given in Figure 5.a. It was observed that the system reached the second steady-state

2400 seconds after the positive step input. Obtained data were used to determine  $\tau$ ,  $\theta$ , and  $K_p$  values as 11.9 min., 1.92 min., 0.016 °C/(mL/min.) respectively.

The data obtained at the end of the positive step inputs were recorded and the system dynamics were examined by giving a negative step effect ( $S_3$  region) to the system. The negative step effect was given by reducing the cooling water flow rate from 400 mL/min to 40 mL/min and the reaction curve was obtained and given in Figure 5.b. It was observed that the system reached the second steady-state 2400 seconds after the given negative step effect.  $\tau$ ,  $\theta$ , and  $K_p$  values were determined as 9.8 min, 5.06 min, and -0.01172 °C/(mL/min), respectively.

*Determination of Model Parameters of the System by Reaction Curve Method:* The reaction curve of positive step input given to the system in the  $S_2$  region is given in Figure 5.a. By applying the reaction curve method,  $\tau$ ,  $\theta$  and  $K_p$  were found as 2.33 min., 15.1 min. and as -0.0124 °C/(mL/min.), respectively. The reaction curve formed because of the negative step effect given to the system in the  $S_3$  region is given in Figure 5.b. Using this figure, model parameters  $\tau$ ,  $\theta$  and  $K_p$  were determined as 1 min., 17.71 min, and 0.0120 °C/(mL/min).

*Determination of PID Control Parameters.* P, PI and PID parameters were found with Ziegler-Nichols and Cohen-Coon tuning methods using model parameters obtained by “Linear Regression” and “Reaction Curve” methods. These parameters are given in Table 5. Positive Effect PID parameters found in two different methods were simulated with the computer program which is Matlab-Simulink.

Matlab control simulations are given in Figure 6.

Figure 6. a-d were compared, and it was observed that the control parameters found by the Cohen-Coon adjustment method were insufficient to control the system.

The simulation of the PID parameters obtained from the Ziegler Nichols method was found to be the most successful among the results obtained. For this reason, optimum control parameters were determined by the mentioned methods and optimized with the Matlab Simulink PID Tuning program extension. PID control parameters obtained by tuning were used as -154, 0.123, and 0.519, respectively.

*Application of Control Action to the System and Experimental PID Control:* The reaction was carried out experimentally with the obtained optimum theoretical PID parameters which were given in Table 5. Experimental control parameters that provide the temperature control of the system as a result of the final optimizations with the trial and error method were given in Table 6. The reaction temperature goes up to about 70°C in cases where no control is applied. With the applied PID control, the temperature inside the reactor was kept constant at 33 °C. Experimentally open-loop operation without PID temperature control and operation under PID control was given in Figure 7.

Table 6. Experimental PID Control parameters that provide temperature control of the system

| Control Parameters | Values   |
|--------------------|----------|
| $K_c$              | -10.8800 |
| $\tau_1$           | -10.8308 |
| $\tau_D$           | -0.7214  |

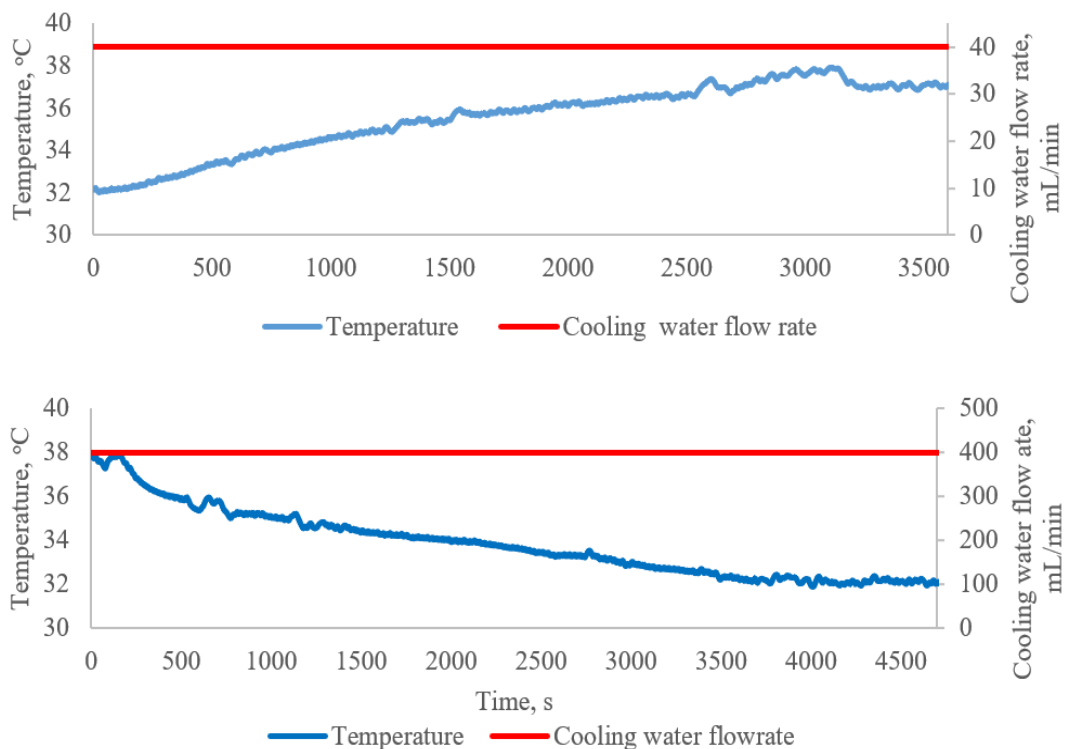


Figure 5. Change in reactor temperature because of negative (a) and positive (b) step effect on cooling water flow rate

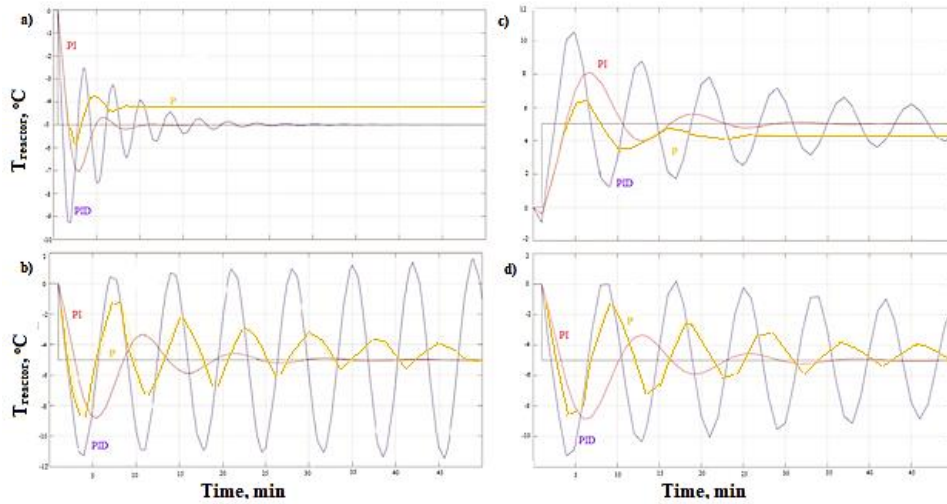


Figure 6. Linear Regression Positive Step Effect (a-b); (a)Simulation of PID parameters obtained by Ziegler Nichols method; (b) Simulation of PID parameters obtained by Cohen-Coon method; (c-d) Reaction curve Positive Step Effect; (c) Simulation of PID parameters obtained by Ziegler Nichols method; (d) Simulation of PID parameters obtained by the Cohen-Coon method

Table 5. Determination of PID control Parameters under positive/negative step inputs by linear regression and reaction curve method

| Method            | Input    | Controller | Cohen-Coon |          |          | Ziegler-Nichols |          |          |
|-------------------|----------|------------|------------|----------|----------|-----------------|----------|----------|
|                   |          |            | $K_c$      | $\tau_I$ | $\tau_D$ | $K_c$           | $\tau_I$ | $\tau_D$ |
| Linear Regression | Positive | P          | -518       |          |          | -491            |          |          |
|                   |          | PI         | -449       | 4.786    |          | -442            | 6.39     |          |
|                   |          | PID        | -675       | 4.43     | 0.678    | -590            | 3.84     | 0.96     |
|                   | Negative | P          | -193       |          |          | -165            |          |          |
|                   |          | PI         | -155       | 8.26     |          | -148            | 16.84    |          |
|                   |          | PID        | -141       | 10.367   | 1.682    | -198            | 10.12    | 2.53     |
| Reaction Curve    | Positive | P          | -549       |          |          | -522            |          |          |
|                   |          | PI         | -477       | 5.872    |          | -470            | 7.758    |          |
|                   |          | PID        | -717       | 5.389    | 0.824    | -627            | 4.66     | 1.165    |
|                   | Negative | P          | -1503      |          |          | -1475           |          |          |
|                   |          | PI         | -1335      | 4.786    |          | -1328           | 3.33     |          |
|                   |          | PID        | -1988      | 4.43     | 0.359    | -1771           | 2        | 0.5      |

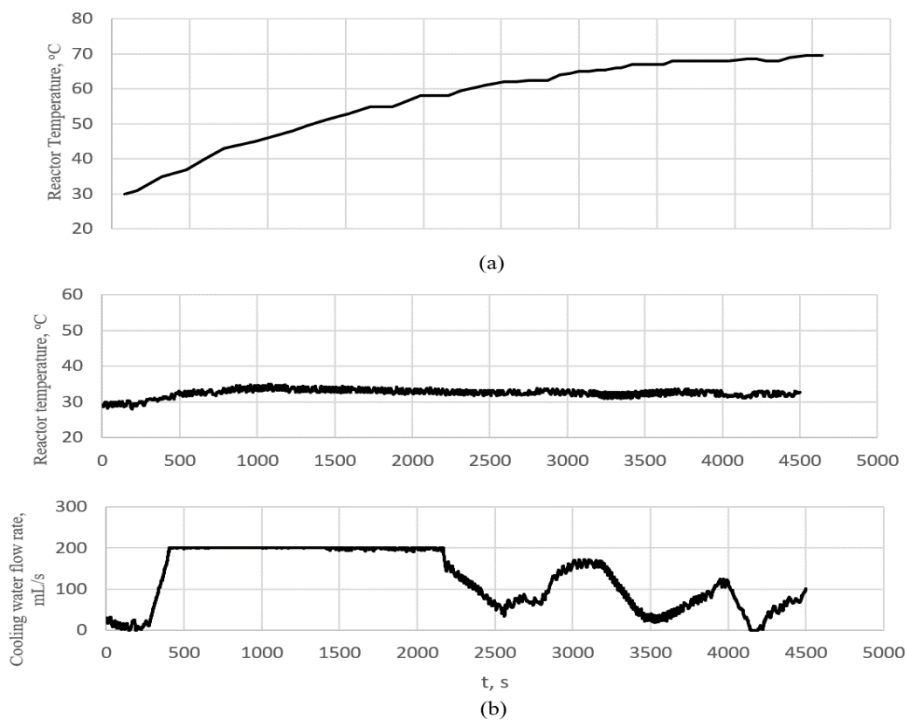


Figure 7 (a) Variation of reactor temperature with time in the uncontrolled system (b) Variation of cooling water flow rate and reactor temperature over time in PID Control system



#### 4. Conclusions

During the dynamic investigations of the exothermic neutralization reaction, a heater was used to represent the heat source. The result of the dynamic analyzes carried out in an isolated reactor was evaluated theoretically and experimentally, and a controller design was carried out for the reactor temperature. It was observed that the process model parameters obtained from negative and positive step inputs given to the cooling water flow rate were different. Since the real system should be taken into consideration while creating the control parameters, it is predicted that the PID controller will continuously have positive effects on the cooling water flow rate, and the reaction volume heated during the process was calculated on the positive step input. At the end of the simulation, it was observed that the control parameters found by the Cohen-Coon adjustment method were insufficient to control the system. To find the optimum control parameters, the Linear Regression method, the PID parameters found by the positive step effect Ziegler-Nichols method were used as the initial value and optimized with the Matlab Simulink PID Tuning extension. Before the control application, the last parameters obtained for the final optimization were used as the initial value. Then, the PID parameters were optimized by trial and error methods while the process was in a closed loop. As a result of all these processes, the temperature of the reaction, which rapidly heated up to 70 °C in an uncontrolled cycle, was kept constant at 33 °C. In future studies, a comparison between a constant flow rate cooler and a PID controller will help optimization studies. Similarly, performance comparison with controller types such as P, PI, GMP can be another subject of study.

#### Declaration

The authors declared no potential conflicts of interest with respect to the research, authorship, and/or publication of this article. The authors also declared that this article is original, was prepared in accordance with international publication and research ethics, and ethical committee permission or any special permission is not required.

#### Author Contributions

Z.Y. Hitit developed the methodology. Z.Y. Hitit and P. Aygener wrote the manuscript together. E. Yorgancioglu and B. Akagun performed the experiments. K. Kesenci, S. Ertunç and B. Akay supervised and improved the study.

#### Acknowledgment

This study was supported by TUBITAK 2209-B Undergraduate Research Projects Industry-Oriented Support Program with the project number of 1139B412001078.

#### References

- Rosival, L., *Pesticides*. Scandinavian Journal of Work, Environment and Health, 1985. **11**(3): p. 189–197.
- Bates, J., *Recommended approaches to the production and evaluation of data on pesticide residues in food*. Pure and Applied Chemistry, 1982. **54**(7): p. 1361–1449.
- Programme, U.N.E., *List of Environmentally Dangerous Chemical Substances and Processes of Global Significance*. IRPTC, 1986.
- Rani, L., K. Thapa, N. Kanojia, N. Sharma, S. Singh, A.S. Grewal, J. Kaushal, *An extensive review on the consequences of chemical pesticides on human health and environment*. Journal of Cleaner Production, 2021. **283**: 124657.
- Akande, M. G., *Health Risks Associated with the Consumption of Legumes Contaminated with Pesticides and Heavy Metals*, 2021. [cited 2021 25 June]; Available from: <https://www.intechopen.com/online-first/78185>.
- Syafrudin, M., R.A. Kristanti, A. Yuniarto, T. Hadibarata, J. Rhee, W.A. Al-Onazi, A.M. Al-Mohaimeed, *Pesticides in drinking water—a review*. International Journal of Environmental Research and Public Health, 2021, **18**(2): 468.
- Al-Maydama, H. M. A., and P.J. Gardner, *The enthalpy of solution of phosphorous acid (H<sub>3</sub>PO<sub>3</sub>) in water*. Thermochimica Acta, 1990, **161**(1): p. 51–54.
- Ann, P. J., J.N. Tsai, I.L. Wong, T. Hsieh, T., & C.Y. Lin, *A simple technique, concentration and application schedule for using neutralized phosphorous acid to control phytophthora diseases*. Plant Pathology Bulletin, 2009, **18**: p. 155–165.
- Förster, H., J. Adaskaveg, D.H. Kim, M., Stanghellini, *Effect of Phosphite on Tomato and Pepper Plants and on Susceptibility of Pepper to Phytophthora Root and Crown Rot in Hydroponic Culture*. Plant disease, 1998, **82**(10): p. 1165–1170.
- Macintire, W. H., S.H. Winterberg, L.J., Hardin, A.J. Sterges, L.B. Clements, *Fertilizer evaluation of certain phosphorus, phosphorous, and phosphoric materials by means of pot cultures*. Agronomy journal, 1950. **42**: p. 543–549.
- Conrath, U., G.J.M. Beckers, V. Flors, P. García-Agustín, G. Jakab, F. Mauch, B. Mauch-Mani, *Priming: getting ready for battle*. Molecular plant-microbe interactions: MPMI, 2006. **19**(10): p. 1062–1071.
- Conrath, U., *Molecular aspects of defence priming*. Trends in plant science, 2011. **16**(10): p. 524–531.
- Luna, E., T.J.A. Bruce, M.R. Roberts, V. Flors, & J. Ton, *Next-generation systemic acquired resistance*. Plant physiology, 2012. **158**(2): p. 844–853.
- Hunt, M. D., J.A. Ryals, D. Reinhardt, *Systemic acquired resistance signal transduction*. Critical Reviews in Plant Sciences, 1996. **15**(5–6): p. 583–606.
- Neuenschwander, U., K. Lawton, J. Ryals, *Plant microbe interactions*. 1996, New York: Chapman and Hall. Systemic acquired resistance, p. 81–106.
- Ryals, J. A., U.H. Neuenschwander, M.G. Willits, A. Molina, H.Y. Steiner, M.D. Hunt, *Systemic Acquired Resistance*. The Plant cell, 1996. **8**(10): p. 1809–1819.
- Klessig, D. F., H.W. Choi, D.A. Dempsey, *Systemic acquired resistance and salicylic acid: past, present, and future*. Molecular plant-microbe interactions, 2018. **31**(9): p. 871–888.

18. Bellows, T. S., *Foliar, Flower, and Fruit Pathogens* In: Handbook of Biological Control. 1999, San Diego: Academic Press, p. 841-852.
19. Chaudhry, M. Q., *Phosphine resistance*. Pesticide Outlook, 2000. **11**(3): p. 88–91.
20. Hashimoto, S., K. Fujiwara, K. Fuwa, *Determination of phosphate ion by gas chromatography with the phosphine generation technique*. Analytical Chemistry, 1985. **57**(7): p. 1305–1309.
21. Lee, K., & I.S. Han, *Evaluation of Thermal Hazard in Neutralization Process of Pigment Plant by Multimax Reactor System*. Journal of the Korean Society of Safety, 2008. **23**(6): p. 91-99.
22. Garrett, K. K., *Potential Antidotes to Phosphine Poisoning*. University of Pittsburgh. In Graduate School of Public Health, 2021, University of Pittsburgh: USA. p. 159.
23. Yurkevich, V., *PI/PID Control for Nonlinear Systems via Singular Perturbation Technique* In: Advances in PID Control. 2011, Rijeka: InTech, p. 113–142.
24. A.Iyswariya, N. Nimitha, A. Veronica & S. Ranganathan, *Design of PI Controller using First Order Plus Time Delay Model for Process Control*. International Journal of Advanced Research in Electronics and Communication Engineering, 2015. **4**(3): p. 687–691.
25. Ziegler J.G., *Optimum settings for automatic controllers*. Transactions of the ASME, 1942. **64**(11): p. 759–768.
26. Li, Y., K. H. Ang, G.C.Y. Chong, *PID control system analysis and design*. IEEE Control Systems Magazine, 2006. **26**(1): p. 32–41.
27. Khosravi, A., A. Chatraei, G. Shahgholian, S.M. Kargar, *System identification using NARX and centrifugal compressor control through the intelligent, active method—Case study: K-250 centrifugal compressor*. Asian Journal of Control, 2022. p. 1–20.
28. Huang, J., & W.J. Hugh, *On a nonlinear multivariable servomechanism problem*. Automatica, 1990. **26**(6): p. 963–972.
29. Isidori, A. and C.I. Byrnes, *Output regulation of nonlinear systems*. IEEE transactions on Automatic Control, 1990. **35**(2): p. 131–140.
30. Gamasu, R. and V.R. B. Jasti, *Robust cohen-coon PID controller for flexibility of double link manipulator*. International Journal of Control and Automation, 2014. **7**(1): p. 357–368.
31. Khalil, H. K., *Universal integral controllers for minimum-phase nonlinear systems*. IEEE Transactions on automatic control, 2000. **45**(3): p. 490–494.
32. Mahmoud, N. A. and H.K. Khalil, *Asymptotic regulation of minimum phase nonlinear systems using output feedback*. IEEE Transactions on Automatic Control, 1996. **41**(10): p. 1402–1412.
33. Foley, M. W., R.H. Julien, B.R.A. Copeland, *A comparison of PID controller tuning methods*. The Canadian Journal of Chemical Engineering, 2005. **83**(4): p. 712–722.
34. Rivera, D. E., M. Morari and S. Skogestad, *Internal model control: PID controller design*. Industrial & engineering chemistry process design and development, 1986. **25**(1): p. 252–265.
35. Seborg, D. E., T.F. Edgar, D.A. Mellichamp, H. Wiley, N.J. Hoboken, *Process Dynamics and Control, 2<sup>nd</sup> Edition*, 2008. **54**(11): p. 3026.
36. Dunn, W., *Introduction to instrumentation, sensors, and process control*. 2005, Boston: Artech House, Inc.



e-ISSN: 2618-575X

INTERNATIONAL ADVANCED RESEARCHES  
and  
ENGINEERING JOURNALJournal homepage: [www.dergipark.org.tr/en/pub/iarej](http://www.dergipark.org.tr/en/pub/iarej)International  
Open Access Volume 06  
Issue 02

August, 2022

**Research Article****A study on the renewable energy potential of incineration of municipal solid wastes produced in Izmir province****Anil Başaran** <sup>a\*</sup> <sup>a</sup>Manisa Celal Bayar University, Engineering Faculty, Department of Mechanical Engineering, Yunusemre, Manisa, 45140, Turkey

## ARTICLE INFO

*Article history:*

Received 09 April 2022

Accepted 04 August 2022

Published 15 August 2022

*Keywords:*

Incineration

Municipal solid waste

Renewable energy

R1 energy efficiency

Waste-to-Energy

## ABSTRACT

The efficient use of existing energy sources along with the development and widespread use of alternative energy sources, especially renewable energy sources becoming important issues. At this point, the energy content of municipal solid wastes (MSW) can be considered a renewable energy source. MSWs contain a large fraction of renewable material and are continuously produced as a result of human activity. Therefore, international authorized institutions such as the U.S. Department of Energy (US DOE), and the U.S. Environmental Protection Agency (US EPA) assess MSWs as renewable and sustainable energy sources. Incineration is one of the options for energy recovery from MSW as a waste-to-energy (WTE) approach. The R1 energy efficiency is a criterion introduced by the European Union Waste Directive (Directive 2008/98/EC) to differentiate waste operation by incineration as either disposal or energy recovery. The paper focused on the evaluation of the MSW incineration potential of İzmir province in consideration of R1 energy efficiency criteria. According to the R1, the MSW energy recovery (both heat and electricity) potentials were investigated considering the amount, composition, and calorific value of MSW generated in İzmir province. The population growth, MSW generation, and calorific value alternation up to 2026 were estimated for İzmir. Based on MSW future projections of İzmir province, overall energy recovery potential was assessed. It is forecasted that the average net calorific value (NCV) of MSW generated in İzmir will exceed 6 MJ/kg. This NCV will be suitable for energy recovery from the İzmir MSW. Assuming R1=0.65, it is predicted that a minimum of 2231 GWh/year of heat energy or 932 GWh/year of electricity can be produced annually in the next years 2022.

**1. Introduction**

Nowadays, one of the reasons for the steady increment in energy demand and dependence on energy is the growth of the World population, industrialization, and technological progress [1]. It is emphasized by energy experts that the fossil fuels in the world may run out [2]. Hence, searching for alternative energy resources especially renewables have gained great attention recently. Municipal Solid Waste (MSW) is considered a renewable energy resource because MSWs contain a large fraction of renewable material and are continuously produced. MSW is a heterogeneous material usually obtained from a collection of wastes generated in urban fields, which naturally alters from region to region. MSW contains a large fraction of renewable materials (or biomass feedstock) like food waste, cardboard, paper, grass clippings, leaves, wood, leather products, and other non-

renewable (or non-biomass feedstock) materials like plastics and other synthetic materials made from petroleum [3]. The rational disposal of MSWs, which naturally arises as a result of our vital activities, is a very important issue in terms of providing maximum economic contribution as well as human health [4].

The US Department of Energy (US DOE) reported that MSW consists of 82% biomass (food, paper, yard wastes, rubber, etc.) and 18% petrochemical wastes, which are combustible materials. Therefore, the US DOE classifies the MSW in the biomass fuel category of renewable energy sources [5]. According to the US Environmental Protection Agency (US EPA), electricity and heat generation with non-recyclable waste materials can be considered renewable energy generation. This process reduces carbon emissions by reducing methane generation from landfills and offsetting energy needs from fossil sources [6]. Energy Information Administration (EIA) has assorted all consumption at MSW combustion facilities as

\* Corresponding author. Tel.: +90 (236) 201 2382.

E-mail addresses: [anil.basaran@cbu.edu.tr](mailto:anil.basaran@cbu.edu.tr) (A. Başaran)

ORCID: 0000-0003-0651-1453 (A. Başaran)

DOI: [10.35860/iarej.1101046](https://doi.org/10.35860/iarej.1101046)© 2022, The Author(s). This article is licensed under the CC BY-NC 4.0 International License (<https://creativecommons.org/licenses/by-nc/4.0/>).

a renewable part of “Waste Energy” [7].

Many countries focus on the policy of using these resources effectively to reduce the consumption of natural resources and struggle with the emerging energy crisis [8]. In this scope, energy generation from MSW is gaining increasing interest in terms of reducing dependence on fossil sources. Energy conversion from MSW in waste-to-energy (WTE) power plants is one of the main ways of integrated waste management. Hence, energy conversion from MSW, as a waste management strategy, is increasing in terms of both the number of facilities and capacity across Europe and, is supported by legal directives [9]. Waste-to-energy is recognized as a promising alternative and a potential renewable energy source to tackle the problem of waste generation [10]. The waste management hierarchy suggested by Directive 2008/98/EC [10] of The European Parliament and The Council Energy is shown in Figure 1. After reducing, reusing, and recycling, material, and energy recovery has a priority in waste management.

Incineration is defined as the controlled burning of waste at high temperatures, and it reduces the volume of waste, generates energy from waste as heat and power, and eliminates pathogens [11,12]. The main purpose of an incineration facility is the conversion of stored energy from waste to useful energy forms. MSW incineration process is composed of three main steps: combustion of MSW in an incinerator, energy recovery from flue gas, and cleaning of air pollutants. Incineration of MSW does not completely dispose of the waste but does remarkably reduce the volume of waste to be landfilled. The reductions via incineration are approximately 90 percent by volume and 75 percent by weight [13]. Some air pollutants, such as CO<sub>x</sub>, SO<sub>x</sub>, and NO<sub>x</sub>, are formed because of the incineration of MSW. In the past, MSW incinerators were considered major sources of such environmental pollutants. On the other hand, the WTE power plants implemented new US EPA regulations on Maximum Achievable Control Technology (MACT) during the 1990s, and then, they have become one of the cleanest sources of heat energy and electricity [14].

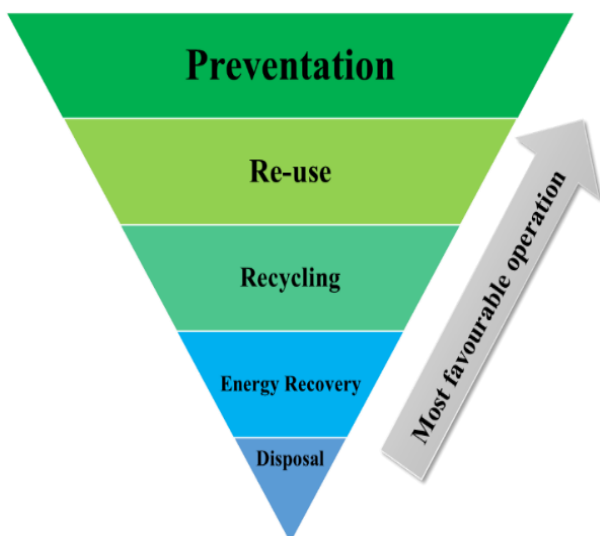


Figure 1. Waste management hierarchy [10]

One of the important issues is the energy conversion efficiency of the input waste during incineration. In this study, R1 efficiency was adopted for waste incineration energy conversion. The criterion of energy efficiency (R1 formula) that was introduced in the Waste Framework Directive in 2008 [10] is an incentive for WTE plants in Europe to improve their efficiency. According to Annex II of the Waste Framework Directive, incineration facilities dedicated to the processing of MSW can be classified as R1 recovery operations where their energy efficiency is equal to or above 0.65 for new plants [10]. In other words, the R1 threshold should be satisfied on the condition that a minimum of 0.65 for energy recovery via MSW incineration. Gohlke [15] investigated efficiency energy recovery from MSW and the resultant effect on greenhouse gas balance. The author reported some energy efficiency performance indicators and concluded that the R1 criterion will lead to the development and implementation of the optimized process and system. Grosso et al. [16] analyzed the R1 formula and exergy efficiency of 97 European plants as energy recovery criteria. According to their study, 43.7% of 97 European WTE plants have R1 efficiency higher than 0.65. In this respect, the energy potential via incineration was theoretically assessed for MSW generated in İzmir using the R1 criteria in this study. According to the R1 criteria,  $R1=0.65$  is the threshold value for energy recovery in incineration facilities. Thus, in the scenario of establishing an incineration plant in İzmir, the energy recovery efficiency of the incinerator should be at least  $R1=0.65$ . Different from the other study in the literature, a 0.65 threshold value of R1 efficiency was adopted to determine the theoretical potential of energy content which can be recovered from İzmir province MSW by the way of incineration. The total produced energy from the MSW in İzmir was calculated assuming the 0.65 value of the R1 efficiency is the minimum value for the energy recovery and it can be increased, but the calculations have been made using this threshold value as the worst scenario for energy recovery from MSW.

İzmir is the third big city in Turkey with a population of nearly four million. It is located in the western region of Turkey and is on the Aegean Sea coast. İzmir is the industrial and tourism center of the Aegean Region and a prospering province in both economy and population. In the present paper, an investigation of the energy potential of MSW in İzmir using incineration technology was carried out. The main objective of this study is to quantitate the contribution of MSW in İzmir to the energy production of the city via the MSW incineration option. This paper provides the theoretical potential of energy content that can be recovered from MSW by the way of incineration and evaluation of the energy potential of MSW in the city according to R1 energy efficiency [10]. Different from the other study in the literature, the current study investigates the incineration potential of MSW generated in İzmir province. As stated earlier, a 0.65 threshold value of R1 efficiency was adopted in this study to assess the theoretical potential of the energy content of MSW

generated in the İzmir province. The population growth, MSW generation, and energy amount projections from 2022 to 2026 were also presented in this study.

## 2. Methodology

The energy content of MSW is the major energy input of the MSW incinerator. The energy content of MSW as an energy source is strictly linked to two parameters: net calorific value (NCV) and quantity of MSW. The energy content of MSW ( $\dot{E}_w$ ) can be written as in Eqn. 1.

$$\dot{E}_w = \dot{m}_{waste} NCV_{waste} \quad (1)$$

where  $\dot{m}_{waste}$  is the MSW feed rate to the incineration facility and  $NCV_{waste}$  is the net calorific value of the MSW. This is because the calculation and estimation of the generation rate and net calorific value of MSW are important for the feasibility of an incineration plant. In this study, the calculation and estimation of the generation rate and net calorific value of MSW produced in İzmir have been conducted.

### 2.1. MSW generation in İzmir

The waste continuously is generated as a result of human activity. Therefore, the population future projection is one of the important parameters for the estimation of MSW generation. İzmir's yearly population growth and MSW generation data were obtained from official reports prepared by the Turkish Statistical Institution (TurkStat) in the current study. According to TurkStat statistics, the population of İzmir is gradually increasing and it is expected to be nearly 4.7 million in 2026 [17,18]. The population growth (from 2008 to 2021) and future projections (from 2022 to 2026) of İzmir city given in the TurkStat report can be shown in Figure 2 [19].

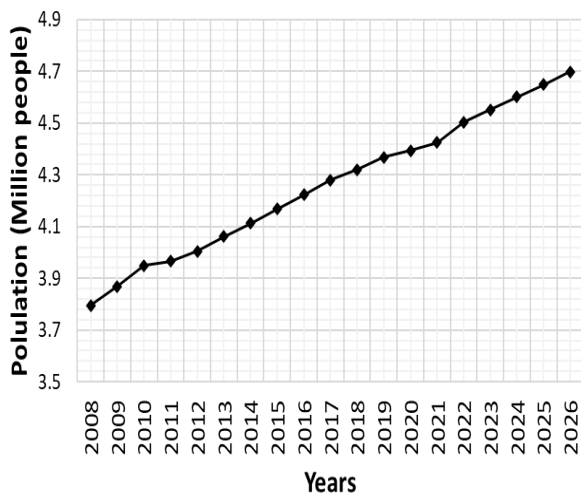


Figure 2. Population growth of İzmir city [17-19]

According to the waste generation data, which covers between 2001 and 2020 years, published by TurkStat, an

average of 1.241 kg of MSW per day has been produced per person in İzmir province [16]. The data available indicate [20] that the average MSW generation in İzmir province is around 440 kg/capita/year. The annual MSW generation from 2008 to 2020 (orange bars) and future estimation (blue bars) of MSW generation from 2020 to 2026 in İzmir province are given in Figure 3. While the annual MSW generation between 2008 and 2020 given in Figure 3 is reported TurkStat data [20], the annual MSW generation between 2022 and 2026 is determined according to the past 2008-2020 MSW data using the least-squares method. It follows from the report prepared by TurkStat that total MSW generation in İzmir increased by 73.3% from 2008 to 2020. Also, it is expected that the MSW production amount is approximately 2.74 million tons per year in 2026. The economic development and growth of the urban population in İzmir province have increased the MSW amount.

### 2.2. Calculation of energy content of MSW

The energy content of the MSW can be determined experimentally by combusting the fuel in a high-pressure oxygen ambience in a bomb calorimeter [21-23]. On the other hand, the complexity of biomass, particularly in case of MSWs, makes it highly difficult to experimentally estimate the calorific value (in other words energy content) [24]. The experimental approaches can be tedious, costly, and time-consuming [21]. Using theoretical approaches not only saves time but also saves high expenses [25]. There are different theoretical approaches in the literature to estimate and calculate the energy value of the MSW because of the non-homogeneous structure of MSW.

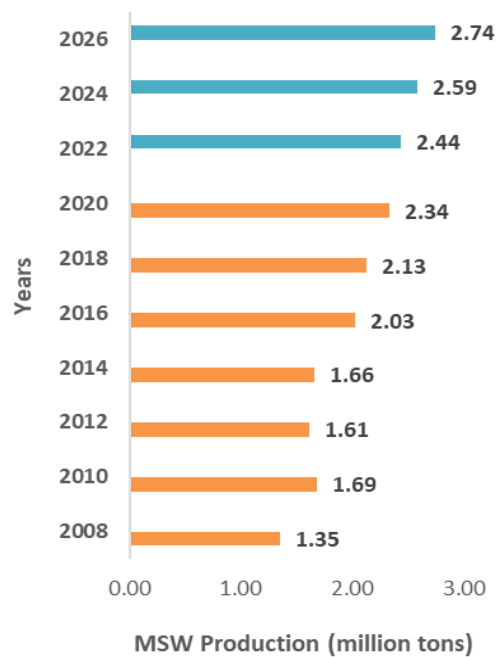


Figure 3. The annual MSW generation and future estimation in İzmir province [20]

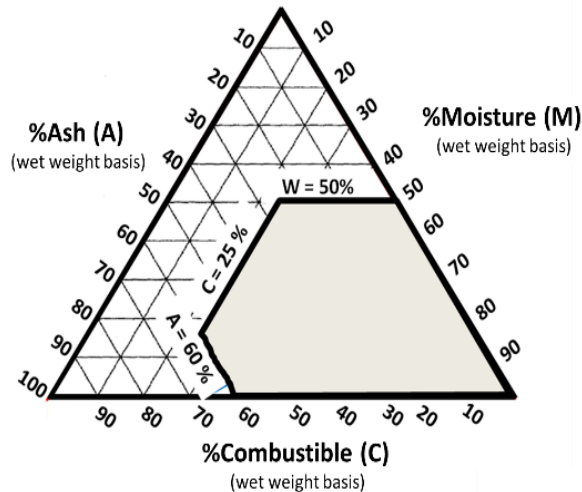


Figure 4. Tanner Diagram adapted from [28, 29]

One of the common theoretical approaches is ultimate analysis. This method is based on the elemental analysis for each component of the MSW that gives rise to the percentages of Carbon, Hydrogen, Oxygen, Nitrogen, Sulfur, and Chlorine elements. Then, the energy content of the MSW is determined depending on these chemical characteristics [24,26]. One of the more accurate ways to evaluate the fuel quality of waste is to divide it into characteristic components (organics, inert materials, plastics, cardboards, etc.). Thanks to this division, combustible matter (%C), water content (%W), and ash content (%A) of the waste are determined [12]. This approach is named proximate analysis. When the waste composition is defined accordingly proximate analysis, the Tanner diagram (Figure 4), which is the graphical plot of combustibility of MSW and based on actual field data from MSW incineration plant, can help to determine combustion characteristics of the MSW [27,28]. If MSW contains ash lower than 60%, moisture lower than 50%, and combustible higher than 25%, it can be said that MSW is suitable for incineration.

Together with proximate analysis, the approach developed for the feasibility studies of World Bank-supported projects was used to estimate the NCV of the MSW in this study. The NCV is calculated using the following expression [30].

$$NCV_{waste} = NCV_{awf} \cdot C - 2445 \cdot W \quad (2)$$

where  $NCV_{waste}$  is the net calorific value (or lower calorific value) of the waste,  $NCV_{awf}$  is ash and water independent heating value of waste,  $C$  and  $W$  are combustible and moisture fractions of waste, respectively. Table 1 exhibits the fraction basis and calorific values of MSW that are calculated based on Eqn (2).

To determine the composition of MSW in İzmir, waste characterization analyzes are carried out by İzmir Metropolitan Municipality in 17 districts of İzmir, including the summer and winter months [31]. This waste characterization analysis was conducted for the years between 2008 and 2013 as well as 2018, and it was reported for these years. Waste composition percentages for 2014-2017 and 2019-2026 are estimated using the least square method. In other words, future projections of the composition for 2014-2017 and years after 2018 were made with curve fitting using the past data (2008-2013 and 2018 [31]). Composition percentages and future projections of İzmir MSW are given in Table 2.

### 2.3. The R1 energy efficiency formula

The R1 is defined to differentiate waste operation by incineration as either disposal or energy recovery of MSW based on threshold values of 0.60 and 0.65. Recovery takes place if  $R1 > 0.65$  for plants permitted during 2009 and later, and for older plants  $R1 > 0.60$ .

$$R1 = \frac{E_p - (E_f - E_i)}{0.97(E_w + E_f)} \quad (3)$$

Table 1. Fractions and calorific values of waste components reported by the World Bank [12]

| Fraction               | Fraction Basis  |            |                    | Calorific values     |              |
|------------------------|-----------------|------------|--------------------|----------------------|--------------|
|                        | Moisture<br>W % | Ash<br>A % | Combustible<br>C % | $NCV_{awf}$<br>kJ/kg | NCV<br>kJ/kg |
| Food and organic waste | 66              | 13.3       | 20.7               | 17000                | 1905         |
| Plastics               | 29              | 7.8        | 63.2               | 33000                | 20147        |
| Paper & cardboard      | 47              | 5.6        | 47.4               | 16000                | 6435         |
| Wood                   | 35              | 5.2        | 59.8               | 17000                | 9310         |
| Metals                 | 6               | 94         | 0                  | 0                    | -147         |
| Glass                  | 3               | 97         | 0                  | 0                    | -73          |
| Inerts                 | 10              | 90         | 0                  | 0                    | -245         |
| Textiles               | 33              | 4          | 63                 | 20000                | 11793        |
| Leather and rubber     | 11              | 25.8       | 63.2               | 23000                | 14267        |
| Fines                  | 32              | 45.6       | 22.4               | 15000                | 2578         |

Table 2. Composition percent of the MSW generated in İzmir [31]

| Composition percentages                 | 2008  | 2009  | 2010  | 2011  | 2012  | 2013  | 2018  | 2020  | 2022  | 2024  | 2026  |
|---|-------|-------|-------|-------|-------|-------|-------|-------|-------|-------|-------|
| Food and organic waste                  | 48.78 | 39.71 | 49.1  | 54.66 | 46.71 | 56.4  | 45.41 | 49.56 | 49.68 | 49.80 | 49.92 |
| Plastics                                | 8.31  | 7.23  | 8.36  | 9.49  | 14.91 | 11.92 | 10.05 | 12.43 | 12.76 | 13.08 | 13.40 |
| Paper & cardboard                       | 12.97 | 11.16 | 9.45  | 9.63  | 12.96 | 8.44  | 6.81  | 10.11 | 10.10 | 10.09 | 10.07 |
| Wood                                    | 1.12  | 4.70  | 0.85  | 1.29  | 1.94  | 0.96  | 1.24  | 1.38  | 1.33  | 1.29  | 1.24  |
| Metals                                  | 1.78  | 0.42  | 0.51  | 0.65  | 1.24  | 0.97  | 0.98  | 0.93  | 0.93  | 0.92  | 0.92  |
| Glass                                   | 5.37  | 5.09  | 4.43  | 5.37  | 6.55  | 4.97  | 6.63  | 5.49  | 5.49  | 5.49  | 5.49  |
| Inerts                                  | 1.71  | 11.21 | 0.73  | 2.12  | 1.25  | 0.83  | 1.42  | 2.78  | 2.79  | 2.79  | 2.80  |
| Fines                                   | 11.18 | 5.8   | 5.02  | 2.79  | 0     | 3.46  | 5.17  | 4.77  | 4.77  | 4.77  | 4.77  |
| Other combustible                       | 8.16  | 13.23 | 8.42  | 12.53 | 12.87 | 9.83  | 17.62 | 11.81 | 11.82 | 11.82 | 11.82 |
| Others                                  | 0.25  | 0.75  | 12.87 | 0.003 | 0     | 0     | 2.32  | 2.31  | 2.31  | 2.31  | 2.31  |
| Hazardous waste                         | 0.31  | 0.56  | 0.13  | 1.01  | 1.5   | 1.79  | 1.14  | 0.92  | 0.92  | 0.92  | 0.92  |
| Waste electrical and electronic devices | 0.07  | 0.14  | 0.13  | 0.41  | 0.07  | 0.43  | 0.32  | 0.22  | 0.22  | 0.22  | 0.22  |

Reported data in ref. [31]  
 Estimated data with least square method using reported past data in ref. [31]

where  $E_p$  is produced energy (electricity or heat),  $E_w$  is the energy content of waste.  $E_f$  and  $E_i$  are the auxiliary fossil fuel energy and imported energy, respectively.

If no fossil fuels are burned and no auxiliary energy is needed, the R1 energy equation can be simplified as below:

$$R1 = \frac{E_p}{0.97E_w} \quad (4)$$

The factor 0.97 in the dominator is meant to take care of heat losses due to radiation and bottom ash [32]. The term  $E_p$  is calculated as defined by [32]:

$$E_p = 1.1(Q_{district} + Q_{process}) + 2.6 W_{electric} \quad (5)$$

The terms  $Q_{district}$  and  $Q_{process}$  stand for heat delivered to district heat and facility internal process heat networks [32]. In other words,  $Q_{district}$  is the heat energy that can be produced for district heating purposes (for example, example, residential heating). Similarly,  $Q_{process}$  is the amount of heat that can be needed in the internal processes of the facility (for example, the production of hot water for use in internal processes in the facility). The sum of  $Q_{district}$  and  $Q_{process}$  is total heat ( $Q_{total}$ ) produced in the plant. Another term  $W_{electric}$  represents the produced electricity.

When the incineration plant is designed to convert waste energy to electricity, produced electricity ( $W_{electric}$ ) according to the R1 formula becomes

$$E_p = 2.6 W_{electric} = 0.97 R1 E_w \quad (6)$$

$$W_{electric} = \frac{0.97 R1 E_w}{2.6} \quad (7)$$

Similarly, when the incineration plant is designed to convert waste energy to heat, produced total heat ( $Q_{total}$ ) according to the R1 formula becomes

$$E_p = 1.1 Q_{total} = 0.97 R1 E_w \quad (8)$$

$$Q_{total} = \frac{0.97 R1 E_w}{1.1} \quad (9)$$

### 3. Results and Discussion

İzmir is a prospering province both in economy and population. The population of İzmir is gradually increasing and it is expected to be nearly 4.7 million in 2026. This population growth gives rise to an increase in the amount of generated MSW. Incineration facilities have been notable in that both the generated MSW can be disposed of and the energy conversion of MSW can be performed.

In this study, the calculation method proposed from the World Bank report is applied for the NCV of the MSW components. The NCV values of the MSW components, which were calculated with Eqn. (2), are listed in Table 1. The NCV of the MSW produced in İzmir was calculated based on the fraction basis of the MSW for the years. The overall NCV of the MSW generated in İzmir was calculated with Eqn. (10):

$$NCV_o = \sum_i x_i \times NCV_i \quad (10)$$

where  $NCV_o$  is overall NCV of the MSW  $x_i$  is composition percentage of the composition  $i$  and  $NCV_i$  is the net calorific value of the composition  $i$  (Table 1). As stated earlier, the composition percentage,  $x_i$  was estimated for 2014-2017 and 2019-2026 (Table 2). Therefore, the NCV of the MSW for İzmir was calculated for 2008-2013 and 2018 and estimated for 2014-2017 and 2019-2026 using Eqn. (10) for the years. "Others", "Hazardous waste" and "Waste electrical and electronic devices" in Table 2 were not involved in the NCV calculation due to the fact that they are not suitable for incineration. "Other combustible" in Table 2 was considered textiles, leathers, and rubbers. Therefore, the NCV value of "Other combustible" ( $NCV_i$ ) was assumed as 13030 kJ/kg which is the arithmetical average of the NCV values of textiles, leathers, and rubbers [12]. Calculated and estimated NCV of the MSW generated in İzmir are given in Figure 5. It can be easily seen from the figure that the NCV has increased over the

years. This increment means that the energy content of the MSW enhances and the usability of the MSW as a fuel in the incineration facilities rises. The average NCV of the MSW in İzmir was calculated as 6634.9 kJ/kg using the Eqn. (2). According to the report published by World Bank, the average net calorific value of the waste should not be less than 6 MJ/kg throughout all seasons to be able to incinerate the waste [12]. It is expected that an incineration plant to be installed for the evaluation of MSW with this calorific value is suitable for energy recovery.

The total energy that can be produced from MSW in İzmir assuming  $R1=0.65$  is represented accordingly by years and future projections in Figure 6. It is observed from Figure 6 that the total annual produced energy ( $E_p$ ) exceeds 2452 GWh in the next years of 2022. This estimated energy potential of the MSW can be used to meet the energy demand of İzmir province in the form of heat and electricity. According to the TurkStat, 2452 GWh energy value is equal to nearly 0.89% of the gross generation of electricity in Turkey. In 2016, 8.6% of Turkey's electricity need was met from renewable energy sources. It is expected that this estimated energy potential of MSW can contribute to meeting energy demand from renewable energy sources. In other words, the incineration of MSW produced in İzmir can contribute to the increase of 8.6% renewable energy in Turkey with an energy value of 2452 GWh.

The electricity and heat energy potentials of the incineration plant for İzmir province were calculated using Eqn. (7) and Eqn. (9). The electricity potential means that total electricity can be produced if the incineration plant is designed to convert MSW energy to electricity. Similarly, the heat energy potential means that total thermal energy can be produced if the incineration plant is designed to convert MSW energy to heat energy. The calculated and

estimated potentials are given in Figure 7. The total electricity consumption in İzmir was nearly 19241 GWh/year in 2016 and 20433 GWh/year in 2019 [33]. It follows from Figure 7 that electricity from MSW with 852 GWh/year could meet nearly 4.43% of the electricity demand of İzmir in 2016. This percentage is encouraging for the establishment of the incineration plant in İzmir province. Also, producible heat energy with R1 criteria is the level that can be used in district heating. The great majority of the heat energy demand of both homes and industry has been met by natural gas in İzmir. The incineration facilities can be a versatile and environmental alternative to natural gas combustion systems for İzmir province. It can be also seen from Figure 7 that heat energy potentials are higher than the electric potential. The main reason for this situation is that the heat conversion rate of energy of waste is higher than the electricity conversion rate in incinerators.

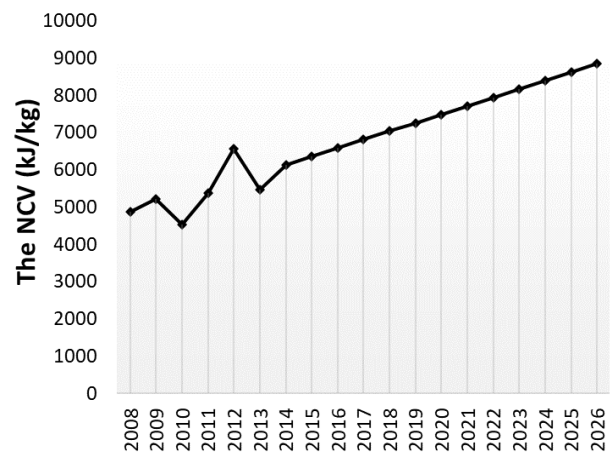


Figure 5. Calculated and estimated NCV of the MSW generated in İzmir [31]

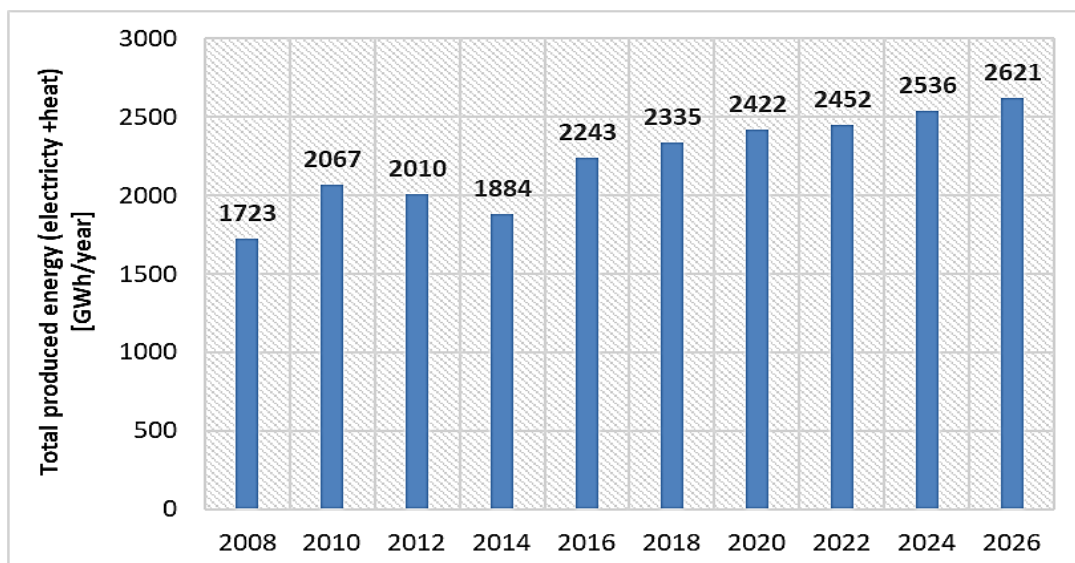


Figure 6. The energy potential of the MSW generated in İzmir province



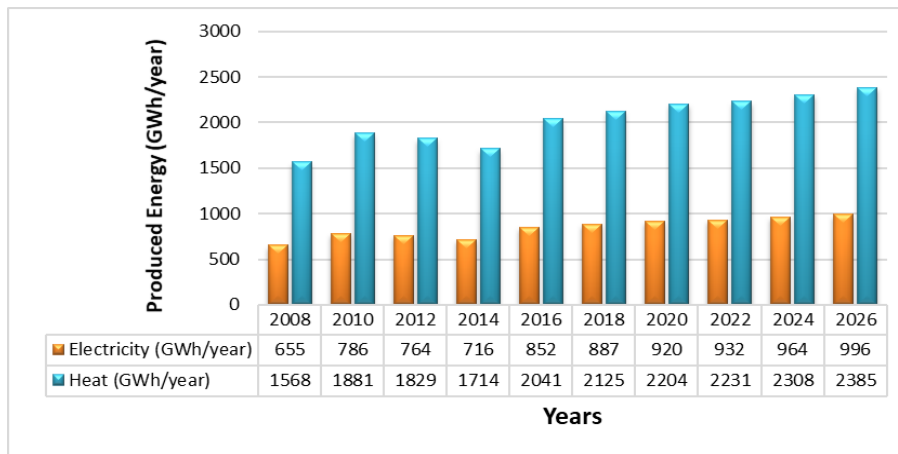


Figure 7. Estimated and calculated heat energy and electricity potentials of the MSW generated in İzmir province

#### 4. Conclusion

The present study has been conducted to assess the energy potential of MSW generated in İzmir in terms of R1 energy efficiency. The MSW generation rate, based on population, the MSW energy content depending on waste fractions, and then heat energy and electricity potentials have been calculated and estimated with the future projections. The results show that;

- In the İzmir province, the population and MSW generation per capita has been increasing. Because of these increments, the overall MSW generation is estimated to be over 2.4 million tons per year after 2022. This amount of MSW can be used for energy recovery with aim of both overcoming waste problems and meeting energy needs.
- It is expected that the NCVs based on the MSW composition show rising over the years. It is forecasted that the average NCV will exceed 6 MJ/kg. This calorific value is suitable for energy recovery from waste. Therefore, the MSW generated in İzmir can be used as a renewable energy source for energy recovery.
- With the assuming  $R1=0.65$  (threshold value of R1 energy efficiency for energy recovery in an incineration plant), it is predicted that a minimum of 2231 GWh/year of heat energy or 932 GWh/year of electricity can be produced annually the next years of 2022. This energy potential can be used to meet energy demand in İzmir with a properly designed incineration plant. It is evident that the evaluation of MSW in incineration plants can contribute to the renewable energy production of İzmir city.

#### Declaration

The author declared no potential conflicts of interest with respect to the research, authorship, and/or publication of this article. The author also declared that this article is original, and was prepared in accordance with international publication and research ethics, and ethical committee permission or any special permission is not required.

#### Author Contributions

A.Basaran developed the methodology, performed the analysis, and improved the study. A. Basaran wrote and proofread the manuscript.

#### Nomenclature

|                   |  |
|-------------------|--|
| $A$               | : Ash content  |
| $C$               | : Combustible matter content                             |
| $E_f$             | : Auxiliary fossil fuel energy                           |
| $E_i$             | : Imported energy  |
| $EIA$             | : Energy Information Administration                      |
| $E_p$             | : Produced energy (electricity or heat)                  |
| $E_w$             | : Energy content of waste                                |
| $E_w$             | : Energy content of MSW                                  |
| $MSW$             | : Municipal Solid Waste                                  |
| $\dot{m}_{waste}$ | : MSW feed rate to incineration facility                 |
| $NCV$             | : Net calorific value                                    |
| $NCV_{awf}$       | : Ash and water independent net heating value            |
| $NCV_i$           | : Net calorific value of the composition $i$             |
| $NCV_o$           | : Overall NCV of the MSW                                 |
| $NCV_{waste}$     | : Net calorific value of the MSW                         |
| $Q_{district}$    | : Heat delivered to district heat                        |
| $Q_{process}$     | : Facility internal process heat networks                |
| $Q_{total}$       | : Produced total heat ( $= Q_{district} + Q_{process}$ ) |
| $TurkStat$        | : Turkish Statistical Institution                        |
| $US$              | : The United States                                      |
| $US\ DOE$         | : The US Department of Energy                            |
| $US\ EPA$         | : The US Environmental Protection Agency                 |
| $WTE$             | : Waste-to-Energy  |
| $W$               | : Water (moisture) content                               |
| $W_{electric}$    | : Produced electricity                                   |
| $x_i$             | : Composition percentage of the composition $i$          |

#### References

1. Boru İpek, A. *Prediction of market-clearing price using neural networks based methods and boosting algorithms.* International Advanced Researches and Engineering

- Journal, 2021. **5**(02): p. 240-246.
2. Bulbul, S., G. Ertugrul, F. Arli, *Investigation of usage potentials of global energy systems*. International Advanced Researches and Engineering Journal, 2018. **2**(01): p. 58-67.
  3. US Energy Information and Administration (US EIA) *Energy from municipal solid waste*. [cited 2021 29 November] Available from: [https://www.eia.gov/energyexplained/index.php?page=biomass\\_waste\\_to\\_energy](https://www.eia.gov/energyexplained/index.php?page=biomass_waste_to_energy).
  4. Abdulvahitoglu, A., İ. Yılmaz, *Projected potential of Landfill gas in Çukurova region*. International Advanced Researches and Engineering Journal, 2018. **2**(02): p. 117-123.
  5. Psomopoulos, C.S., A. Bourka, and N.J. Themelis, *Waste-to-energy: A review of the status and benefits in USA*. Waste Management, 2009. **29**(5): p. 1718-1724.
  6. The U.S. Environmental Protection Agency. *Energy Recovery from Waste 2016*. [cited 2021 29 November] Available from: <https://archive.epa.gov/epawaste/nonhaz/municipal/web/html/index-11.html>.
  7. US Energy Information and Administration (US EIA). *Methodology for Allocating Municipal Solid Waste to Biogenic and Non-Biogenic Energy May 2007 Report*. [cited 2021 29 November] Available from: <https://www.eia.gov/renewable/renewables/msw.pdf>.
  8. Ünal, A., A. Öz, *Using of recycling materials in the construction sector*. International Advanced Researches and Engineering Journal, 2019. **3**(03): p. 137-143.
  9. Branchini, L. *Waste-to-Energy Advanced Cycles and New Design Concepts for Efficient Power Plants*. 2015. Springer International Publishing: Switzerland, doi: 10.1007/978-3-319-13608-0.
  10. Directive 2008/98/EC of the European Parliament and of the Council of 19 November 2008 on waste and repealing certain directives. vol. L312/13. 2008. doi:2008/98/EC.; 32008L0098.
  11. Tan, S.T., W.S. Ho, H. Hashim, C.T. Lee, M.R. Taib, and C.S. Ho, *Energy , economic and environmental (3E) analysis of waste-to-energy (WTE) strategies for municipal solid waste (MSW) management*. Energy Conversation and Management, 2015. **102**: p. 111-120.
  12. Ashworth, D.C., P. Elliott, and M.B. Toledano, *Waste incineration and adverse birth and neonatal outcomes: A systematic review*. Environ Int 2014. **69**: p. 120-132.
  13. Rand, T., J. Haukohl, and U Marxen, *Municipal Solid Waste Incineration: Requirements for a Successful Project*. 2000. The World Bank: Washington, USA.
  14. American Society of Mechanical Engineers (ASME). *Waste-to-Energy: A Renewable Energy Source from Municipal Solid Waste (Executive summary of report)*. [cited 2021 29 November] Available from: <http://energyrecoverycouncil.org/wp-content/uploads/2016/03/ERC-ASME-WTE-White-Paper-08.pdf>.
  15. Gohlke, O. *Efficiency of energy recovery from municipal solid waste and the resultant effect on the greenhouse gas balance*. Waste Managment and Research, 2009. **27**(9): p. 894-906.
  16. Grosso, M., A. Motta, and L. Rigamonti, *Efficiency of energy recovery from waste incineration, in the light of the new Waste Framework Directive*. Waste Management, 2010. **30**(7): p. 1238-1243.
  17. Turkish Statistical Institute. Population Projection, 2013-2075 bulletin, No: 15844, 14 Feb. 2013. [cited 2022 February 14] Available from: <https://data.tuik.gov.tr/Bulten/Index?p=Nufus-Projeksiyonlari-2018-2080-30567#>.
  18. Turkish Statistical Institute. Population Projection, 2018-2080 bulletin, No:30567, 21 Feb. 2018. [cited 2022 February 14] Available from: <https://data.tuik.gov.tr/Bulten/Index?p=Nufus-Projeksiyonlari-2018-2080-30567#>.
  19. Turkish Statistical Institute. Population statistics, Turkey 2022. [cited 2022 July 11] Available from: <https://biruni.tuik.gov.tr/medas/?kn=95&locale=tr>.
  20. Turkish Statistical Institute. Waste statistics, Turkey 2022. [cited 2022 July 11] Available from: <https://biruni.tuik.gov.tr/medas/?kn=119&locale=tr>.
  21. Ibikunle, R.A., A.F. Lukman, I.F. Titiladunayo, and A.R. Haadi, *Modeling energy content of municipal solid waste based on proximate analysis: Rk class estimator approach*. Cogent Engineering, 2022. **9**(1): 2046243.
  22. Cordero, T., F. Marquez, J. Rodriguez-Mirasol, and J.J. Rodriguez, *Predicting heating values of lignocellulosic and carbonaceous materials from proximate analysis*. Fuel, 2001. **11**(11): p. 1567-1571.
  23. Parikh, J., S.A. Channiwala, and G.K. Ghosal, *A correlation for calculating HHV from proximate analysis of solid fuels*. Fuel, 2005. **84**(5): p. 487-494
  24. Özyüğüran, A., Yaman, S. , Küçükbayrak, S. *Prediction of calorific value of biomass based on elemental analysis*. International Advanced Researches and Engineering Journal, 2018. **2**(03): p. 254-260.
  25. Adeleke, O.A., S.A. Akinlabi., T.C. Jen, and I. Dunmade, *Evaluation and Prediction of Energy Content of Municipal Solid Waste: A review*. IOP Conference Series: Materials Science and Engineering, 2021. **1107**(1): 012097.
  26. Janna, H., M.D. Abbas, M.M. Al-Khuzai, and N. Al-Ansari, *Energy Content Estimation of Municipal Solid Waste by Physical Composition in Al-Diwaniyah City, Iraq*. Journal of Ecological Engineering, 2021. **22**(7): p. 11-19.
  27. Komilis, D., K. Kissas, and A. Symeonidis, *Effect of organic matter and moisture on the calorific value of solid wastes: An update of the Tanner diagram*. Waste Management, 2014. **34**(2): p. 249-255.
  28. Tanner, V.R. *Die Entwicklung der Von-Roll-Müllverbrennungsanlagen (The development of the Von-Roll incinerators)* (in German). Schweizerische Bauzeitung, 1965. **83**: p.251-260.
  29. Lombardi, L., E. Carnevale, and A Corti, *A review of technologies and performances of thermal treatment systems for energy recovery from waste*. Waste Management, 2015. **37**: p. 26-44.
  30. Öztürk, İ., A.O. Arıkan, M. Altınbaş, K. Alp, and H. Güven, *Solid Waste Recycling and Treatment Technologies (in Turkish)*. Union of Municipalities of Turkey, 2015. Ankara, Turkey.
  31. TMMOB Chamber of Environmental Engineers. İzmir Environmental Status Report 2021 (in Turkish).
  32. Solheimslid, T., H.K. Harneshaug, and N. Lømmen, *Calculation of first-law and second-law-efficiency of a Norwegian combined heat and power facility driven by municipal waste incineration – A case study*. Energy Conversation and Management, 2015. **95**: p. 149-159.

33. Governorship of İzmir. Statistics of İzmir (in Turkish) [cited 2021 29 November] Available from: <http://www.izmir.gov.tr/istatistiklerle-izmir>.

**Research Article**

# A Mixed-Integer Linear Programming approach for university timetabling problem with the multi-section courses: an application for Hacettepe University

## Department of Business Administration

Akın Özkan <sup>a,\*</sup>  and Aydın Ulucan <sup>b</sup> 

<sup>a</sup>Mus Alparslan University, Faculty of Economics and Administrative Sciences Department of Business Administration, Mus, Turkey

<sup>b</sup>Hacettepe University, Faculty of Economics and Administrative Sciences Department of Business Administration, Ankara, Turkey

## ARTICLE INFO

*Article history:*

Received 18 May 2022

Accepted 04 August 2022

Published 15 August 2022

*Keywords:*

Integer programming

Multi-section courses

Timetabling

University course timetabling

## ABSTRACT

University course timetabling is an NP-Complete problem type which becomes even more difficult due to the specific requirements of each university. In this study, it was aimed to solve a university course timetabling problem by using integer programming and to develop assignment models that can be easily adapted to similar problems. The models that we developed for the solution are based on the integer programming model of Daskalaki et al. [1]. In addition, the models were developed taking into account the fact that there was an availability of multi-section courses, the minimum overlap of elective courses, and the ability to divide courses into sessions in terms of effective use of the capacity. In this framework, two different models (model 1 and model 2) were developed. Whereas model 1 assumes that all courses are processed as a single session (If a course has 3 time periods per week, then it is taught as a single session), model 2 assumes courses can be assigned by divided into multiple sessions (If a course has 3 time periods per week, then it can be divided into 1+1+1 or 2+1 sessions.). In model 2, a structure in which the model itself could determine how to split the courses in the framework of predetermined options was developed. Both models were formulated in such a way as to maximize the satisfaction of the lecturers. Finally, a larger scale problem was derived from the first problem and the performance of these two models were compared for both problems. The results showed that the optimal solution was obtained within the specified constraints, and the solution time significantly increased with an increase in the size of the problem.

**1. Introduction**

Many timetabling problems such as nurse rostering, sports timetabling, transportation planning, university course schedules planning and university exam schedules planning have been the subject of operations research for more than 40 years [2]. The timetabling problem which is the most difficult to solve belongs to the problem class called NP-Complete. It is difficult to solve such problems optimally and efficiently. The course scheduling problem also falls under the class of NP-Complete problem due to the rapid increase in the number of decision variables and the rapid growth of the solution space [3-5]. What makes it difficult to solve the problem is that the solution time dramatically increases as the problem size grows [1]. The increase in solution time also depends on the structure of the course timetabling problem because this problem

varies depending on each institution that has its own specific requirements. The fact that courses can be mandatory, elective, or in multi-section status can be shown as an example of these requirements. To accomplish most of the wishes and requirements of the instructors and students is also an important and difficult task. In the literature, there are many studies in which different methods have been used and different models have been developed for the timetabling problem by taking into account these and similar reasons.

Educational timetabling problems are usually divided into two main categories: high school timetabling problems and university timetabling problems. These problems in themselves are also divided into two categories: course timetabling and exam timetabling [6, 7]. The university examination timetabling problem can be defined as assigning courses to a specific number of

\* Corresponding author. Tel.: +90-436-249-4949.

E-mail addresses: [a.ozkan@alparslan.edu.tr](mailto:a.ozkan@alparslan.edu.tr) (A. Özkan), [aulucan@hacettepe.edu.tr](mailto:aulucan@hacettepe.edu.tr) (A. Ulucan)

ORCID: 0000-0003-2862-2496 (A. Özkan), 0000-0002-0439-2211 (A. Ulucan)

DOI: [10.35860/iarej.1118213](https://doi.org/10.35860/iarej.1118213)

© 2022, The Author(s). This article is licensed under the CC BY-NC 4.0 International License (<https://creativecommons.org/licenses/by-nc/4.0/>).

classrooms suitable for the requirement of each course and usually to specific time periods for five days a week or for ten days two weeks. The focus of this study is university course timetabling problems. The university course timetabling problem can be defined as assigning a course to specific time periods only for five days a week and to specific classrooms suitable for student capacity and the requirement of the course. In both problem types mentioned above, for those called “hard constraints”, there should never be an overlap; and for the remaining constraints called “soft constraints”, the aim should be to minimize the number of overlaps. It is seen that the constraints are divided into two groups as hard and soft constraints in many of the timetabling studies [6-10]. Hard constraints must be fulfilled fully so that the generated solution would be a feasible solution and there would be no overlap. The possibility of assigning a lecturer or student to maximum one course in the same time slot can be shown as an example of such constraints. Soft constraints are not indispensable but desirable constraints for increasing the quality of a timetabling. In practice, it is impossible to fully satisfy all soft constraints. For this reason, in most timetabling studies, these constraints are included in the objective function of mathematical programming models. For example, in this paper, the level of satisfaction of lecturers is optimized in the objective function.

Since the university course timetabling problem differs depending on the structure of each institution, there is no specific problem structure. When looking at past studies, it seems that different models and different solution methods have been used to solve this problem both because of unspecific problem structure and because of NP-Complete problem structure. As Babaei et al. [9] and Feizi-Derakhshi et al. [11] mentioned in their studies, these methods and approaches which solved the timetabling problem can be classified under four categories. The first category includes techniques based on Operations Research. Graph Coloring [3, 12, 13], Linear Programming (LP)/ Integer Linear Programming (IP) [1, 14-18], Goal Programming [19], and Constraint Satisfaction Programming [4, 20, 21] can be given as examples of these techniques. The second category includes approaches based on the metaheuristic strategies. As examples of these, many heuristic approaches including primarily the tabu search [22-24] and genetic algorithm [25, 26] methods can be shown. The third category includes methods based on Multi-criteria and multi-purpose approaches. The final category of these approaches includes Modern Intelligence Novel Methods. Fuzzy theory [27, 28], hybrid [29-31] and artificial intelligence-based approaches can be shown as examples of this category.

In our study, primarily, it was aimed to solve a university course timetabling problem by using integer programming and to create assignment models that can

easily be adapted to many universities that have similar structures. In this framework, two models were developed. These models that we developed for the solution are based on the integer programming model of Daskalaki et al. [1]. In addition, the models were developed taking into account the availability of multi-section courses, the minimum overlap of elective courses, and the ability to split courses in terms of effective use of the capacity. Model 1 solves the timetabling problem by meeting all the requirements of the course program of Hacettepe University Business Administration (HUBA). Since all courses in HUBA are given as a single session in the morning or afternoon, it is assumed in model 1 that all courses are presented as only a single session. Unlike Model 1, Model 2 contains the assumption that course hours can be assigned by dividing instead of the single session.

The contributions of this study are: (1) The fact that the courses can become mandatory, elective, and in multi-section status was taken into account in the both models; (2) In the Model 2, a structure in which the model itself can determine how to split the courses in the framework of predetermined options (e.g., assigning a 3-hour course as  $2 + 1$  or as a single session) was developed. Also, in this paper, a larger scale problem (problem 2) was derived from the HUBA problem (problem 1) and then the performances of both models were compared. This last analysis is important in that it shows how dramatically the solution time for the NP-Complete problem class changes. Both models have an objective function. These objective functions maximize the satisfaction of the teaching staff and minimize the overlap of elective courses.

## 2. Structure of University Course Timetabling Problem Section

University course problems differ depending on the structure of each institution, its possibilities, and its own specific requirements. For this reason, although the basic structure of the models developed to solve the university course problem is generally similar, the specific requirements render the models more complex and different.

The structure of the university course timetabling mainly consists of day, time period, student group, lecturer, course, and classroom dimensions. We can explain these dimensions through the example of HUBA modeled in our study as follows:

The time period refers to a one-hour interval, and there are eight time periods per day between 09:00 am and 17.45 pm, from Monday to Friday.

The student groups are the student cluster taking common courses. Therefore, in HUBA, which has a four-year training program, every training year refers to a student group. The courses in the curriculum are taught by lecturers who are experts in their field. In HUBA, which course will be taught by which lecturer is determined in advance by the decisions

of the board of directors.

The courses in the curriculum are divided into mandatory and elective. Mandatory courses are courses that students must take in order to graduate from a program. In terms of elective courses, students have the option of taking or not taking these courses according to their interests or claim. However, they have to take a certain number of these courses to complete the total amount of credit required for graduation. In HUBA, all courses in the first two years are in the mandatory course category, and most of the courses in the last two years are in the elective course category. Because of the lack of staff and physical space in the HUBA, the course timetabling problem should be resolved in such a way that the overlap of the elective courses given to student groups is minimized. In addition, due to the same reasons, some mandatory courses are divided into sections. For this reason, the course timetabling problem should be modeled in such a way that the students can take any section of the mandatory course according to their own program.

All courses in HUBA are processed as a single session in a way that they will be three hours per week. The courses that require special equipment are taught in the laboratory, and the others are taught in normal classrooms. Some courses outside the department are taught by the faculty. For this reason, the department's courses should not be assigned to the classrooms and time periods in which these courses are held.

### 3. Modeling the University Course Timetabling Problem

Two different models are developed for solving the course timetabling problem. While Model 1 completely meets HUBA's requirements, Model 2 meets the need for programs that the courses can be divided into parts according to the time period. The notation used in these models is mostly similar to the notation used in the study of Daskalaki et al. [1]. The sets, decision variables, and parameters used in both models respectively defined below:

#### 3.1 Sets

- The set of days that are appropriate for assigning in a week is indicated by the letter  $I$ , e.g.  $I = \{1,2,3,4,5\}$ .
- The set of the time periods that are appropriate for assigning in a day is indicated by the letter  $J$ . The time period usually refers to a time of one-hour, which is received 45-minutes lesson and 15-minutes break. For this reason, in Model 2, the set of the time period in a day that starts at 09:00 and ends at 17.45 is as follows:  $J = \{1,2,3,4,5,6,7,8\}$ . In Model 1, on the other hand, as all courses in HUBA are given as a single session in the morning or after lunch, the set of the time period (a time period is three hours) in a day is as follows:  $J = \{1,2\}$ .

- The set of the student groups is indicated by the letter  $K$ , e.g.  $K = \{1,2,3,4\}$ .
- The set of the lecturers is indicated by letter  $L$ , e.g.  $L = \{Lec\#1, lec\#2, \dots, Lec\#L\}$ .
- The set of the courses is indicated by letter  $M$ , e.g.  $M = \{course\#1, course\#2, \dots, course\#M\}$ .
- The set of the classrooms is indicated by the letter  $N$ , e.g.  $N = \{class\#1, class\#2, \dots, class\#N\}$ .

#### 3.2 Decision Variables

In this study, two decision variables were included in both models. The first (i.e., basic) decision variable which is adopted as the set of binary variables is denoted as follows:

$$x_{i,j,k,l,m,n} = \begin{cases} 1, & \text{when course } m \text{ taught by lecturer } l \text{ to the student} \\ & \text{group } k \text{ is assigned for the } j\text{th time period of day} \\ & i \text{ in classroom } n. \text{ where } i \in I, j \in J, k \in K, l \in L, \\ & m \in M, n \in N \\ 0, & \text{otherwise} \end{cases}$$

The second (i.e., auxiliary) decision variable which is adopted as the set of integer variables is denoted as follows:

$$y_{i,j,k} = \begin{cases} Z^+, & \text{when the number of conflicts in the } j\text{th} \\ & \text{time period of day } i \text{ of student group } k \text{ is.} \\ & \text{where } i \in I, j \in J, k \in K \\ 0, & \text{when there is no conflict.} \end{cases}$$

#### 3.3 Parameters

The parameter sets are defined in the form of subsets according to the basic indices  $I, J, K, L, M$ , and  $N$ . Thus, the number of variables is further reduced and modeling of constraints becomes much easier. These parameters are the followings:

$K^1 = \{k \in K : k = \text{the student groups of lower-grade years, usually from the first two years in a four-year department.}\}$

$K^2 = \{k \in K : k = \text{the student groups of higher-grade years, usually from the last two years in a four-year department, and there are also elective courses in this period.}\}$

$K_l = \{k \in K, \text{ the set of the student group taught by lecturer } l. \}$

$L_i = \{l \in L, \text{ the set of the lecturer available on day } i. \}$

$L_k = \{l \in L, \text{ the set of the lecturer who teaches the student group } k. \}$

$L_{ki} = L_k \cap L_i$

$M_k = \{ m \in M, \text{ the set of the course designed for the student group } k. \}$ .

$M_k^C = \{ \text{ the set of mandatory course designed for the student group } k, k \in K^2. \}$ .

$M_n = \{ m \in M, \text{ the set of the course taught in the classroom } n. \}$ .

$M_{kl} = M_k \cap M_l, M_{kln} = M_k \cap M_l \cap M_n$

$M_k^{Sec} = \{ m \in M, \text{ the set of the multi-section course designed for the student group } k. \}$ .

$M_{ks}^{Sec} = \{ m \in M, (k, s) \in K \times S, k \text{ the set of the } s^{\text{th}} \text{ section of the multi-section course designed for the student group } k. \text{ The set of } S \text{ shows the total number of sections in one multi-section course, } s \in \{1, 2, \dots, Sec\#S\}. \}$

$N_{mk} = \{ n \in N, \text{ the set of the classroom that fits student group } k \text{ for the course } m \}$ .

$I_n = \{ i \in I, \text{ the set of the day on which classroom } n \text{ is suitable for use} \}$ .

$I_l = \{ i \in I, \text{ the set of the day on which lecturer } l \text{ is suitable for lecture} \}$ .

$I_{ln} = I_l \cap I_n$

$J_{in} = \{ j \in J, \text{ the set of the time period of the day } i \text{ on which classroom } n \text{ is suitable for use} \}$ .

$J_{itn} = \{ j \in J, \text{ the set of the time period of the day } i \text{ on which lecturer } l \text{ and classroom } n \text{ are suitable for assigning} \}$ .

$PRA = \{ (i, j, k, l, m, n) \in I \times J \times K \times L \times M \times N, PRA, \text{ course } m \text{ taught by lecturer } l \text{ to student group } k \text{ is pre-assigned for } j^{\text{th}} \text{ time period of day } i \text{ in classroom } n, \text{ that is, } x_{i,j,k,l,m,n} = 1. \}$

$C_{i,j,m} = \{ \text{ cost coefficient of course } m \text{ for } j^{\text{th}} \text{ time period of day } i, i \in I, j \in J, m \in M \}$

$a_k^1 = \text{ total number of courses for student group } k \text{ (only Model 1)}.$

$a_k^2 = \text{ total number of time periods for student group } k \text{ (only Model 2)}.$

$b_m = \text{ total length of course } m \text{ (only Model 2)}$

$hm = \text{ total number of time periods for course } m \text{ (only Model 2)}$

### 3.3 Model 1 (with single session)

Model 1 is modelled to meet all the requirements of course timetabling of HUBA. The constraints of this model are as follows:

$$\forall i \in I, \quad \forall j \in J, \quad \forall l \in L_i \quad (1)$$

$$\sum_{k \in K} \sum_{l \in L_{ki}} \sum_{m \in M_{kl}} \sum_{n \in N_{mk}} x_{i,j,k,l,m,n} \leq 1,$$

$$\begin{aligned} \forall k \in K^1, \quad \forall i \in I, \quad \forall j \in J, \quad \forall s \in S \\ \sum_{l \in L_{ki}} \sum_{m \in M_{kl} - M_k^{Sec}} \sum_{n \in N_{mk}} x_{i,j,k,l,m,n} \\ + \sum_{l \in L_{ki}} \sum_{m \in M_{ks}^{Sec}} \sum_{n \in N_{mk}} x_{i,j,k,l,m,n} \leq 1 \end{aligned} \quad (2)$$

$$\begin{aligned} \forall k \in K^2, \quad \forall i \in I, \quad \forall j \in J, \quad \forall s \in S \\ \sum_{l \in L_{ki}} \sum_{m \in M_{kl} - M_k^{Sec}} \sum_{n \in N_{mk}} x_{i,j,k,l,m,n} \\ + \sum_{l \in L_{ki}} \sum_{m \in M_{ks}^{Sec}} \sum_{n \in N_{mk}} x_{i,j,k,l,m,n} \leq 1 + y_{i,j,k} \end{aligned} \quad (3)$$

$$\begin{aligned} \forall k \in K^2, \quad \forall i \in I, \quad \forall j \in J, \quad \forall s \in S \\ \sum_{l \in L_{ki}} \sum_{m \in M_{kl}^C - M_k^{Sec}} \sum_{n \in N_{mk}} x_{i,j,k,l,m,n} \\ + \sum_{l \in L_{ki}} \sum_{m \in M_{ks}^{Sec}} \sum_{n \in N_{mk}} x_{i,j,k,l,m,n} \leq 1 \end{aligned} \quad (4)$$

$$\begin{aligned} \forall n \in N, \quad \forall i \in I_n, \quad \forall j \in J_{in} \\ \sum_{k \in K} \sum_{l \in L_{ki}} \sum_{m \in M_{kln}} x_{i,j,k,l,m,n} \leq 1, \end{aligned} \quad (5)$$

$$\begin{aligned} \forall k \in K \\ \sum_{l \in L_k} \sum_{m \in M_{kl}} \sum_{n \in N_{mk}} \sum_{i \in I_{ln}} \sum_{j \in J_{itn}} x_{i,j,k,l,m,n} = a_k^1, \end{aligned} \quad (6)$$

$$\begin{aligned} \forall k \in K, \forall l \in L_l, \forall m \in M_{kl} \\ \sum_{n \in N_{mk}} \sum_{i \in I_{ln}} \sum_{j \in J_{itn}} x_{i,j,k,l,m,n} = 1 \end{aligned} \quad (7)$$

$$\begin{aligned} \forall (i, j, k, l, m, n) \in PRA \\ x_{i,j,k,l,m,n} = 1 \end{aligned} \quad (8)$$

Equation (1) ensures that every lecturer can be assigned at most one student group, one classroom, and one course in every time period of the week. Equation (2) ensures that every student group can be assigned at most one course, one lecturer, and one classroom in every time period of the week. However, this constraint provides that only mandatory courses of students in the same lower-grade student groups do not overlap. In addition, this constraint allows the sections of the multi-section mandatory courses to overlap in accordance with the structure of this problem. Equation (3) and Equation (4) are designed for higher-grade student groups that have mostly elective courses. Equation (3) is a soft constraint that allows the least overlap of elective courses of higher-level student groups. For this reason, it is used for the decision variable “y” that indicates the number

of overlapping elective courses in this constraint. At least the conflict is ensured by minimizing this decision variable in the objective function. Equation (4) is almost the same as Equation (2). The only difference, Equation (4) ensures that mandatory courses of students in the same higher-grade student groups do not overlap. Equation (5) ensures that every classroom in every time period of the week can be assigned at most one student group, one lecturer, and one course. Equation (6) is to ensure that all courses of every student group take place in the course timetabling. Equation (7) is to ensure that every course takes place only once in the course timetabling. Equation (8) ensures that course  $m$  taught by lecturer  $l$  to student group  $k$  is pre-assigned for  $j^{\text{th}}$  time period of day  $i$  in classroom  $n$ .

### 3.5 Objective Function

In general, the main purpose of the course timetabling is to assign the course appropriately under certain constraints. These assignments can be done with constraints (*i.e.*, with constraint satisfaction programming) without objective function, or different objective functions can be used depending on the structure of the problem. For example, Daskalaki et al. [1] used a model that minimizes the objective function by determining one cost coefficient for each course according to every time period of every day in a week. Thus, in this way, courses were able to be assigned to the desired time period and day. Similarly, the purpose of Bakir and Aksop [32]'s study was to minimize the objective function in terms of student and lecturer satisfaction.

$$\text{Min } Z = \sum_{i \in I} \sum_{j \in J} \sum_{k \in K} y_{i,j,k} + \sum_{i \in I} \sum_{j \in J} \sum_{m \in M} C_{i,j,m} * \left( \sum_{k \in K} \sum_{l \in L_k} \sum_{n \in N_{mk}} x_{i,j,k,l,m,n} \right) \tag{9}$$

The objective function of this study consists of two parts. In the first part, the overlap of elective courses is minimized. For this, we use the decision variable  $y_{i,j,k}$ ,  $i \in I$ ,  $j \in J$ ,  $k \in K$ , which minimizes the number of overlaps of elective courses of student groups  $k$  for  $j^{\text{th}}$  time period of day  $i$ . In the second part, the satisfaction level of the lecturer is maximized. For this, we use the cost coefficient  $C_{i,j,m}$ ,  $i \in I$ ,  $j \in J$ ,  $m \in M$ , which is formed by giving the minimum value for the most desired time period of day, and the maximum value for the minimum desired time period of day. In these models, these cost coefficients are determined using values between 1 and 5. In addition, these two parts can be multiplied by constant coefficients of appropriate magnitude to form a priority order in the objective function.

### 3.6 Model 2 (with multi-session)

In Model 1, all courses in HUBA can be assigned to only one of two different time periods (morning and afternoon)

due to the fact that they are held once a week. For this reason, each course entered as a parameter into the model is considered as a time period in Model 1; thus, there is no need for additional constraints that ensure a course to have consecutive time periods in the day. The opposite is true in Model 2 because the course hours can be assigned in this model by dividing instead of the single session. As a result, additional constraints are needed to ensure that the courses have consecutive time periods throughout the day. Also, a new decision variable  $w_{i,k,h,m,n}$   $i \in I$ ,  $k \in K$ ,  $h \in H_m$ ,  $m \in M$ ,  $n \in N$  is used in model 2. This decision variable ensures that the model itself can determine how to partition the courses in the framework of predetermined options (*e.g.*, to assign a 3-hour course as 2 + 1 or as a single session). The fact that the partitioning is left to the model itself is important in terms of solution quality. A different approach can be seen in Daskalaki et al. [1]. In their study, how the courses would be divided was entered as a parameter into the model.

The decision variable that indicates which part of any course will be given on any day is as follows:

$$w_{i,k,h,m,n} = \begin{cases} 1, & \text{when the } h\text{th section of course } m \\ & \text{given to the student group } k \text{ is} \\ & \text{assigned on day } i \text{ in classroom } n. \\ & \text{where } i \in I, k \in K, h \in H_m, m \in M, \\ & \quad \quad \quad n \in N \\ 0, & \text{otherwise} \end{cases}$$

where  $h$  refers to the number of time periods of part or a whole of a course. For example, if  $h \in H_m = \{1,2\}$  for a 2-hour course  $m$ , this course can be assigned as 1+1 or a single session. Similarly, if  $h \in H_m = \{1,2,3\}$  for a 3-hour course  $m$ , this course can be assigned as 1+1+1, 2+1 or a single session.

The above constraints (1), (2), (3), (4), (5), and (8) were taken in the same way and included in Model 2. In addition, the objective function can also be used in Model 2. The other constraints of Model 2 are as follows:

$$\forall k \in K \sum_{l \in L_k} \sum_{m \in M_{kl}} \sum_{n \in N_{mk}} \sum_{i \in I_{ln}} \sum_{j \in J_{itn}} x_{i,j,k,l,m,n} = a_k^2, \tag{10}$$

$$\forall k \in K, \forall l \in L_l, \forall m \in M_{kl} \sum_{n \in N_{mk}} \sum_{i \in I_{ln}} \sum_{j \in J_{itn}} x_{i,j,k,l,m,n} = b_m \tag{11}$$

$$\forall i \in I, \quad \forall k \in K, \quad \forall l \in L_{ki}, \quad \forall m \in M_{kl}, \quad \forall n \in N_{mk} \sum_{j \in J_{itn}} x_{i,j,k,l,m,n} - \sum_{h \in H_m} (w_{i,k,h,m,n} * h) = 0 \tag{12}$$

$$\forall k \in K, \quad \forall m \in M_k, \quad \forall h \in H_m - hm \sum_{i \in I} \sum_{n \in N_{mk}} (w_{i,k,h,m,n} + w_{i,k,hm,m,n}) = 1 \tag{13}$$



$$\forall k \in K, \quad \forall m \in M_k, \quad \forall i \in I$$

$$\sum_{h \in H_m - hm} \sum_{n \in N_{mk}} w_{i,k,h,m,n} \leq 1 \quad (14)$$

$$\forall i \in I, \forall k \in K, \forall l \in L_{ki}, \forall m \in M_{kl}, \forall n \in N_{mk}, \forall h \in H_m \wedge h > 1, \forall t \in \{1, \dots, h-1\}, \quad (15)$$

$$x_{i,1,k,l,m,n} - x_{i,t+1,k,l,m,n} \leq (1 - w_{i,k,h,m,n})$$

$$\forall i \in I, \forall k \in K, \forall l \in L_{ki}, \forall m \in M_{kl}, \forall n \in N_{mk}, \forall h \in H_m \wedge h > 1, \forall t \in \{1, \dots, h-1\}, \quad (16)$$

$$x_{i,8,k,l,m,n} - x_{i,8-t,k,l,m,n} \leq (1 - w_{i,k,h,m,n})$$

$$\forall i \in I, \forall k \in K, \forall l \in L_{ki}, \forall m \in M_{kl}, \forall n \in N_{mk}, \forall h \in H_m \wedge h > 1, \forall j \in J, \forall t \in \{2, \dots, h-1\} \wedge j+t \leq 8, \quad (17)$$

$$-x_{i,j,k,l,m,n} + x_{i,j+1,k,l,m,n} - x_{i,j+t,k,l,m,n} \leq (1 - w_{i,k,h,m,n})$$

Equation (10) ensures that the number of all courses of every student group  $k$  in the model is equal to the total number of their time periods. Equation (11) ensures that the number of course  $m$  in the course timetabling is equal to the number of its time periods. Equation (12) ensures that the number of course  $m$  on day  $i$  is equal to  $h$ ,  $h \in H_m$ . Equation (13) ensures that all time periods for every course during a week are in the course timetabling.  $hm$  in these constraints represents the total number of time periods for course  $m$ . If the value of the decision variable is  $w_{i,k,h,m,n}$  is 1, it means that the relevant course is assigned as a single session. If the course  $m$  is not a single session, Equation (14) ensures each part of the course  $m$  to be assigned to a different day. For example, if a 3-hour course is divided into 2 and 1 (i.e., 2+1), 2-hours part and 1-hour part must be assigned to different days. Eqs. (15, 16, 17) ensure that time periods follow each other if the course is assigned to more than one-time period on a day. Equation (15) ensures a consecutive sequence when a course is assigned to the first time period of the day. Equation (16) ensures a consecutive sequence when a course is assigned to the last time period of the day. Finally, Equation (16) ensures a consecutive sequence when a course is assigned to the other time periods of the day.

#### 4. Optimal Solution of Course Timetabling Problem

Model 1 and Model 2 developed in the scope of the study were applied to data of Hacettepe University Department of Business Administration (HUBA).

In the fall semester curriculum of HUBA, 33 courses are offered in total. All of these courses are given as a 3-hour single session. For this reason, the total number of time periods are taken as 33. However, the total number of time periods is 99 because the time period is considered as 1-hour in Model 2.

In Table 1, the total number of courses in HUBA is given taking into account the mandatory and elective course categories. For these courses, there is available seven regular classrooms and one specialized classroom (lab). Also, these courses are assigned to 23 lecturers.

The problem of HUBA (problem 1) and a larger scale problem (problem 2) were modeled with the Python programming language and solved using solver Gurobi6.2.5-64bit. The solution found is a proposed timetable for both problems.

Table 1. Number of mandatory/elective courses offered for each student groups

| Courses   | Student groups |        |       |        | Total |
|-----------|----------------|--------|-------|--------|-------|
|           | First          | Second | Third | Fourth |       |
| Mandatory | 5              | 7      | 2     | 2      | 14    |
| Elective  | 0              | 0      | 9     | 8      | 19    |
| Total     | 5              | 7      | 11    | 10     | 33    |

The students of HUBA have 14 mandatory and 19 elective courses for the fall semester. These courses were planned as follows: 5 mandatory courses for the first year, 7 mandatory courses for the second year, 2 mandatory and 9 elective courses for the third year, and 2 mandatory and 8 elective courses for the fourth year. In Table 2, the solution of problem 1 in Model 1 is shown using the code numbers of the courses and classrooms. Looking at this table, it seems that there is no overlap among all mandatory courses, but there is a few overlaps among elective and multi-section mandatory courses in accordance with the structure of the problem. Also, it appears that all the courses required by the curriculum exist in the course timetabling and are assigned to suitable classrooms without overlap.

In Model 2, as mentioned above, one day is divided into eight time periods to be between 09: 00 am and 17: 45 pm. Thus, the courses can be assigned by splitting according to the hours of the course. In these problems, since all courses are 3-hour courses, these courses can be split in the framework of predetermined options (e.g., a 3-hour course can be assigned as 2 + 1 or as a single session). The solution of problem 1 obtained using model 2 is shown in Table 3. Similarly, as also shown in this table, firstly, there appears no overlap among all mandatory courses. Secondly, there seem to be a few overlaps among elective and multi-section mandatory courses. Thirdly, it appears that all the courses required by the curriculum exist in the course timetabling and are assigned to suitable classrooms without overlap. Finally, it is seen that the time periods of the course assigned to more than one time period on a day are in a consecutive sequence, and this course is assigned to the same classroom.

Table 2. Course timetabling for the fall semester – Model 1

|                 |           | Time periods |                |                 |             | Time Periods  |           |
|-----------------|-----------|--------------|----------------|-----------------|-------------|---------------|-----------|
| Group           | Days      | Morning      | Afternoon      | Group           | Days        | Morning       | Afternoon |
| Student group 1 | Monday    | M101-01, D5  |                | Student group 3 | Monday      | M311, D6      | M317, D5  |
|                 |           | M101-02, D4  |                |                 |             |               |           |
|                 | Tuesday   |              |                |                 | Tuesday     | M301-01, A1   | M321, D 5 |
|                 |           |              |                |                 |             | M301-02, D4   |           |
|                 | Wednesday |              | M107, D6       |                 | Wednesday   | M313, D4      | M305, D3  |
|                 | Thursday  | M105, D5     |                |                 | Thursday    | M303, D3      | M319, D7  |
| Friday          |           | M103, D4     | Friday         | M307, LAB-C     | M309, D5    |               |           |
| Student group 2 | Monday    | M203, D3     | M205-02, LAB-C | Student group 4 | Monday      | M403, A1      | M409, D8  |
|                 | Tuesday   |              |                |                 | Tuesday     | M425, D7      | M417, D7  |
|                 | Wednesday | M201, D3     |                |                 | Wednesday   | MAN401-01, D6 | M407, D7  |
|                 | Thursday  | M209, A1     | M205-02, LAB-C |                 | Thursday    | M415, D7      | M405, D3  |
|                 |           |              | M207-01, D4    |                 |             |               |           |
| Friday          |           | M207-02, D6  | Friday         | MAN419, D7      | M401-02, D7 |               |           |

The code numbers indicate which course belongs to which student group and which department, and the digit after "-" indicates the section of the course. The dark grey cells represent mandatory courses, while the light grey cells represent elective courses.

**5. The Performance of the Model 1 and Model 2**

The solution of the course timetabling problem becomes increasingly difficult due to the special needs of each educational institution, increasing the number of courses, lecturers, and classrooms. Depending on the size of the problem, the solution of the models developed for the solution of the timetabling problems sometimes takes a very long time and sometimes the solution becomes impossible. For this reason, the solution performance of the models developed for the university course timetabling problem in terms of problem 1 and problem 2 are compared in Table 4. For these problems of different sizes, the number of courses varied from 33 to 66, the number of lecturers from 23 to 46, and the number of time periods from 33 to 198. When both problems are solved by Model 1, the solution times are 1.6 and 32.7 seconds. On the other hand, when both problems are solved by Model 2, the solution times are 13.1 and 163.5 seconds.

The solution times are also significantly affected by both the number of binary variables and the number of constraints. Therefore, within the scope of problem 1 and problem 2, some significant results of both models are shown in Table 5. For problems 1 and 2, Model 1 contained 283-686 equations, 2150-4280 integer variables, and 2130-4260 binary variables, respectively, while the non-zero values varied from 9450 to 17440. On the other hand, Model 2 contained 27144-77648 equations, 11795-70770 integer variables, and 11715-70290 binary variables, respectively, while the non-zero values varied from 152930 to 930360.

**6. Conclusions**

In this study, firstly, using integer programming, the course timetabling problem of the Hacettepe University Business Administration Department was solved optimally considering the level of satisfaction of the lecturers. Secondly, this problem was also solved under the assumption that the courses can be assigned by splitting. Two models were developed to reach these solutions by taking into account that the courses can be mandatory, elective, and multi-section status. Also, these models allow a minimum overlap of the elective and multi-mandatory courses provided that students should have the chance to choose at least one of the multi-section mandatory courses. Within the scope of these models, new constraints were developed to ensure that at least one of the multi-section mandatory courses can be chosen and that the courses can be split by the model itself in the framework of predetermined options. These new constraints that we developed extend the research in this area of timetabling, and they provide that these models can be easily adapted to the problems in similar structures.

The solution of the university course timetabling problem, which is about assigning the courses in the curriculum in the way that there is no problem in terms of student groups and lecturers, becomes more difficult as the size and special requirements of the problem increase. The results obtained in this study support this situation. Looking at the solution tables, it can be seen that the optimal solutions are obtained within the specified constraints and that the solution times significantly increase depending on the problem size.

Table 3. Course timetabling for the fall semester – Model 2

| Group           | Days       | Time periods |            |               |            |              |            |            |         |
|-----------------|------------|--------------|------------|---------------|------------|--------------|------------|------------|---------|
|                 |            | PER1         | PER2       | PER3          | PER4       | PER5         | PER6       | PER7       | PER8    |
| Student group 1 | Monday     | M101-01,D8   |            | M105,D4       |            |              |            |            | M107,D6 |
|                 |            | M101-02,A1   |            |               |            |              |            |            |         |
|                 | Monday     |              |            | M103,A1       |            |              |            | M107,D3    |         |
|                 | Wednesday  | M105,D8      |            |               |            |              |            |            |         |
|                 | Thursday   |              |            |               | M103,D3    |              |            |            |         |
| Friday          | M101-02,A1 |              |            |               |            | M101-01,D5   |            |            |         |
| Student group 2 | Monday     |              |            | M205-01,LAB-C |            |              | M207-01,D3 |            |         |
|                 | Tuesday    |              |            | M209,D6       |            |              | M207-02,D5 |            |         |
|                 | Wednesday  |              |            |               | M209,D7    | M207-01,D4   |            |            |         |
|                 | Thursday   |              |            | M205-01,LAB-C |            | M207-02,D8   |            | M201,D6    |         |
|                 | Friday     |              | M203,D4    |               |            | M205-02,LABC |            |            | M201,D7 |
| Student group 3 | Monday     |              |            |               |            |              | M311,D6    |            |         |
|                 | Tuesday    | M309,D4      |            | M303,D3       | M307,LAB-C |              | M319,D6    |            | M321,D5 |
|                 | Wednesday  | M301-01,A1   |            | M311,D8       | M313,D6    | M317,D6      |            | M321,D5    |         |
|                 |            | M301-02,D5   |            |               |            |              |            |            |         |
|                 | Thursday   |              | M301-01,D7 | M313,D7       |            | M305,D4      |            | M301-02,D3 |         |
| Friday          | M305,D4    | M319,D6      | M303,D3    |               | M317,D6    | M309,D8      |            | M307,LAB-C |         |
| Student group 4 | Monday     | M403,D3      |            |               |            | M401-02,A1   |            | M417,D3    |         |
|                 |            |              |            |               |            | M401-01,D4   |            |            |         |
|                 | Tuesday    | M405,D3      |            | M407,D8       | M425,D3    |              | M415,D8    |            |         |
|                 | Wednesday  |              | M419,D4    |               | M405,A1    | M409,D5      | M417,D7    | M407,D6    |         |
|                 | Thursday   |              | M419,D3    | M403,D8       |            | M401-01,D3   |            |            |         |
| Friday          |            |              |            |               | M401-02,D7 |              |            |            |         |
|                 |            |              |            | M409,A1       |            |              |            | M425,D5    |         |

The code numbers indicate which course belongs to which student group and which department, and the digit after "-" indicates the section of the course. The dark grey cells represent mandatory courses, while the light grey cells represent elective courses.

Table 4. The solution times

|           | Problem sizes  |         |           |                 |                              | Solution times   |                  |
|-----------|----------------|---------|-----------|-----------------|------------------------------|------------------|------------------|
|           | Student groups | Courses | Lecturers | Classrooms/Labs | Time Periods For of M 1/ M 2 | Model 1 (Second) | Model 2 (Second) |
| Problem 1 | 4              | 33      | 23        | 8/1             | 33/99                        | 1,6              | 13,1             |
| Problem 2 | 8              | 66      | 46        | 16/2            | 66/198                       | 32,7             | 163,5            |

M 1: Model 1, M 2: Model 2.

Table 5. The solution sizes

|           | Model 1     |                            |                  | Model 2     |                              |                  |
|-----------|-------------|----------------------------|------------------|-------------|------------------------------|------------------|
|           | No. of rows | No. of columns             | No. of non-zeros | No. of rows | No. of columns               | No. of non-zeros |
| Problem 1 | 283         | 2150 integer (2130 binary) | 9450             | 27144       | 11795 integer (11715 binary) | 152930           |
| Problem 2 | 686         | 4280 integer (4260 binary) | 17440            | 77648       | 70770 integer (70290 binary) | 930360           |

## Declaration

The authors declared no potential conflicts of interest with respect to the research, authorship, and/or publication of this article. The authors also declared that this article is original, was prepared in accordance with international publication and research ethics, and ethical committee permission or any special permission is not required.

## Author Contributions

A. Özkan developed the methodology, analyzed and wrote the manuscript. A. Ulucan supervised, improved and proofread the study. This study was derived from the PhD thesis of A. Özkan.

## References



- Daskalaki, S., T. Birbas, and E. Housos, *An integer programming formulation for a case study in university timetabling*. European Journal of Operational Research, 2004. **153**(1): p. 117-135.
- Burke, E.K., et al., *A graph-based hyper-heuristic for educational timetabling problems*. European Journal of Operational Research, 2007. **176**(1): p. 177-192.
- D. de Werra, D., *The combinatorics of timetabling*. European Journal of Operational Research, 1997. **96**(3): p. 504-513.
- Deris, S., S. Omatu, and H. Ohta, *Timetable planning using the constraint-based reasoning*. Computers & Operations Research, 2000. **27**(9): p. 819-840.
- Parker, R.G. and R.L. Rardin, *Discrete optimization*. 2014: Elsevier.
- Burke, E.K. and S. Petrovic, *Recent research directions in automated timetabling*. European Journal of Operational Research, 2002. **140**(2): p. 266-280.
- MirHassani, S. and F. Habibi, *Solution approaches to the course timetabling problem*. Artificial Intelligence Review, 2013. **39**(2): p. 133-149.
- Vermuyten, H., et al., *Developing compact course timetables with optimized student flows*. European Journal of Operational Research, 2016. **251**(2): p. 651-661.
- Babaei, H., J. Karimpour, and A. Hadidi, *A survey of approaches for university course timetabling problem*. Computers & Industrial Engineering, 2015. **86**: p. 43-59.
- Birbas, T., S. Daskalaki, and E. Housos, *School timetabling for quality student and teacher schedules*. Journal of Scheduling, 2009. **12**(2): p. 177-197.
- Feizi-Derakhshi, M.-R., H. Babaei, and J. Heidarzadeh. *A survey of approaches for university course timetabling problem*. in *Proceedings of 8th international symposium on intelligent and manufacturing systems (IMS 2012)*. 2012.
- Dandashi, A. and M. Al-Mouhamed. *Graph Coloring for class scheduling*. in *ACS/IEEE International Conference on Computer Systems and Applications-AICCSA 2010*. 2010. IEEE.
- Welsh, D.J. and M.B. Powell, *An upper bound for the chromatic number of a graph and its application to timetabling problems*. The Computer Journal, 1967. **10**(1): p. 85-86.
- Dimopoulou, M. and P. Miliotis, *Implementation of a university course and examination timetabling system*. European Journal of Operational Research, 2001. **130**(1): p. 202-213.
- Dimopoulou, M. and P. Miliotis, *An automated university course timetabling system developed in a distributed environment: A case study*. European Journal of Operational Research, 2004. **153**(1): p. 136-147.
- Daskalaki, S. and T. Birbas, *Efficient solutions for a university timetabling problem through integer programming*. European Journal of Operational Research, 2005. **160**(1): p. 106-120.
- Al-Yakoob, S.M. and H.D. Sherali, *Mathematical programming models and algorithms for a class-faculty assignment problem*. European Journal of Operational Research, 2006. **173**(2): p. 488-507.
- Al-Yakoob, S.M. and H.D. Sherali, *Mixed-integer programming models for an employee scheduling problem with multiple shifts and work locations*. Annals of Operations Research, 2007. **155**(1): p. 119-142.
- Badri, M.A., et al., *A multi-objective course scheduling model: Combining faculty preferences for courses and times*. Computers & operations research, 1998. **25**(4): p. 303-316.
- Kang, L. and G.M. White, *A logic approach to the resolution of constraints in timetabling*. European Journal of Operational Research, 1992. **61**(3): p. 306-317.
- Zhang, L. and S. Lau. *Constructing university timetable using constraint satisfaction programming approach*. in *International Conference on Computational Intelligence for Modelling, Control and Automation and International Conference on Intelligent Agents, Web Technologies and Internet Commerce (CIMCA-IAWTIC'06)*. 2005. IEEE.
- Alvarez-Valdes, R., E. Crespo, and J.M. Tamarit, *Design and implementation of a course scheduling system using Tabu Search*. European Journal of Operational Research, 2002. **137**(3): p. 512-523.
- Aladag, C.H., G. Hocaoglu, and M.A. Basaran, *The effect of neighborhood structures on tabu search algorithm in solving course timetabling problem*. Expert Systems with Applications, 2009. **36**(10): p. 12349-12356.
- Hao, J.-K. and U. Benlic, *Lower bounds for the ITC-2007 curriculum-based course timetabling problem*. European Journal of Operational Research, 2011. **212**(3): p. 464-472.
- Deris, S., et al., *Incorporating constraint propagation in genetic algorithm for university timetable planning*. Engineering applications of artificial intelligence, 1999. **12**(3): p. 241-253.
- Wang, Y.-Z., *An application of genetic algorithm methods for teacher assignment problems*. Expert Systems with Applications, 2002. **22**(4): p. 295-302.
- Asmuni, H., E.K. Burke, and J.M. Garibaldi. *Fuzzy multiple heuristic ordering for course timetabling*. in *Proceedings of the 5th United Kingdom workshop on computational intelligence (UKCI 2005)*. 2005. Citeseer.
- Chaudhuri, A. and K. De, *Fuzzy genetic heuristic for university course timetable problem*. Int. J. Advance. Soft Comput. Appl, 2010. **2**(1): p. 100-123.
- Abdullah, S., E.K. Burke, and B. McCollum. *A hybrid evolutionary approach to the university course timetabling problem*. in *2007 IEEE congress on evolutionary computation*. 2007. IEEE.
- Kohshori, M.S. and M.S. Abadeh, *Hybrid genetic algorithms for university course timetabling*. International Journal of Computer Science Issues(IJCSI), 2012. **9**(2).

31. Badoni, R.P., D. Gupta, and P. Mishra, *A new hybrid algorithm for university course timetabling problem using events based on groupings of students*. Computers & Industrial Engineering, 2014. **78**: p. 12-25.
32. Bakir, M.A. and C. Aksop, *A 0-1 integer programming approach to a university timetabling problem*. Hacettepe Journal of Mathematics and Statistics, 2008. **37**(1): p. 41-55.



## Research Article

# Predicting acceptance of the bank loan offers by using support vector machines

Mehmet Furkan Akça <sup>a,\*</sup>  and Onur Sevli <sup>b</sup> 

<sup>a</sup>Burdur Mehmet Akif Ersoy University, Graduate School of Natural and Applied Sciences MSc Student in Computer Engineering, Burdur, 15030, Turkey

<sup>b</sup>Burdur Mehmet Akif Ersoy University, Faculty of Engineering and Architecture, Department of Computer Engineering, Burdur, 15030, Turkey

## ARTICLE INFO

### Article history:

Received 16 January 2022

Accepted 13 June 2022

Published 15 August 2022

### Keywords:

Bank loan approval  
Comparison with kernels  
Machine learning  
Support vector machine

## ABSTRACT

Loans are one of the main profit sources in banking system. Banks try to select reliable customers and offer them personal loans, but customers can sometimes reject bank loan offers. Prediction of this problem is an extra work for banks, but if they can predict which customers will accept personal loan offers, they can make a better profit. Therefore, at this point, the aim of this study is to predict acceptance of the bank loan offers using the Support Vector Machine (SVM) algorithm. In this context, SVM was used to predict results with four kernels of SVM, with a grid search algorithm for better prediction and cross validation for much more reliable results. Research findings show that the best results were obtained with a poly kernel as 97.2% accuracy and the lowest success rate with a sigmoid kernel as 83.3% accuracy. Some precision and recall values are lower than normal ones, like 0.108 and 0.008 due to unbalanced dataset, like for 1 true value, there are 9 negative values (9.6% true value). This study recommends the use of SVC in banking system while predicting acceptance of bank loan offers.

## 1. Introduction

Primary business of a bank is lending. The main source of profit is the interest on the loan [1, 2]. On the one hand, banks decide whether the borrower is defaulter or non-defaulter before giving the loan to customers [3]. On the other hand, they offer personal loans to some customers who are reliable, but generally, customers reject personal loans like in our samples in dataset [4]. Due to this problem, the prediction of which customer will accept the personal loan is an important task for the banking system.

For several problems, the banking industry requires more accurate predictive modeling system [5]. Bank workers can make those models with manually, but this process takes long time and lots of man-hours. At this point, machine learning (ML) techniques are extremely beneficial to predict outcomes when dealing with huge amounts of data [5]. So, those models can be applied to banking system via using ML techniques. After that predictive model, if we can predict which customers will accept personal loan offers of banks using machine learning, the loan approval process will be automated, so banks can save lots of man-hours and improve customer service [6]. In this study, Support Vector Machine (SVM)

algorithm will be used to predict which customer will accept personal loan offer of banks because of classification problem.

SVM was first time officially used by Boser et al (1992) in the article titled "A Training Algorithm for Optimal Margin Classifiers" [7]. SVM is a modern non-linear, non-parametric classification algorithm that has a lot of promise. It is appropriate for binary classification applications and includes features of non-parametric applied statistics, neural networks, and ML [8]. The structure of SVM has several computational advantages, including special direction at a finite sample and a lack of correlation between algorithm complexity and sample dimension [9]. In the situation of non-regularity in the data (i.e. not evenly distribution of the data or having an uncertain distribution), SVM can be a valuable tool for insolvency analysis [8]. SVM algorithms solve non-convex and more general optimization issues as well as convex problems (e.g., linear programming, quadratic programming, second order cone programming; integer programming, semi-infinite programming) [10].

Li *et al* applied SVM to credit assessment by using real life credit card data (245 bad records and 755 good

\* Corresponding author. Tel.: +90-248-213-3150.

E-mail addresses: [akcemehtmetfurkan@gmail.com](mailto:akcemehtmetfurkan@gmail.com) (M. F. Akça), [onursevli@mehmetakif.edu.tr](mailto:onursevli@mehmetakif.edu.tr) (O. Sevli)

ORCID: 0000-0003-0289-9606 (M. F. Akça), 0000-0002-8933-8395 (O. Sevli)

DOI: [10.35860/iarej.1058724](https://doi.org/10.35860/iarej.1058724)

© 2022, The Author(s). This article is licensed under the CC BY-NC 4.0 International License (<https://creativecommons.org/licenses/by-nc/4.0/>).

records, with 14 variables) obtained from a Chinese commercial bank. They state that SVM is better than basic grade criterion used by the bank to predict accuracy in the field of credit assessment [9]. Dall'Asta Rigo applied six ML techniques (SVM, LR, MARS, RF, XGB, and Stacking) on four real-life credit scoring datasets (Home Credit, German Credit, Credit Card Default, Give Me Credit) for classification problem [11]. Xu *et al* used 4 machine learning methods (RF, XGBT, GBM, and NN) to predict factors affecting repayment of borrowers. They conclude that the RF performs well in the classification task of default [12]. Huang *et al* explain that SVM and NN achieve better prediction accuracy than traditional statistical methods in credit rating analyses for the US and Taiwan markets [13]. Kadam *et al* used the SVM and Naïve Bayes (NB) to predict loan approval. They conclude that NB fulfills of needs of bankers [14]. Bayraktar *et al* compared commonly used machine learning

methods with deep learning methods (Classification Restricted Boltzmann Machine and Multilayer Artificial Neural Networks) [15]. Aphale and Shinde used various ML techniques (Neural Network, Discriminant Analysis, Naïve Bayes, K-Nearest Neighbor, Linear Regression, Ensemble Learning, and Decision Tress) to predict the creditworthiness of borrowers [3].

It is a fact that all articles in the literature focus on credit risk management, credit rating, loan repayment, decision-aid for loaners, and credit default. However, this study aims at predicting acceptance of the bank loan offers by utilizing Support Vector Machine (SVM) algorithm. It can be said that this study is the first research to use SVM in predicting acceptance of the loan offer of a bank to customers. Therefore, this study will contribute to loan and banking system due to no existing of any article or study related to same topic in the literature.

Table 1. Features and statistical characteristics of the dataset

| Feature Names      | Description   | Mean     | Standard Deviation | Min Value | Max Value | Feature Type |
|--------------------|---|----------|--------------------|-----------|-----------|--------------|
| ID                 | Customer's unique ID number   | 2500.50  | 1443.52            | 1         | 5000      | Categorical  |
| Age                | Customer's age  | 45.33    | 11.46              | 23        | 67        | Numeric      |
| Experience         | Work experience by number of years  | 20.10    | 11.46              | -3        | 43        | Numeric      |
| Income             | 0.1% Percentage of annual income  | 73.77    | 46.03              | 8         | 224       | Numeric      |
| ZIP Code           | ZIP Code of where customer lives  | 93152.50 | 2121.85            | 9307      | 96651     | Categorical  |
| Family             | Family Size   | 2.39     | 1.14               | 1         | 4         | Numeric      |
| CC Avg             | 0.1% Percentage of average credit card spending per month                     | 1.93     | 1.74               | 0         | 10        | Numeric      |
| Education          | Level of education (1-Undergraduate, 2-Graduate, 3-Advanced)                  | 1.88     | 0.83               | 1         | 3         | Categorical  |
| Mortgage           | If any house mortgage, its value.   | 56.49    | 101.71             | 0         | 635       | Numeric      |
| Personal Loan      | Acceptance of personal loan offer by the customer in the last campaign season | 0.09     | 0.29               | 0         | 1         | Categorical  |
| Securities Account | Is there any securities account with the customer?                            | 0.10     | 0.30               | 0         | 1         | Categorical  |
| CD Account         | Is there any certificate of deposit account with the customer?                | 0.06     | 0.23               | 0         | 1         | Categorical  |
| Online             | Is this customer using internet banking?                                      | 0.59     | 0.49               | 0         | 1         | Categorical  |
| Credit Card        | Is this customer using a credit card issued by bank?                          | 0.29     | 0.45               | 0         | 1         | Categorical  |

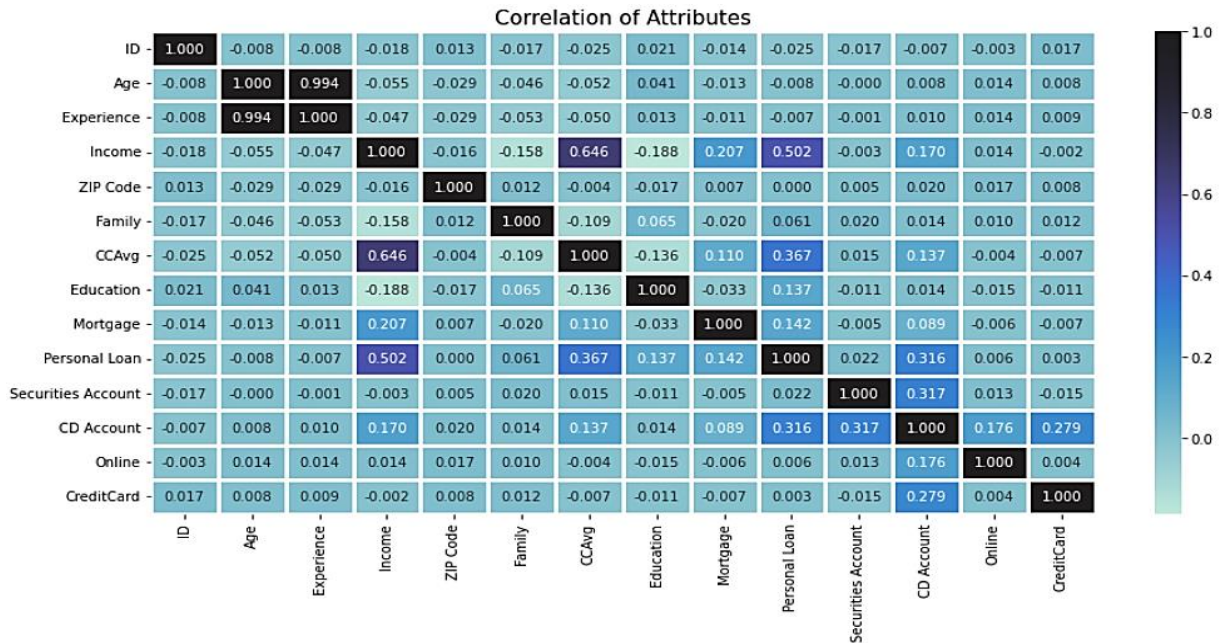


Figure 1. Correlation of attributes

## 2. Material and Methods

### 2.1 Dataset

This publicly available dataset was obtained from Kaggle and shared by Walke [4]. The dataset belongs to “Thera Bank” and contains 5000 customers’ demographic information like “Age” and “Income” columns, and relationship with bank data like “Mortgage” and “Securities Account” columns. And customers’ response to the last campaign, like the Personal Loan column. Among these customers, only 480 (or 9.6%) accepted this offer[4].

When the bank loan dataset was checked, selected features from dataset for this study are seen in Table 1. In addition, table 1 shows mean, standard deviation, min value, max value and feature type. There are no missing values or duplication, and also no values of string type. This information is important because some machine learning algorithms cannot work with string values, and missing values and duplication can badly affect prediction results. If a string value is existed, a label encoder could be used to solve that problem.

After these details, columns which are useless for this study must be selected. At the beginning, the correlation matrix at Figure 1 should be checked for a visualization of how the columns affect the target column, Personal Loan. As can be seen in the correlation matrix, each column has a positive or negative impact on the target value. ID column and ZIP Code column were deleted because ID is a unique value for everybody in dataset; ZIP Code is decreasing prediction accuracy. After these deletions and details, dataset can be used for ML algorithms.

### 2.2 Methods

Before the classification process, we must know the general process of how to apply machine learning algorithms. Figure 2 shows general process of this ML study with grid search and 5-fold cross validation. In this study, SVM algorithms were used to predict the acceptance of bank personal loan offers. Before this prediction, we must separate the Personal Loan column to another data frame because that column will be our target column. After this process, we can use train test split (TTS), but generally, TTS is not a reliable method for machine learning prediction because TTS works differently with different random state values. So, we are creating train and test data using Cross Validation.

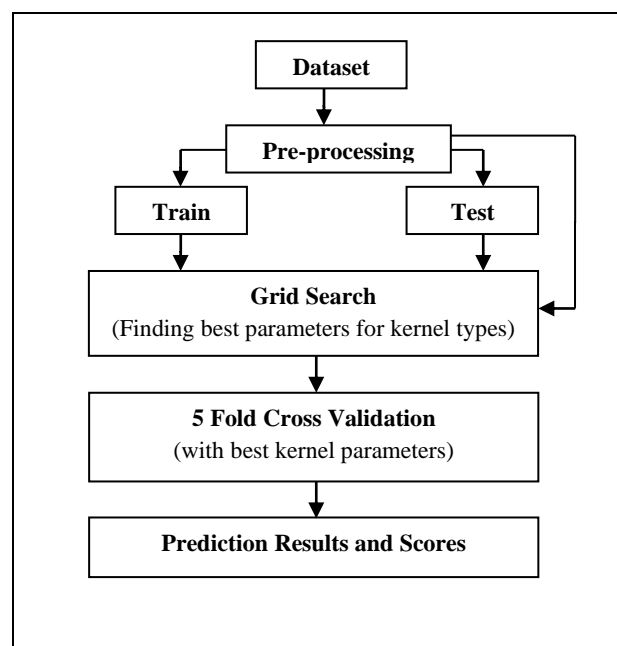


Figure 2. Our study process



### 2.2.1 Support Vector Classifier (SVC)

A support vector machine (SVM) is a supervised learning model (invented by Vladimir Vapnik) and used for classification and prediction of data [16]. However, SVM is generally used in classification problems. Each data item as a point in n-dimensional space is represented in the SVM method. Each feature's value corresponds to the value of a specific coordinate. Then the hyper-plane that clearly separates the two classes to complete categorization is located [17]. There are several hyperplanes from which to choose to split the two kinds of data points. The aim is to determine a plane with the largest margin, or the largest range among data points from both groups. Expanding the margin distance adds reinforcement, making following data points easier to classify categorize [18].

There have been many kernel functions in SVM. However, following 4 kernel functions are popular [19]:

- **Linear kernel:**

$$K(x_i, x_j) = x_i^T * x_j \quad (1)$$

- **Polynomial kernel:**

$$K(x_i, x_j) = (\gamma x_i^T * x_j + r)^d, \gamma > 0 \quad (2)$$

- **RBF kernel:**

$$K(x_i, x_j) = \exp(-\gamma \|x_i - x_j\|^2), \gamma > 0 \quad (3)$$

- **Sigmoid kernel:**

$$K(x_i, x_j) = \tanh(\gamma x_i^T * x_j + r) \quad (4)$$

Where,  $\gamma$ ,  $r$  and  $d$  are kernel parameters

In this study, above kernel types and grid search algorithm will be used to find the best parameters. After this selection, cross validation will be applied to predict results and take several metric results like accuracy, precision, recall and f1 score.

## 3. Experimental Study and Findings

In this study, confusion matrix, accuracy score, precision score, recall score and f1 score metrics will be used to evaluate SVM algorithm.

### 3.1 Evaluation Metrics

The performance of a model can be explained using evaluation metrics. The ability of evaluation metrics to differentiate between model results is a key feature [20].

#### 3.1.1 Confusion Matrix

It is a N X N matrix in which N is the number of classes being predicted [20]. For this article confusion matrix as Table 2 will be used.

Table 2. Representation of cells in confusion matrix

|          | Predicted:0 | Predicted:1 |
|----------|-------------|-------------|
| Actual:0 | TN          | FP          |
| Actual:1 | FN          | TP          |

### 3.1.2 Accuracy Score

The percentage of correct guesses in the total number of predictions is called accuracy [20]. Accuracy was calculated with following equation (5).

$$\text{Accuracy} = (TP + TN) / (TP + TN + FP + FN) \quad (5)$$

### 3.1.3 Precision Score

The fraction of accurately detected affirmative cases is known as precision [20]. Precision score show us the perfectness of predictive model [21]. Precision was calculated with following equation (6).

$$\text{Precision} = (TP) / (TP + FP) \quad (6)$$

### 3.1.4 Recall Score

The fraction of real positive instances that are accurately detected is referred to as recall [20]. Recall was calculated with following equation (7).

$$\text{Recall} = (TP) / (TP + FN) \quad (7)$$

### 3.1.5 F1 Score

For a classification problem, the F1-Score is the harmonic mean of precision and recall values [21]. F1 was calculated with following equation (8).

$$F1 = 2 * \left( \frac{\text{Precision} * \text{Recall}}{\text{Precision} + \text{Recall}} \right) \quad (8)$$

## 3.2 Results

Support vector machine algorithm with 4 kernel types, results shown in below with Table 3. Confusion matrices and other metrics are mean version of 5-fold cross validation results. All metric scores were generalized in Table 4.

According to the Table 3 and Table 4, all our kernels have a successful accuracy score, but we cannot evaluate with just one parameter, accuracy score. It can be said that scores over 80% is good scores, so our precision scores except sigmoid kernel is successful. About recall scores there is one kernel (polynomial) we can say is successful. About F1 scores polynomial and rbf kernels are successful. Reason for lower scores, we do not have a balanced dataset, so there are a few positive results, so when SVM kernels try to classify that few positive results, there is failure happening especially with sigmoid kernel.

We can clearly say that according to this paper if we have an unbalanced dataset we cannot get successful results with sigmoid kernel, we can choose polynomial kernel.

There exists no any article or study related to same topic with this study. Some studies related to bank loan approval and banking system topics are given in Table 5.

Table 3. Confusion Matrix

|             | Actual Value | Predicted Value |      |
|-------------|--------------|-----------------|------|
|             |              | 0               | 1    |
| Linear SVC  | 0            | 895.2           | 8.8  |
|             | 1            | 40.2            | 55.8 |
| Poly SVC    | 0            | 892.4           | 11.6 |
|             | 1            | 16.4            | 79.6 |
| Sigmoid SVC | 0            | 832.4           | 71.6 |
|             | 1            | 95.2            | 0.8  |
| Rbf SVC     | 0            | 895.2           | 8.8  |
|             | 1            | 23.4            | 72.6 |

Table 4. Metric results

| Kernel Type | Metrics  |           |        |       |
|-------------|----------|-----------|--------|-------|
|             | Accuracy | Precision | Recall | F1    |
| Linear      | 0,951    | 0,863     | 0,581  | 0,694 |
| Poly        | 0,972    | 0,872     | 0,829  | 0,850 |
| Sigmoid     | 0,833    | 0,108     | 0,008  | 0,009 |
| Rbf         | 0,967    | 0,893     | 0,757  | 0,818 |

Table 5. Comparison with similar studies in the literature

| Authors of the Article        | Highest Score ML Technique | Accuracy |
|-------------------------------|----------------------------|----------|
| Sheikh <i>et al.</i> [21]     | Logistic Regression        | 81.1%    |
| Vimala and Sharmili [22]      | SVM                        | ~79%     |
| Fati [23]                     | Logistic Regression        | 79%      |
| Madaan <i>et al.</i> [24]     | Random Forest              | 80%      |
| Sreesouhry <i>et al.</i> [25] | Logistic Regression        | 77%      |
| Yaurita and Rustam [26]       | SVM (Rbf)                  | 85%      |
| Kumar <i>et al.</i> [27]      | Decision Tree              | 95%      |
| Ndayisenga [28]               | SVM                        | 77%      |

#### 4. Conclusion

Literature review shows that machine learning algorithms have played a significant role in the prediction of acceptance of personal bank loan offers.

SVM is among the best-performing statistical-learning or machine-learning algorithms in terms of accuracy [29, 30, 31]. In this study, a support vector machine algorithm with four kernel types was used. According to the results of the analyses, the best results were obtained with a polynomial kernel (97%) and the worst results with a sigmoid kernel (83%). Some precision and recall values are very low

compared to normal because our dataset is an unbalanced dataset, meaning for every true value, there are 9 negative values. When we use an unbalanced dataset, this problem can occur. But the general performance of support vector machines is satisfying, and we can say that SVM with a polynomial kernel is a good choice to predict loan results like in our study. When we compare with similar studies, there are different types of ML algorithms used. Generally, accuracy scores between 77% and 85%.

After the comparison we can say that SVM with polynomial kernel is successful for banking system classification problems because our study's accuracy and other metric scores are higher than similar study's.

Finally, if banking systems use a machine learning method to predict acceptance of bank loan offers, they can predict their future profit easily.

#### Declaration

The authors declared no potential conflicts of interest with respect to the research, authorship, and/or publication of this article. The authors also declared that this article is original, was prepared in accordance with international publication and research ethics, and ethical committee permission or any special permission is not required.

#### Author Contributions

M.F. Akça developed the methodology and performed the analysis. O. Sevli supervised and improved the study. M.F. Akça and O. Sevli wrote the manuscript together.

#### References


1. Arun, K., G. Ishan, and K. Sanmeet, *Loan approval prediction based on machine learning approach*. IOSR J. Comput. Eng, 2016. **18**(3): p. 18-21.
2. Bhandari, M., *How to predict loan eligibility using machine learning models*. [cited 2022 02 January]; Available from: <https://towardsdatascience.com/predict-loan-eligibility-using-machine-learning-models-7a14ef904057>.
3. Aphale, A.S., and S.R. Shinde, *Predict loan approval in banking system machine learning approach for cooperative banks loan approval*. International Journal of Engineering Research & Technology, 2020. **9**(8): 991-995
4. Walke, K. *Bank personal loan modelling*. [cited 2021 03 October]; Available from: <https://www.kaggle.com/krantisswalke/bank-personal-loan-modelling>.
5. Tejaswini, J., T.M. Kavya, R.D.N. Ramya, P.S. Triveni, and V.R. Maddumala, *Accurate loan approval prediction based on machine learning approach*. Journal of Engineering Sciences, 2020. **11**(4): p. 523-532.
6. Pandey, N., R. Gupta, S. Uniyal, and V. Kumar, *Loan approval prediction using machine learning algorithms approach*. International Journal of Innovative Research in Technology, 2021. **8**(1): p. 898-902.

7. Boser, B.E., I.M. Guyon, and V.N. Vapnik, *A training algorithm for optimal margin classifiers*, in Proceedings of the fifth annual workshop on Computational learning theory, 1992. Association for Computing Machinery: Pittsburgh, Pennsylvania, USA: p. 144–152.
8. Auria, L., and R.A. Moro, *Support vector machines (SVM) as a technique for solvency analysis*. DIW Berlin Discus. Paper, 2008. [cited 2022 02 January] Available from [https://papers.ssrn.com/sol3/papers.cfm?abstract\\_id=1424949](https://papers.ssrn.com/sol3/papers.cfm?abstract_id=1424949).
9. Li, J., J. Liu, W. Xu, and Y. Shi, *Support vector machines approach to credit assessment*, in Computational Science-ICCS 2004, Lecture Notes in Computer Science 3039, Berlin Heidelberg: Springer. p. 892-899.
10. Tian, Y., Y. Shi, and X. Liu, *Recent advances on support vector machines research*. Technological and Economic Development of Economy, 2012. **18**(1): p. 5-33.
11. Dall'Asta Rigo, E.Y., *Evaluation of stacking for Predicting credit risk scores*. MSc Thesis at TED University Graduate School Applied Data Science, 2020. p. 1-75.
12. Xu, J., Z. Lu, and Y. Xie, *Loan default prediction of Chinese P2P market: a machine learning methodology*. Scientific Reports, 2021. **11**: 1-19.
13. Huang, Z., H. Chen, C.J. Hsu, W.H. Chen, and S. Wu, *Credit rating analysis with support vector machines and neural networks: A market comparative study*. Decis. Support Syst., 2004. **37**: 543-558.
14. Kadam, A.S., S.R. Nikam, A.A. Aher, G.V. Shelke, and A.S. Chandgude, *Prediction for loan approval using machine learning algorithm*. International Research Journal of Engineering and Technology (IRJET), 2021. **8**(4): 4089-4092.
15. Bayraktar, M., M.S. Aktas, O. Kalipsiz, O. Susuz, and S. Bayraci, *Credit risk analysis with classification restricted boltzmann machine*. in Proceeding of 26<sup>th</sup> Signal Processing and Communications Applications Conference (SIU), 2018, p. 1-4.
16. IBM. [cited 2022 02 January]; Available from: <https://www.ibm.com/cloud/learn/supervised-learning>.
17. Ray, S. *Understanding support vector machine (SVM) algorithm from examples (along with code)*. September 13, 2017 [cited 2022 02 January]; Available from: <https://www.analyticsvidhya.com/blog/2017/09/understain-g-support-vector-machine-example-code/>.
18. Gandhi, R. *Support vector machine-Introduction to machine learning algorithms*. [cited 2022 02 January]; Available from: <https://towardsdatascience.com/support-vector-machine-introduction-to-machine-learning-algorithms-934a444fca47>.
19. Hsu, C.W., C.C. Chang, and C.J. Lin, *A practical guide to support vector classification*. Technical Report 2003, Department of Computer Science and Information Engineering, University of National Taiwan. p. 1-12.
20. Srivastava, T, *11 important model evaluation metrics for machine learning everyone should know*. August 6, 2019 [cited 2022 02 January]; Available from: <https://www.analyticsvidhya.com/blog/2019/08/11-important-model-evaluation-error-metrics/>.
21. Sheikh, M.A., A.K. Goel, and T. Kumar. *An Approach for Prediction of Loan Approval using Machine Learning Algorithm*. in Proceedings of the International Conference on Electronics and Sustainable Communication Systems (ICESC 2020), IEEE Xplore Part Number: CFP20V66-ART, 2020. p. 490-494.
22. Vimala, S., and K. Sharmili. *Prediction of loan risk using naive bayes and support vector machine*. in International Conference on Advancements in Computing Technologies - ICACT 2018. International Journal on Future Revolution in Computer Science & Communication Engineering (Special Issue), 2018. 4(2): p. 110-113. Available from: [http://www.ijfrcsce.org/index.php/ijfrcsce/Special\\_Issue/ICACT\\_2018\\_Track](http://www.ijfrcsce.org/index.php/ijfrcsce/Special_Issue/ICACT_2018_Track).
23. Fati, S.M., *Machine learning-based prediction model for loan status approval*. Journal of Hunan University Natural Sciences, 2021. **48**(10): p. 1-8.
24. Madaan, M., A. Kumar, C. Keshri, R. Jain, and P. Nagrath, *Loan default prediction using decision trees and random forest: A comparative study*. in IOP Conference Series: Materials Science and Engineering. 2021. IOP Publishing, p.1-12.
25. Sreesouthry, S., A. Ayubkhan, M.M. Rizwan, D. Lokesh, and K.P. Raj, *Loan Prediction Using Logistic Regression in Machine Learning*. Annals of the Romanian Society for Cell Biology, 2021. **25**(4): p. 2790-2794.
26. Yaurita, F., and Z. Rustam. *Application of support vector machines for reject inference in credit scoring*. in Proceedings of the 3<sup>rd</sup> International Symposium on Current Progress in Mathematics and Sciences 2017 (ISCPMS2017), AIP Conf. Proc. 2023, 020209-1-020209-6; <https://doi.org/10.1063/1.5064206>.
27. Kumar, R., et al., *Prediction of loan approval using machine learning*. International Journal of Advanced Science and Technology, 2019. **28**(7): p. 455 - 460.
28. Ndayisenga, T., *Bank loan approval prediction using machine learning techniques*. MSc Dissertation in Data Science in Actuarial Science at the African Center of Excellence in Data Science in University of Rwanda, 2021. p. 1-28.
29. Maroco, J., D. Silva, A. Rodrigues, M. Guerreiro, I. Santana, and A. de Mendonca, *Data mining methods in the prediction of Dementia: A real-data comparison of the accuracy, sensitivity and specificity of linear discriminant analysis, logistic regression, neural networks, support vector machines, classification trees and random forests*. BMC research notes, 2011. **4**(299): p. 1-14.
30. Guenther, N., and M. Schonlau, *Support vector machines*. The Stata Journal, 2016. **16**(4): p. 917-937.
31. Prasad, K.G.S., P.V.S. Chidvilas, and V.V. Kumar, *Customer loan approval classification by supervised learning model*. International Journal of Recent Technology and Engineering, 2019. **8**(4): 9898-9901.



e-ISSN: 2618-575X

INTERNATIONAL ADVANCED RESEARCHES  
and  
ENGINEERING JOURNAL

Journal homepage: [www.dergipark.org.tr/en/pub/iarej](http://www.dergipark.org.tr/en/pub/iarej)International  
Open Access Volume 06  
Issue 02

August, 2022

**Research Article**

## Research on the success of unsupervised learning algorithms in indoor location prediction

Fatma Önay Koçoğlu <sup>a,\*</sup> 

<sup>a</sup>Muğla Sıtkı Koçman University, Faculty of Engineering, Software Engineering Department, Muğla, Turkey

**ARTICLE INFO***Article history:*

Received 31 March 2022

Accepted 09 June 2022

Published 15 August 2022

*Keywords:*

Clustering

External indices

Fuzzy c-Means

Indoor location prediction

Indoor positioning

Internal indices

k-Means

Position prediction

Unsupervised learning

**ABSTRACT**

With location-based smart applications, the flow of life can be facilitated and support can be provided in case of security and emergency situations. Indoor location detection provides various conveniences in complex structures such as hospitals, schools, shopping centers, etc. Indoor location detection studies are carried out by using data related to location and signal and machine learning methods. Machine learning has become frequently used as a solution method in this field, as in many other fields. When the studies in the literature are examined, it is seen that the studies are mainly focused on producing solutions with supervised machine learning algorithms. Unsupervised algorithms are frequently used to determine the labels of data groups that do not have labels. In this direction, it can be seen as the first step in labeling the data collected in indoor positioning studies and then using it for training predictive models to be developed with supervised learning methods. For this reason, the results to be obtained regarding the success and usefulness of cluster analysis will constitute an important basis for further studies. In this study, it is aimed to examine the success of unsupervised learning, in other words, clustering algorithms. The Wireless Indoor Localization Data Set and well-known k-Means and Fuzzy c-Means algorithms have been used with different distance measure. The obtained methods performances have been evaluated with internal and external indices. The results show that the clustering algorithms can cluster correctly data points in the range of 93-95% according to the accuracy and F measure value. Although performances indicators are very close to each other according to the internal indexes, it can be stated that the model obtained using the Manhattan distance measure and the k-Means algorithm has higher performance in terms of clustering success.

**1. Introduction**

Positioning technologies are among the important technological study topics of today. These technologies are important in terms of determining the location, enabling active monitoring and routing. Positioning techniques are applied in two areas, indoor and outdoor. Global Positioning Systems (GPS), which uses satellite data and can detect position with a very low error, is widely used today. Position estimation is performed by a GPS receiver by measuring the difference between the arrival time of the satellite signals [1]. However, there are elements that prevent or attenuate line of sight and signal transmission, such as buildings, walls, roofs. Since these factors reduce the power and efficiency of satellite and radio signals, GPS is not as effective in determining location indoors and in high-rise urban areas. On the other hand, as a result of the increase in the use of mobile devices such as mobile

phones, mobile communication systems enable location detection and monitoring indoors with Global System for Mobile Communications (GSM) signals. Although they differ in scope, method and type of location, technologies used via mobile devices or equipment for indoor localization include ultrasound, infrared, Wi-Fi, Bluetooth, Zig-Bee, Ultrawide Band, inertial navigation, magnetic-based methods, and Radio Frequency Identification (RFID) [2].

With location-based smart applications, the flow of life can be facilitated and support can be provided in case of security and emergency situations. Indoor location detection provides various conveniences in complex structures such as hospitals, schools, shopping centers, etc. In applications such as directing people, especially in closed areas such as museums and airports, tracking products in areas such as factories and warehouses, following elderly patients in need of support in areas such

\* Corresponding author. Tel.: +90 252 211 5581.

E-mail addresses: [fonaykocoglu@mu.edu.tr](mailto:fonaykocoglu@mu.edu.tr)

ORCID: 0000-0002-1096-9865

DOI: [10.35860/iarej.1096573](https://doi.org/10.35860/iarej.1096573)

© 2022, The Author(s). This article is licensed under the CC BY-NC 4.0 International License (<https://creativecommons.org/licenses/by-nc/4.0/>).

as hospitals or nursing homes, finding a specific store in shopping centers, offering location-based advertisements, detecting of abnormal situations in units where security measures are intense etc. indoor localization technologies are used. In today's world, extracting information from data and using that information is very valuable. Although location data does not make sense on its own, transforming this data into new applications with dynamically personalized content can be transformed into important profits with a small additional bandwidth usage [3]. Moreover, along with various IoT protocols such as Bluetooth and WiFi, the connection between various devices has led to the emergence of more integrated systems. So, especially with the development of the IoT, it is clear that indoor location detection will appear in more applications and will become even more important in the next days [4].

In this study, it is aimed to examine the success of unsupervised learning methods, one of the machine learning methods, in indoor location estimation. The rest of this paper is as follows in "Literature Review" studies in literature have been given which point out the problem, in "Methodology" section the data, methods, performance indicators have been detailed, in "Results" section results has been presented, and "Discussion" and "Conclusion" sections include assessment of results.

## 2. Literature Review

Positioning studies are carried out by using data related to location and signal and machine learning methods. Machine learning has become frequently used as a solution method in this field, as in many other fields. [5] have stated that supervised learning techniques deal with labeled data in the data collection stage of indoor localization, and she counted SVM among the most frequently used algorithms. [6] have examined the success of machine learning approaches with k-nearest neighbor (k-NN), rule-based classifier and random forest (RF) algorithms to predict indoor location using RSSI-based fingerprint method. [7] have presented an indoor positioning system (IPS) and motion tracking system for the elderly. Using the obtained data sets and Weka software tool, SVM, k-NN, RF and DT machine learning algorithms have been tested and the best classifier has been determined. [8] have presented an indoor location algorithm with the characteristics of WIFI fingerprint signals and a Naive Bayes machine learning algorithm. [9] has developed a mobile application that allows users to capture and create their own RSSI maps using the generated models to obtain the current indoor location. The models were obtained with Non-Nested Generalized Exemplars (NNge), Instance Based Learner (Ibk), Random Tree, RF and Random Committee machine learning algorithms. [10] have proposed an indoor localization approach based on fingerprints of Received

Signal Strength Indicator (RSSI) measurements using Long Short-Term Memory (LSTM) Neural Networks. [11] have developed an integrated system for indoor location fingerprinting using Deep Neural Network (DNN) and improved k-NN algorithm. [12] have proposed a model for indoor localization with machine learning (ML) and deep learning (DL) algorithms in non-line-of-sight (NLoS) conditions using partial knowledge of channel state information (CSI). [13] have aimed to explore the possible improvement of system accuracy based on radio technology Bluetooth Low Energy through k-NN, Support Vector Machines (SVM), RF and Artificial Neural Network (ANN) machine learning approaches. [14] have pointed out a large number of mobile phone models causing changes in the measured received signal strength (RSS) in indoor positioning, they propose a deep learning-based system using cellular metrics to provide consistent performance in invisible tracking phones. [15] have used machine learning algorithms to developed a sensing platform consisting of a sensor toolkit with an environmental data server to provide indoor location awareness. These algorithms include k-NN, SVM, Decision Tree (DT), Adaptive Boosting, RF, Lightgbm, Xgboost, Gaussian Naive Bayes, and Gradient Boosting Classifier. [16] have developed an indoor positioning algorithm based on Back Propagation Neural Network (BPNN) to solve the low position calculation efficiency and positioning accuracy due to the complexity of indoor environments.

When the studies in the literature are examined, it is seen that the studies are mainly focused on producing solutions with supervised machine learning algorithms. In this study, it is aimed to examine the success of unsupervised learning, in other words, clustering algorithms in determining indoor location. Clustering algorithms are frequently used to determine the labels of data groups that do not have labels. In this direction, it can be seen as the first step in labeling the data collected in indoor positioning studies and then using it for training predictive models to be developed with supervised learning methods. For this reason, the results to be obtained regarding the success and usefulness of cluster analysis will constitute an important basis for further studies.

## 3. Methodology

### 3.1 Data

The Wireless Indoor Localization Data Set, which is open access in the UCI Machine Learning Repository, was used in the study [17]. The use of an open data set allows comparison with studies to be developed by different researchers. In the data set, there are 8 attributes one of which is a class attribute and 2000 records. There are 4 different class values in the dataset, which includes the signal strength of seven WiFi

| X1              | X2              | X3              | X4              | X5              |
|-----------------|-----------------|-----------------|-----------------|-----------------|
| Min. :-74.00    | Min. :-74.00    | Min. :-73.00    | Min. :-77.00    | Min. :-89.00    |
| 1st Qu. :-61.00 | 1st Qu. :-58.00 | 1st Qu. :-58.00 | 1st Qu. :-63.00 | 1st Qu. :-69.00 |
| Median :-55.00  | Median :-56.00  | Median :-55.00  | Median :-56.00  | Median :-64.00  |
| Mean :-52.33    | Mean :-55.62    | Mean :-54.96    | Mean :-53.57    | Mean :-62.64    |
| 3rd Qu. :-46.00 | 3rd Qu. :-53.00 | 3rd Qu. :-51.00 | 3rd Qu. :-46.00 | 3rd Qu. :-56.00 |
| Max. :-10.00    | Max. :-45.00    | Max. :-40.00    | Max. :-11.00    | Max. :-36.00    |
| X6              | X7              | X8              |                 |                 |
| Min. :-97.00    | Min. :-98.00    | 1:500           |                 |                 |
| 1st Qu. :-86.00 | 1st Qu. :-87.00 | 2:500           |                 |                 |
| Median :-82.00  | Median :-83.00  | 3:500           |                 |                 |
| Mean :-80.98    | Mean :-81.73    | 4:500           |                 |                 |
| 3rd Qu. :-77.00 | 3rd Qu. :-78.00 |                 |                 |                 |
| Max. :-61.00    | Max. :-63.00    |                 |                 |                 |

Figure 1. Descriptive statistics of the data

signals received by a smartphone in an indoor area, and these values indicate four different rooms. The class attribute field will not be included in the analysis, it will be used to measure clustering success after clusters are obtained. The descriptive statistics of attributes has been given in the Figure 1.

All values have been converted to values in the range of [0,1] by using the linear data transformation method as in Equation (1):

$$x_{normal\ value} = \frac{(x - x_{min})}{(x_{max} - x_{min})} \quad (1)$$

### 3.2 Clustering

Classification and clustering are the basic functions of machine learning. In classification, groups must reflect some reference class. In clustering, the categories are discovered within the dataset itself [18]. Data clustering is the work of bringing together similar records, in other words generate homogeneous sub-groups, in multidimensional data and revealing relationships based on some similarity criteria and model [19]. The important thing in clustering is to bring together similar records. Therefore, the most important measure is similarity. The similarity of records in the same cluster should be maximum (maximum), while the similarity of records in different clusters should be minimum (minimum). Within the scope of the study, models were developed with k-Means, Fuzzy c-Means and algorithms.

#### *k-Means Algorithm:*

Records in the data set are assigned to a number of clusters determined by the user according to the similarity measure. In a dataset of numeric values, the measure of similarity is the distance between two data points. The distance is calculated according to the Euclidean, Manhattan and Minkowski distance formulas. The steps of the algorithm are given below [20]:

- The number of clusters is determined (k).
- Cluster centers as many as the determined number of clusters are determined randomly.
- The distance of each observation in the data set to the determined cluster centers is calculated and assigned to the cluster to which it is closest.
- Cluster centers are recalculated after all observations have been assigned.
- The third and fourth steps are repeated for the specified number of iterations, until the cluster centers do not

change, and it falls below a predetermined very small threshold value.

#### *Fuzzy c-Means:*

Fuzzy c-Means is the extension of k-Means with Fuzzy logic approach. Accordingly, each data point does not belong to only one cluster. Therefore, each data point has membership degrees for the specified clusters. Clusters are determined by considering these membership degrees. The steps of the algorithm are given below [21]:

- The number of clusters (c), turbidity parameter (m), stopping criterion ( $\epsilon$ ) are determined.
- Initial membership degrees are randomly determined and a membership matrix is created.
- Cluster centers are calculated.
- New membership degrees and membership matrix are calculated according to cluster centers.
- By checking the stopping criterion, the algorithm is renewed or terminated with the second step.

### 3.3 Distance measure:

Let each record in the data set consist of values of  $n$  different attributes. In this case, each record is represented by the vector  $x_k = [x_{k,1}, x_{k,2}, \dots, x_{k,n}]^T$  and if the data set consists of  $N$  observations, the data set will be represented by  $X = \{x_k | k = 1, 2, \dots, N\}$ . Distance measures have been used for numerical data points as a measure of similarity in cluster analysis. The data set used within the scope of the study consists entirely of numerical values. So, models have been prepared by using Euclidean (Equal (2)) and Manhattan (Equal (3)) distance measurements as distance measures.

$$d_E(x_i, x_j) = \left( \sum_{k=1}^n (x_{i,k} - x_{j,k})^2 \right)^{1/2} \quad (2)$$

$$d_M(x_i, x_j) = \sum_{k=1}^n |x_{i,k} - x_{j,k}| \quad (3)$$

### 3.4 Performance Evaluation

Various indicators are used to test the performance of the models developed in the artificial learning process. For cluster analysis, these indicators are called internal and external indices. External indexes are also used in the measurement of success of models in which the supervised learning method is used. A confusion matrix (Table 1) is created by comparing the labels produced by the model with the actual labels of the data set. The values of the indicators are calculated over this matrix. Internal indexes are calculated regarding the similarity of cluster elements to each other as a result of clustering.

Within the scope of the study, accuracy measure from external indices and Dunn, Silhouette, Davies-Bouldin, and C index indices from internal indices have been used. The calculations of these index measures are given in Appendix.

Table 1. Confusion matrix

|                 |          | Actual Class        |                     |
|-----------------|----------|---------------------|---------------------|
|                 |          | Positive            | Negative            |
| Predicted Class | Positive | True Positive (TP)  | False Positive (FP) |
|                 | Negative | False Negative (FN) | True Negative (TN)  |

**4. Results**

The results of the clustering algorithm according to accuracy measure and F score have been given in Figure 2 and Figure 3. When the results are examined, Fuzzy c-Means can estimate correctly room 4 with an accuracy value of 99.6%,

regardless of the distance measure, and this value is the highest accuracy value obtained. The models developed with Fuzzy c-Means have predicted correctly room 1 with 98% accuracy and room2 with 98.6% accuracy rates and the highest success.

The accuracy values of each model have been averaged to determine the success of predicting all rooms correctly. According to the Manhattan distance, the average accuracy value obtained with the k-Means algorithm is 93.7% and the average accuracy value obtained with the Fuzzy c-Means algorithm is 95.2%. According to the Euclidean distance, the average accuracy value obtained with the k-Means algorithm is 94.3% and the average accuracy value obtained with the Fuzzy c-Means algorithm is 94.1%.

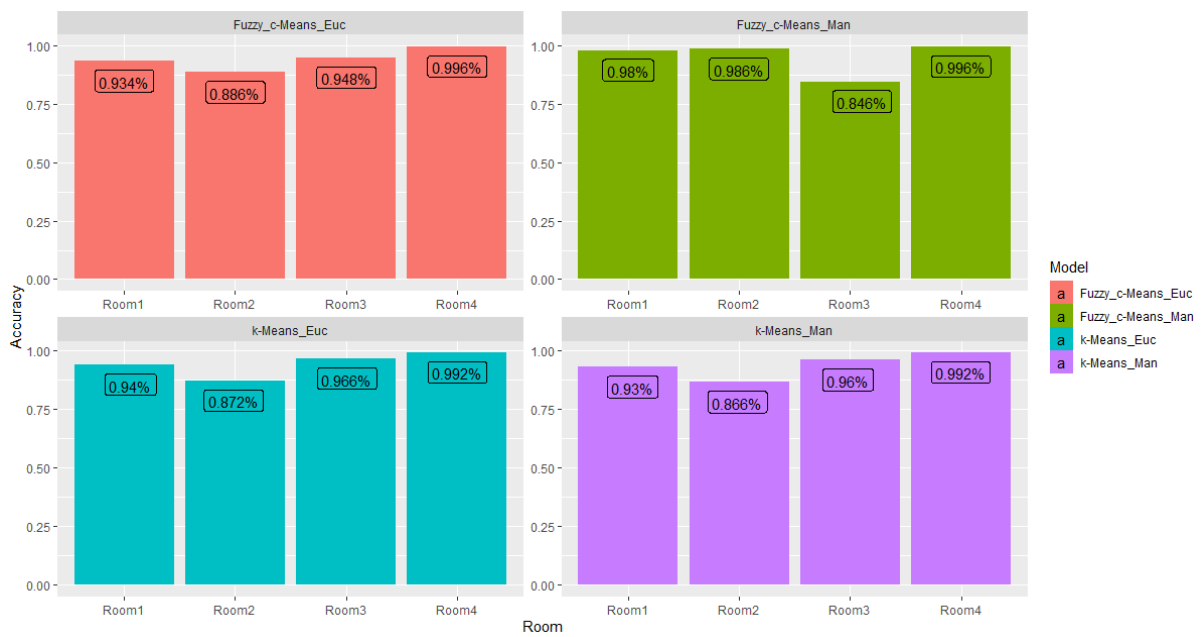


Figure 2. Results of clustering algorithms according to accuracy measure

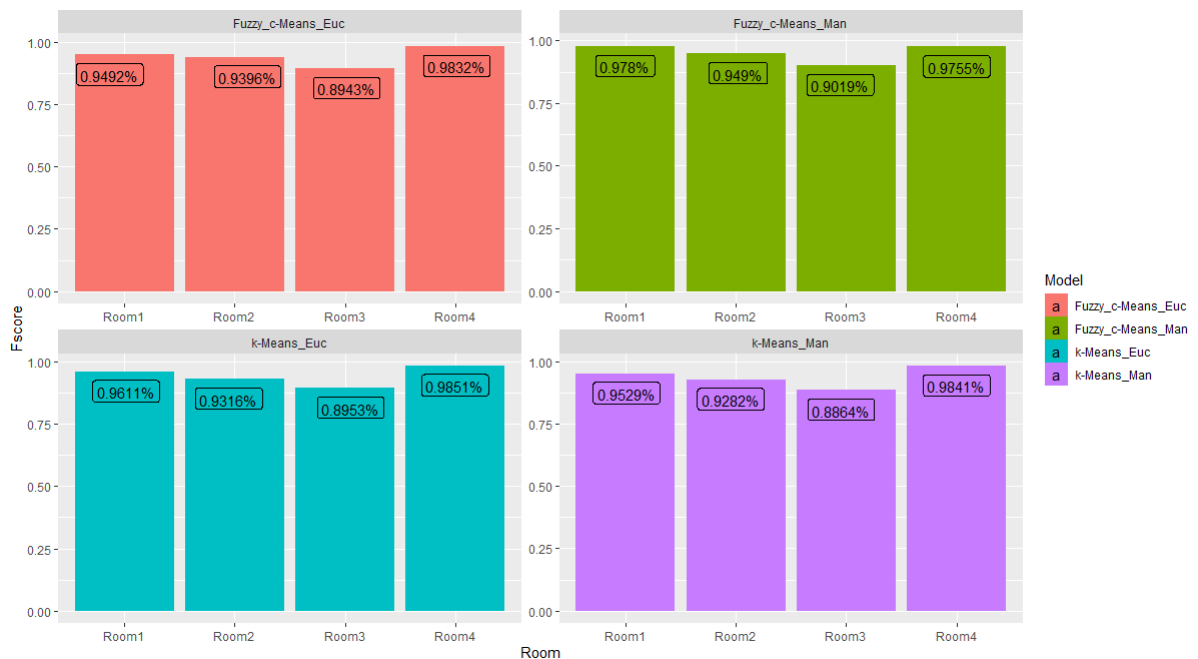


Figure 3. Results of clustering algorithms according to F score measure.

Table 2. Results of clustering algorithms according to internal indexes

|     | KM_M         | KM_E         | FCM_M | FCM_E        |
|-----|--------------|--------------|-------|--------------|
| DI  | <b>0,042</b> | 0,035        | 0,027 | 0,029        |
| SI  | 0,421        | <b>0,423</b> | 0,378 | 0,420        |
| DBI | 0,891        | 0,868        | 0,927 | <b>0,866</b> |
| CI  | <b>0,059</b> | 0,065        | 0,090 | 0,066        |

CI: C index, DBI: Davies-Bouldin Index, DI: Dunn Index, FCM\_E: Fuzzy c-Means Euclidean Distance, FCM\_M: Fuzzy c-Means Manhattan Distance, KM\_E: k-Means Euclidean Distance, KM\_M: k-Means Manhattan Distance

The F score values of each model have been averaged to determine the success of predicting all rooms correctly. According to the Manhattan distance, the average accuracy value obtained with the k-Means algorithm is 93.8% and the average accuracy value obtained with the Fuzzy c-Means algorithm is 95.1%. According to the Euclidean distance, the average accuracy value obtained with the k-Means algorithm is 94.3% and the average accuracy value obtained with the Fuzzy c-Means algorithm is 94.2%.

As a result of successful clustering, Dunn and Silhouette should get maximum values, Davies-Bouldin and C index should get minimum values. When Table 2 regarding the internal index values is examined, the models produced with k-Means-Manhattan distance according to Dunn and C indices, k-Means-Euclidean distance according to Silhouette index, Fuzzy c-Means-Euclidean distance according to Davies-Bouldin index have been successful. In addition, it is seen that the results are close values.

## 5. Conclusions

As stated in the method section, clustering models have been obtained according to different distance measures by using the data set and the specified methods. As a result of running these models, all records in dataset have been assigned to four different clusters. The resulting cluster labels have been compared with the labels in the original data set expressing the location. Thus, it has been determined whether the clustering algorithms can make a correct clustering, and whether the users in the rooms and the users in the clusters determined by the algorithms match each other. The determined performance indicators have been calculated and the success of the clustering method has been evaluated according to these indicators.

When the results are evaluated according to internal and external indexes, different situations arise. While the external indices show the success of the Fuzzy c-Means algorithm, the inner indices indicate the success of the k-Means algorithm. At this point, external indexes should be taken as a basis for classification success. In the study, not only the accuracy measure was considered, but the F measure was especially preferred in order to include the results of different performance measures in the evaluation. Both performance measures produced parallel results when the separate success

values obtained for the classes were averaged, and the most successful model was determined as Fuzzy c-Means using Manhattan's distance.

When the similarities of the elements within the cluster are examined, it is seen that the success of the clustering analysis has changed. According to the distances of the elements in each cluster, the results point to the k-Means algorithm, which mainly uses the Manhattan distance. It can be natural for this situation to occur. This situation can be evaluated from two perspectives. The evaluation is made according to the data points within the cluster, not a reference point. In other words, higher intra-cluster similarities have been obtained in the clusters obtained with k-Means. However, this situation can be interpreted as that although the data patterns in the main data set show similar features, this high similarity cannot produce a fully effective result in spatial clustering. On the other hand, average values for each model have been obtained for external indices. However, when the prediction accuracies on the basis of rooms are examined, it will be seen that there are variations in the prediction success.

When it is desired to perform location prediction on a data set without a class label, the correct number of clusters must be determined absolutely. Internal indexes will need to be used when determining this number. Even if this situation causes performance losses in the next location estimation stage, in general terms, clustering analysis can also achieve results that can compete with classification models.

## Declaration

The author declared no potential conflicts of interest with respect to the research, authorship, and/or publication of this article. The author also declared that this article is original, was prepared in accordance with international publication and research ethics, and ethical committee permission or any special permission is not required.

## Author Contributions

F.Ö. Koçoğlu is responsible for all sections of the study.

## References

1. Hazas, M., J. Scott, and J. Krumm, *Location-aware computing comes of age*. Computer, 2004. **37**(2): p. 95–97.
2. Oguntala, G., R. Abd-Alhameed, S. Jones, J. Noras, M. Patwary, and J. Rodriguez, *Indoor location identification technologies for real-time IoT-based applications: An inclusive survey*. Computer Science Review, 2018. **30**: p. 55–79.
3. Curran, K. E. Furey, T. Lunney, J. Santos, D. Woods, and A. McCaughey, *An evaluation of indoor location determination technologies*. Journal of Location Based Services, 2011. **5**(2): p. 61–78.
4. Nath, R.K., R. Bajpai, and H. Thapliyal, *IoT based indoor location detection system for smart home environment*, in *IEEE International Conference on Consumer Electronics (ICCE)*. 2018. Las Vegas, USA: p. 1-3.
5. Roy P. and C. Chowdhury, *A survey of machine learning*



- techniques for indoor localization and navigation systems. *J Intell Robot Syst*, 2021. **101**(3): p. 63.
6. Jedari, E., Z. Wu, R. Rashidzadeh, and M. Saif, *Wi-Fi based indoor location positioning employing random forest classifier*, in *International Conference on Indoor Positioning and Indoor Navigation (IPIN)*, 2015. Calgary, Canada: p. 1–5.
  7. Tabbakha, N.E., W.-H. Tan, and C.-P. Ooi, *Indoor location and motion tracking system for elderly assisted living home*, in *International Conference on Robotics, Automation and Sciences (ICORAS)*, 2017. Melaka, Malaysia: p. 1–4.
  8. Chao C. and M. Xiaoran, *An innovative indoor location algorithm based on supervised learning and wifi fingerprint classification*, in *Signal and Information Processing, Networking and Computers*, 2018. Singapore: pp. 238–246.
  9. Nuño-Maganda, M.A., H. Herrera-Rivas, C. Torres-Huitzil, H. Marisol Marín-Castro, and Y. Coronado-Pérez, *On-device learning of indoor location for wifi fingerprint approach*. *Sensors*, 2018. **18**(7).
  10. Elbes, M., E. Almaita, T. Alrawashdeh, T. Kanan, S. AlZu'bi, and B. Hawashin, *An indoor localization approach based on deep learning for indoor location-based services*, in *IEEE Jordan International Joint Conference on Electrical Engineering and Information Technology (JEEIT)*, 2019. Amman, Jordan: p. 437–441.
  11. Dai, P., Y. Yang, M. Wang, and R. Yan, *Combination of DNN and improved KNN for indoor location fingerprinting*. *Wireless Communications and Mobile Computing*, 2019. p. e4283857.
  12. Ouameur, M.A., M. Caza-Szoka, and D. Massicotte, *Machine learning enabled tools and methods for indoor localization using low power wireless network*. *Internet of Things*, 2020. **12**: 100300.
  13. Polak, L., S. Rozum, M. Slanina, T. Bravenec, T. Fryza, and A. Pikrakakis, *Received signal strength fingerprinting-based indoor location estimation employing machine learning*. *Sensors*, 2021. **21**(13): 4605.
  14. Rizk, H., M. Abbas, and M. Youssef, *Device-independent cellular-based indoor location tracking using deep learning*. *Pervasive and Mobile Computing*, 2021. **75**: 101420.
  15. Ge, H., Z. Sun, Y. Chiba, and N. Koshizuka, *Accurate indoor location awareness based on machine learning of environmental sensing data*. *Computers & Electrical Engineering*, 2022. **98**: 107676.
  16. Xie, Y., T. Wang, Z. Xing, H. Huan, Y. Zhang, and Y. Li, *An improved indoor location algorithm based on backpropagation neural network*. *Arab J Sci Eng*, 2022. <https://doi.org/10.1007/s13369-021-06529-z>.
  17. Rohra, J.G., B. Perumal, S. J. Narayanan, P. Thakur, and R. B. Bhatt, *User localization in an indoor environment using fuzzy hybrid of particle swarm optimization & gravitational search algorithm with neural networks*, in *Proceedings of Sixth International Conference on Soft Computing for Problem Solving*. 2017. Singapore: p. 286–295.
  18. Rokach L. and O. Maimon, *Clustering methods*, in *Data Mining and Knowledge Discovery Handbook*, O. Maimon and L. Rokach, Eds. 2005, Boston, MA: Springer, p. 321–352.
  19. Omran, M.G.H., A. P. Engelbrecht and A. Salman, *An overview of clustering methods*. *Intelligent Data Analysis*, 2007. **11**(6): p. 583–605.
  20. Ghosh S. and S. K. Dubey, *Comparative analysis of k-means and fuzzy cmeans algorithms*. *International Journal of Advanced Computer Science and Applications*, 2013. **4**(4): p. 35–39.
  21. Izakian H. and A. Abraham, *Fuzzy C-means and fuzzy swarm for fuzzy clustering problem*. *Expert Systems with Applications*, 2011. **38**(3): p. 1835–1838.

## Appendix

$$\text{Accuracy} = \frac{TP + TN}{TP + FP + FN + TN} \quad (\text{A.1})$$

$$\text{Dunn} = \min_{1 \leq i \leq n} \left\{ \left\{ \min_{\substack{1 \leq j \leq n \\ i \neq j}} \frac{d(c_i, c_j)}{\max_{1 \leq k \leq n} (d'(c_k))} \right\} \right\} \quad (\text{A.2})$$

$$\text{Silhouette}(k) = \frac{1}{n} \sum_{i=1}^n \frac{b_i - a_i}{\max(b_i, a_i)} \quad (\text{A.3})$$

$$\text{Davies - Bouldin} = \frac{1}{n} \sum_{i=1}^n \max_{i \neq j} \left\{ \frac{\alpha_i + \alpha_j}{d(c_i, c_j)} \right\} \quad (\text{A.4})$$

$$\text{C\_Index} = \frac{S_W - S_{\min}}{S_{\max} - S_{\min}} \quad (\text{A.5})$$

$c_i$  and  $c_j$ , cluster centers

$d(c_i, c_j)$ , distance between  $c_i$  ve  $c_j$

$d'(c_k)$ , distance between records in set  $k$

$a_i$ , average distance of record  $i$  in the cluster from all other records in the same cluster

$b_i$ , minimum value of the mean distances of record  $i$  to the records in other clusters

$\alpha_i$ , average distance of records in cluster  $i$  from their cluster center

$S_W$  is the sum of the NW distances between all the pairs of points inside each cluster

$S_{\min}$  is the sum of the NW smallest distances between all the pairs of points in the entire data set

$S_{\max}$  is the sum of the NW largest distances between all the pairs of points in the entire data set.



## Research Article

## A real-time accurate positioning system using BLE and wireless mesh network in a shipyard environment

Nalan Özkurt <sup>a,\*</sup> , Hilal Kılınç <sup>b, c</sup> , Ekrem Özgürbüz <sup>d</sup>  and Hasan Hüseyin Erkan <sup>e</sup> 

<sup>a</sup>Yasar University, Department of Electrical and Electronics Engineering, Bornova/Izmir 35100, Turkey

<sup>b</sup>Sedef Shipbuilding INC. R&D Center, Tuzla/Istanbul 34940, Turkey

<sup>c</sup>Istanbul Cerrahpaşa University, Department of Maritime Transportation and Management Engineering, Istanbul, 34100, Turkey

<sup>d</sup>Sistematik OTVT, Atasehir/Istanbul 34750, Turkey

<sup>e</sup>SadeLabs, Narlıdere/Izmir 35000, Turkey

## ARTICLE INFO

## Article history:

Received 03 November 2021

Accepted 10 August 2022

Published 15 August 2022

## Keywords:

Digitalization

IoT

Positioning

Shipbuilding

Shipyard

## ABSTRACT

Digitalization of the shipyard environment is a challenging problem, and also it is necessary for competing the international ship manufacturers. Thus, this study introduced a real-time accurate positioning system that is an indispensable part of a digital manufacturing system. The system implementation and measurements took place in Sedef Shipyard, the largest shipbuilding facility in Turkey. Since the shipyard includes indoor and outdoor environments, Bluetooth Low Energy (BLE) systems provide the best solution for locating the staff. The most challenging problem is to determine the positions in the metallic surroundings. The constructed system solves this problem by placing gateways and sensors at essential locations and using a mesh network. With the designed user interface, the position of the staff can be monitored accurately in real time, and reports can be generated.

### 1. Introduction

The shipyard industry in Turkey has a history of more than 700 years and has experienced significant global growth, especially in recent years. As a result, the industry has sufficient facilities, technology, and workforce to make the most of global opportunities. However, the desired level of digitalization has not been reached yet, and therefore, R&D and innovation should be more important within the scope of Industry 4.0 [1].

A shipyard is a very complex environment where production parameters and dimensions change and a highly flexible working environment. This makes the control of production lines complex and requires the active participation of human resources in the business. Processes such as cutting sheet metal parts, bending-shaping-processing of unique pieces, pipe manufacturing, and combining different components with welding operations in the pool-sled will be implemented during the custom ship production. The most crucial factor determining work efficiency in these fields comes from the control and management of human-machine interaction. To achieve this goal, staff and equipment should be precisely localized in the shipyard. Wireless systems provide excellent convenience in environments such as shipyards, especially

inside ships. However, such environments are entirely covered with metals, which are very good conductors, causing communication not to be provided. Because metals cause the reflection of incoming waves, transmission cannot be made from entirely metal-covered rooms such as ships. Another problem is the multipath effect. Many copies of the transmitted signal reflected from the environment may reach the receiver at different times, causing the signal to be weakened or interfered [2]. Therefore the challenges in this positioning problem can be summarized as

- The field includes both outdoor and indoor areas,
- There is a mass of metallic surroundings caused by the ships and machines,
- There are several moving big machines such as cranes that may cause interferences.

A few studies have been done to cope with these difficulties and to model the communication channel in a ship or metal-dense environment. For example, Estes et al. modeled losses by performing narrowband experiments on American Navy ships. As a result of the experiments, they observed that even though there are losses, energy can pass through non-conductive openings [3]. In another study, the

\* Corresponding author. Tel.: +90-232-570-8244; Fax: +90-232-570-7000.

E-mail addresses: [nalan.ozkurt@yasar.edu.tr](mailto:nalan.ozkurt@yasar.edu.tr) (N. Özkurt), [hilal.kilinc@sedefshipyard.com](mailto:hilal.kilinc@sedefshipyard.com) (H. Kılınç), [ekrem.ozgurbuz@sistematikotvt.com](mailto:ekrem.ozgurbuz@sistematikotvt.com) (E. Özgürbüz), [hasan.erkans@sadelabs.com](mailto:hasan.erkans@sadelabs.com) (H. Erkan)

ORCID: 0000-0002-7970-198X (N. Özkurt), 0000-0001-6348-9753 (H. Kılınç), 0000-0002-6174-9221 (E. Özgürbüz), 0000-0002-9698-8513 (H. Erkan)

DOI: [10.35860/iarej.1018524](https://doi.org/10.35860/iarej.1018524)

© 2022, The Author(s). This article is licensed under the CC BY-NC 4.0 International License (<https://creativecommons.org/licenses/by-nc/4.0/>).

statistical model of the channel was obtained by making measurements in the ultra-wideband (UWB) frequency band in the ship cabin environment. As a result of experiments with the measurement system consisting of transceiver antennas, network analyzer, and computer, it has been shown that the propagation characteristics are different from indoor and outdoor [4].

Although the Global Positioning System (GPS) has become the standard for outdoor location detection, studies are still ongoing in indoor location detection. Since they offer higher sensitivity, lower cost, and ease of use properties, Wi-Fi, optical and Bluetooth Low Energy (BLE) systems are good choices for reliable indoor positioning applications [5]. Although a wide area is covered with a Wi-Fi network, its sensitivity is very low. In BLE 4.0 or 5.1 technologies, on the other hand, positioning accuracy, which can be lower than 1m, can be achieved even if the range is reduced to 75 meters. A wide range and high sensitivity are provided by Ultra-wideband communication UWB. However, its cost is higher than the others. Thus, it is suitable for applications where the location must be determined precisely. On the other hand, RFID can work more closely and is mainly used in stock counting, cafeteria, or door entry applications. Furthermore, BLE systems provide the highest battery life compared to power consumption. A detailed comparison can be found in [6]. Thanks to its advantages, BLE systems are used in different and challenging indoor positioning applications such as museums [7,8] and in an university campus by combining with different sensor data [9]. However, there is still a gap in literature about the studies in shipyards.

Therefore, an experimental staff positioning system based on BLE was constructed and analyzed to fill in the gap in the shipyard localization problem and to make a step in the digitalization of the shipyard environment. This system includes 400 location sensors, 4870 staff tags and 200 gateway over 191,000 m<sup>2</sup> Sedef Shipyard in Tuzla, İstanbul, Turkey. The number of gateways was selected heuristically to cover the shipyard area and show the project's feasibility. The system is flexible and the numbers can be easily increased. The gateways were located in open areas, inside buildings and inside ships to cover the working site. To make an empirical analysis of the BLE positioning system, some experiments were done and the results were discussed in this paper. The system also includes a graphical user interface that can be used to report the activities of the shipyard workers. Thus, the contributions of this study can be summarized as:

- To implement a digital system that determines the locations of the staff and machines in a shipyard environment,
- To show that the indoor location of a worker or machine in a metallic surrounding such as inside of a

ship can be found,

- To provide a user interface to track the movements of the workers and machines inside the shipyard campus.

After giving some necessary background information on indoor and outdoor positioning systems in Section 2, the construction of the system and the results of the measurements were demonstrated in Section 3. Finally, discussions are made and conclusions are drawn.

## 2. Background

### 2.1 Indoor/Outdoor Positioning Systems

Global Positioning System (GPS) has become the standard for outdoor location detection; however, studies are still ongoing for indoor location detection. There are more suitable methods such as Wi-Fi and optical systems, Bluetooth Low Energy (BLE) for indoor positioning applications [5]. Wi-Fi network provides a wide range of connection, but its sensitivity is very low. On the other hand, achieved positioning accuracy in BLE 4.0 or 5.1 technologies can fall below 1m, even if the range is lower than Wi-Fi. As mentioned earlier, Ultra-broadband communication UWB, has a wide range and high sensitivity, which makes it suitable for precise measurement. RFID is suitable for locating and counting stocks rather than indoor positioning. Moreover, BLE systems provide the highest battery life when compared in terms of power consumption [6].

### 2.2 Bluetooth Low Energy

BLE systems of especially widespread Internet of Things (IoT) applications are frequently used. Traditional BLE systems use star topology and are an important constraint coverage. To cope with this limitation, BLE 5.0 was proposed by first changing the physical layer signal bandwidth [5]. In addition, BLE 5.0 offers innovations in data rate, coverage and advertising channel functionality. As message capacity increases, two types of advertising channels are recommended. While the first channel is the same as the old versions, the second channel can also use 37 channels formerly known as data channels for messages [5]. Secondly, a mesh network is proposed to solve the coverage constraint. The advantage of the mesh network over the star network is that it can reach a wider coverage area over other devices on the network. Of course, for this structure to work efficiently, a more complex network management system should be defined [10]. The BT-SIG Smart Network Working Group was established at the beginning of 2015 to determine the standards for the mesh network structure [11]. Afterward, IETF (Internet Engineering Task Force) published the "IPv6 over Bluetooth Low Energy" RFC 7668 protocol to facilitate IoT capacity and access over the internet [11]. Thus, BLE nodes can communicate with each other via IPv6 packets and connections are made over IPSP (Internet

Protocol Support Profile) and use UDP protocol. This provides communication efficiency and allows routing at the IP layer [5]. BLE systems use the RSSI (Received Signal Strength Indication) technique, which measures the incoming signal strength among positioning techniques. To estimate the exact distance from a device using RSSI, an empirical model can be employed as in [12] that is expressed as

$$d = \alpha + \beta \left( \frac{R}{T} \right) + \gamma \quad (1)$$

where  $\gamma$  is the actual distance,  $\alpha$  and  $\beta$  are the empirical regression coefficients,  $R$  is the RSSI value and  $T$  is a reference value which is the received signal strength for a device located at 1 meter away from the receiver.

The further away the signal comes from, the weaker it will be. For example, the P mobile device in Figure 1 represents stations broadcasting on A, B, and C. In this case, there will be  $LS_1 < LS_3 < LS_2$  relationship between the signal strengths coming to the mobile device. However, reflection and multipath effects, especially indoors, can negatively affect the calculation [13, 14].

### 2.3 Mesh Network

In a mesh network structure, two types of nodes or gateways are used: routers (mesh routers, coordinators) and routers. The mesh network structure is shown in Figure 2. The coordinator is usually equipped with multiple wireless access devices and manages the routing algorithm. IEEE 802.11s standard defines integration of the WLAN link layer and mesh functions. Important mechanisms for spontaneous networking and message forwarding (routing) between mesh nodes, thus described in detail in IEEE 802.11s [15, 16]. An essential characteristic of the link determined in the model is the airtime cost (in  $\mu s$ ) that can be estimated as:

$$c_a = \left( O + \frac{B_t}{r} \right) \frac{1}{1 - e_{fr}} \quad (2)$$

where  $O$  is a constant for the channel access and MAC protocol overhead.  $B_t$  represents the test frame size,  $r$  denotes the test frame data rate (in Mbps), and finally  $e_{fr}$  stands for the expected frame error rate. As can be inferred from Equation (2), airtime cost depends both frame rate and error rate [15]. A more detailed analysis can be found in [17].

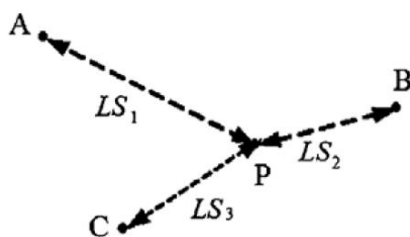


Figure 1. Positioning with RSSI [13]

There are various proactive, reactive or hybrid routing protocols proposed for mesh networks [18]. Among them, Zigbee is often used in case of low data rate and small packets. While routers constantly forward incoming messages to other routers, the coordinator sets up the routing structure and network and collects data from other routers. The Zigbee network automatically configures itself and dynamically reconfigures to repair itself if nodes are disabled or removed. As an interoperable standard, devices from many manufacturers can communicate seamlessly, helping Zigbee gain wide acceptance in home automation and industrial IoT. Costs are modest due to the many OEM equipment options on the open market [19].

### 3. Implementation of the System

Sedef Shipyard is the largest private shipyard in Turkey in terms of size and production capacity. The total area for production is 194,000 m<sup>2</sup> of which 51,000 m<sup>2</sup> is indoor production facilities in Tuzla plant. Thus, the positioning system was constructed using 200 gateways and 400 location sensors to locate 4870 staff wearing BLE 5 tags. The block diagram of the positioning system is shown in Figure 3.

The location sensors constantly broadcast their positions and tags scans the location sensor broadcasts around them. Then, tags collect location sensor ID and corresponding RSSI values and broadcasts them in Bluetooth range. The gateways receives the broadcast of the tags and send to server through Wi-Fi network of shipyard. Finally, the information is sent to Digital Shipyard platform. However, when the mobile receiver is inside the ships, gateways may not be able to reach Wi-Fi network because of the metallic surrounding. Thus, a mesh structure was constructed to gather data and reach wireless network. The mesh structure uses a routing algorithm as described in Figure 2.

Each gateway collects data from tags, if it could not connect to the wireless network, then sends data to another gateway in mesh. Travelling from one gateway to another, data reaches to coordinator gateway. Finally, the coordinator gateway sends all data gathered from the mesh network to the Wi-Fi network.

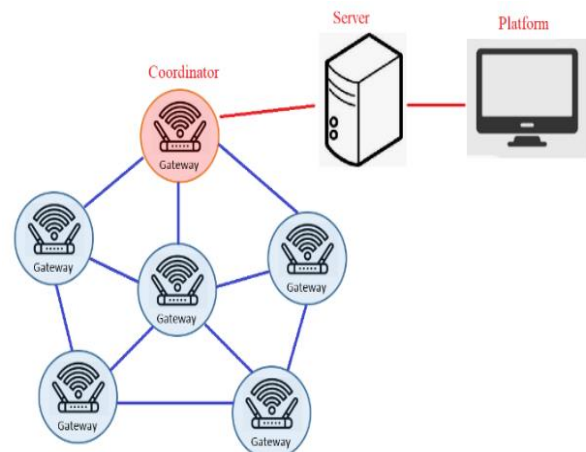


Figure 2. Mesh structure

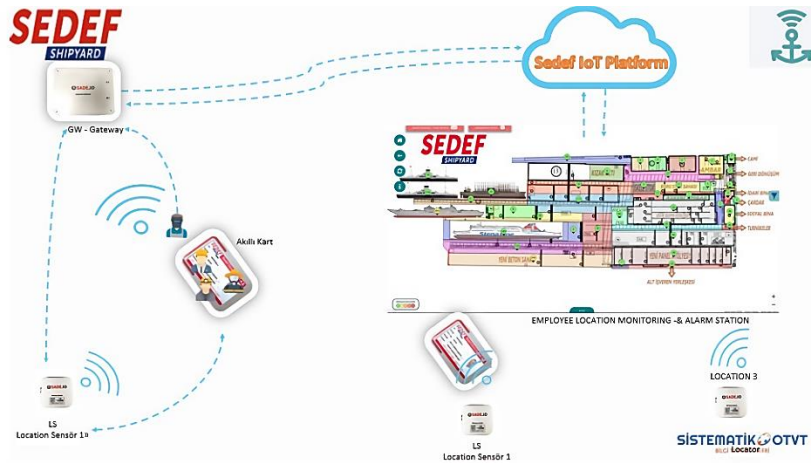


Figure 3. Real time shipyard positioning system

BLE technology is used in the design for staff identification cards and location sensors. The task of the ID cards is to listen to the broadcast emitted by the location sensors placed in the environment and to broadcast the ID information they receive from the nearest station together with their own information. As stated in the literature summary, power consumption, flash memory and RAM memory capacity are among the most important criteria for choosing a BLE device. The models produced by Nordic company produce the best circuits in terms of energy efficiency and the current drawn by the nRF chipset is much lower than the others.

Therefore, nRF52832 IC was used for ID cards in this study. The selected flash memory capacity is 256KB and the RAM memory capacity is 16KB, which is sufficient for the application to be made. PCB antenna was used for location sensors and personnel cards used in this project. It has a transmission power from -20 to +4dBm and thus provides a range of up to 40 meters. In order to ensure both long battery life and not enlarging the card sizes, 3V-3000mAh Lithium battery is used in the personnel cards and provides a lifetime of up to 3 years. Another important feature of the nRFxx

modules is the easy assembly of the circuit without the need for many peripherals. It can be used with application-specific software [20].

The gateways also have BLE infrastructure in order to access the broadcasts made by tags by using nRF52832 IC. Its range reaches up to 50m. Gateways have a Wi-Fi infrastructure and antenna so that the collected packets can be transmitted to the server. Since it is supplied with 220V AC, it includes a power circuit, but there is also a backup battery circuit with a rechargeable battery to prevent interruptions of up to 4 hours in power cuts. MicroUSB circuit is also added for updating and communication. It also has a GSM module designed with M95 integrated circuit for communication.

The locations of the gateways were demonstrated in Figure 4. In this figure, indoor gateways were shown in light blue, where outdoor gateways were denoted by blue and red. The dark blue gateways were located on newly constructed poles for the project. Similarly, Figure5 shows the positions of the location sensors. The indoor location sensors are denoted as light blue and outdoor location sensors in shipyard are shown as blue and red.

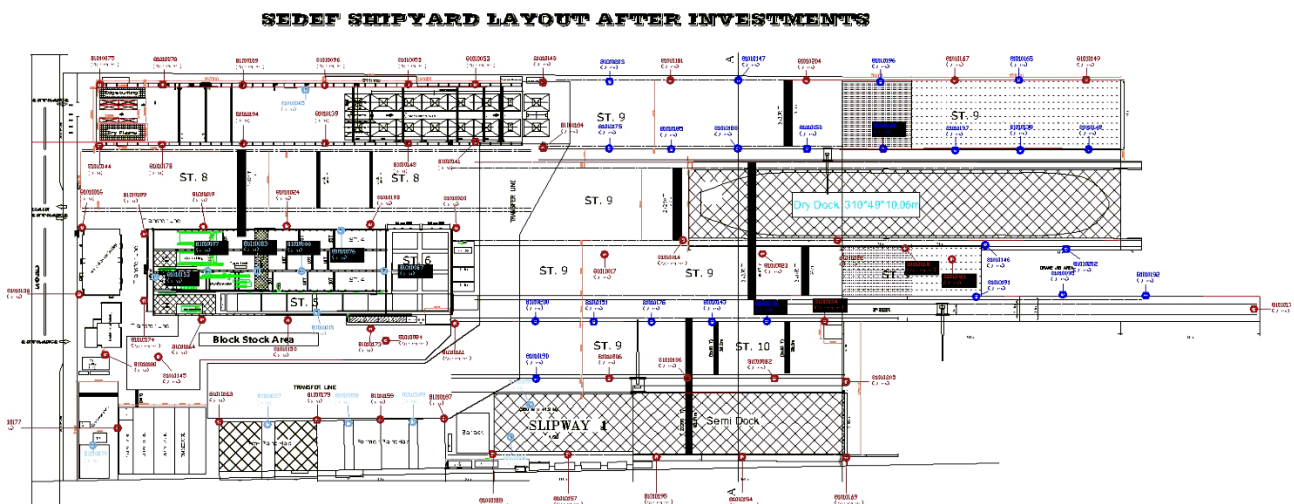


Figure 4. The locations of the indoor (light blue) and outdoor gateways (blue and red).

**SEDEF SHIPYARD LAYOUT AFTER INVESTMENTS**

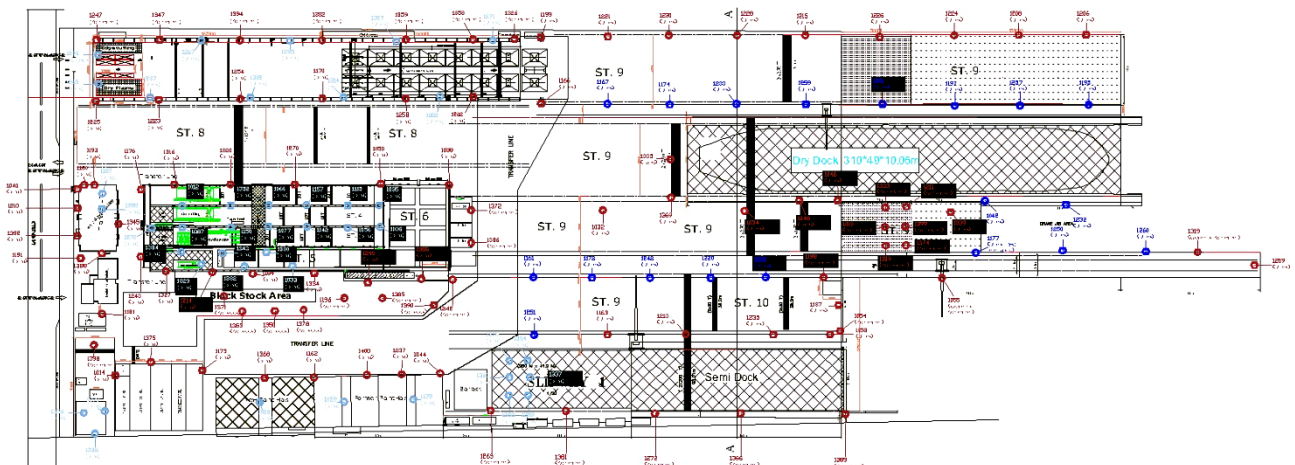


Figure 5. The indoor (light blue) and outdoor (blue and red) location sensors in shipyard

After the construction of the system, several on-site experiments were conducted to see the performance of the system. The tests included the followings:

- Adjustment of location sensor broadcast range in order to test the communication between the ID cards and location sensors. The broadcasting range adjustments were made, and the positions were changed if necessary to cover all areas.
- ID Card-Gateway communication tests to see if gateways can collect the ID and location information through BLE.
- Gateways-Server communication test which observes whether or not all the gateways can send the collected info directly or through the mesh network. Fine-tuning of the gateway locations were completed after this step.
- Staff position location experiments were implemented by walking an employee with an ID card following predefined routes. Then the locations were downloaded from the server to detect the accuracy of the locations. Figure 6 shows one of these experiments. In this

experiment employee left the main building at 11:15 following the orange line and yellow stars show the positions of the location sensors which are communicated. The person reaches dock at 11:27 and then moves back with another route which is shown in red. Finally, he completes the experiment at 11:55 at the main building.

- In the final test, more ID cards were given to employees and their positions were detected via the software interface of the system. Sample screens of the systems were given in Figure 7. In Figure 7.a the numbers inside the green and red markers show the position and the number of the of the workers inside the ship in Figure 7.b. is the list and details of the locations. Similarly, Figure 7.c and 7.d illustrates the workers inside the administrative building. Finally, Figure 7.e shows a sample view from the menus. Therefore, the location of individual worker, or all workers can be monitored in once, the details of the recordings can extracted to track the activities.



Figure 6. Experiment map for positioning accuracy

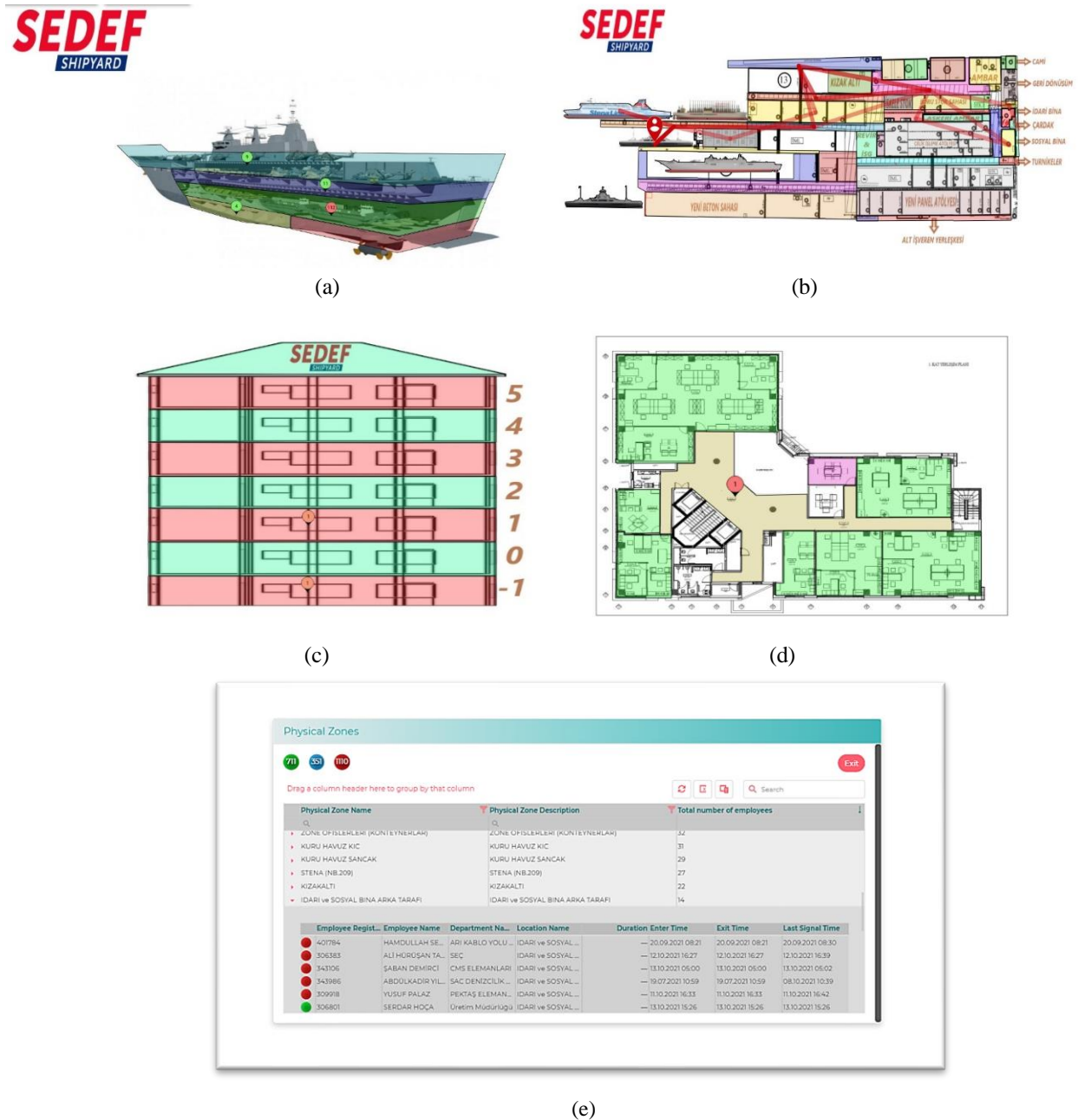


Figure 7. Graphical user interface of positioning system: a) Total number of workers inside the ship, b) tracking of a worker inside ship, c) number of workers inside the entire building, d) number of workers inside one floor of the building, e) a screenshot from user console

#### 4. Discussions

A challenging case of indoor positioning was studied in this project. For increase the productivity and also safety, the workers and the machines should be traced inside the shipyard environment. Especially, determining the accurate locations inside the ship is a difficult problem. As explained in the previous sections with the combination of BLE, Wi-Fi and Zigbee technology, these challenges were overcome. The position and movements of the workers inside the metallic compartments of the ship were determined as illustrated in Figure 7.

Therefore, the advantage of the proposed method over

other indoor positioning systems lies in the usage of a hybrid approach to cover the entire shipyard which includes a large open area, inside of the building and inside of a metallic ship. One limitation may be the resolution of the measurement when compared with UWB communication systems. The proposed system will not offer a centimeter-level resolution, however, determining in which room the workers are is sufficient in practice.

#### 5. Conclusions

This study introduces a real time positioning system which is designed and implemented in Sedef Shipyard. Locating the

staff and the machines in this huge area is a tremendous step in digitalizing the shipyard environment. The problem is challenging due to surrounding metal density, open and closed areas and mobile work machines. It is shown that an accurately working system was constructed by using and hybrid system using BLE, Zigbee and Wi-Fi via mesh networks.

### Declaration

The authors declared no potential conflicts of interest with respect to the research, authorship, and/or publication of this article. The authors also declared that this article is original, was prepared in accordance with international publication and research ethics, and ethical committee permission or any special permission is not required.

### Author Contributions

N. Ozkurt developed the infrastructure methodology of digitalization the shipyard. H. Kilinc provided all shipbuilding data and the compatibility of the yard for the process and made literature search. E. Ozgurbuz created the interface that performed the analysis. H. Erkan developed the electronic hardware of the shipyard substructure. All Authors wrote the manuscript together.

### Acknowledgment

This work was supported by the TUBITAK under TEYDEB 1511 project (project no: 1190128), Turkey.

### References

1. Arisoy, F., Kilinc, H., Cil, İ., *An Analysis on Industrial Internet of Things in Digital Transformation of Shipyard Industry in Turkey*, Global Journal of Computer Sciences: Theory and Research, 2021. **11**(2), p. 67–87.
2. Haupt, R.L., *Wireless Communications Systems: An Introduction*. 2019, USA: Wiley – IEEE Press.
3. Estes, D.R.J., Welch, T.B., Sarkady, A.A., Whitesel, H., *Shipboard radio frequency propagation measurements for wireless networks*, MILCOM Proceedings Communications for Network-Centric Operations: Creating the Information Force, USA, October 2001. **1**: p. 247-251.
4. Zhai, S., Jiang, T., Li, D., Li, B., *Statistical Characterization of UWB Propagation Channel in Ship Cabin Environment*, 2012 IEEE International Conference on Communications (ICC), Canada, June 2012. **1**: p. 6386-6390
5. Darroudi, M.S. and Gomez, C., *Bluetooth Low Energy Mesh Networks: A Survey*, Sensors, 2017. **17** (7), p.1467.
6. Çil, İ., Arisoy, F., Kılınç, H., Yunus, A., *A comparative analysis of indoor positioning technologies in shipyard digitalization context*, Journal of Marine Technology and Environment, 2022. **1**, p.15-25.
7. Spachos, P., Plataniotis, K.N., *BLE Beacons for Indoor Positioning at an Interactive IoT-Based Smart Museum*, IEEE Systems Journal, 2020. **14**(3), p. 3483-3493.
8. Handojo, A., Octavia, T., Lim, R., Anggita, J.K., *Indoor positioning system using BLE beacon to improve knowledge about museum visitors*, TELKOMNIKA Telecommunication, Computing, Electronics and Control, 2020. **18**(2), p. 792-798.
9. Montecchiari, L., Trotta, A., Bononi, L., Di Felice, M., *Bluetooth Mesh Technology for the Joint Monitoring of Indoor Environments and Mobile Device Localization: A Performance Study*, 2022 IEEE 19th Annual Consumer Communications & Networking Conference (CCNC), 2022. **1**: p. 193-199.
10. IETF, IPv6 over Bluetooth Low Energy, [cited 2020 May]; Available from: <https://tools.ietf.org/html/rfc7668>.
11. Bluetooth SIG. *Specification of the Bluetooth System, Covered Core Package; Version 5*. 2016, USA: Bluetooth Special Interest Group.
12. Ramirez R, Huang CY, Liao CA, Lin PT, Lin HW, Liang SH. *A Practice of BLE RSSI Measurement for Indoor Positioning*. Sensors, 2021. **21**(15): p.5181.
13. Sakpere, W., Adeyeye-Oshin, M., Mlitwa, N.B.W., *A state-of-the-art survey of indoor positioning and navigation systems and Technologies*, South African Computer Journal, 2017. **29** (3): p. 145-197.
14. Cao Y, Kandula H, Li X. *Measurement and Analysis of RSS Using Bluetooth Mesh Network for Localization Applications*. Network. 2021; 1(3): p.315-334.
15. Rethfeldt M, Brockmann T, Beichler B, Haubelt C, Timmermann D., *Adaptive Multi-Channel Clustering in IEEE 802.11s Wireless Mesh Networks*, Sensors, 2021. **21**(21): p.7215.
16. Hernández-Solana, A., Pérez-Díaz-De-Cerio, D., García-Lozano, M., Bardají, A.V., Valenzuela, J., *Bluetooth Mesh Analysis, Issues, and Challenges*, IEEE Access, 2020. **8**, p. 53784-53800.
17. Akyildiz, I.F., Wang X. and Wang W, *Wireless Mesh Networks: A Survey*, Computer Networks Journal, 2005. **47** (4): p.445-487.
18. Vijayakumar, K.P, Ganeshkumar, P., Anandaraj, M., *Review on Routing Algorithms in Wireless Mesh Networks*, Int. Jour. of Computer Science and Telecommunications, 2012. **3**(5): p. 87-92.
19. Zigbee vs. Bluetooth: Choosing the Right Protocol for Your IoT Application, [cited 2020 June]; Available from: <https://www.digi.com/blog/post/zigbee-vs-bluetooth-choosing-the-right-protocol>.
20. nRF52832 Product Specification, [cited June 2020], Available from: [https://infocenter.nordicsemi.com/pdf/nRF52832\\_PS\\_v1.4.pdf](https://infocenter.nordicsemi.com/pdf/nRF52832_PS_v1.4.pdf)